1958

Proceedings

SYMPOSIUM ON RIGID RADOMES

Lincoln Laboratory

MASSACHUSETTS INSTITUTE OF TECHNOLOGY

Unclassified

3?0

Unclassified

Volume 1 of 2

8, 9, 10 September 1958

Proceedings

SYMPOSIUM ON RIGID RADOMES

Issued 15 October 1958

Lincoln Laboratory

MASSACHUSETTS INSTITUTE OF TECHNOLOGY

Lincoln Laboratory is a technical center operated by Massachusetts Institute of Technology with the joint support of the U.S. Army, Navy and Air Force under Air Force Contract AF 19(122)-458.

Unclassified

PREFACE

Advancements in the development of rigid radomes for ground environments have been rapid since Lincoln Laboratory became actively involved in 1953. The necessity for sheltering very large antennas and for transmitting ever higher frequencies has compounded the technical problems relating to geometry, materials, and construction so that literally hundreds of engineers in the United States and Canada are now fully involved in producing solutions. The task of keeping these people informed of system requirements and of recent developments has not been easy.

Therefore, with the endorsement of the Joint Services Advisory Committee, Lincoln Laboratory conducted a Symposium on Rigid Radomes on 8, 9, and 10 September 1958 at M.I.T.'s Kresge Auditorium in Cambridge, Massachusetts. Its expressed purpose was to provide an opportunity to present and to discuss in an informal atmosphere the systems requirements and technologies that relate to the development of large rigid radomes for ground environments. Areas of interest were: Systems requirements, environmental conditions, electrical performance design, electrical measurement techniques, mechanical design, structural analysis, and materials and processes.

The response was excellent. We are indebted to the speakers for their careful preparation and for the quality of their papers. And to the session chairmen for the skill with which they moderated each session. But the success of the symposium was also due in large part to the enthusiastic participation of the 200 attendees whose questions and observations contributed importantly to the vitality of the meetings.

Now that these Proceedings are being disseminated as the final act of the symposium, it seems appropriate to give recognition to those who were most instrumental in planning and coordinating the affair. I refer to the Symposium Committee composed of A. Cohen, P. Davis, M. M. Hannoosh, A. E. Johnson, and S. C. Nilo.

J. A. Vitale
Division Head

October 15, 1958

PROGRAM

and

TABLE OF CONTENTS

SESSION I
SYSTEM REQUIREMENTS

Chairman: Prof. W.H. Radford
Associate Director, Lincoln Laboratory

SESSION II
ELECTRICAL THEORY AND MEASUREMENT

Chairman: Dr. G.A. Miller
National Research Council of Canada

*Speaker

SESSION III
STRUCTURAL THEORY AND MECHANICAL DESIGN

Chairman: Prof. J. Kempner
Polytechnic Institute of Brooklyn

SESSION IV
MATERIALS DEVELOPMENT

Chairman: Prof. Albert G.H. Dietz
Massachusetts Institute of Technology

FIELD TRIP TO LINCOLN LABORATORY

Open house at radome facilities of Lincoln Laboratory.

Informal discussion groups:

Radome System Requirements and Electrical Design
Discussion Leader – Mr. A. Cohen

Structural Design and Materials Developments
Discussion Leader – Mr. S. C. Nilo

*Speaker

ANALYTICAL METHODS FOR THE PREDICTION OF RADOME PERFORMANCE[+]

T.E. Tice, P.D.Kennedy, J.R.Baechle, S.N.C. Chen

Antenna Laboratory, Department of Electrical Engineering

Ohio State University, Columbus, Ohio

ABSTRACT

The three most important detrimental effects of a radome on a radar system are the loss of signal power, the increase in side lobe level, and the boresight error. For large radomes where optical methods are applicable, analysis of these effects is often based on ray-tracing methods and the electrical properties of infinite plane dielectric sheets, while more rigorous electromagnetic formulations must be used for very small radomes. A different approach is called for in the analysis of radomes where the effects of structural members predominate. Here, one studies the currents induced on the structural members and the consequent scattered radiation.

[+]Note: The research described in this paper was performed under Contract AF 30(602)-1620 between the Rome Air Development Center and The Ohio State University Research Foundation.

ANALYTICAL METHODS FOR THE PREDICTION

OF RADOME PERFORMANCE †

T.E.Tice, P.D. Kennedy, J.R. Baechle, S.N.C. Chen

Antenna Laboratory, Department of Electrical Engineering

Ohio State University, Columbus, Ohio

INTRODUCTION

Before going into the details of radome analysis, it may be of value to very quickly review the effects of a radome on a radar system in order to bring into focus the reasons why certain properties are of interest. It is probably safe to say that the three most important of the radome's detrimental effects are the loss of signal power, the increase in sidelobe level, and the tracking error or boresight shift, although the one which would be of most interest would depend on the individual application. To take an example of signal loss, a radome which attenuates the outgoing and incoming signals by 0.5 db is equivalent to a loss of transmitter power of 21% or a reduction of detection range of 6%. As for sidelobe level, an increase of one or two db means that much increase in noise level when there are ground reflections, celestial noise sources, or jamming sources present. The effects of tracking error on a fire control or missile guidance system are obvious, and this factor would probably govern the design of radomes for this type of radar.

†Note: The research described in this paper was performed under Contract AF 30(602)-1620 between the Rome Air Development Center and The Ohio State University Research Foundation.

In the history of airborne radomes, the emphasis has been almost exclusively on self-supported, dielectric structures of uniform thickness and cross-section, and this background applies directly to the air-inflated and rigid foamed plastic ground-based radomes. On the other hand, the introduction of large radomes incorporating substantial rib structures has required a new body of theory which recognizes the predominant effect of the structural members. The analysis of these two distinct radome types will be discussed separately.

RADOMES WITH UNIFORM WALLS

While few radomes consist entirely of flat dielectric sheets, much can be learned about the design of practical radomes from a study of the electrical properties of infinite plane sheets. Not only is such information helpful in a preliminary design, but it can be used in more elaborate analysis procedures. The analysis of the transmission and reflection of electromagnetic waves by such dielectric sheets is essentially a straightforward problem based on Maxwell's equations and the necessary continuity of the electric and magnetic fields at the boundaries between the various media. As with many other problems which are simple in concept, many analytical complications arise when there are several such boundaries, and various artifices such as reflection and transmission factors, etc., have been devised to permit systematic analysis of complex situations. (See Reference 5, Chapter 2, by J. H. Richmond). It is not necessary to go into this here because the characteristics of many configurations have been tabulated for convenient use in radome design.[1,2,3,4,5]

Dielectric sheets for radome applications may be divided into three catagories: electrically thin sheets, which are less than 0.1 wavelength thick (as measured in the dielectric); half wave homogeneous sheets, which are designed to be a multiple of a half wavelength in thickness at some particular angle of incidence; and multi-layer sheets, of which a variety of types have been designed to combine superior mechanical properties and good electrical characteristics.

Mechanical strength is usually the limiting factor in the application of electrically thin radomes; this in turn is governed by the wavelength at which the radome is to be used. However, if a thin wall design can be used, high transmission and small insertion phase differences are readily obtained. This is illustrated by Fig. 1, which gives the transmission through two types of walls which might be used for ground-based radomes: the thin fabric-reinforced flexible sheet of an air-inflated radome ($d=0.0156\lambda$, $\epsilon_r=3.5$ $\lambda_o= 4$ inches) and a rigid, foamed plastic construction ($d=0.12\lambda$, $\epsilon_r = 1.2$, $\lambda_o = 25$ inches). (A distinction must be made between perpendicular and parallel polarization[6], and the coefficients are not the same for these two cases. Perpendicular polarization is used for illustration in this paper, and the coefficients for the other polarization are similar.)

If mechanical requirements and operating frequency rule out a design which can be described as electrically thin, a second possibility is a half-wave sheet, which derives its desirable electrical properties from the cancellation of reflections from the front and rear surfaces of the sheet. Thus, it is possible to make the transmission coefficient very high at some particular wavelength, λ_o, and angle of incidence, θ_o.

For a lossless sheet, the thickness giving this result is

$$t = \frac{n\lambda_0}{2\sqrt{\epsilon_r - \sin^2 \theta_0}}$$

where n can be any positive integer. Fortunately, when this is done the properties are fairly satisfactory over a range of incidence angles, as illustrated by Fig. 2. It will be noted that the characteristics are not as desirable as those of the thin wall, but may still be adequate for many purposes.

The multilayer dielectric sheets are intended to have good electrical properties with a higher strength-to-weight ratio than an equivalent solid sheet. The sandwich construction combining strong and relatively heavy skins separated by a light core material such as plastic foam or honeycomb is typical of this type of radome, although other types of sandwiches are in use.

Together with its mechanical advantages, the sandwich type of radome wall can be designed for broadband operation by the use of several adjacent sandwiches. Also other configurations, such as ones having a denser core, for the single sandwich may have improved electrical and mechanical properties over the half wave wall of comparable weight.

Fig. 3 shows the calculated transmission properties of a panel similar to one which was intended for a 55 ft., S-band radome. It will be noted that at the higher incidence angles these characteristics deteriorate more rapidly than the previous examples but that for angles of incidence encountered in practice they compare quite favorably.

The material just covered has presented typical properties of flat dielectric sheets, but this is obviously only the first step in the prediction of

radome performance. The remaining elements of the procedure will be seen to follow logically from this statement of the most common method of analysis: the aperture excitation of the antenna is assumed or measured and the modification of this excitation by the radome is determined. For large antennas and radomes, this can be done by quasi-optical principles which essentially involve passing rays from various parts of the antenna aperture through incremental sections of the radome under the assumption that the infinite-sheet characteristics will apply for each such incremental area. To do this, it is necessary to investigate the angle of incidence of each ray. This task can become quite complex with small streamlined airborne radomes, but is straight-forward for the spherical shape which is typical of ground radomes. As a matter-of-fact, the geometry of the sphere is very favorable in that the central ray of the antenna always encounters the radome wall at normal incidence if the antenna gimbals are at the center of the sphere and symmetry exists for the other rays of the antenna.

However, once the incidence angles of the various rays and the corresponding attenuations and phase delays have been noted, this information leads to a representation of an equivalent or modified antenna aperture, possibly of a number of radiators whose phases and amplitudes have been adjusted according to the original excitation and the effects of the radome, and it remains to compute the radiation pattern of this modified aperture. (See, for example, Reference 7 and Reference 5, Chapter 13 by Samuel Wolin.) This is done by conventional antenna theory and leads to a vector sum of the respective field intensities evaluated at the various points in the far-field region of interest.

This is a fairly complete analysis and can be interpreted in terms of signal loss, pattern distortion, tracking error, or other characteristics as may be required.

Where tracking error is the problem of greatest interest, it is much simpler and more profitable to apply ray-tracing techniques exclusively rather than to attempt to combine them with radiation pattern calculations. (See, for example, Reference 5, Chapter 4 by H. A. Schetne.) For example, one can take the central ray of the antenna and observe its deflection upon its passage through the radome. For this purpose only Snell's law of refraction and simple geometrical principles are required, although the computation must be carried out very carefully so that the small deviation of the ray will be correctly determined. The results of some calculations of this type which were carried out for configurations intended to represent typical foamed plastic radomes are presented in Fig. 4. Several points were also calculated by finding the insertion phase difference for several rays and the resultant tilting of the antenna's equiphase contours. These points agree fairly closely with the calculations of the refraction of the central ray only.

For small antennas and radomes, the optical methods described above cannot be used, and the problem must be attacked by a more exact formulation of the electromagnetic problem. This is particularly true when the antenna and radome are in very close proximity. Fortunately this is not the case for large ground-based radomes, and we need not be concerned with this problem here.

STRUCTURALLY-SUPPORTED RADOMES

The foregoing section describes analytical methods that apply primarily to radomes with uniform walls such as the widely used air-inflated radomes or the rigid foamed plastic types now being developed. In contrast, a completely different approach is employed in the analysis of radomes which consist of a structural frame covered with thin plastic sheets. In such cases, the structure itself is responsible for most of the radome's electrical effects, and attention is therefore focussed on the disturbances in the electromagnetic fields caused by the ribs and other parts of the structure. Essentially, these effects are explained and analyzed in terms of the currents that are induced on or within the ribs by the fields of the antenna. These currents are required in order to satisfy the boundary conditions in the electromagnetic formulation of the problem, and it is the radiation from them that distorts the antenna characteristics. This radiation is frequently referred to as "scattered" radiation, and the addition of it to the original undisturbed fields gives the field configuration exists when the radome or other "scatterer" is present.

The currents induced on a conducting surface are frequently encountered. For example, if there is a plane wave incident on a plane conducting sheet, it is known that the electric field must be zero at this surface and, as a consequence, the magnetic field just outside the surface is twice that of the undisturbed incident field. Furthermore, electric currents must flow on the conducting surface in order to satisfy Ampere's law. It is possible and correct to visualize these currents radiating in the absence of the metal sheet; that is, both back toward the source of energy and in the original direction of propagation.

The latter radiation will cancel the incident energy and produce zero net field in the space beyond the metal sheet. (At least this is one way of looking at it.) With this brief review we can discuss what happens when a conducting cylinder is placed in an electromagnetic field. As might be expected, the current is more intense on the side toward the source, and in the case where the electric field is parallel to the axis of the cylinder, the currents are also parallel to the axis. If the magnetic field is parallel to the axis, the electric current runs circumferentially around the cylinder, and by using the equivalence of a current loop to a magnetic dipole, it can be said that there is magnetic current parallel to the cylinder's axis.

The volume currents which flow inside a dielectric body when it is placed in an electromagnetic field are somewhat more difficult to visualize than surface currents, but like them, they are necessary to satisfy the boundary conditions of the problem and are responsible for the scattered radiation.

However, for purposes of radome analysis, we are not so much interested in these currents themselves as in their effects, and for this reason it is most convenient to assume an equivalent current along the axis of the cylinder which has the same radiation as the actual current and then to relate this equivalent current to the incident field. Thus, a rib of a given type is characterized by its "induced current ratio", which is the ratio of the total effective current in the rib to the total equivalent current in a strip of the aperture having the same width as the rib itself. This definition can be applied to ribs of all shapes and materials placed in fields of any polarization and, furthermore, the current ratio can be evaluated by fairly simple experiments.

To illustrate some typical values for this ratio, we shall now present data for metal and dielectric cylinders which has been obtained analytically and checked experimentally[9]. Fig. 5 gives data which applies to metal ribs. It is apparent that the induced current is greater when the electric field is parallel to the cylinder axis than when it is perpendicular to the axis. Furthermore, the use of a smaller number of larger ribs would be advantageous in comparison with a larger number of smaller ribs having the same total projected area since the total induced current would be less. Fig. 6 shows the induced current ratio for dielectric ribs. Here, both the dielectricconstant and diameter must be considered, and it will be noted that the currents are comparable for both polarizations. In addition to these cylinders, for which the results were mainly obtained by calculation, ribs with rectangular cross-sections have been studied experimentally, and data on the induced current ratio as a function of both width and depth are given in Reference 8.

The possibility of reducing the scattering from a metal cylinder by surrounding it with a concentric dielectric sleeve has been investigated analytically and experimentally, and the general results are indicated by Figs. 7 and 8. It will be noted that the scattering from smaller cylinders can be reduced more than that from larger cylinders, and calculations show that the degree of improvement , for any given core diameter, does not vary much with the dielectric constant of the sleeve, although, as would be expected, the optimum sleeve diameter is greater for a lower dielectric constant. Unfortunately, the sleeve has the disadvantage of increasing the scattering when the electric field is perpendicular to the cylinder axis, and whether this difficulty can be minimized is not yet known.(The data given is for parallel polarization.)

The data presented on the induced current ratio was obtained by analysis of an infinite cylinder, so it remains to examine the radiation from a finite cylinder such as a radome rib. When a cylinder at least several wavelengths long is being considered, the currents on the object are very nearly the same as if the object were a section of an infinitely long cylinder. With this assumption, the radiation from a group of ribs can be determined by linear antenna theory. Consequently, when an array of parallel ribs is considered, the pattern is quite directive in a plane parallel to the ribs and, in addition, a series of lobes is observed in a plane perpendicular to the ribs because of the interference between the radiation from the various members. This is illustrated by Fig. 9. By these considerations, the scattered fields can be described qualitatively, and the induced current ratio is the key to the quantitative evaluation. The standard example for explanation here is a plane array of several equally-spaced and parallel ribs placed in an antenna aperture. The first step in the analysis is to visualize the aperture as being composed of a number of strips having the same width as the radome. With a proper assumption of the antenna excitation, the equivalent currents on the various strips can be found, and this establishes a figure for the total antenna signal, that is, the main beam signal strength. The induced currents in the various ribs are then found as the product of the equivalent current of the excitation and the induced current ratio of the type of rib in question. The sum of the currents in the various ribs then establishes a figure for the scattered radiation. A numerical example of this type of calculation is given in reference 8.

This procedure is also used in one method of measuring the induced current ratio. A simple array of parallel ribs and an antenna is arranged as

shown in Fig. 9 with the spacing between ribs chosen so that the secondary lobes of the scattered radiation can be easily distinguished from the antenna radiation. The pattern of this assembly is recorded and the intensity of the scattering relative to the antenna signal is noted. With the dimensions of the antenna and ribs taken into account, this figure serves to evaluate the induced current ratio for the ribs under test.

When the ribs do not form such a regular pattern, but rather the irregular patterns which are typical of practical space-frame designs, the analysis is much more complicated but not really different in principle. Basically, it is necessary to find the current on each rib by a consideration of its excitation and induced current ratio. In general, a given rib will be neither exactly parallel nor perpendicular to the electric field, and there will be two types of scattering from it - one due to the parallel component and the other due to the perpendicular component. Now, with these various currents established, it remains to integrate their effects in order to determine the total scattered field. This is a formidable task under any circumstances and perhaps would be feasible only with a great deal of simplification.

One method which has been devised for doing this makes use of a geometrical description of the constant-phase and constant-amplitude contours of the radiation from each rib, and a systematic procedure for adding up the contributions of each rib to the total field at any specified test point. The spacing of the constant-amplitude contours is determined by the length of the rib, while their rotation corresponds to the inclination of the rib. On the other hand, the orientation of the constant-phase contours depends on the position of the center

of the rib relative to the center of the array, and the spacing between them is determined by the distance in wavelengths between the origin and the rib center. With the radiation of each rib described in terms of the quantities mentioned above, the computation proceeds by choosing a point at which the radiation is to be found, and then calculating the in-phase and quadrature components of each rib's contribution in turn by formulas which are derived from the geometrical description of the contours. The details of describing each rib's radiation and the computer procedure for computing the total pattern are described in Reference 9.

One application of this procedure would occur in studying the advantages of a "random" rib geometry over a more uniform rib geometry. It is apparent that extreme concentrations of scattered energ , such as occur with a perfectly regular array of parallel ribs, can be avoided to some extent, but the degree of improvement depends on many factors, such as the lengths and spacings of the ribs, besides the extent to which the orientation of the ribs is made non-uniform.

We have been referring to the scattered radiation as if it existed independently of the radiation from the antenna itself; this it does not actually do, and of course the real problem is to predict the antenna pattern after the radome has been put in place. This, by the definition of scattered energy, is the sum of the incident, or undisturbed, signal and the signal reradiated, i.e. scattered, by the parts of the radome; and in principle the total field can be found by adding these two components at each point of interest. To do this, one must make the best possible assumption for the antenna excitation,

compute the antenna radiation by the standard methods and the scattered radiation by the methods outlined above, and then find the vector sum of these at each point of interest. This point of interest may be in the center of the antenna beam, in the sidelobe region of the antenna, or at the ''cross over'' point if a tracking system is being studied. At the time of this writing, the manner in which the currents induced in a space-frame radome introduce boresight error is not understood very well, but the most promising theory is that the error is due to the non-uniformity of the radome. Whether the tracking depends on phase comparison or amplitude comparison or whether simultaneous or sequential lobing is used, several different signals from slightly different antenna arrangements must be compared, and it is possible that the error may be introduced as the antenna ''looks'' through two different sections of the radome. If the problem can actually be analyzed by this approach, the procedures relating to the induced currents and their effects will be directly applicable.

ACCURACY OF PERFORMANCE PREDICTIONS

In discussing the degree to which analytical predictions will be borne out by experiment, the conclusions will be somewhat different for the two general classes of radomes discussed, principally because a greater amount of experience has been accumulated in the application of radomes with uniform walls. The tabulated characteristics of eletrical characteristics can be used confidently under ordinary circumstances, and the semi-optical methods of analysis will be successful where the criteria of having a large antenna and radome are met.

The prediction of the performance of structurally-supported radomes is far from an exact science for two reasons: first, the unknown (although measurable with great difficulty) nature of antenna characteristics in some cases, and second, several factors which are recognized but not yet fully understood in the present state of the analysis. The former is especially true when changes in the side lobe level are investigated. If the antenna sidelobes are more the result of construction errors than of deliberate design, then their amplitude and phase cannot possibly be known with enough accuracy to permit adding the scattered signal to get an accurate picture of the sidelobe structure with the radome in place. However, a calculation of the scattered signal can be used to set an upper limit on the sidelobe signal increase. If this can be accepted as a useful result, a comparative evaluation of competitive radome designs can be made accurately. The same general remarks apply to the calculation of signal attenuation except that somewhat better results can be obtained for this quantity because the antenna main lobe is much less sensitive to antenna errors.

Further refinements are being made in the theory which should eventually improve the accuracy of predictions. These relate principally to the change in the scattering from a rib when it is not normal to the direction of propagation - the original analysis was limited by this assumption. In addition, the scattering from the individual ribs is being exhaustively studied. Still another question which will be answered conclusively is that of electrical interaction between ribs in the array. If these points can be successfully resolved, the prediction of structurally-supported radome performance will be limited main-

ly by the accuracy of our knowledge about the excitation of the antenna with which the radome is to be used and by any voluntary restriction of effort in carrying out detailed analyses.

REFERENCES

1. Radar Scanners and Radomes, McGraw-Hill Book Company, Inc., 1948.
2. "Graphs of Transmission and Phase Data of Plane Dielectric Sheets for Radome Design", Report No. NADC-EL-5313, 1 July 1953, U.S. Naval Air Development Center.
3. "Tables of Transmission and Reflection Coefficients of Lossy, Symmetrical Dielectric Radome Sandwiches", Report No. NADC-EL-52188, 22 Oct. 1953, U. S. Naval Air Development Center.
4. Webster, R. E., Moore, D. P., "Transmission Coefficients of Elliptically Polarized Waves Incident on Homogeneous Isotropic Panels", Report No. 663-5, 31 December 1956, Antenna Laboratory, The Ohio State University Research Foundation; prepared under Contract AF 33(616)-3277, Air Research and Development Command, Wright Air Development Center, Wright-Patterson Air Force Base, Ohio. (Report Confidential)
5. Techniques for Airborne Radome Design, Technical Report No. 57-67, September 1957, Wright Air Development Center, ASTIA Document No. AD 142 001. (Report Confidential)
6. Stratton, J. A., Electromagnetic Theory, McGraw-Hill Book Company, 1941.

7. Tricoles, G., "A Physical Optics Radome Error Prediction Method", Proceedings of The OSU-WADC Radome Symposium, June 1957, ASTIA Document No. AD 130 930. (Report Confidential)

8. "Effects of Radome Discontinuities on Antenna Patterns", Final Engr. Report 722-4, 31 December 1957, Antenna Laboratory, The Ohio State University Research Foundation; prepared under Contract AF 30(602)-1620, Rome Air Development Center, Griffis Air Force Base, New York.

9. "Effects of Radome Discontinuities on Antenna Patterns", Interim Engr. Report 722-6, 1 July 1958, Antenna Laboratory, The Ohio State University Research Foundation; prepared under Contract AF 30(602)-1620, Rome Air Development Center, Griffis Air Force Base, New York.

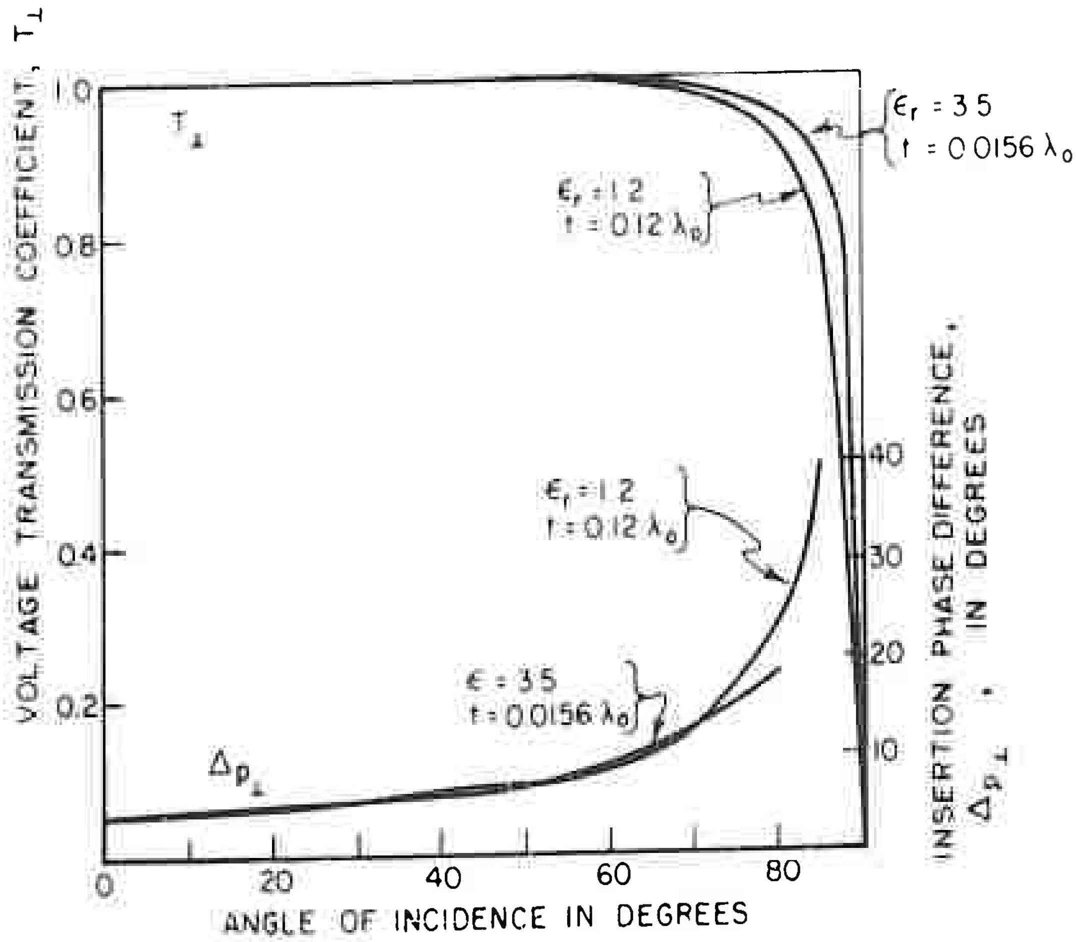

FIG. 1. CHARACTERISTICS OF LOSSLESS THIN RADOME WALLS (PERPENDICULAR POLARIZATION).

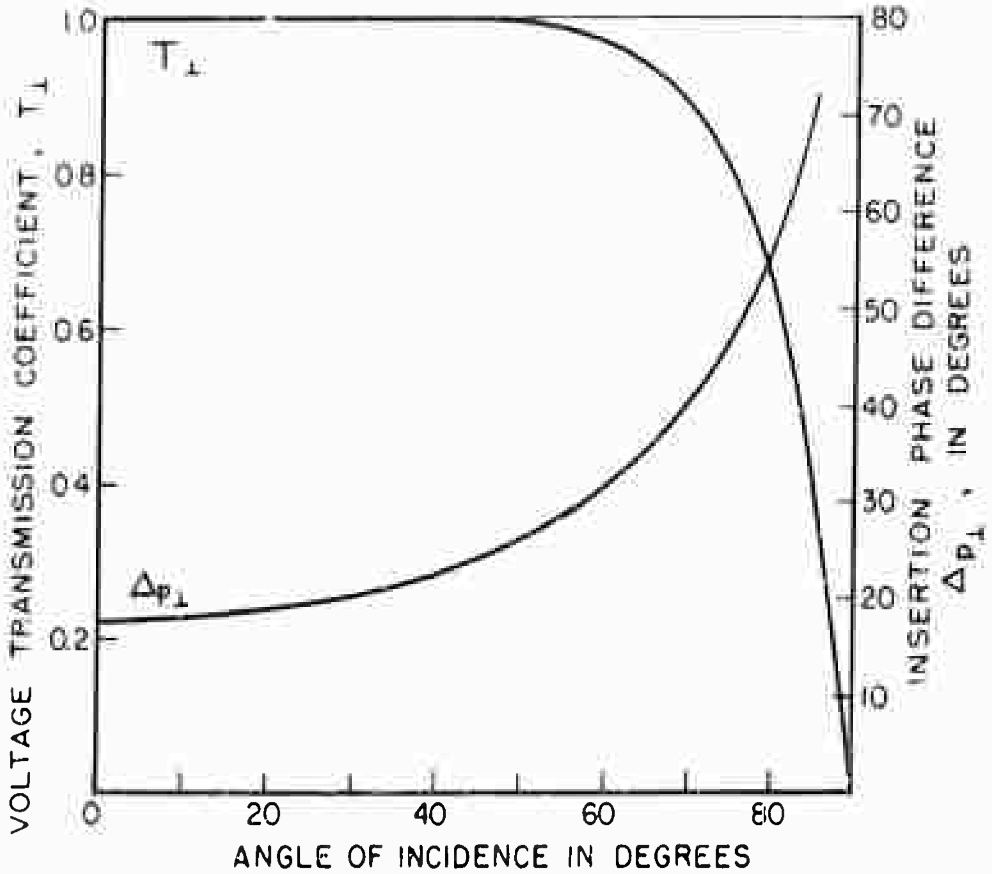

FIG. 2. CHARACTERISTICS OF LOSSLESS HALF-WAVE RADOME WALL (PERPENDICULAR POLARIZATION, $\epsilon_r = 1.2$).

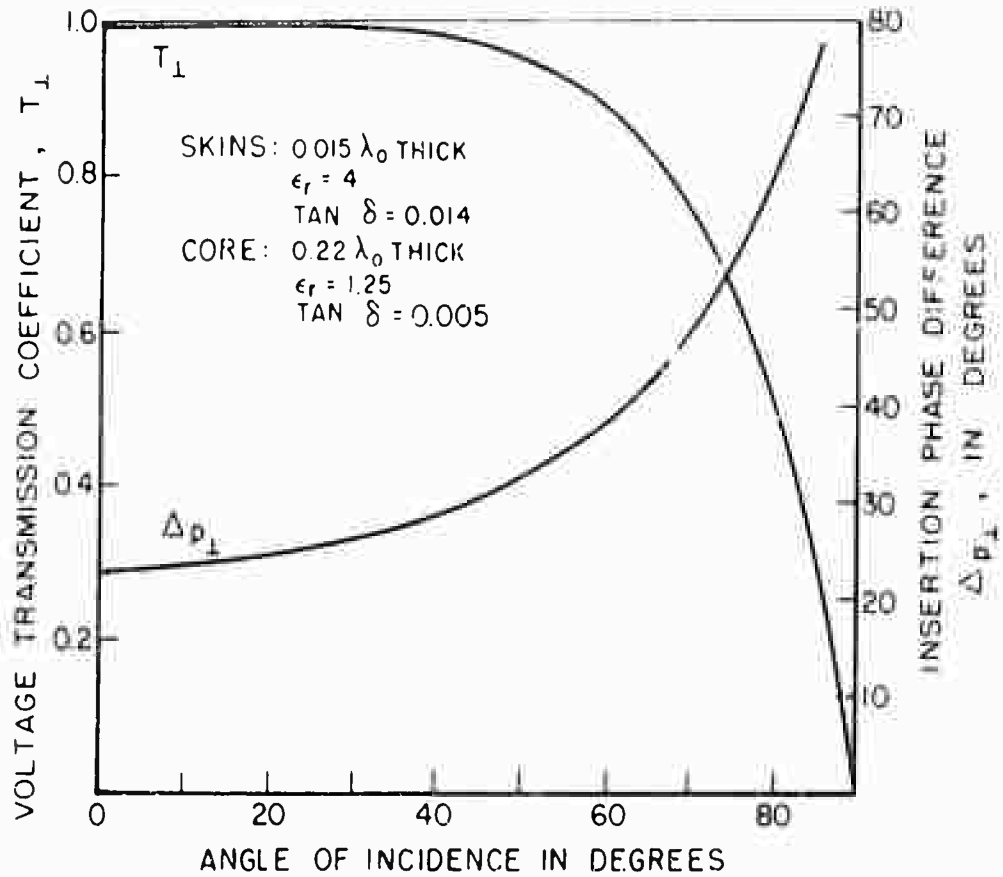

FIG. 3. CHARACTERISTICS OF SANDWICH RADOME WALL (PERPENDICULAR POLARIZATION).

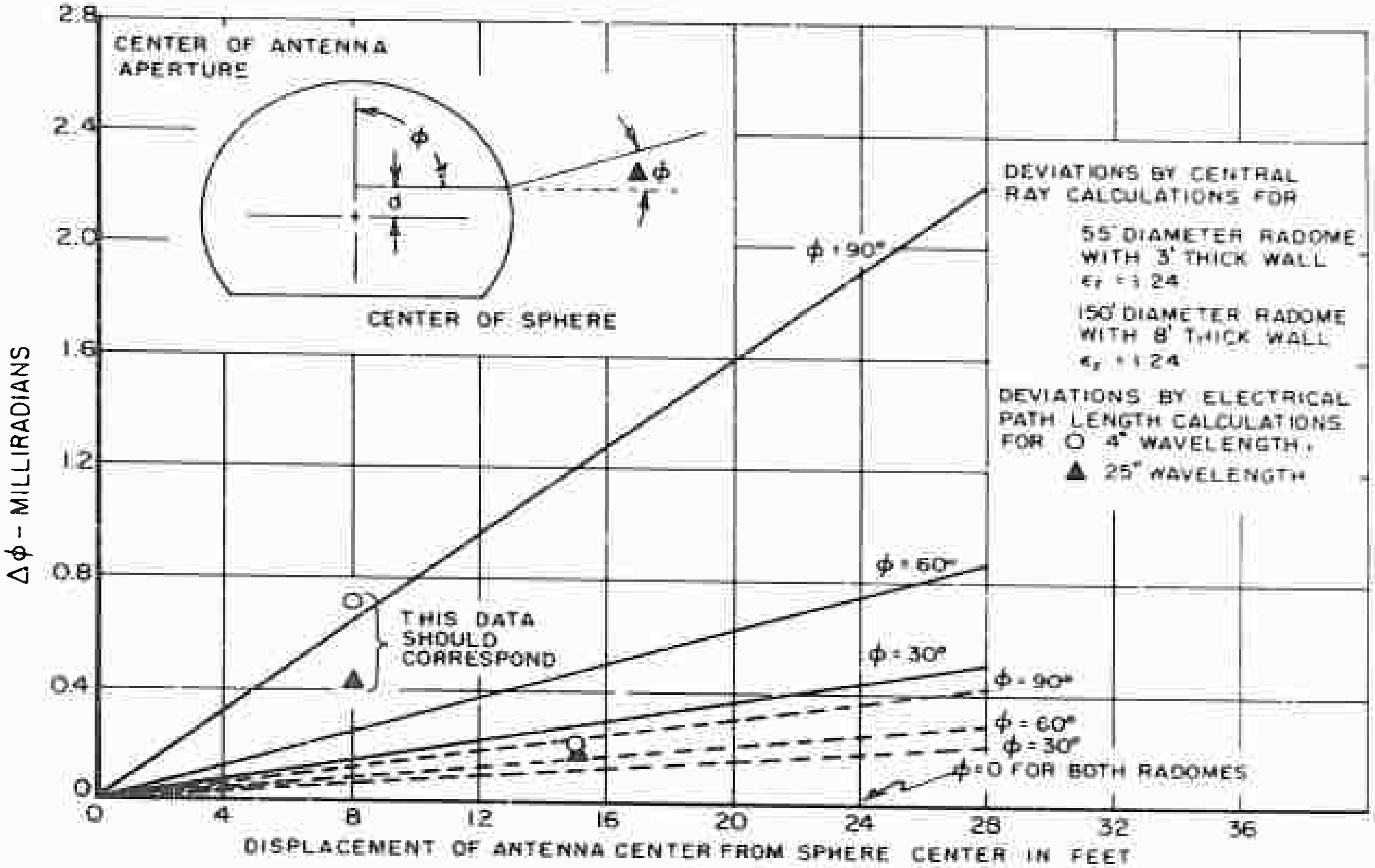

FIG. 4. TRACKING ERRORS WITH A SPHERICAL DIELECTRIC RADOME.

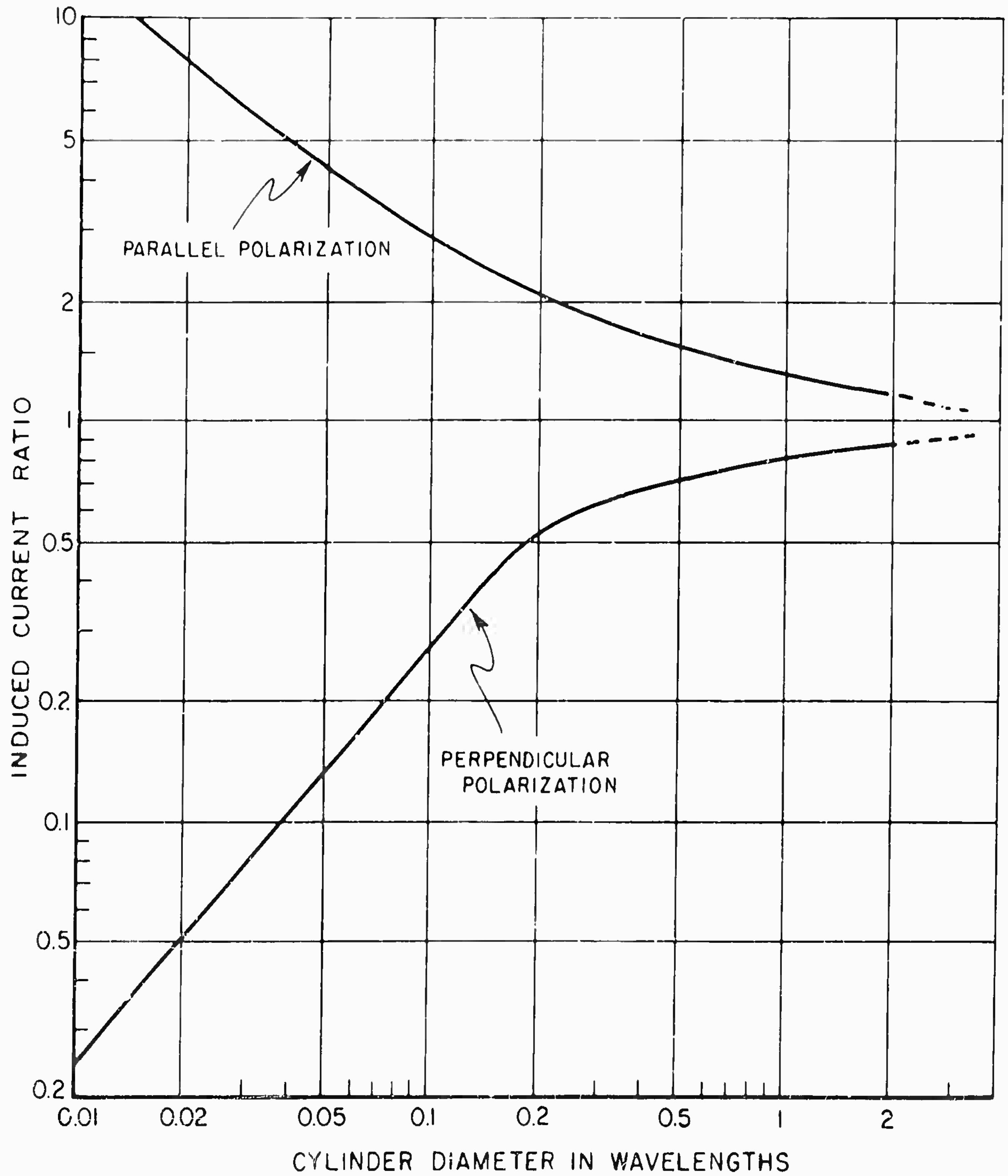

FIG. 5. INDUCED CURRENT RATIO FOR METAL CYLINDERS.

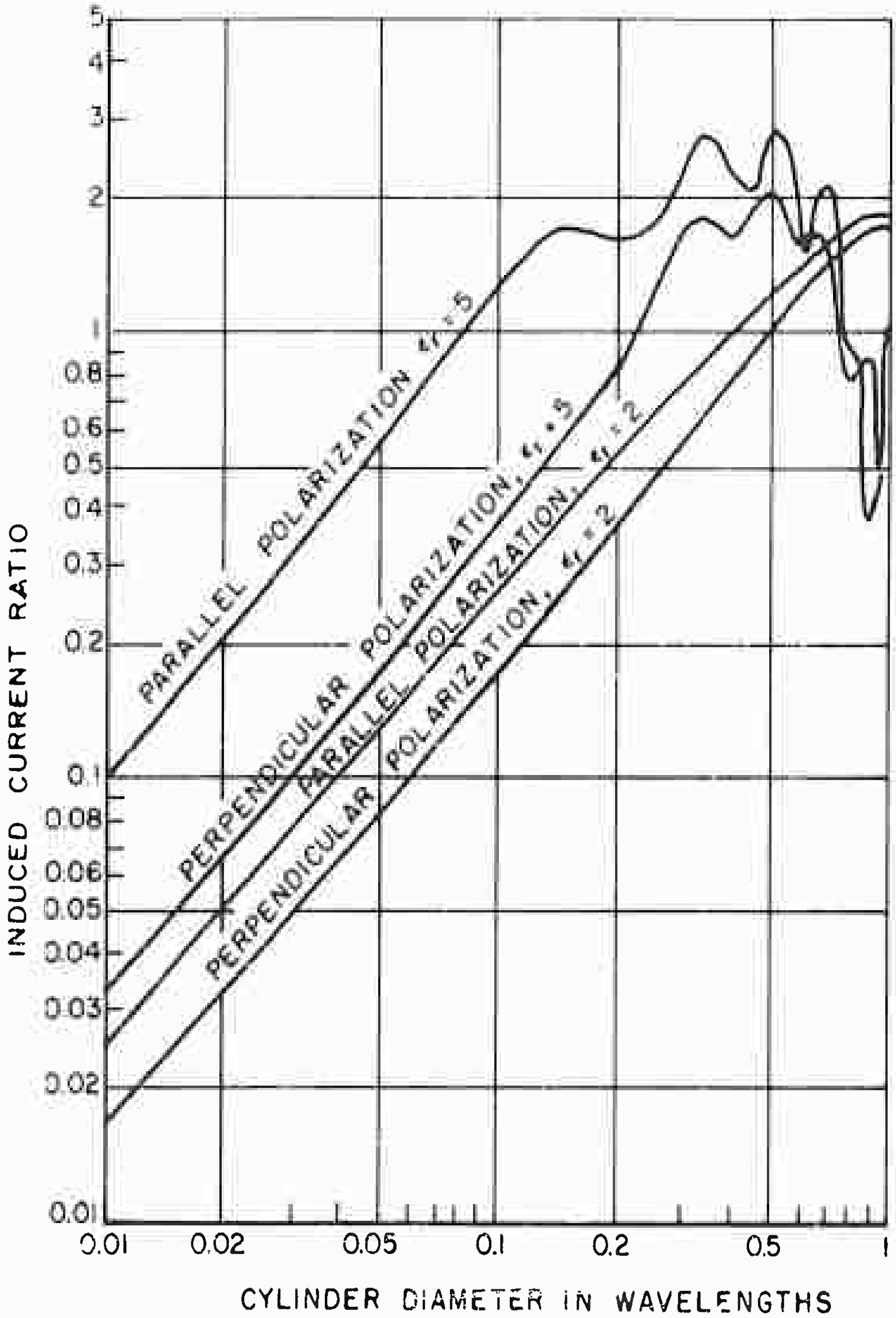

FIG. 6. INDUCED CURRENT RATIO FOR DIELECTRIC CYLINDERS.

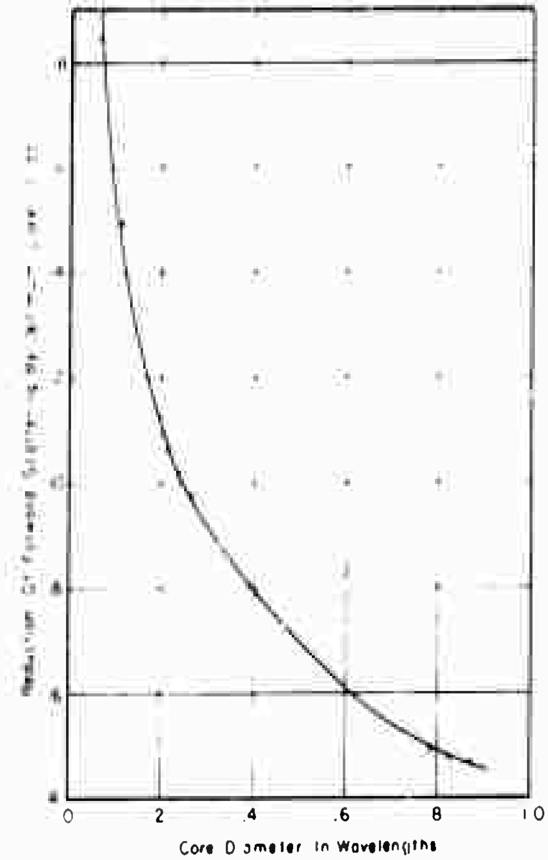

FIG. 7. SLEEVE EFFECTIVENESS VS CORE DIAMETER.

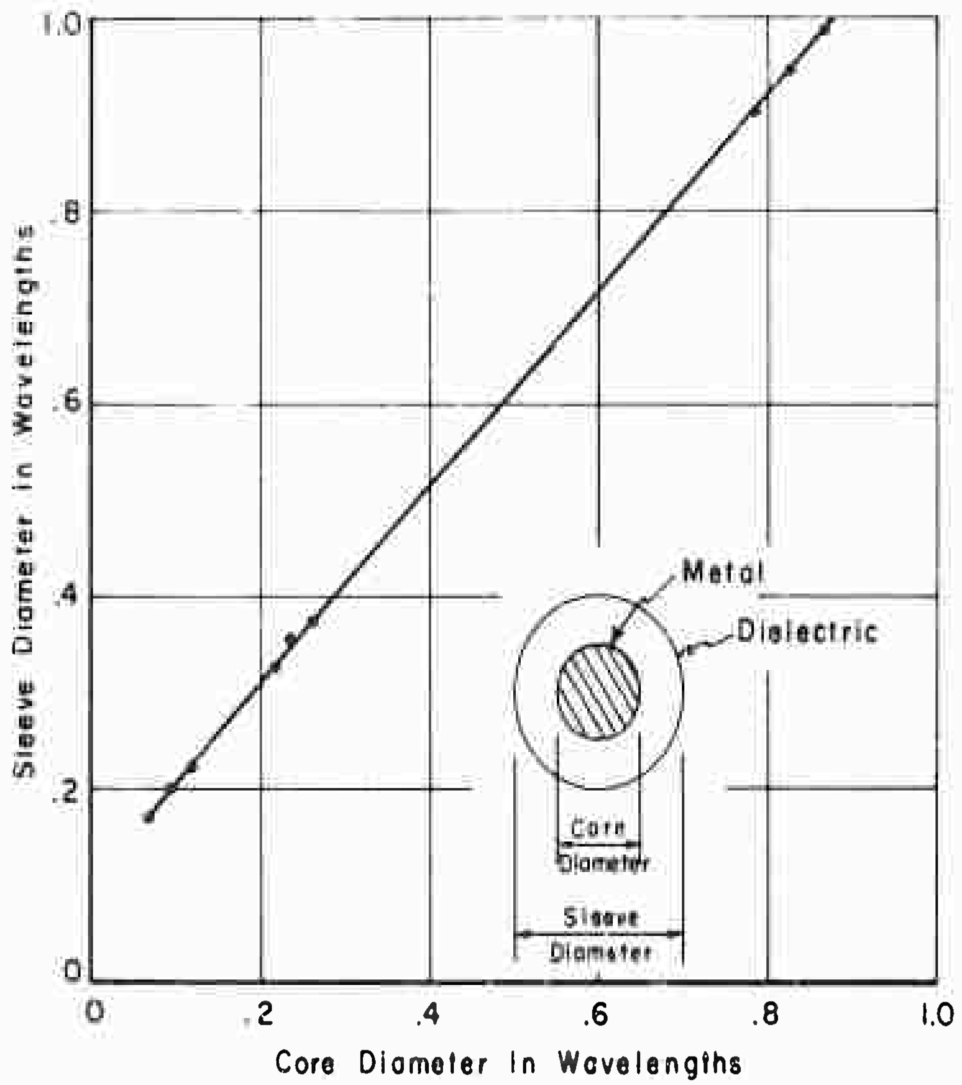

FIG. 8. OPTIMUM SLEEVE DIAMETER VS CORE DIAMETER FOR SLEEVE WITH RELATIVE DIELECTRIC CONSTANT OF 16.

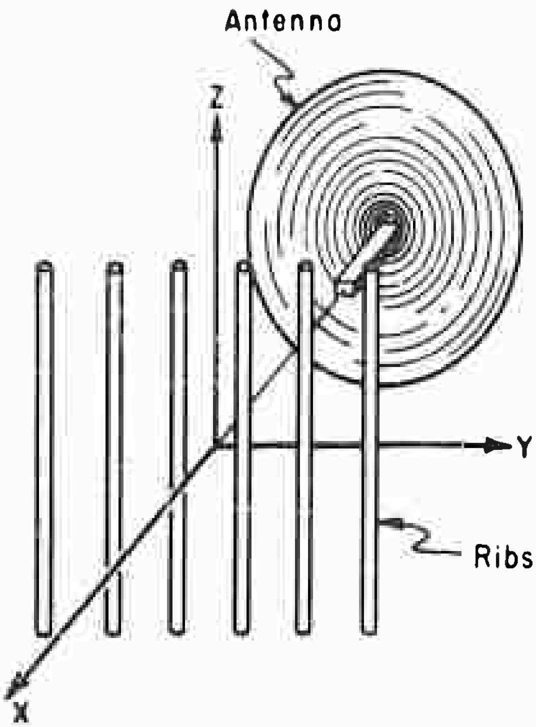

a. Parallel Rib Array

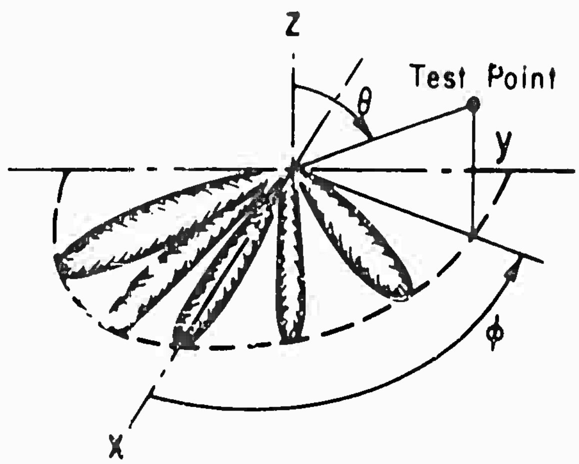

b. Radiation of Parallel Rib Array

FIG. 9

WIND CRITERIA FOR RADOME DESIGN

James M. Austin, Department of Meteorology
Massachusetts Institute of Technology

R. L. Hensel, Jr., Sc.D.
M.I.T., Lincoln Laboratory
Lexington, Massachusetts

Purpose

It is the purpose of this paper to discuss the nature, extent and reliability of wind speed information available which is applicable to the design of land-based radomes. A secondary purpose is to indicate what information should be secured by the meteorologist for use by designers in the refinement of radome structural design.

Background

In the past, steady state structural design techniques have been used and dynamic and miscellaneous effects have been incorporated in the "catch-all" term safety factor. Large structural safety factors representing extra material cannot be permitted if the severe electrical requirements are to be met. However, before optimum structural design with maximum electrical performance can be achieved, a quantitative knowledge of the wind speed environment, both "steady state" and transient, is essential.

The atmosphere is simply a low density fluid with various portions at elevated energy levels primarily as a result of solar radiation. Energy and momentum transfer take place resulting in wide ranges of atmospheric turbulence, even down to the molecular level. Thus, there is never really a "steady" wind and anemometers producing such records are simply too insensitive to detect the smaller, high frequency turbulence. However, the energy of a portion of the atmosphere may fluctuate around a particular

---

The work reported in this document was performed at Lincoln Laboratory, a technical center operated by Massachusetts Institute of Technology with the joint support of the Army, Navy, and Air Force under contract.

level for a time and an average force corresponding to a "steady" wind is exerted on structures. As storms develop, the average energy level, as represented by the average "steady state" speed, increases. This is usually a gradual process with long intervals at high average speeds possible and there often are periods of extreme average speeds of short duration and one or more peak gusts. The storm usually subsides in the same fashion.

From the standpoint of the radome or antenna designer, the dynamic or unsteady state character of the wind environment is represented by the momentary fluctuations that go to make up the "average" wind speed. Gust periods from 10-min to 0.1-sec or less are considered pertinent for radome and antenna design. From the standpoint of the meteorologist interested in predicting long-term weather patterns, however, the velocity or power fluctuations with periods lasting days and weeks are important.

Whether or not a gust represents a steady state or a transient load on a structure depends upon: (1) the relative size of the gust and the structure, (2) the dynamic response rate of the structure, and (3) the rapidity with which a change in wind velocity can be translated into a change in static pressure distribution around a structure. At high wind speeds, say 150-mph, some eddies which create short period gusts may have the physical dimensions equal to or exceeding those of the radomes and consequently, such gusts may represent steady state rather than transient loads on the radome. With "average" or small gusts and/or very large radomes, either the full velocity effect is not experienced or local gust loading is experienced, and either case represents effectively a transient

loading. Available evidence indicates considerable variation in the shape and the size of gusts as a result of many factors, which are discussed later. It is quite possible that a gust which will encompass a large ground radome longitudinally may not do so laterally or vertically. Very unusual external pressure distributions would result on the radomes and these could be superimposed on non-uniform pressure distributions resulting from buildings, etc., in the upstream velocity field. Many structural problems can arise as a result of the complex, dynamic character of the wind. The most obvious is fatigue failure as a result of stress reversals. All turbulence above certain amplitudes and frequencies is important. Further, gusts above a given amplitude superimposed on a stress level corresponding to 150-mph steady wind, for example, are much more harmful than the same gusts at the 50-mph level.

Extent and Reliability of Existing Data

Introduction - The most important information is the upper limit of wind speeds, their frequency and the turbulence at these high energy levels. The frequency, duration and turbulence of moderate winds decreases in importance as the speed decreases. Wind speed levels less than 40-50-mph will not be considered unless data at higher levels are not available. Radar equipment is often located atop mountains or high cliffs which can and do experience speeds at least 100 percent higher than adjacent low-level and often sheltered meteorological stations. Such significant differences are caused by elevation, simple orographic velocity gradients, such topographical features as funnels (P-Mountain, Thule)

and, of course, the above-mentioned sheltering. It is well established that periods of strong winds occur with hurricanes and intense cyclonic storms of the middle and northern latitudes. The latter storms predominate during the winter half of the year and are most intense over oceanic areas. Consequently, radome sites along coastal areas, or on islands, are more frequently exposed to strong winds than those in the interior of large land masses.

One of the principal reasons for the lack of reliable data in some regions of interest has been the employment of completely inadequate instrumentation. Ice accumulation, glaze or rime, on the unheated cup or vane anemometers alters their aerodynamic characteristics, they read low and are frequently destroyed. Figure 1 is an actual photograph of a thoroughly iced cup anemometer. This is a typical operating installation at a NEAC site and the photograph was taken by Lincoln Laboratory personnel at Saglek Bay, Newfoundland during November, 1955. Note the proximity of the anemometer to the buildings. Rime is a porous ice ($SG \approx 0.5$) caused by impingement of supercooled water droplets (see Figure 2). Heavy riming occurs during severe storms in the Arctic, particularly at high elevations and near bodies of water. Light riming occurs almost continually in the latter areas. Because of the importance of icing conditions the arctic and temperate-tropical data are considered separately.

Steady State Data

Arctic - Migratory cyclones along the east coast of the continent

FIGURE 1 Rime ice accumulation on an unheated cup anemometer at Saglek, November 1955.

FIGURE 2 Typical rime feathers atop Mount Washington, New Hampshire.

[illegible] high wind speeds in the Labrador - Greenland - Baffin Island area. The best data from an elevated site in the path of such cyclones is the long record from Mount Washington Observatory. Even though this station is well south of the Arctic, it provides a good guide as to what could be expected at a similarly exposed site further to the northeast. In many respects the Thule exposure is similar to that of Mount Washington.

The privately owned Mount Washington Observatory (elevation 6,288 ft) has maintained a first order weather station at the summit since about 1933. Table 1 shows a summary of the expectancy (days/month) of 5-min averages of varying mean wind speed levels for the period 1933-43 and the maximum 5-min averages for the period 1933-52. The top of the mountain is indeed a windy spot with winds greater than 100-mph expected to occur 5-7 days/month during the winter. The highest wind speeds officially recorded in America, occurred here on April 11-12, 1934 and were published in the press as a peak gust of 231-mph (approximate duration 1.2-sec). However, Mount Washington Observatory personnel indicated that the value must be reduced to 185-mph primarily to correct for the lifting effect of the wind sweeping up the southeast slope against the anemometer, whose rotor plane was not quite horizontal. This is a large correction and since the loading is proportional to the velocity squared, the accuracy of such a correction is rather important. A short written description of the account of another severe storm is illustrative of the conditions and the difficulty

TABLE 1

Summarized Wind Speed Data at the Summit

of Mount Washington, New Hampshire

Wind Speed MPH	Period 1933-43 (1) 5 Min. Average Wind Speed Expectancy-Number of Days/Month > 100	> 75	> 50	Period 1933-53 (2) Observed Maximum 5 Min. Average Speed MPH
Month				
January	7	19	27	154
February	6	17	26	144
March	5	19	27	180
April	3	14	23	188
May	1	9	21	164
June	1	6	16	136
July	1	3	12	110
August	1	2	12	110
September	2	7	17	136
October	2	13	23	161
November	3	14	17	150
December	6	18	26	173

(1) Mount Washington Observatory News Bulletin No. 13, 1944.

(2) Mount Washington Observatory News Bulletin No. 22, June 1953.

of securing accurate data. In December, 1[illegible], hurricane winds lasted for a full week. On the day when the winds seemed to be reaching a climax, an observer tried to reach the anemometer but was unable to lift his arms to even get onto the ladder. The velocity went unrecorded, but was estimated near 200-mph. Later in the day the anemometer was de-iced and a 5-min average showed 140-mph or approximately 170-175-mph gusts. Early in their history a modified heated cup anemometer or Pelton Type Wheel was employed and apparently was not considered very successful at high wind speeds. Since 1946-48 a heated pressure tube anemometer has been adopted as the standard and the data since then are considered more accurate than previously.

Next of value are data from the various defense line sites. Quite frequently they are atop mountains and cliffs and even when at fairly low elevations are more exposed than the usual Canadian weather stations in the Arctic. Thule and the Pole Vault-Pine Tree complex were the first systems installed and are in a geographical region of high winds as confirmed by their data. A summary (10) is available of maximum wind data from nine AC&W sites of the 64th Air Division for the period January 1954 to February 1956 inclusive. The extreme gust speeds are presented in Table 2 and the one-minute mean wind speeds at the time of extreme gusts in Table 3. An analysis of these data in terms of maximum gust factors is presented later. The percentage frequency of maximum <u>daily</u> gust speeds is shown in Table 4. The authors of

TABLE 2

Extreme Gust Speeds (mph) at Nine AC&W Stations

January 1954 through February 195[illegible]

	JAN	FEB	MAR	APR	MAY	JUN	JUL	AUG	SEP	OCT	NOV	DEC
Cartwright	63	69	75	71	n a	40	34	50	111	68	82	86
Frobisher	82	80	n a	n a	n a	n a	n a	69	77	69	54	64
Goose	50	75	n a	n a	71	26	48	48	61	60	52	63
Harmon	72	100	70	38	n a	n a	53	60	94	74	80	74
Hopedale	78	105	82	79	60	66	78	66	91	74	73	86
Red Cliff	66	78	57	60	69	63	63	62	89	92	110	86
Resolution	65	80	67	50	39	52	68	85	63	75	78	74
Saglek	60	105	78	95	32	58	60	82	85	50	82	55
St. Anthony	139*	120	124	98	84	96	88	80	82	75	100	90

* Estimated - limit of recorder scale is 125-mph.

TABLE 3

Mean (One-Minute) Wind Speed (mph) at the Time of Extreme Gusts at Nine AC&W Stations

January 1954 Through February 1956

	JAN	FEB	MAR	APR	MAY	JUN	JUL	AUG	SEP	OCT	NOV	DEC
Cartwright	52	46	51	45	n a	26	61	33	72	44	57	61
Frobisher	76	72	n a	n a	n a	n a	n a	56	51	45	39	43
Goose	33	48	n a	n a	48	17	27	31	37	37	36	37
Harmon	46	54	45	22	n a	n a	40	47	73	50	45	51
Hopedale	58	78	52	60	41	49	56	42	76	51	47	56
Red Cliff	42	55	39	50	46	46	36	32	47	79	73	55
Resolution	45	64	48	30	24	46	57	62	51	54	45	45
Saglek	36	75	49	48	23	34	39	61	58	39	53	45
St. Anthony	102	95	80	69	57	59	65	59	66	56	82	66

TABLE 4

Percentage Frequency of Maximum Daily Gust Speeds
in MPH by Speed Groups
January 1954 Through February 1956

	0-10	11-20	21-30	31-40	41-50	51-60	61-70	71-80	81-90	91-100	101-110	111-120	121-130	131-140
Cartwright	-	4	13	32	26	16	7	2	1					
Frobisher	-	13	34	25	16	5	4	3						
Goose	6	32	27	17	12	4	1	1						
Harmon	1	9	15	25	27	13	6	2	*	1				
Hopedale	*	5	22	26	21	15	6	4	1	*	*			
Red Cliff	-	2	12	21	30	19	9	4	1	1	1			
Resolution	1	10	21	27	22	10	7	3	*					
Saglek	3	17	24	23	15	9	4	2	*	*				
St. Anthony	-	1	8	15	23	20	15	11	5	1	1	*	*	(*)
COMBINED	1	8	18	23	22	14	8	4	2	1	*	*	*	(*)

* Less than ½%

( ) Based on the extrapolated extreme of Table I, of Reference 10.

C76-109

the report state --- "the representativeness of the records to true wind speed is not considered high" --- and consider the primary reasons to be inadequate instrumentation and poorly selected anemometer locations. We further observe that on the average the records were available for a total of only 13 full months during the indicated 26-month period, i.e., January 1954 to February 1956.

Lincoln Laboratory has installed two 55-ft rigid radomes at two NEAC sites reported to have extremely severe weather. A careful survey was made of the wind records for these locations and is reported in detail below.

One radome was installed at Thule, Greenland, August 1955 and is atop P-Mountain, which is 2400-ft above the surrounding area, 2650-ft above sea level. The radome is situated such that there is a strong funneling effect for winds from the east-south quadrant and the record shows 95 percent of the winds above 60-mph came from the SE. For the period 8-55 to 4-58 the frequency of peak gusts and one-hour averages for various wind speeds is presented in Table 5.

TABLE 5

Frequency of Occurrence of High Winds
P-Mt. Thule, Greenland; El - 2650-ft
Period of Record: October 1955 - March 1958 (2)

Wind Speed, MPH	> 125	124-100	99-75	74-40
Number of Occurrences				
Peak Gusts	1 (125-130) (1)	4	9	126
1 hr. Averages	0	1 (115)	3	43

(1) Estimated - Wind speed beyond range of recorder.
(2) Data from daily reports sent to Lincoln Laboratory

In October 1955, Lincoln Laboratory personnel observed a storm in which 1-2 minute average wind speeds obtained from an indicator (0-150-mph range), operated by the output voltage of the three cup anemometer (which simultaneously operated the standard recorder), exceed 115-mph for approximately a ½-1 hour period. Gusts reached 130-135-mph. In May 1958, a storm occurred which, according to civilian personnel present, pinned the recorder needles at the limit of their scale, i.e., 125-mph. Estimates of the peak gusts vary from 150 to 180-mph. In the three year period, 1955-58, gusts $\geq$ 105-mph have been reported six times.

The second radome was erected at Saglek, June 1956. Figure 3 is a photograph of the Saglek installation on the tip of an 1800-ft cliff rising from the open sea providing very strong orographic lifting as the winds blow off the sea up over the cliff. A record from 10-15-53 to 9-13-54 obtained from the construction contractor, Canadian Marconi Company, (12) and two AWS reports (2) (11) is presented in Part B of Table 6. Gusts in excess of 100-110-mph occurred on at least 9 days during this period.

Summarized Air Force data for Saglek during the period October 1954 to February 1956 was presented previously in Tables 2 and 3. (Note that for the first nine months of this period no records were available.) Wind information from different sources present conflicting evidence in some severe storms. On February 10, 1955, a severe storm occurred during which an inflated rubber radome and the antenna were destroyed.

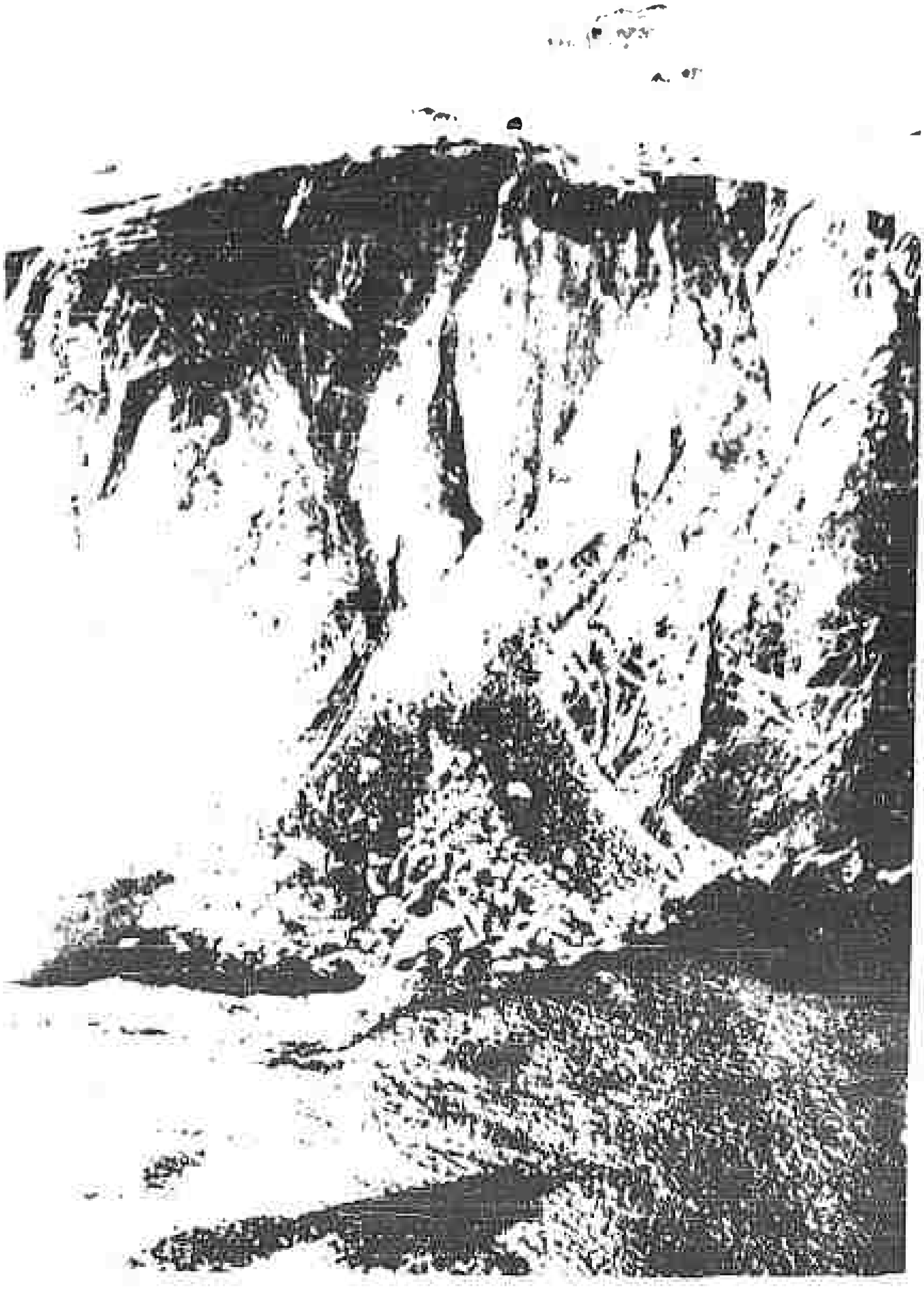

FIGURE 3 Air view of the cliff at Saglek Bay, Newfoundland.

In addition to the standard 125-mph recorder an indicator with a scale of 150-mph was in service. Gusts were "estimated" by construction personnel at 180-mph. This storm would seem to appear in reference (10) as a 105-mph peak gust in February (Table 2). Reference 5 notes gusts of 138-mph for this storm. Again in November 1955, Lincoln Laboratory personnel observed a storm with 5-10-min average of 125-mph with gusts up to 150-160-mph. The 0-150-mph indicator was operating. The highest peak gust in reference (10) for this month is 82-mph (see Table 2).

During the period June 1956 to August 1958, Lincoln Laboratory received daily data sheets concerning the performance of the rigid radome on which were included peak gust and maximum one hour speeds as taken from the recorder at the radome site. These data are summarized in Part A of Table 6.

On September 28, 29, and 30, 1957, Lincoln Laboratory personnel experienced another storm during which two tropospheric towers were blown down and three anemometers were lost. The recorders were pinned and estimates of peak gust ranged from the 136-mph Air Force record (reflected in Table 6, Part A) to 180-mph estimated by Arctic construction personnel of the Canadian Marconi Company.

Summarizing, gusts in excess of 100-mph appear to have occurred at Saglek at least 18-19 times during the past five years and in excess of 125-mph at least 5-6 times.

TABLE [illegible]

Occurrence of High Winds

Saglek Bay, Newfoundland; El-1800-ft

Part A

Period of Record: June 1956-August 1958

Wind Speed, MPH	≥ 120	120-100	99-75
Number of Occurrences			
Peak Gusts	2	5	40
1-hr Average	1	2	18

Part B

Period of Record: 1953 and 1954

Approximate Date	Wind Speed MPH	Remarks
10-15-53	80-100	Presumably gusts. Icing
11-20-53	90 average; gusts from 30 to 120 in seconds.	
12-20-53	80 average; gusts to 120	
3-15-54	80 average	Icing
3-25-54	Gusts to 103	Icing - Anemometer bearings frozen
4-7-54	80 average	Anemometer inoperable 40% of time - Icing
4-24-54	90 average; Gusts to 140 (estimated) for ten days	Icing
7 - 54	120 mph peak gust	
9-13-54	Gusts estimated > 100	Inflated radome destroyed
10 - 54	135 mph peak gust	

At St. Anthony, Newfoundland, the storm of January 1954 is described as follows in reference 2. "A rubber radome blew away at gusts of 80-95-mph. During the next four hours the wind increased to average of 110-mph with gusts of 120-mph to 140-mph. which condition lasted for the next six hours." (Recorder range was limited to 125-mph.) The estimated peak gust of 139-mph reported in reference 10 apparently occurred in this storm. The Summary of reference 10 states "An extreme of 178-mph was reported (unqualified estimate)." This value does not appear elsewhere in the report. On 3-14-55 at St. Anthony, the recorder showed an average of 100-mph with gusts exceeding 125-mph (reference 12). A vertical radiation tower collapsed. The next day the recorder was pinned at the limit of its range (125-mph) and an indicating vacuum tube voltmeter showed gusts up to 150-mph. Table 2 (reference 10) apparently reports this storm as having a peak gust of 124-mph.

Several Air Force surveys (2) (11) reported the following peak gusts for 1954 only from two other NEAC sites along the eastern Canadian coast line which were not reported in reference 10.

Station	Peak Gusts, MPH
Harmon A. F. Base	120 (March); 145 (Nov-Dec); and > 90 in four other months.
Hopedale	121 (Feb)

The low-level radar sites experience much lower wind speeds. The relative frequency and duration of the different levels of low

wind speed should be substantially the same as would be obtained from summaries of the Canadian weather service data (Dept. of Transport). The western end of the DEW Line has been reporting steady winds of 80-90-100-mph frequently during the past year. The terrain is relatively flat, icing is not a severe problem and the data should be reasonably accurate. These steady speeds are in contrast with peak gusts of only 100-110-mph suggested by the Meteorological Atlas of Canada for this region, and it appears that the general level of winds in the Arctic is significantly higher than previously believed. Much of this difference is considered to represent instrument location and site exposure even at the lower elevations.

A study (6) of 29 weather stations in Alaska and the Aleutian chain showed 9 stations with speeds over 100-mph (see Table 7). These 9 are observed to be in southern Alaska where icing is a less severe problem and it is expected that the data are reliable. Most stations are considered low-level.

Temperate-Tropic Latitudes - The maximum wind speeds in low latitudes undoubtedly occur with tropical hurricanes. When these intense storms move into middle latitudes, usually off the east coasts of the continents, they are frequently still accompanied by hurricane force winds. Since a tropical hurricane is small in horizontal extent, the probability is low that a particular weather bureau station will experience the maximum wind speed which can

TABLE 7

Maximum Wind Speeds, MPH in Alaska

Average Period of Record Nine Years

Station	Extreme 2-Min. Av.	Max. Gust Observed	Max. Gust Calculated*
Adak	100	-	122
Amchitka	115	-	140
Cold Bay	120	-	146
Umnak Island	135	-	165
Cape Newenhorn	-	141	
Elmendorf, A.F.B.	-	115	
Kodiak, NAS	-	106	
Middleton Island	-	135	
Northeast Cape	-	104	

* Max. Gust (Cal) = Extreme 2-Min Speed x 1.22

TABLE 8

Fastest Mile and Wind Speed Frequency

Ten Cities Along Eastern and Southern U. S. Coast Line[1]

Location	Fastest Mile, MPH	Annual % Frequency of Occurrence Wind Speed, MPH[2]			Years Record
		0-12	13-31	> 31	
Mobile	98	73	27	+[3]	41
Miami	132	77	23	+	45
Savannah	90	79	20	1	45
New Orleans	98	75	25	+	62
St. Louis	91	76	24	+	61
New York City	113	NI	NI	NI	44
Providence	95	69	31	+	49
Corpus Christi	110	52	48	+	59
Brownsville	106	52	48	+	33
Port Arthur	91	70	30	+	16

(1) Report issued by U. W. Weather Bureau. April 24, 1956; "Wind Data for Selected U. S. Cities"

(2) Eight wind speed classifications presented in report

(3) + indicates less than 1%

occur with such a storm. Hence, even a long record of wind observations from a particular site may not indicate the maximum speed which could occur at the site. There are not very many stations outside continental United States with reliable long-term records. It was not until the second World War, with its emphasis on flying and logistics, that knowledge of wind speeds in tropical regions was of vital interest. However, even now the extreme upper limits are poorly defined since the equipment very frequently is blown away as the winds approach 200-mph. For example, at Blue Hills Observatory, Mass., (site elevation 635-ft above sea level or about 300-ft above surrounding terrain - anemometer height above ground - 53-ft) on 9-21-38 the wind averaged 121-mph for 5-min and then increased until the instrument blew away when indicating a gust of 186-mph. The next severest storm at this site produced a peak gust of 125-mph on 8-31-54.

The relative frequency of wind speed levels at various locations along the eastern coast line of the United States is indicated by Table 8. The ten stations with the highest reported fastest mile were selected from a report (9) covering some 110 cities throughout the United States. The Blue Hills data did not appear in this report. These are low-level locations and it is estimated that the peak gusts would be at least 20 percent higher than the fastest mile for the extreme wind speeds and even greater for lesser speeds. At San Juan, Puerto Rico the highest wind speed is reported as an estimated fastest mile of 149-mph.

There are available two reports (3) (7) which present a survey for 39 air bases and weather stations in the vicinity of Japan and Okinawa.

Frequency of peak gusts and 10-min average speeds in one case and 1-min average speeds in the other, above 75-mph are presented in Table 9 for three classes of wind speeds. The average period of record is 6 years and 9 years respectively. It is seen that a few stations account for the majority of winds above 100-mph. The following peak gusts, mph, have been reported: (a) 202 (estimated); (b) 160; (c) 153; (d) 150 (Estimated from recorded 1-min average of 125 using a gust factor of 1.20); (e) 144; (f) 124; (g) 122; (h) 119; (i) 118; and (j) 111. There have also been reported 1-min averages of: (a) 150 (estimated); (b) 140; (c) 125; (d) 111; and (e) 104. The 10-minute averages are missing for the station with the highest gusts.

There are a number of radome sites in the Far East. From the Okinawa sector, the following reports have been received by Lincoln Laboratory from FEAF regarding the 1956-57 hurricane seasons. Site #54 experienced steady winds of 115-mph and gusts up to 139-mph during typhoon Agnes (8-20-57) and during typhoon Faye (9-25-57) steady winds of 139-mph with gusts 173-mph. Site #52 experienced typhoon Faye on September 26. Duration of peak of storm was about 2 hours with "average" winds of 150-160-mph. Occasional gusts in excess of 200-mph were reached during a thirty-minute period at storm peak. Finally, the anemometer was pegged at 230-mph (this destructive gust was reported in a separate telegram from FEAF as 200 knots) before it was blown off its mast. There may be some confusion with the two systems of units. It was also stated that typhoon Emma, September 1956, produced gusts in excess of 200-mph but the specific site or sites were not

TABLE 9

Monthly Maximum Surface Wind Speeds In

Vicinity of Japan and Okinawa - 39 Stations

Wind Speed, MPH		> 120	120-100	100-75
Number of Stations (Reference 3)		(Average years of record - 6)		
8	(Peak Gust	0	0	0
	(10 Min. Av.	0	0	0
14	(Peak Gust	0	0	< 8
	(10 Min. Av.	0	0	< 8
1	(Peak Gust	0	0	2
	(10 Min. Av.	0	1	1
1	(Peak Gust	1 (124)	0	1
	(10 Min. Av.	0	0	0
1	(Peak Gust	2 (153 + 1[illegible]2)	1 (119	2
	(10 Min. Av.	NA	NA	NA

Wind Speed, MPH		> 125	> 100	> 75
Number of Stations (Reference 7)		(Average years of record - 9)		
5	(Peak Gust	0	0	0
	(1 Min. Av.	0	0	0
7	(Peak Gust	0	0	< 3
	(1 Min. Av.	0	0	< 3
Kadona,	(Peak Gust	1 (144)	5	13
Okinawa	(1 Min. Av.	0	2 (111 + 104)	9
Central Ab.	(Peak Gust	3 {202E, 160, 148}	4 (111, 104)	11
Iwo Jima	(1 Min. Av.	2 (150E) (140)	3 (125)	4

indicated. Altitudes of the installed radomes do not exceed 1500-ft.

It would appear from the available temperate-tropical data that in hurricane situations peak gusts in excess of 200-mph are possible even at low-level stations. For high-level sites, exposure factors such as cliffs and funneling should further increase the speeds. Speeds of rotation in excess of 300-mph are believed to occur within tornadoes. However, these phenomena are not considered in this report because they usually occur over the interior of land masses, are short-lived, and affect relatively small areas.

Transient State

Within the lowest 3000-ft of the atmosphere the degree of turbulence varies over a wide range. The intensity depends upon the distance from the earth's surface, the roughness of the surface, the wind speed and the vertical stability of the atmosphere. This latter factor exerts an important control. When the atmosphere is unstable ($\frac{\partial T}{\partial Z} < -1^{\circ}C/100$ m where T is temperature and Z height), such as on a sunny day, the vertical overturning of the atmosphere greatly increases the turbulent fluctuations. With a stable atmosphere ($\frac{\partial T}{\partial Z} > -1^{\circ}C/100$ m), such as observed on a clear night, vertical eddies are damped thereby markedly reducing the turbulence. This aspect of turbulent flow is frequently referred to as "convective" turbulence. The eddy motion arising from the surface roughness is defined as "mechanical" turbulence.

A. Power Spectra

An anemometer fixed in space responds to all the eddies and through a power-spectrum analysis one can obtain information on eddy sizes and energies. Examples of such analyses are given by Cramer et al (1) Panofsky and Deland (4) and Van der Hoven (8). For detailed information the reader is referred to these articles and their bibliographies. An important consideration for this discussion is that all but one of the investigations have been conducted at low wind speeds and consequently the results have limited application to the turbulence spectrum at high speeds. However, in their analyses of data from O'Neill, Nebraska, and Brookhaven, Long Island, Panofsky and Deland provide some information on the variability of the convective portion of the spectrum (frequency of 30 cycles/hour, and the mechanical portion (frequency of 200 cycles/hour). The conclusions, based on observations at elevations from 3-ft to 300-ft, are summarized in the following statement from the abstract: "The spectrum of lateral velocity components can be divided most clearly into low-frequency convective and high-frequency mechanical portions. The convection portion is almost entirely a function of lapse rate or short-wave radiation, with a tendency to increase with height. It is essentially independent of wind speed and ground roughness. The mechanical portion, on the other hand, is sensitive to ground roughness and independent of stability, and also tends to decrease with height. Since the convective part of the spectrum can be large at daytime, the total variance of lateral velocity shows a

tremendous diurnal variation.

The properties of the spectrum of the longitudinal wind component are similar as those of the lateral component. However, the low-frequency portion of the spectrum is considerable even in stable air, showing that the largest eddies at night are elongated along the wind. Further, the effect of ground roughness on the "mechanical" high-frequency portion of turbulence is not as great as that corresponding section of the lateral spectrum.

The vertical spectrum in the lowest 30-feet or so is entirely controlled by the proximity of the ground. Low-frequency energy increases upward, high-frequency decreases. There is little separation between convection and mechanical turbulence; the effect of surface roughness is large over the whole spectrum, and the total variance is sensitive to stability. Above 50-feet, the separation of mechanical and convective turbulence makes its appearance gradually until, at 300-ft, the low-frequency energy is largely controlled by radiation intensity; the high-frequency energy by wind speed. A continued shift toward lower frequencies toward greater heights is therefore encountered only in unstable air."

Van der Hoven's study is worthy of note because it provides a power-spectrum analysis of Brookhaven data during a period when the wind speed was relatively high and the atmosphere was probably in a state of neutral equilibrium. Figure 4 is a reproduction of that portion of his diagram where these higher speed data were utilized.

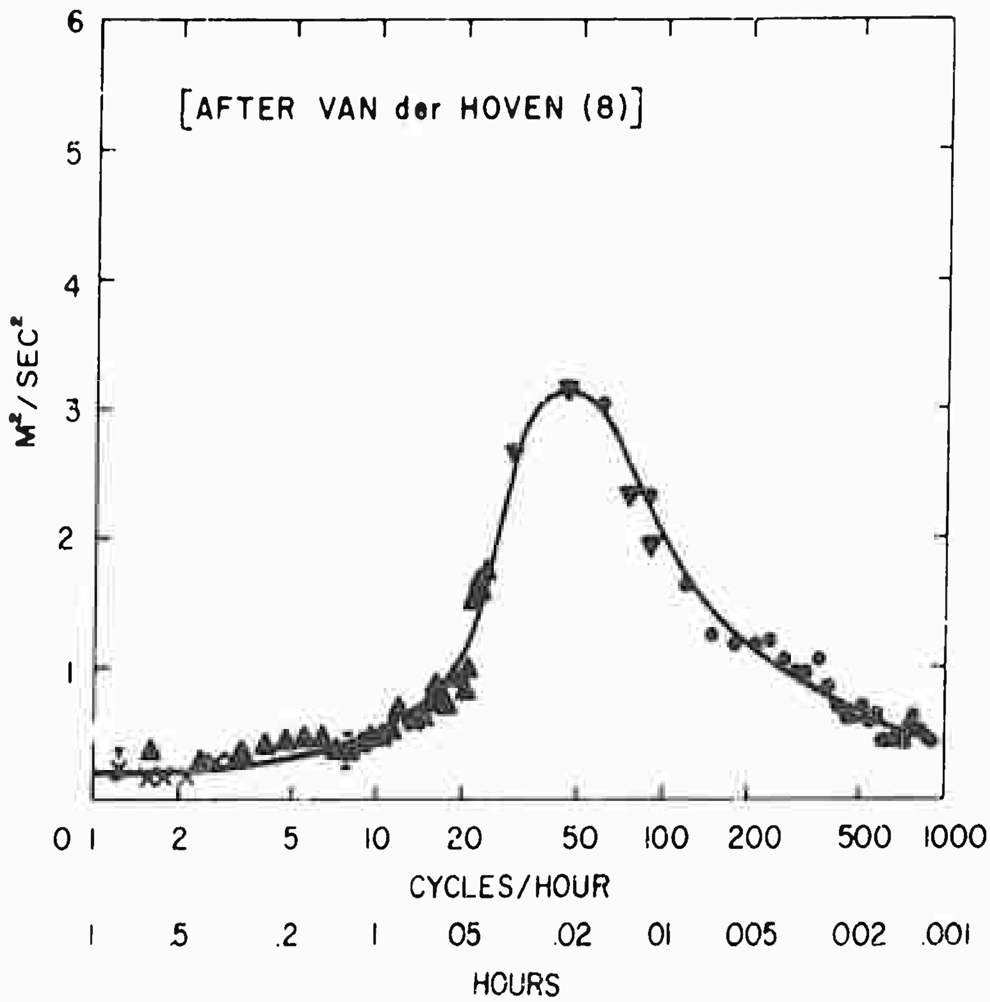

FIG. 4 HORIZONTAL WIND-SPEED SPECTRUM AT BROOKHAVEN NATIONAL LABORATORY AT ABOUT 100-M HEIGHT.

The mean speed during a 30-hour period was 30-mph with a peak hourly speed of 45-mph. This hour of data was analyzed to determine the power spectra at frequencies above 15 cycles/hour. With the logarithmic scale along the abscissa representing frequency the quantities plotted on the ordinate are the spectral estimates multiplied by the frequency, so that the variance contributed within a frequency range is given by the area under the spectral curve. It is significant to note that the major eddy-energy peak is at a period of about 1-minute. The spectral gap in the range from 1 to 10 cycles/hour has been confirmed by other analyses.

The question now arises as to what the spectrum would be like for steady winds in excess of 100-mph. Here a neutral state of stability would also be anticipated. The trend from lower speeds to those analyzed by Van der Hoven definitely indicates that the eddy energies increase with increasing mean wind speed. Further, it would be anticipated that the peak would shift toward the high frequency end, e.g., at 135-mph the peak might be expected at a period of about 20-seconds. The multitude of sizes of roughness elements found at all sites should guarantee that at all wind speeds there will be a broad spectrum of eddy sizes.

B. Gust Factors

Frequently, it is desired to obtain an estimate of the ratio of gust speed to the average wind speed. Two relationships have been utilized, namely,

(1) The ratio of the standard deviation of the fluctuations to the mean speed (gustiness coefficient), and

(2) The ratio of the peak gust speed to the mean.

From the foregoing discussion of the eddy spectrum it is apparent that gust factors depend upon roughness, stability, elevation and wind speed. An additional important variable is the length of time over which the mean wind is measured. As demonstrated by Figure 4, the total variance around the mean speed increases with time. Consequently, it is important to specify the averaging-time when enumerating gust factors.

Table 10 gives an example of gustiness coefficients obtained by Cramer et al (1) from the comparatively smooth site at O'Neill, Nebraska. The mean speed is a 20-minute average.

TABLE 10

Mean Values of Gustiness Coefficients $G_{(x)}$, $G_{(y)}$, $G_{(z)}$

40 Feet Above the Surface - O'Neill, Nebraska

(Gustiness Coefficient is the ratio of the standard deviation of the eddy velocity components to the mean wind speed. The x-direction is along the mean wind, $\bar{u}$.)

Day (Unstable)				Night (Stable)			
$\bar{u}$ mpu	G_x	G_y	G_z	$\bar{u}$ mpu	G_x	G_y	G_z
9.0 (8)*	0.18	0.14	0.06	8.0 (17)	0.14	0.09	0.06
6.0 (9)	0.17	0.18	0.08	5.3 (19)	0.09	0.07	0.04

*The number of cases represented are in parentheses.

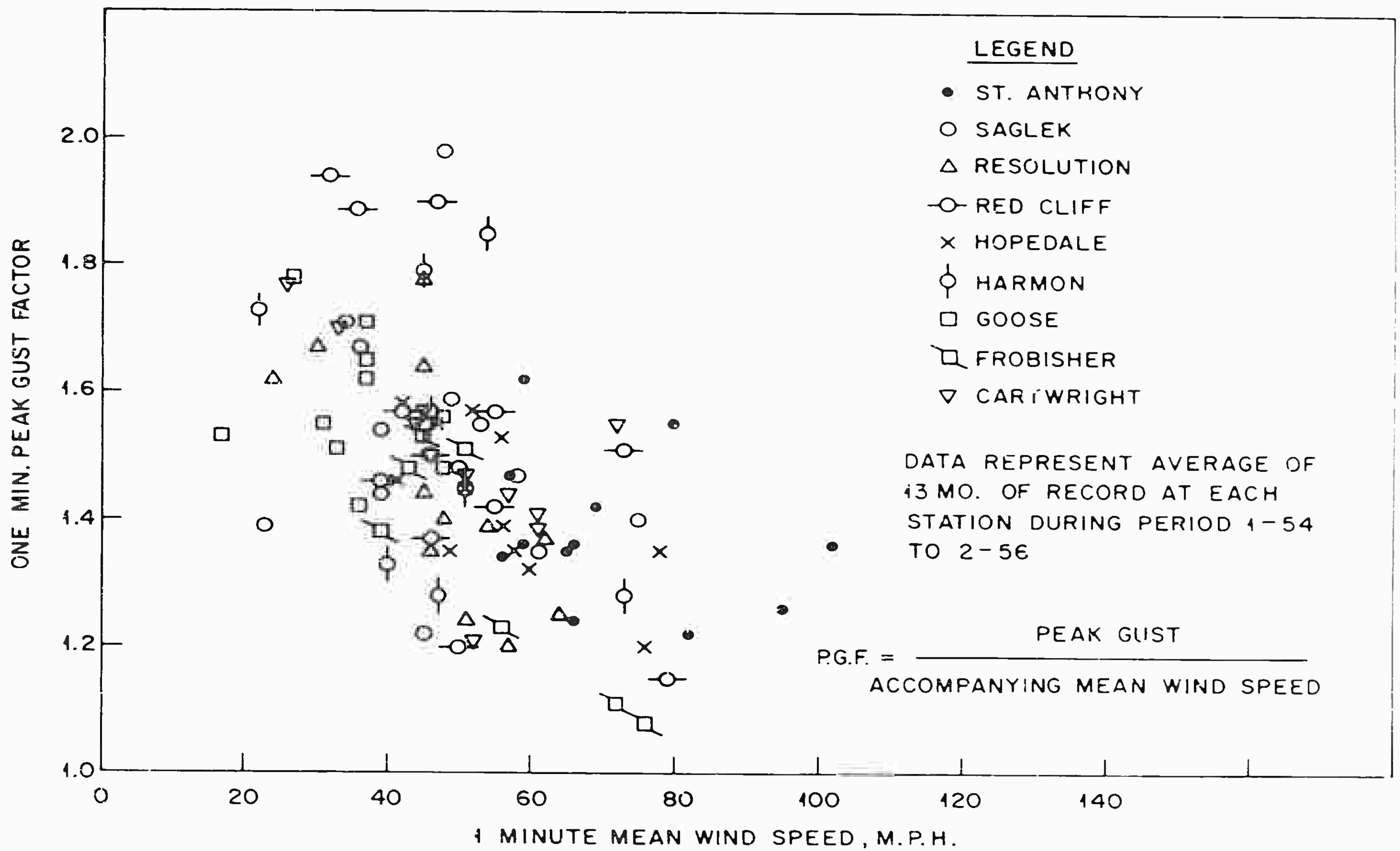

FIG. 5. PEAK GUST FACTOR ACCOMPANYING 1 MIN. MEAN WIND SPEEDS. NEAC SITES

The one-minute peak gust factors, defined as the ratio of the peak gust to the one-minute mean wind at the time of the peak gust, were calculated from Tables 2 and 3 and are plotted in Figure 5. The extreme variability is typical and is a function of the nature of the storms, the location, the immediate topography of the station, and, of course, icing of the equipment. In the mean, the gust factor decreases from approximately 1.7 to 1.3 as the one-minute mean wind speed increases from 20-mph to 80-mph. The highest gust occurred at St. Anthony and was estimated at 139-mph (limit of recorder scale was 125-mph) and the highest one-minute average of 102-mph occurred at the same time giving a gust factor of 1.36. The values of gust factors to be expected at extreme winds can hardly be deduced from these limited data; however, it seems reasonable to expect that above 150-mph one-minute mean speed the maximum peak gust factor would be less than 1.3.

The Canadian Meteorological Atlas states the following relationship between the peak gust speed, V_G, and the one-hour average speed, V_M, where V_G is in excess of 65-mph and V_M in excess of 35-mph.

$$V_G = 25 + 1.22\ V_M$$

The foregoing analysis of the turbulent state of the atmosphere emphasizes the need for more factual information during periods of strong winds.

Estimation of the Wind Regime at a New Site

The problem of extrapolating available wind data to a proposed radome site may be illustrated by the situation at Thule. Since 1946 the weather station has been located in a sheltered valley. The radar site atop P-Mountain is on an exposed site approximately 2,650-ft above sea level. A climatological summary of the first 3 years of record in the valley reported no speeds in excess of 75-mph while a later summary of 6 years of record shows speeds in excess of 47-mph only 0.3 percent of the time. Recent reports from P-Mountain show that gusts in excess of 125-135-mph have been observed and others estimated as high as 150-180-mph. The difference in the exposure of the two stations is the principal factor which accounts for the vastly different wind regimes. The normal increase of wind speed with elevation makes a minor contribution.

Because the majority of reliable wind reports come from airport stations, the designer for a radome on an exposed mountain or ridge may be confronted with a situation similar to Thule. To estimate the wind regime at a new site it is advocated that the following factors be considered:

(1) Is the site in a region which is known to be affected by intense cyclonic storms and, consequently, should the entire area experience strong winds on occasions? Meteorological literature contains extensive information on the frequency of occurrence of such storms, and their principal tracks.

(2) What are the relative exposures of the site and nearby stations which have wind records?

(3) In the event that the region is climatologically similar to northeast America as far as storminess is concerned, the information from Mount Washington, Saglek and Thule can be utilized to estimate the expected maximum wind speed.

Except for occasional mountain observatories, meteorological stations have been established in cities and at airports. The installation and operation of adequate instrumentation at radome sites could contribute materially to our knowledge of atmospheric motion near the earth's surface. As such data are accumulated, the future designer of structures on exposed sites would not be confronted with the current paucity of information.

Conclusions

1. Wind speeds in excess of 125-140-mph have frequently been reported from radar sites at elevated, exposed locations in the Arctic during the past 5 years.
2. It is well-established that the accuracy of these extreme wind speed data are very poor primarily because of: (a) Heavy icing and frequent destruction of anemometers during severe storms; (b) Inappropriate location of anemometers at the site; and (c) Recording equipment with ranges limited to 0-125-mph.
3. During the past 5 years covered in this survey, data have been reported perhaps 60 percent of the time from the sites with highest winds and worst icing. Undoubtedly, during a 10-20-year period of continuous, reliable record with adequate equipment properly located, wind speeds far higher than the above values would be observed. Peak

gusts in excess of 200-mph are considered possible for such sites as St. Anthony, Saglek and Thule.

4. Some temperate and tropical regions must expect maximum gusts in excess of 200-mph during intense tropical hurricanes even at elevations below 1000-ft.

5. The spectrum of the atmospheric turbulence has not been studied at elevated, exposed locations and data at high winds are lacking. Existing data, although limited, indicate how the spectrum is changing with increasing wind speed up to 45-mph. The validity of extrapolation to speeds of the order of 150-mph is questionable.

REFERENCES

1. Cramer, H. E.; Record, F. A., and Vaughan, H. C.: The study of diffusion of gases or aerosols in the lower atmosphere. Final Report, Contract No. AF 19(604)-1058, Air Force Cambridge Research Center.

2. Icing Conditions Relating to Radome Shelters: April 1955 by Tech. Serv. Div.; Hdq. 5th Weather Group.

3. Monthly Maximum Surface Wind Speeds for 25 Locations in Japan and Ryukyu Islands, by Clim. Div., Tokyo Weather Central, Hdq. 1st Weather Wind, APO 925; September 1956.

4. Panofsky, H. A. and Deland, R. J. (1957): Structure of turbulence at O'Neill, Nebraska, and its relation to the structure at Brookhaven National Laboratory, Upton, Long Island. Final Report, Contract No. AF 19(604)-1027, Air Force Cambridge Research Center.

5. Randolph, Robert C., Captain, USAF, Director of Plans and Programming: Letter to D. G. Bagley, Lincoln Laboratory on April 25, 1958.

6. A Study of Weather Conditions Influencing the Selection of Design Factors for Snow/Ice Load and Wind Stresses, Study #7-1000, by Climatology Branch, Hdq. 7th Weather Group, APO 942; December 28, 1954.

7. Surface Wind Data for 14 Air Bases in the Far East by Climatology Branch, Hdq. 7th Weather Group, APO 942; December 1956.

8. Van der Hoven, Isaac, (1957): Power spectrum of horizontal wind speed in the frequency range from 0.0007 to 900 cycles per hour. J. Meteor., Vol. 14, pp 160-164.

9. Wind Data for Selected U. S. Cities, L.S. 5611, by U. S. Dept. of Com., Weather Bureau, April 24, 1956.

10. Wind Speed Recording at AC&W Sites, Report No. 5G-112, by Tech. Serv. and Clim. Div., Hdq. 5th Weather Group, April 1956.

11. Bell, J. A., Major, USAF - Letter to S. L. Hensel, Jr., September 29, 1955.

12. Rowe, R. J., Canadian Marconi Company, Private Communication to D. G. Bagley, Lincoln Laboratory, December 12, 1957.

A STUDY OF AERODYNAMIC LOADS ON LARGE SPHERICAL RADOMES FOR GROUND INSTALLATION

J. W. Bezbatchenko
Goodyear Aircraft Corporation, Akron, Ohio

ABSTRACT

Wind-tunnel tests were made by Goodyear Aircraft Corporation on a series of model radomes of various geometries mounted on both cylindrical and square bases. The measurements of aerodynamic forces and pressures obtained in these tests, when integrated with data reported by other investigators, yielded a family of curves that can be applied to radome design. Some conclusions useful in radome design and test were drawn on the basis of this work. It was established that the influence of nearby buildings should be taken into account since their presence has an appreciable effect on radome loads. The effects of environmental conditions, particularly gusts, on radomes are discussed briefly to point out those areas in which additional work is required for more efficient radome design.

INTRODUCTION

Accurate aerodynamic loads due to winds are required for the efficient structural design of large spherical radomes. To date little has been done in the way of systematic testing of spherical radomes to yield design data that would account for geometrical variations. Recent studies of large ground radomes have afforded Goodyear Aircraft Corporation (GAC) the opportunity to develop a set of aerodynamic load curves for use in radome design. These studies of aerodynamic loads on large radomes were made in fulfillment of Goodyear Aircraft contracts with the Bell Laboratories[1a] and Radio Corporation of America.[2]

A wind-tunnel-testing program was conducted in conjunction with this work to obtain aerodynamic data on a series of radome models. Since the geometry of the radomes was undecided at the time of the tests, the primary geometrical parameters were varied so data would be available on numerous applicable configurations.

Aerodynamic data reported by other observers were integrated with the Goodyear Aircraft test data, thus extending geometrical parameters so that load curves could be defined for radome design. Not all geometrical variations were considered because the practical aspect of immediate application of test results dictated a brief program. However, it is believed that the principal parameters were covered and that the test data can be considered indicative of results to be expected for variations in aerodynamic loads. It is hoped that data from other sources and from future testing programs will be integrated

---

[a]Superior numbers in the text refer to items in the List of References.

with the data obtained by Goodyear Aircraft to build a set of curves that will serve as a reliable guide in radome design.

FORCE COMPONENTS

The aerodynamicist, in analyzing the loads on radomes, is particularly concerned with the evaluation of force components that are mutually perpendicular to each other, referenced to the wind vector. The component parallel to the wind is known as drag, that vertical and perpendicular to the wind as lift, and that in the horizontal plane and perpendicular to the wind as side force. The moments about each of these vectors are rolling moment, yawing moment, and pitching moment, respectively. These forces and moments may be expressed in nondimensional or coefficient forms that are applicable to radomes of the same geometrical proportions by use of the appropriate reference area, linear dimension, and the dynamic pressure of the wind. Mathematically, these forces and moments are expressed, in keeping with conventional aerodynamic practice, as shown in Figure 1.[3]

FLOW PHENOMENON

An additional factor to be considered in the applicability of such coefficients to radomes of any size is the Reynolds number of the radome. The Reynolds number is a scaling parameter that is a measure of the type of air flow over the radome surface. Two distinct types of air boundary layers are encountered: laminar and turbulent. Each has a different local velocity profile and energy level. In a turbulent boundary layer velocity components normal to the general direction of air flow are caused mainly by surface irregularities; whereas a laminar boundary layer is characterized by a smooth parallel flow.

DRAG	$D = C_D qS$	PITCHING MOMENT	$M = C_m qSD$
LIFT	$L = C_L qS$	YAWING MOMENT	$N = C_n qSD$
SIDE FORCE	$Y = C_Y qS$	ROLLING MOMENT	$\mathcal{L} = C_{\ell} qSD$

WHERE

q = DYNAMIC PRESSURE OF WIND, OR

$$q = \frac{1}{2}\rho V^2 \ (LB/FT^2) \begin{cases} \rho = \text{MASS DENSITY OF AIR (SLUG/FT}^2\text{)} \\ V = \text{WIND SPEED (FPS)} \end{cases}$$

S = REFERENCE AREA, OR

$$S = \frac{\pi D^2}{4} \ (FT^2)$$

D = RADOME DIAMETER (FT)

Figure 1 - Expressions for Aerodynamic Forces and Moments[3]

A characteristic pressure distribution is associated with each type of flow over a radome as indicated by pressure distributions in coefficient form for a sphere (Figure 2). The incremental surface pressure relative to ambient is ΔP, q is the dynamic pressure of the wind. The maximum negative pressure is attained near the poles of the sphere, and the pressure exerted by a turbulent boundary layer is substantially higher than that resulting when the boundary layer is laminar. In addition, the pressure on the after side of the sphere is considerably different. When the air flow is laminar, the flow

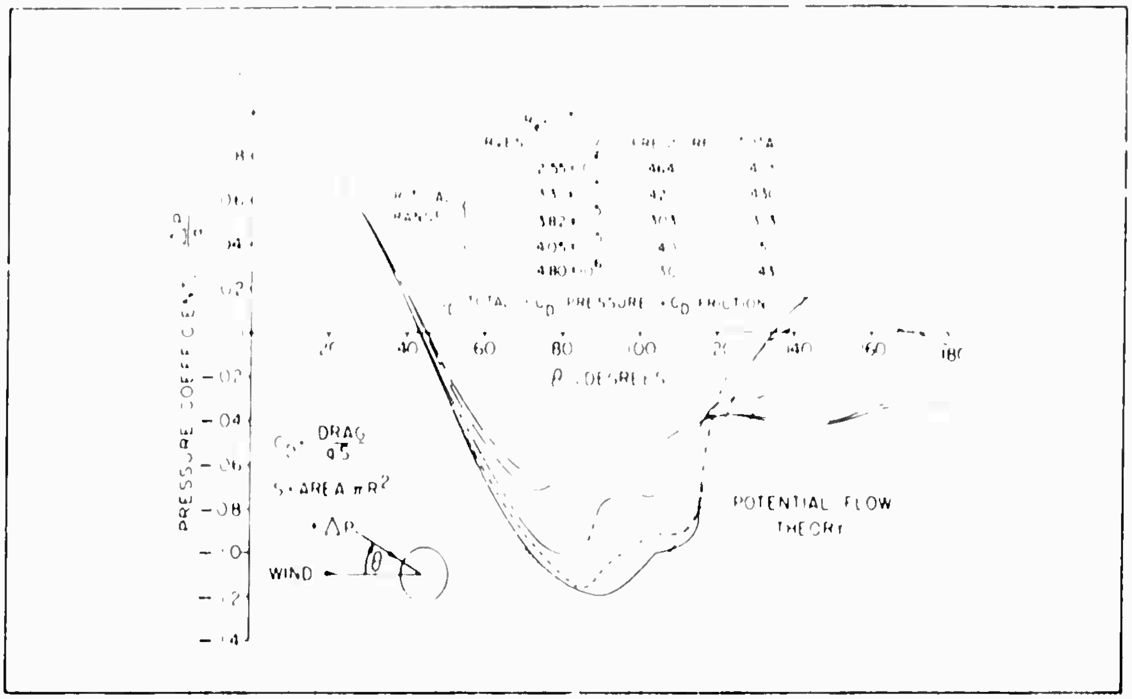

Figure 2 - Pressure Coefficient versus θ (Reynolds Number Parameters)

separation takes place soon after the air passes the pole; but when the flow is turbulent, flow separation is delayed until the boundary-layer air is well down the after side of the sphere.

As might be expected, the aerodynamic force also is quite variable, and, for a sphere, the drag coefficient, which is the only aerodynamic force due to geometrical symmetry, is a function of Reynolds number. Figure 3 shows the drag coefficient plotted against Reynolds number for a sphere. The Reynolds number, which is a measure of the type of flow, is defined as

$$R_e = \frac{VD}{\mu/\rho}$$

where

V = wind velocity (fps)

D = radome diameter (ft)

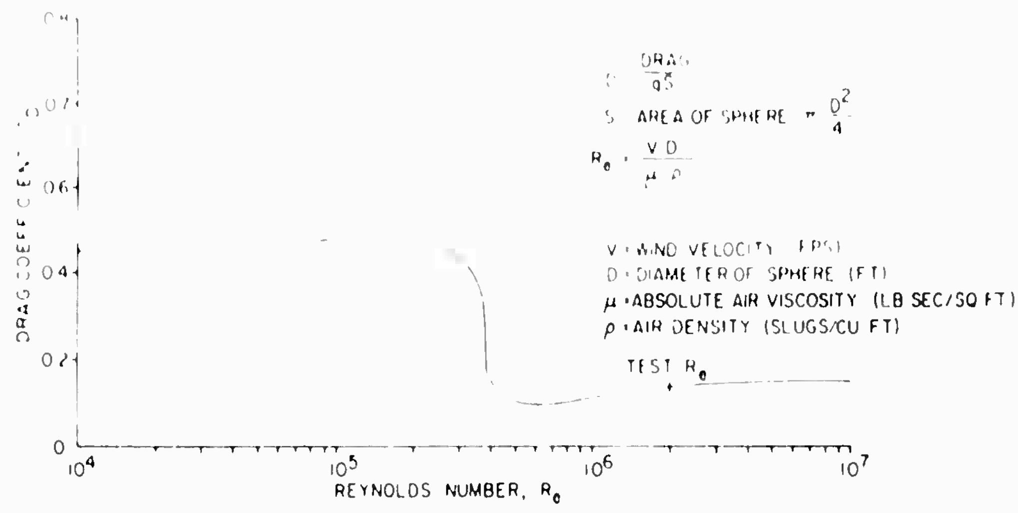

Figure 3 - Drag Coefficient versus Reynolds Number for Sphere

μ = absolute air viscosity (lb sec/ft^2)

ρ = air density (slugs/cu ft)

If the Reynolds number for the radome is well above or below the critical value at which transition from laminar to turbulent flow occurs, aerodynamic force-and-moment coefficients remain relatively constant. The coefficient of a sphere then is applicable as it is for radomes, if associated with the same Reynolds-number region.

Since the flow phenomenon over spheres is similar to that over radomes, the wind-tunnel testing of model radomes at the proper Reynolds number is essential if aerodynamic data applicable to the full-scale product are to be obtained. Most ground radomes are well above the critical Reynolds number so models of these also must be above the critical value if reliable test results

are to be obtained. Since the diameter of the model must be scaled down, the velocity must be increased so the Reynolds number will be above the critical value.

TEST PROCEDURE

Scale models of radomes were tested in Goodyear Aircraft's 43-by-61-in. wind tunnel at a Reynolds number of 2×10^6. Forces, moments, and pressure distributions were measured with the radomes mounted on cylindrical bases and square bases. Various radome cut off angles (β) were studied. For the square-based radomes, various base-width dimensions relative to radome diameter were considered. A ground plane was installed in the test section to simulate the effect of the ground. Figure 4 shows typical installations.

The diameter of the radome for all tests was 13.5 in., the wind speed was approximately 160 mph; the wind tunnel turbulence factor was approximately 1.6. Since the radome is symmetrical about the vertical plane, which contains the vertical axis, the drag, lift, and pitching moment constitute the complete force picture. In all these tests the balance system of the wind tunnel measured these quantities simultaneously.

RADOMES ON CYLINDRICAL BASES

Figure 5 shows the various geometries that were tested in the wind tunnel; for all but one of these configurations, the center line of the radome was at a fixed distance above the ground plane.

The drag coefficients, C_D, of the cylindrically based radomes tested were plotted as shown in Figure 6, where the cut-off angle, β, is the parameter.

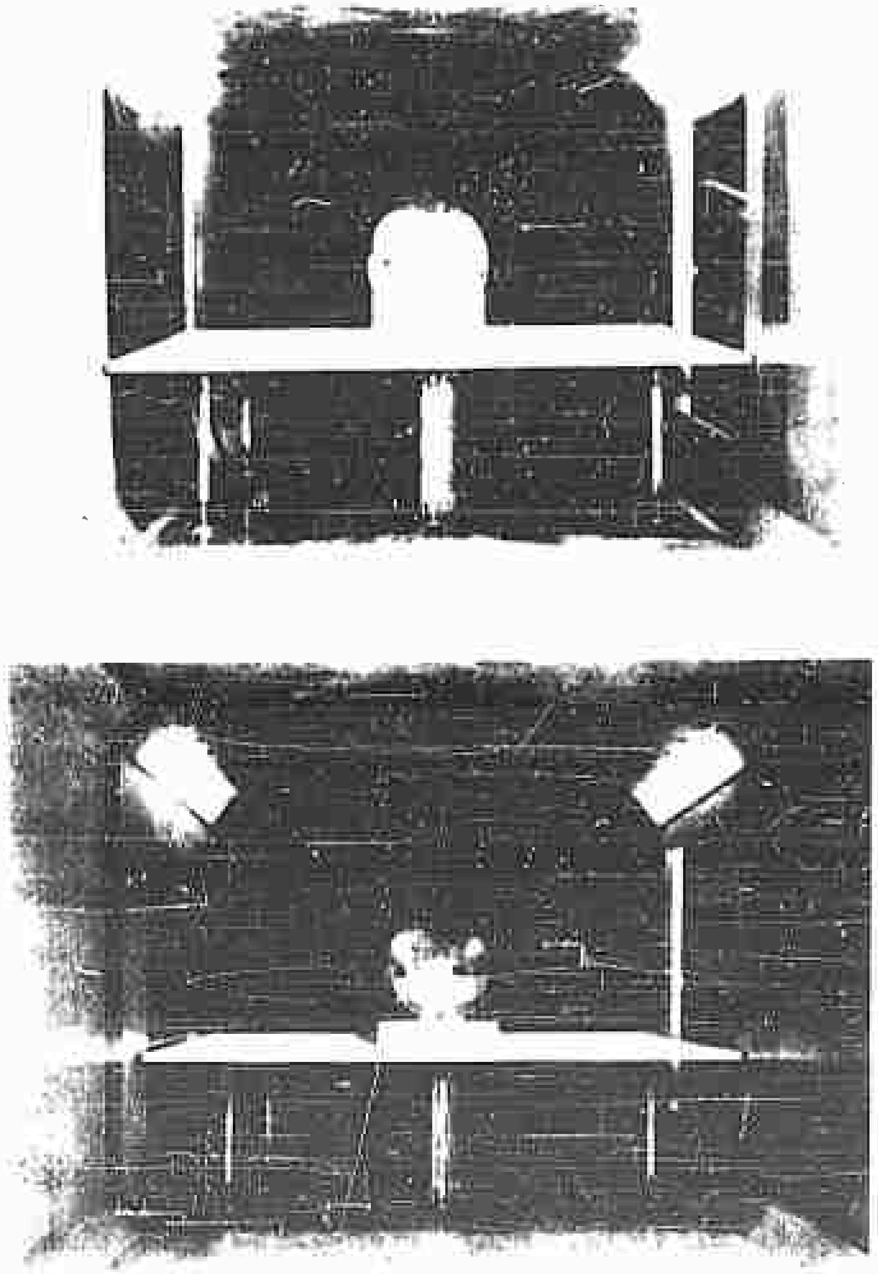

Figure 4 - Typical Installations of Cylindrically Based (Top) and Square-Based (Bottom) Radomes in GAC Wind Tunnel

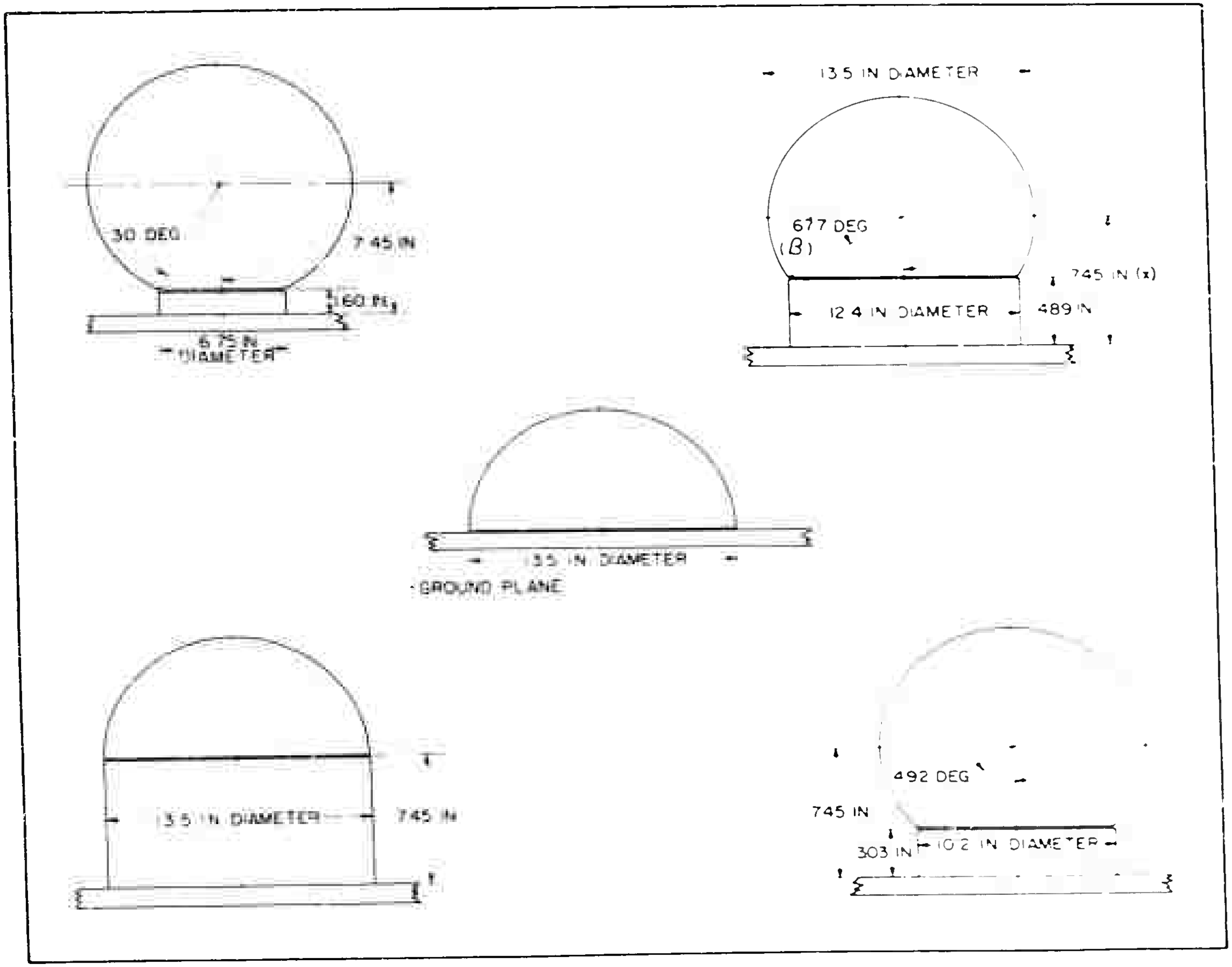

Figure 5 - Geometrical Configurations of Cylirdrically Based Radomes
Tested in GAC Wind Tunnel

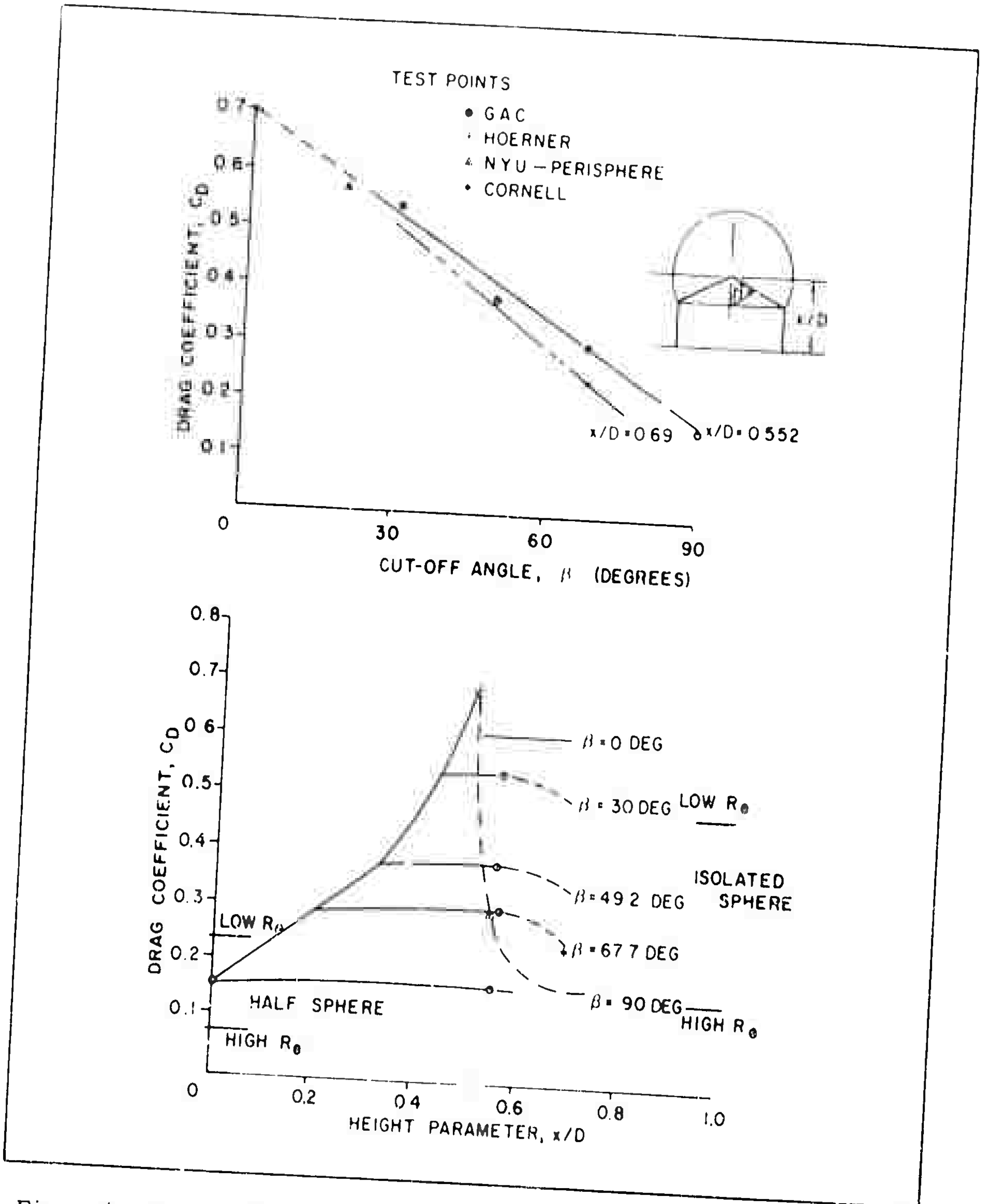

Figure 6 - Drag Coefficient versus Cut-off Angle and Height Parameter for Cylindrically Based Radomes

If the small change in drag with the height parameter, x/D, for β = 90 deg and data from a Cornell test on a radome for which β = 67.5 deg, are taken into account, perhaps the drag will have the tendency shown. The β lines terminate at the minimum possible values of x/D for the particular β. Hoerner[4] reports the drag coefficient of a sphere in contact with the ground to be 0.7, the drag coefficient for a sphere elevated from the ground until x/D = 0.54 is 0.3 as determined by New York University (NYU) tests on the 1939 New York World's Fair perisphere.[5] For reference purposes the high and low Reynolds number values of drag are noted for isolated spheres and for half spheres if the ground plane is considered as a reflection plane. The drag attained a value somewhere between these flow regimes for the half sphere situated on the ground plane. Even at high Reynolds numbers, the ground boundary layer affects the flow (Figure 7).

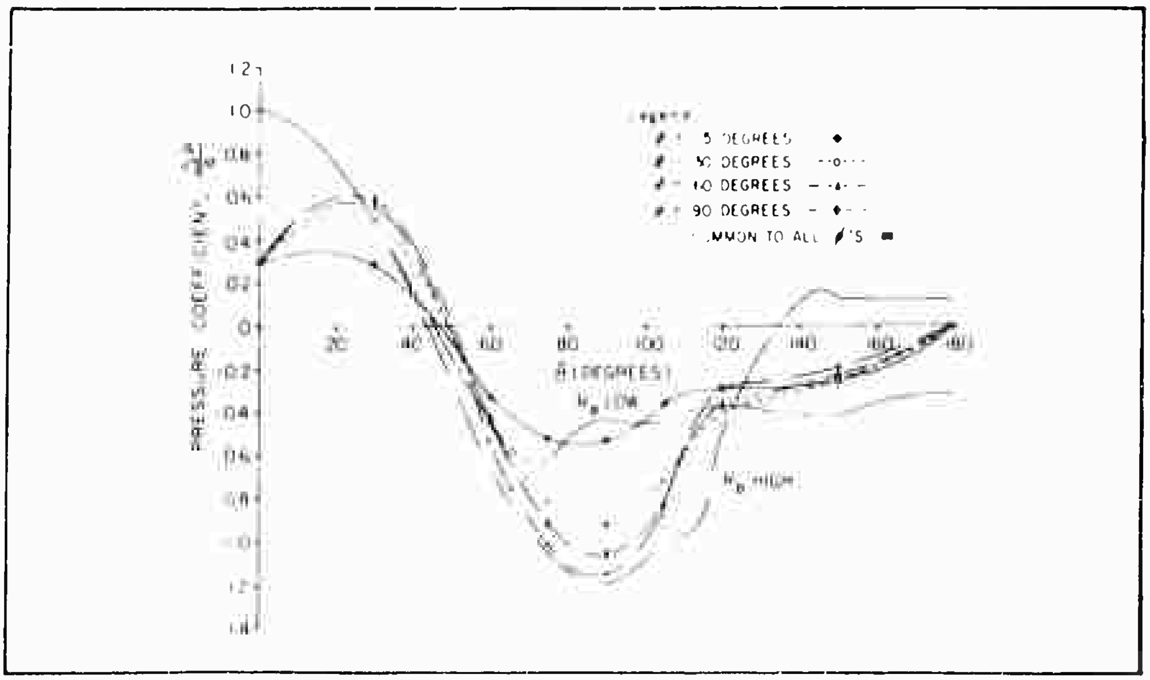

Figure 7 - Pressure Distribution over Radome Mounted on Ground Plane (β = 90 Deg)

When the drag coefficient was cross plotted as a function of β, a linear relationship resulted. An additional test point for β = 19 deg was obtained from the NYU perisphere tests. The character of the curve for another height parameter is suggested by data obtained at Cornell Aeronautical Laboratory.[6]

Lift on the radome as a function of x/D, with β as the parameter, is shown in Figure 8 along with a cross plot of lift as a function of β with x/D as the parameter. Note that the Cornell lift data are somewhat higher than those measured in the GAC test series.

The pitching moment coefficient about the axis in the plane of the base and perpendicular to the wind axis was plotted as shown in Figure 9. Forces tangential to the radome surface are responsible for the pitching moment for the 90-deg cut-off angle configuration. If these tangential forces, which are caused by friction, were not present and only the pressure vectors were considered, the moment about the reference axis would be zero, since the pressure vectors are directed through this center.

The pressure distribution over the radome also is of interest to the designer. In the Goodyear Aircraft test series, the surface pressures were measured on all radome configurations at regular intervals along a surface element on the sphere, which was traced by the intersection of tilted planes having a common longitudinal axis parallel to the wind with the radome surface. These tilted planes are dimensioned by the angle ϕ from the horizontal plane. The angle θ is measured in this plane referenced from the leading edge. Figure 10 shows the locations of these measured points. Appendix A provides pressure distribution curves for each of the radomes tested. Figure 11 is typical of

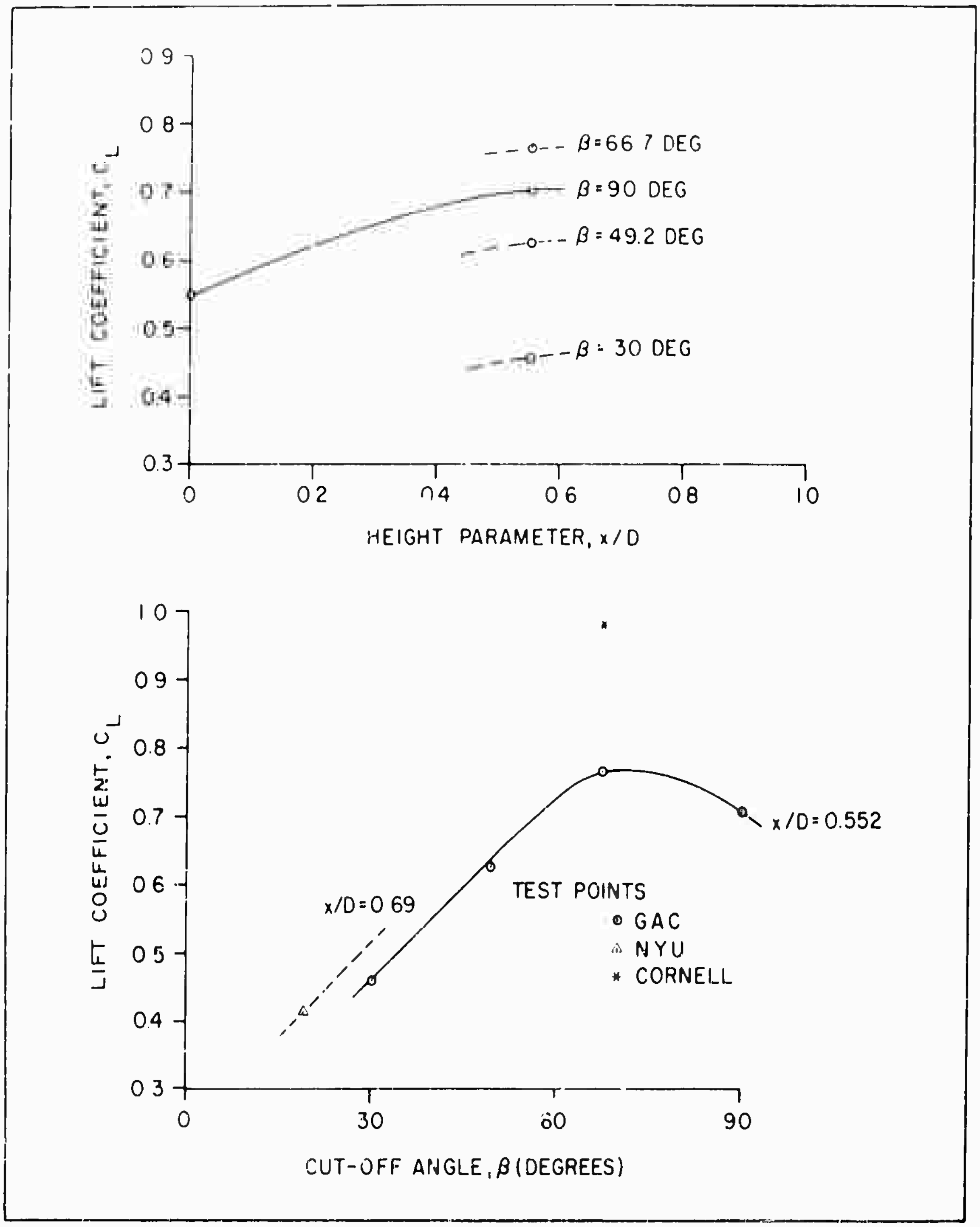

Figure 8 - Lift Coefficient versus Base Size Ratio and Cut-off Angle for Cylindrically Based Radome

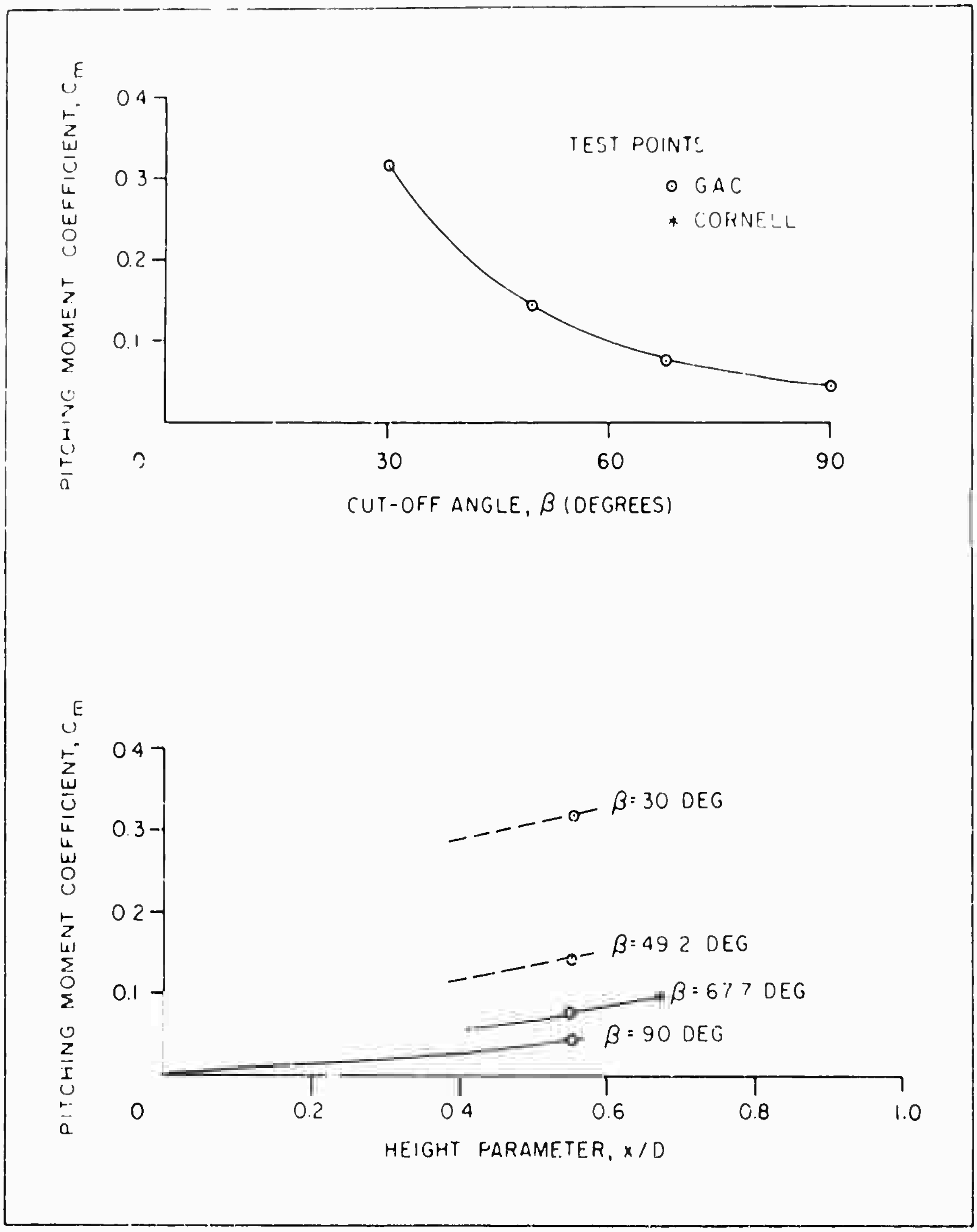

Figure 9 - Pitching Moment Coefficient versus Cut-off Angle and Height Parameter for Cylindrically Based Radome

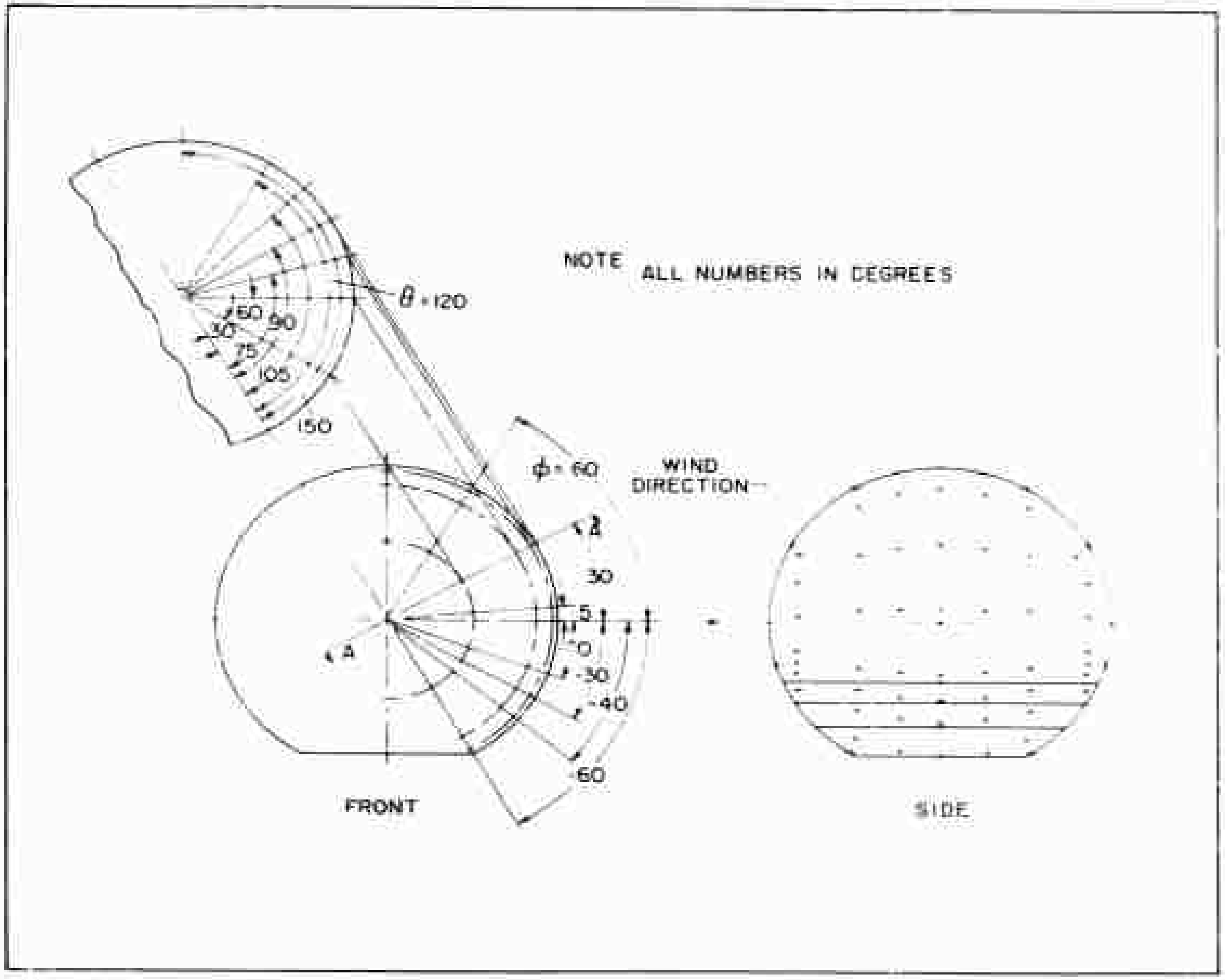

Figure 10 - Radome Pressure Tap Locations

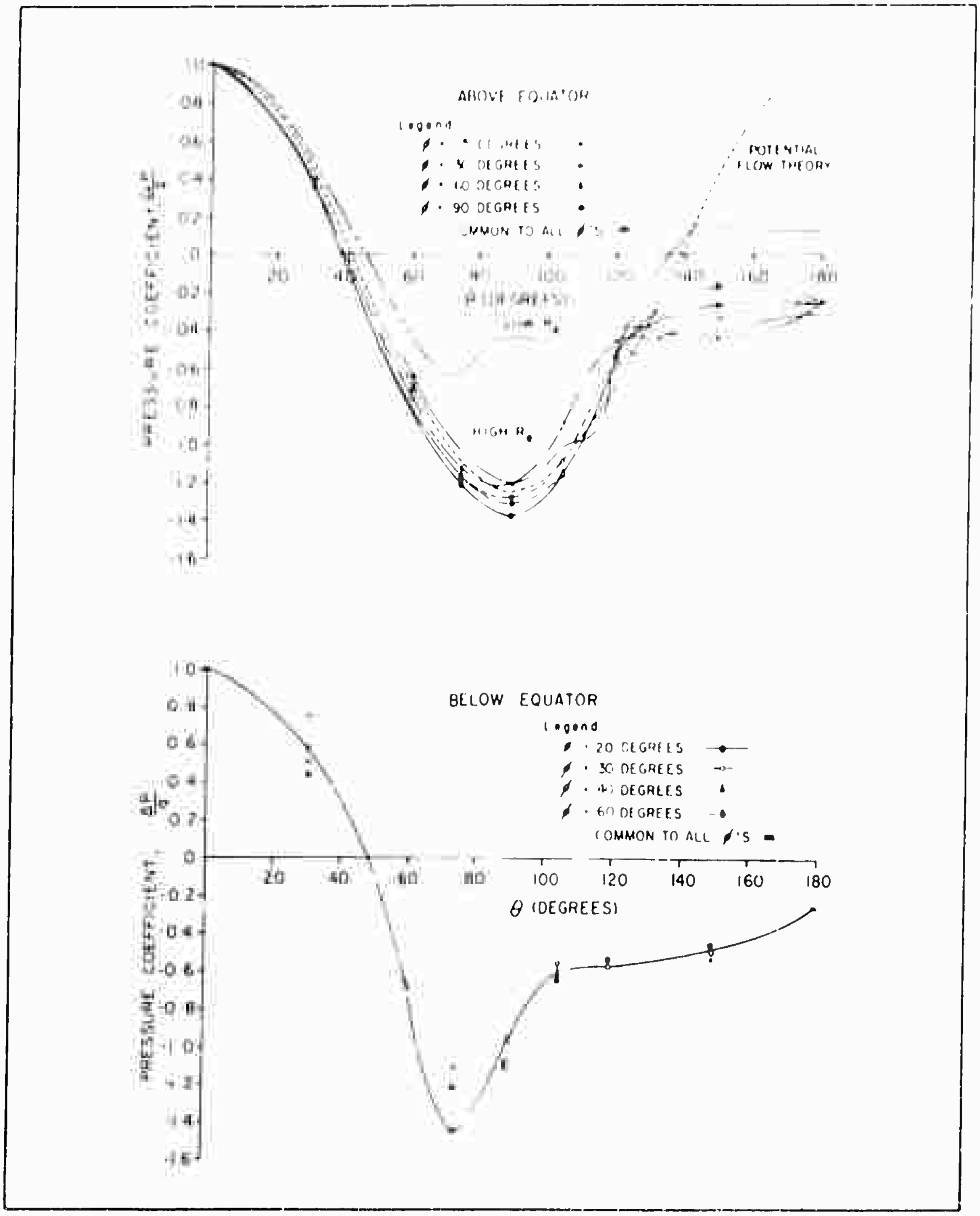

Figure 11 - Pressure Distribution over Radome Mounted on Cylindrical Base (β = 49.2 Deg)

the pressure distribution curves. For reference purposes, the pressure distributions for spheres at high and low Reynolds numbers and that given by potential flow theory are included. Note that the negative pressure coefficient at the pole is higher than that for the high Reynolds number sphere and even higher than that based on potential flow theory. On the after part of the sphere the pressure remains negative and the separated flow characteristics encountered are similar to those obtained with low Reynolds number configurations.

RADOMES ON SQUARE BASES

The various square-based radome configurations tested in the Goodyear Aircraft wind tunnel are shown in Figure 12. The position of the radome center line above the ground plane remained constant for all configurations so that the height parameter $x/D = 0.511$. The cut-off angle, β, and the base size ratio, b/D, were the geometrical parameters in these tests. Use of the square base necessitates the consideration of an additional factor, that of orientation of the base relative to the wind.

The drag, lift, and pitching moments as functions of the base orientation angle, ψ, were measured for each configuration, as shown in Figure 13. Note that drag reaches its maximum value at $\psi = 45$ deg. Pitching moment and lift also reached maximum value at $\psi = 45$ deg for three configurations; this did not hold true, however, for two of the configurations tested.

The designer is particularly concerned with the maximum drag and pitching moment that will be experienced when the radome is exposed to a wind from any aspect. Thus, the aerodynamic properties for the angle ψ of 45 deg are

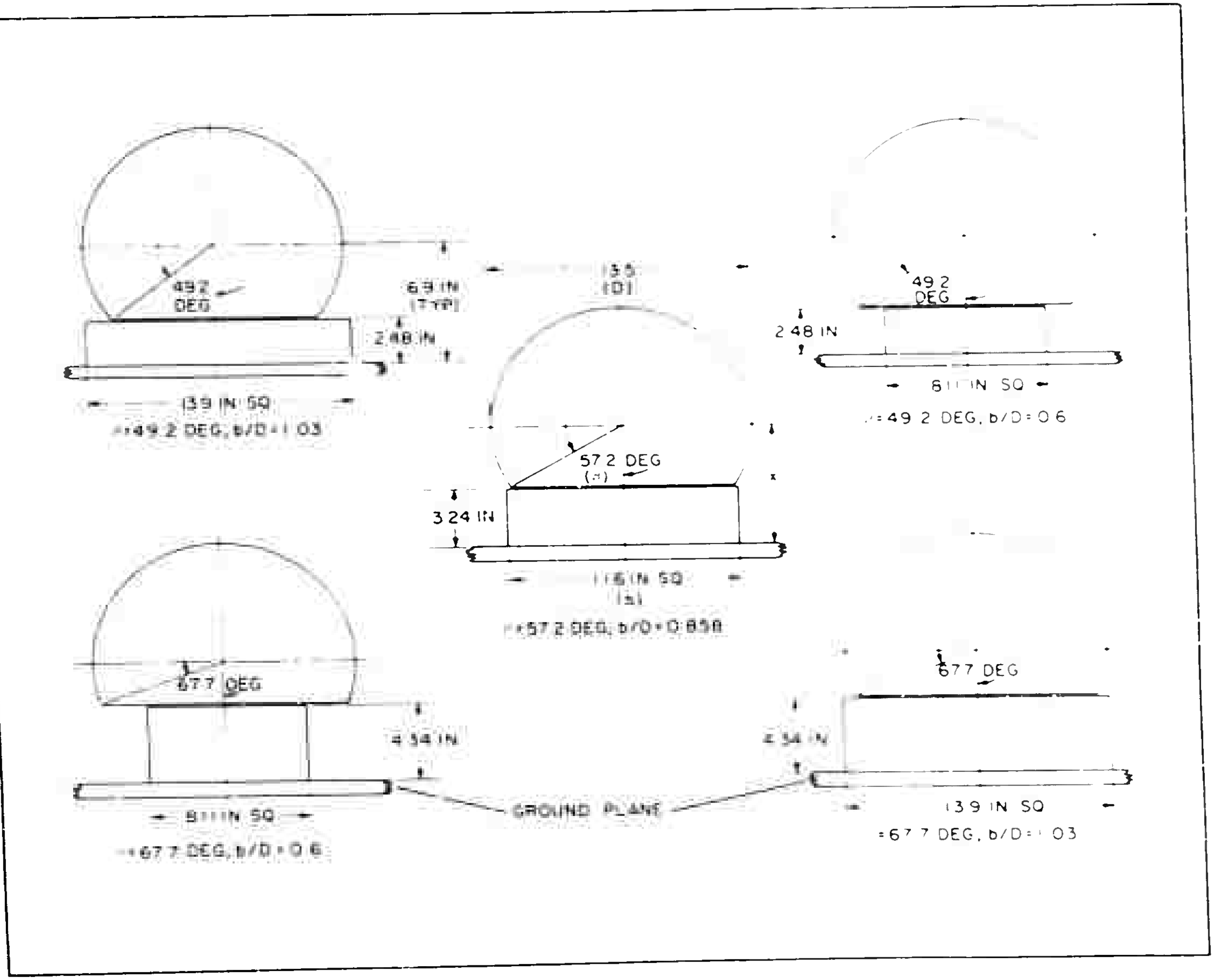

Figure 12 - Geometrical Configurations of Square-Based Radomes Tested in GAC Wind Tunnel

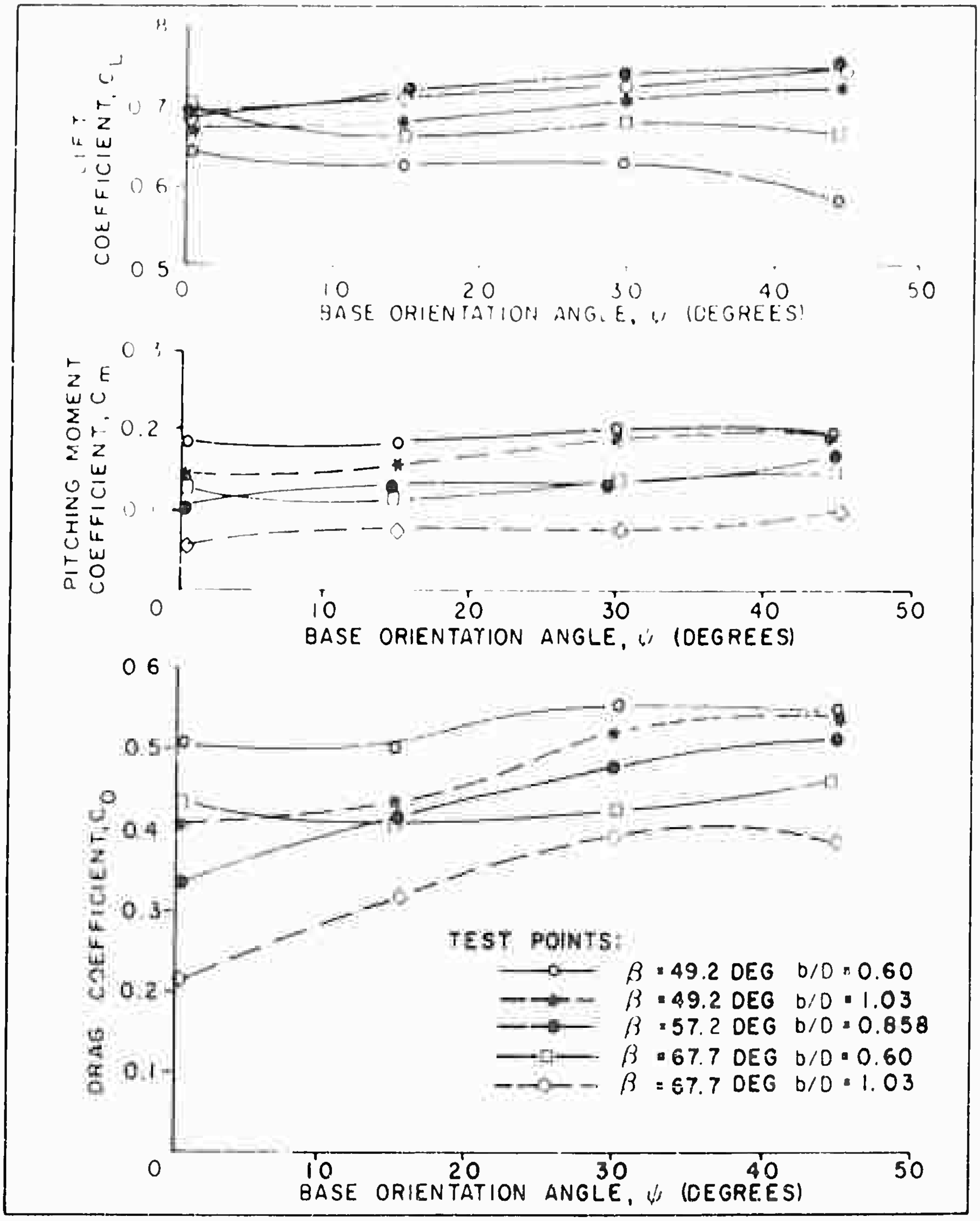

Figure 13 - Drag, Lift, and Pitching Moment versus Base Orientation Angle for Radome Mounted on Square Base

the most significant. In Appendix B the aerodynamic properties for ψ = 0, 15, and 30 deg are reported.

The radome drag coefficient as a function of β and b/D is described in Figure 14. As is true of radomes mounted on cylindrical bases, the drag coefficient change with changes in the angle β is quite pronounced but the drag level is larger for square-based radomes. The drag level at β = 90 deg, however, was quite similar to that of the cylindrical-based radomes. The change in drag with base size ratio, b/D, is not too great. The hash lines on each curve of Figure 14 are the points at which the radome base circle circumscribes the base square. To the left of the hash line, the radome overhangs the base in some regions at the base periphery. Lift on the square-based radomes is illustrated in Figure 15. This factor also is generally higher than that experienced with cylindrically based radomes. The lift levels encountered at β = 90 deg for the cylindrically based radomes were considered acceptable in this plot.

The pitching moment about the reference point at the base of the radome is as shown in Figure 16. It was assumed that the pitching moment coefficient at β = 90 deg approached that of the previously described radome, which had been set on the ground plane, without the square base.

The surface pressures over the square-based radomes were measured on all configurations for all angles of ψ. Observation of the pressure data and the aerodynamic force and moment data showed that an increase in negative pressure at the pole is responsible for the increase in lift, and the increase in

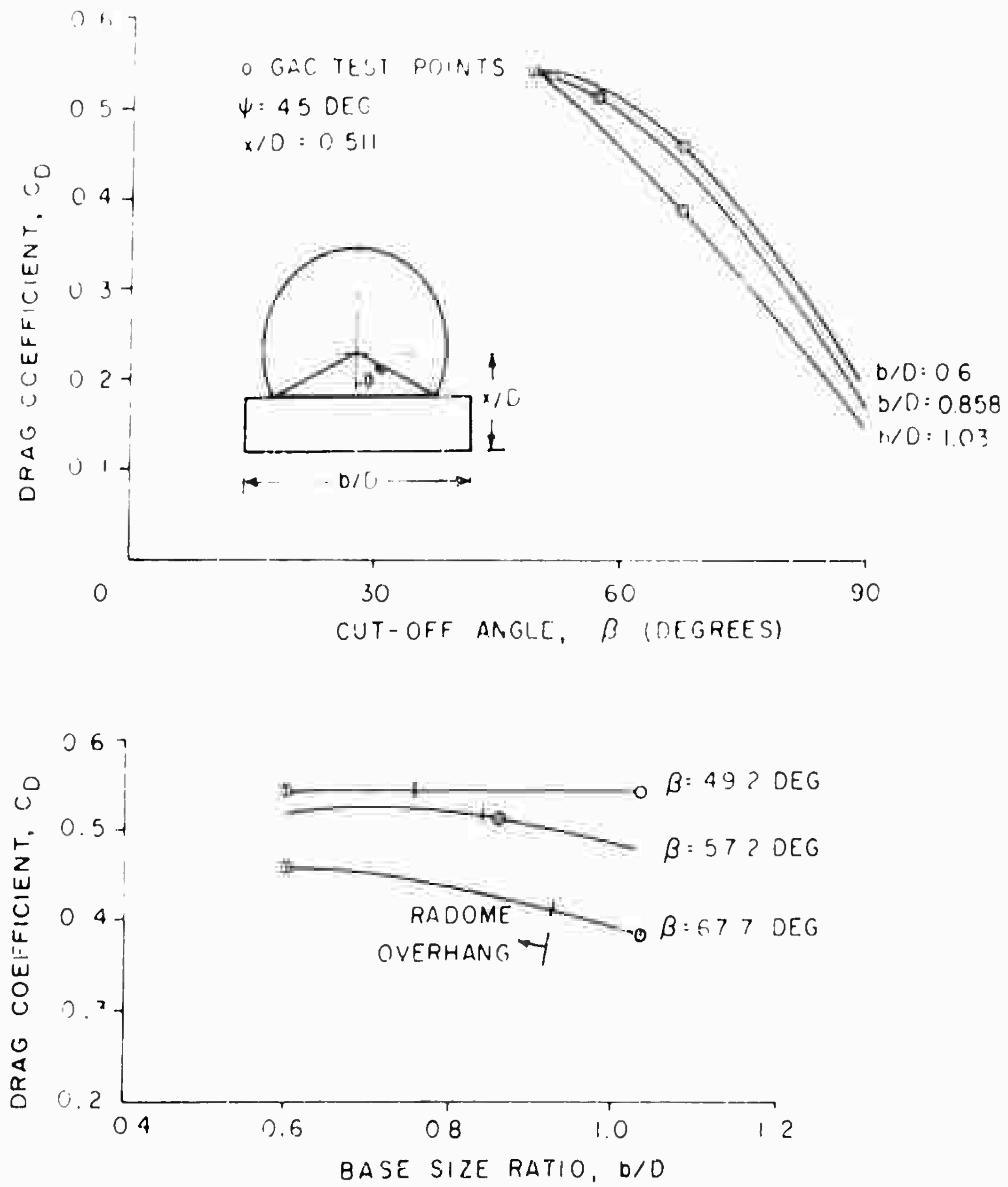

Figure 14 - Drag Coefficient versus Cut-off Angle (Top) and Base Size Ratio (Bottom) for Radome Mounted on Square Base

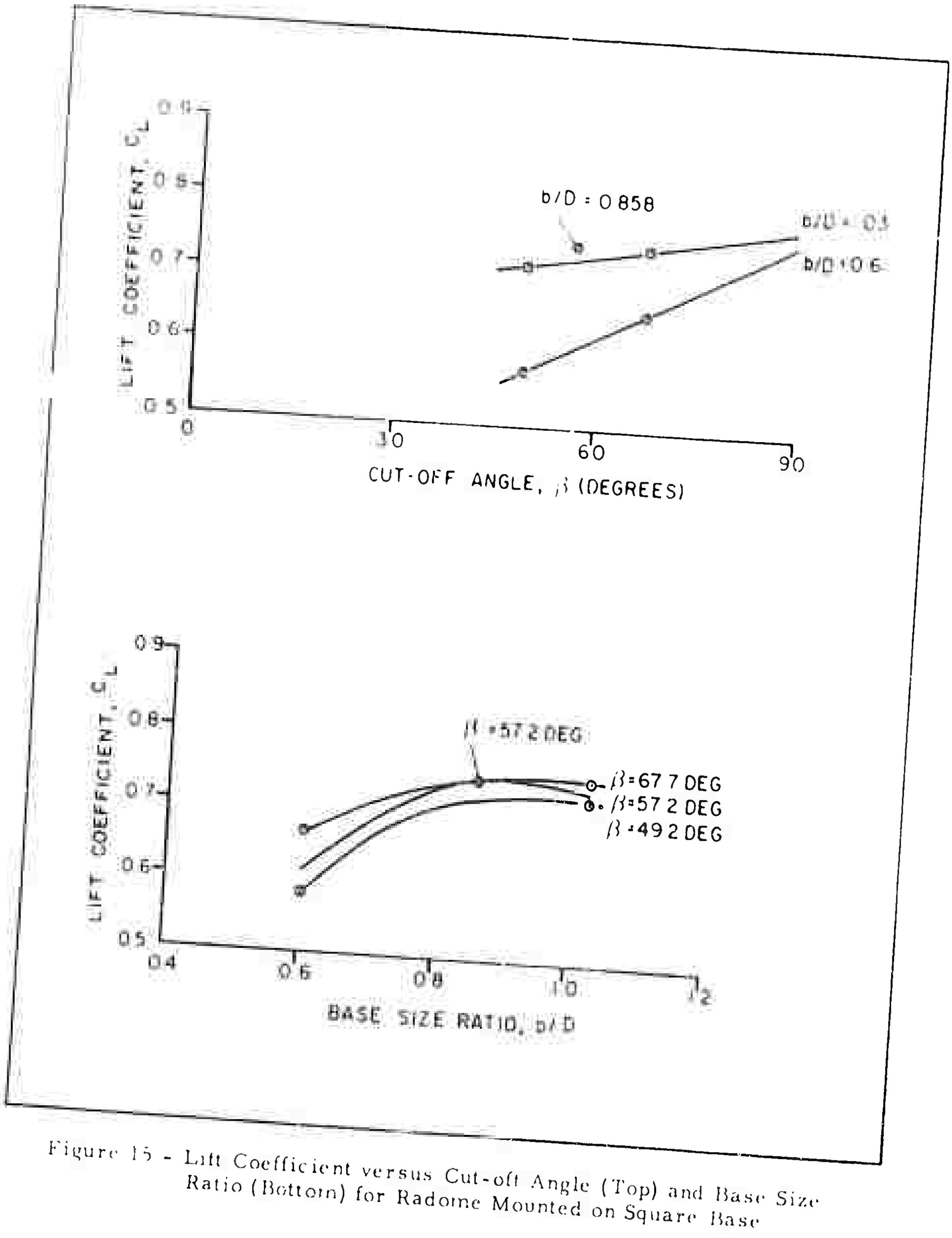

Figure 15 - Lift Coefficient versus Cut-off Angle (Top) and Base Size Ratio (Bottom) for Radome Mounted on Square Base

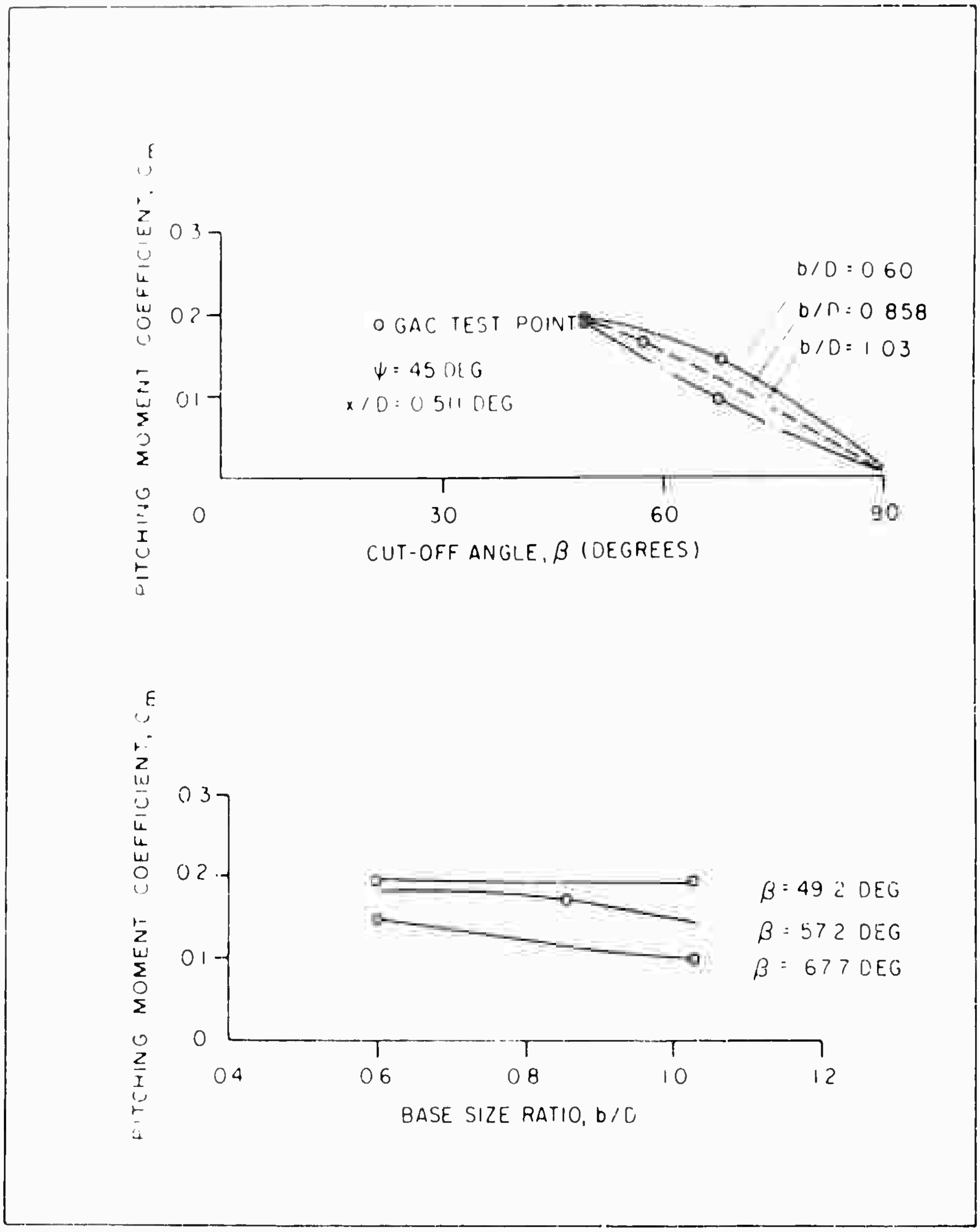

Figure 16 - Pitching Moment Coefficient versus Cut-off Angle (Top) and Base Size Ratio (Bottom) for Radome Mounted on Square Base

negative pressure along the after part of the radome is responsible for the increase in drag with the base orientation angle of Ψ.

The designer's interest is in the most critical Ψ case, or the pressure distribution for Ψ = 45 deg. Data for other values of Ψ are included in Appendix B. A typical set of pressure distributions for Ψ 45 deg is shown in Figure 17 for a β = 49.2 deg, b/D = 1.03 configuration. The negative pressure coefficient at the pole as well as in the after region of the radome increased over that for the configuration mounted on a cylindrical base. The high and low Reynolds number sphere distributions and that given by potential flow theory are shown here as they were for the cylindrically based radome. The pressure in the region of the pole exceeds that on isolated spheres at high Reynolds numbers and that indicated by theory. Along the after part of the radome the flow separation characteristics of low Reynolds number configurations is evident but higher negative levels are realized.

As the base size parameter, b/D, is reduced (Figure 18), the negative pressure at the pole and along the after part of the radome is reduced, but below the radome equator at a plane angle ϕ nearest the base, the pressure is being affected most.

A typical distribution for a larger cut-off angle with the same b/D ratio (1.03) is shown in Figure 19. Here negative pressures are increased more at the pole and decreased on the after side.

INFLUENCE OF NEARBY BUILDINGS

Any buildings located in the immediate vicinity of a radome will affect the

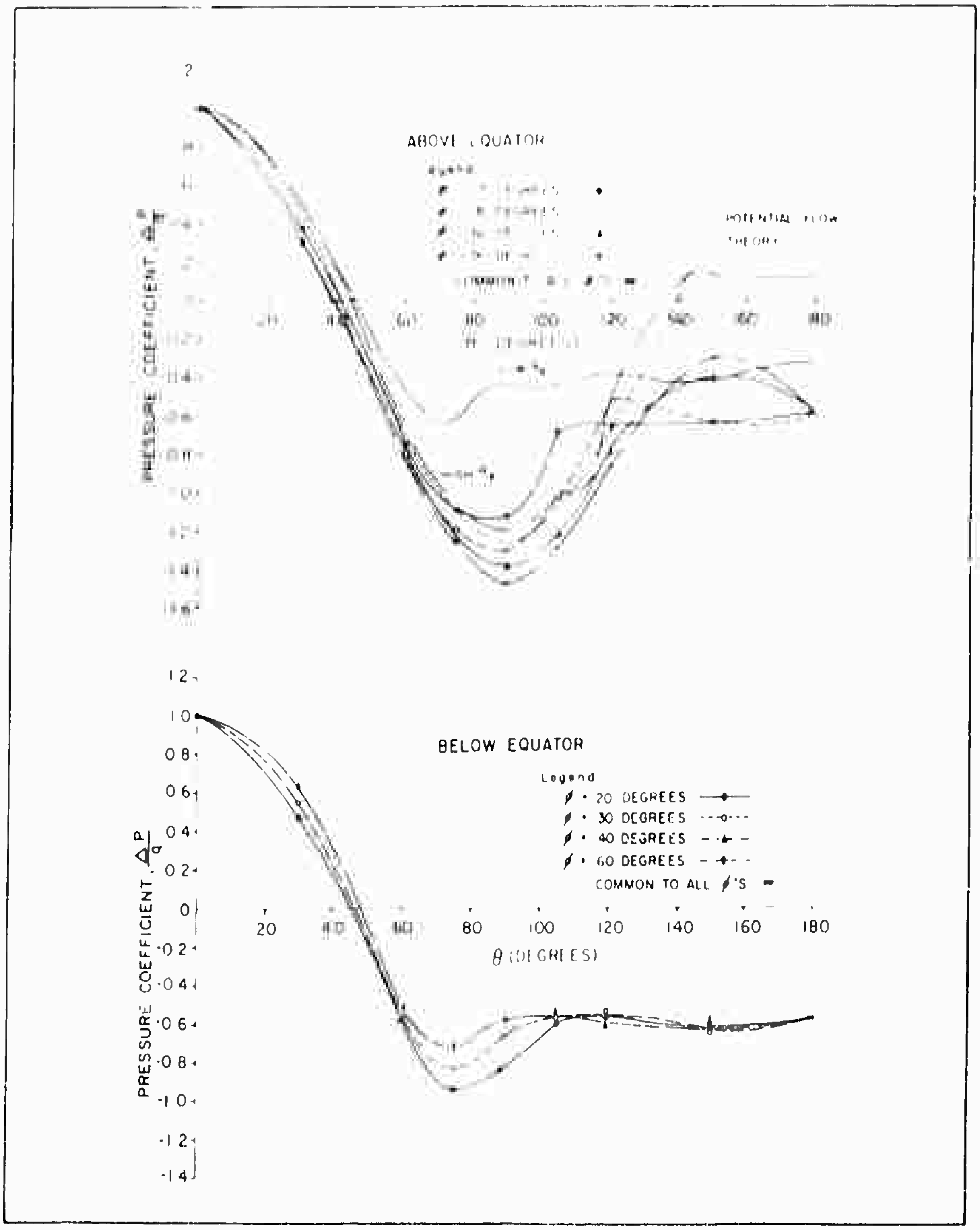

Figure 17 - Pressure Distribution over Radome Mounted on Square Base (β = 49.2 Deg, ψ = 45 Deg, b/D = 1.03)

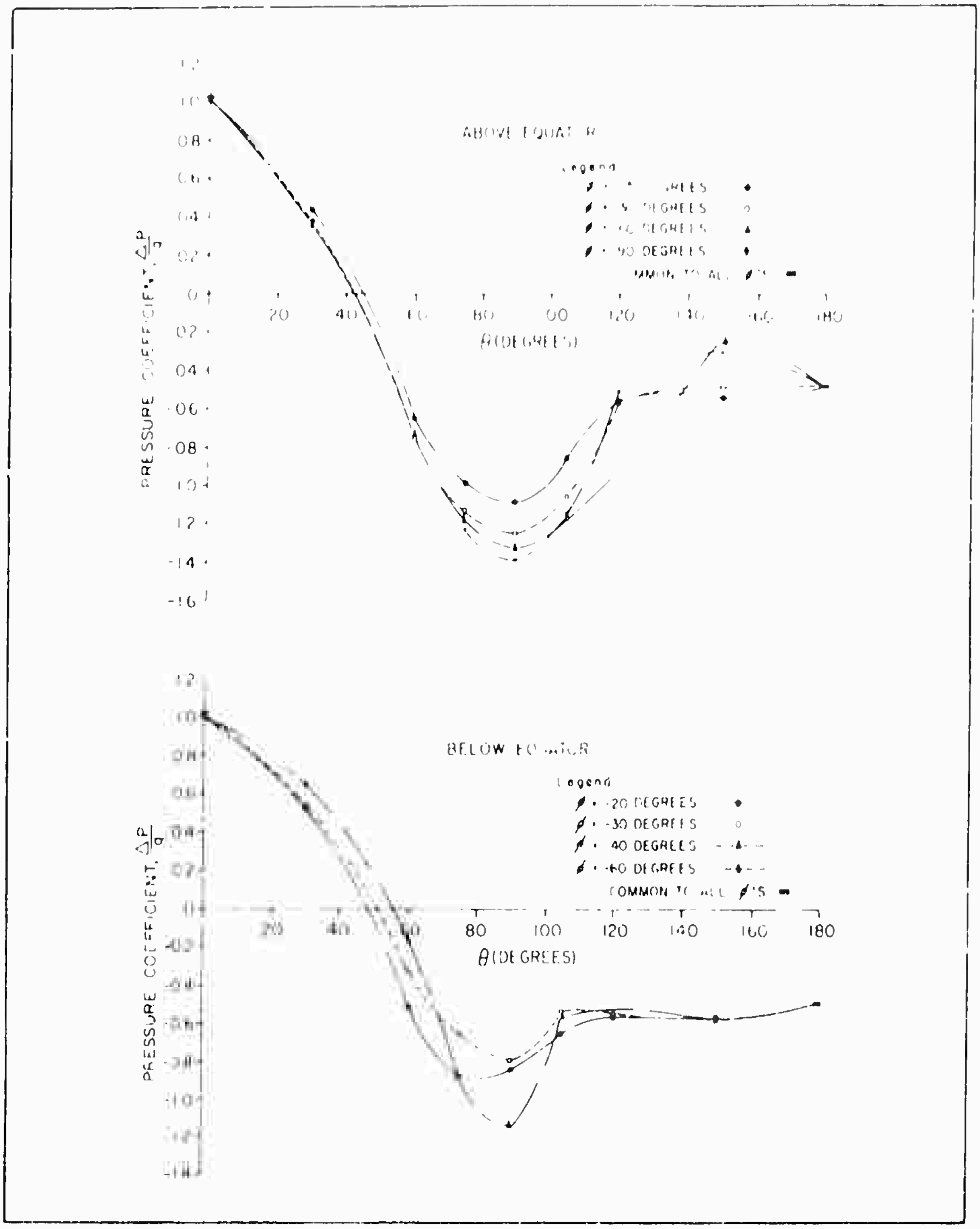

Figure 18 - Pressure Distribution over Radome Mounted on Square Base (β = 49.2 Deg, Ψ = 45 Deg, b/D = 0.60)

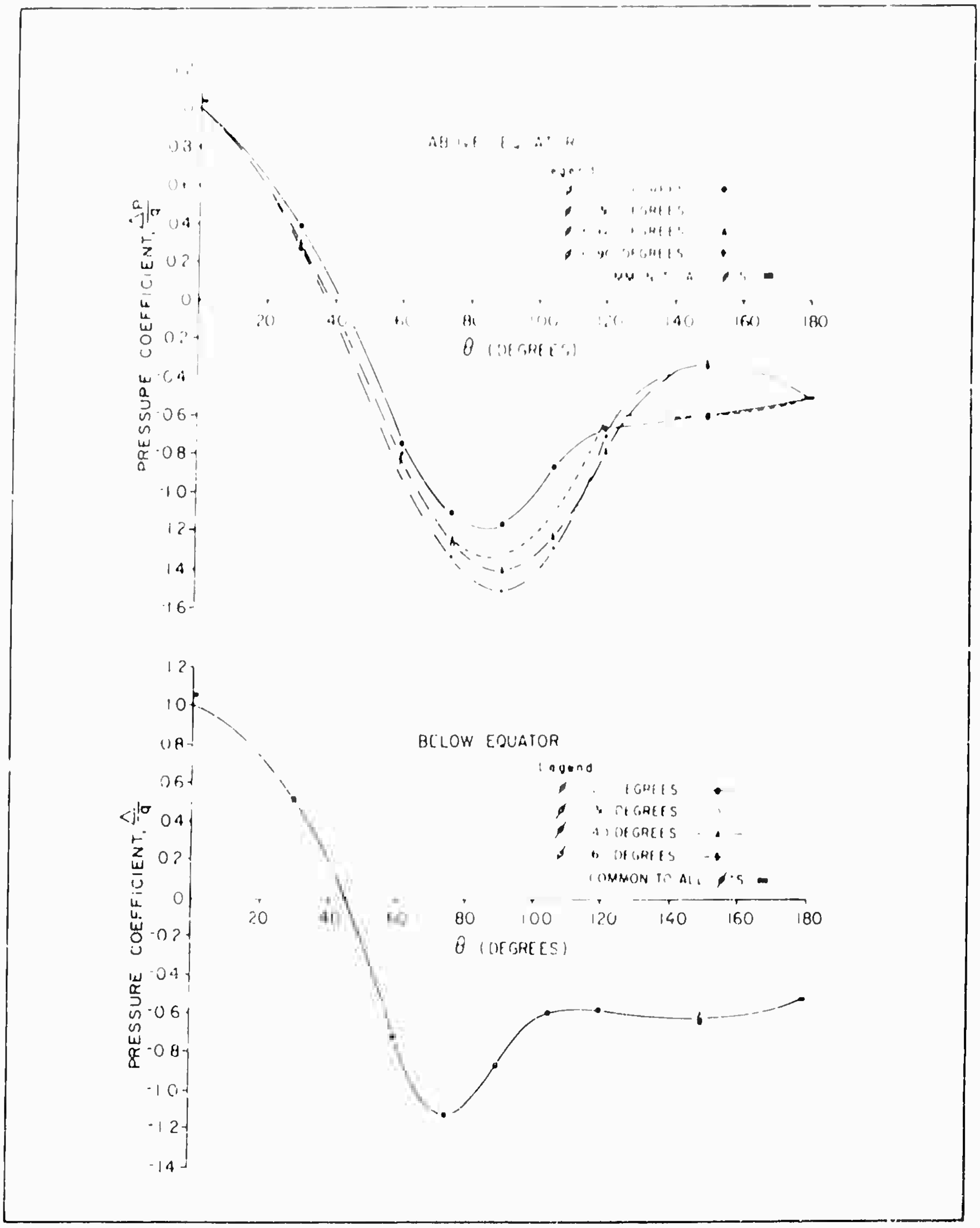

Figure 19 - Pressure Distribution over Radome Mounted on Square Base
(β = 67.7 Deg, Ψ = 45 Deg, b/D = 1.03)

aerodynamic loads on the radome to some extent, depending on the position of the buildings relative to the radome and to the wind. It was necessary to evaluate the effects of a nearby building on the aerodynamic loads to be encountered by the radome installation developed by Goodyear Aircraft for RCA. Since the addition of a model of the adjoining building to the radome model would have resulted in excessive blockage in the GAC wind tunnel, these tests were conducted in the University of Detroit (U of D)[7] 7-by-10-ft wind tunnel. The purpose in reviewing these tests is not so much to report the numbers as it is to indicate the necessity of evaluating the effects of nearby buildings in the design of any radome.

One of the configurations tested (the β = 49.2, b/D = 1.03 radome) is shown in Figure 20 as installed in a wind-tunnel test section. Figure 20 shows the downstream view with the building in the ψ = 0 position. The building and the base for the radome were rotated as a unit at 30-deg increments until the building was upstream. A comparison of the aerodynamic measurements (Figure 21) with and without the building show the appreciable effect of the building on the loads exerted on the radome. Drag, lift, and pitching moment can increase if the radome is exposed to winds from any direction. Side force, which is perpendicular to the wind and in the horizontal plane, can be attributed to the fact that the configuration is not symmetrical relative to the wind. It was observed that the advantage of lesser aerodynamic loads can be gained by orienting the radome installation approximately 120 deg relative to the prevailing winds.

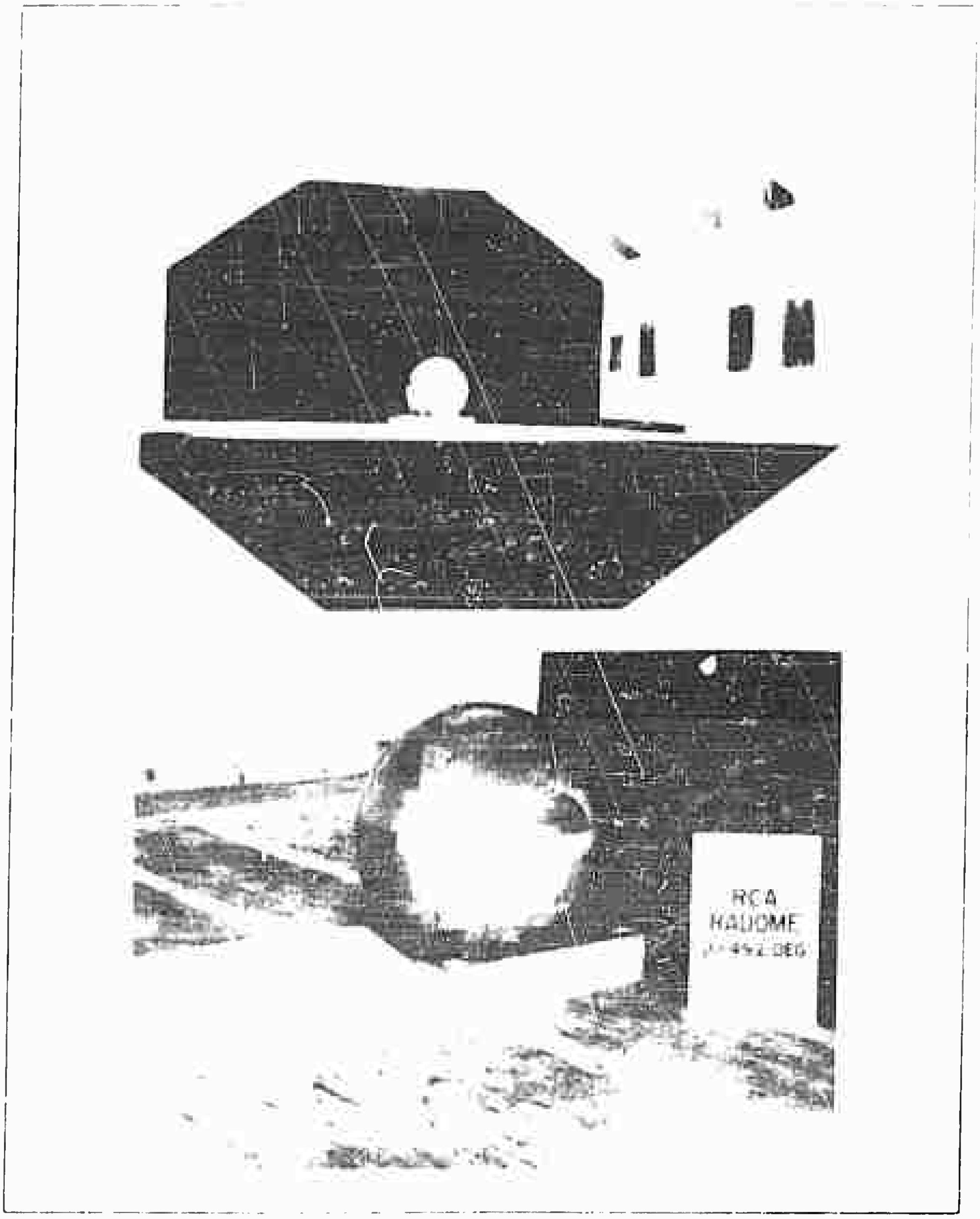

Figure 20 - Typical Installations of Square Based Radomes

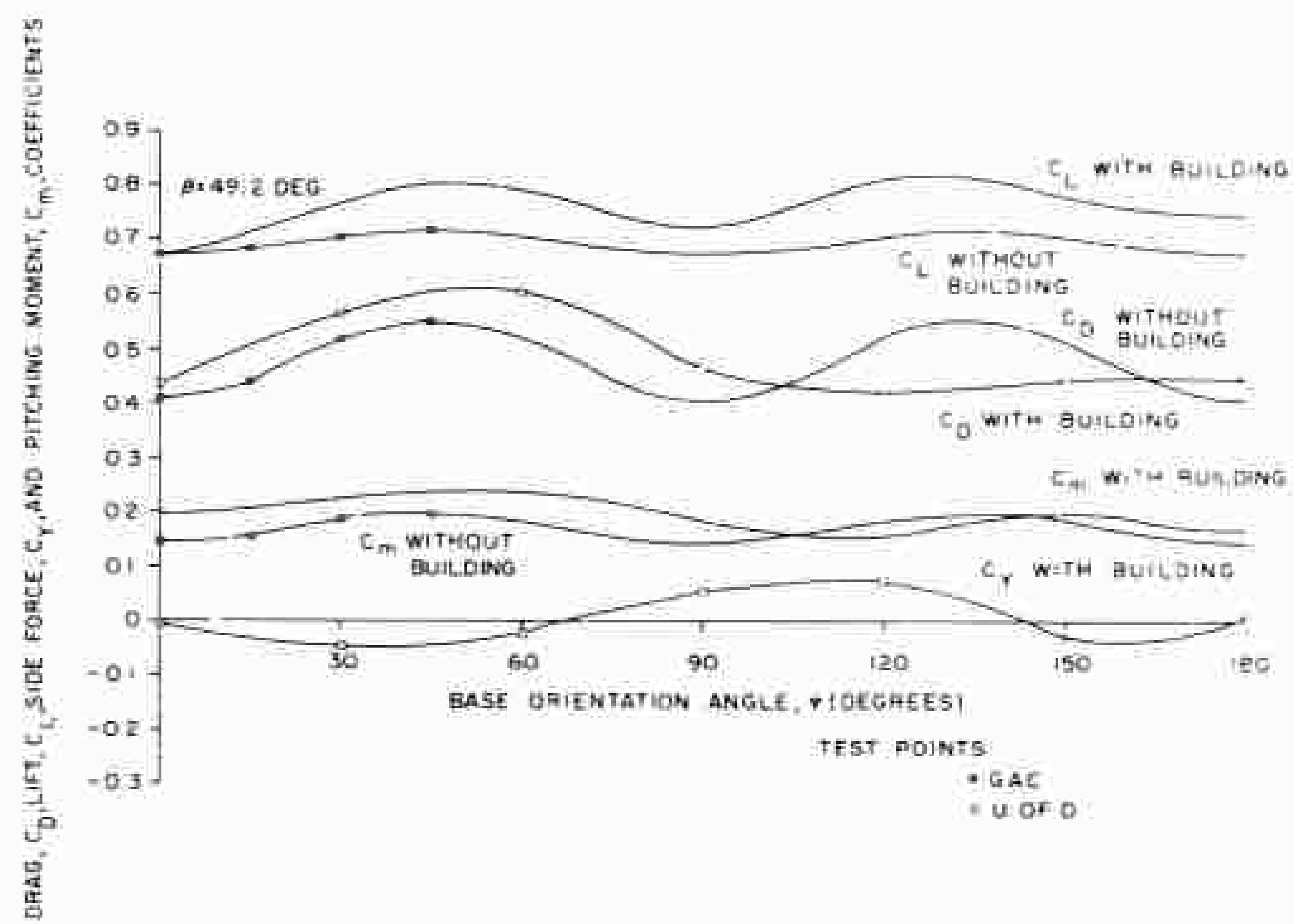

Figure 21 - Building Interference Effects on Radome Installation

FORCE MEASUREMENT CHECKS

As a check on the validity of the wind-tunnel force measurements, the measured surface pressures on certain radomes were integrated in the lift and drag directions. Figure [illegible] compares the lift and drag coefficients. The differences were acceptable for all conditions except when β = 61.7 deg and b/D = 1.03.

ENVIRONMENTAL CONSIDERATIONS

Thus far, the aerodynamic loading on radomes has been defined by assuming ideal steady-state wind conditions and for installations on generally flat terrain. Unfortunately, nature does not provide these ideal conditions. Wind gusts always must be considered, and, for some installations, the conditions encountered on mountain tops must be evaluated. For purposes of design, a steady-state wind may sometimes be defined on the basis of the transient nature of the wind and the local history. Such an assumption, however, would be largely a matter of judgment and so would tend to be excessively conservative. Therefore, a more rational means is being sought to define the environment that the radome must withstand.

Of particular concern to the radome designer is how gust loads should be treated: as transient or as equivalent steady-state winds. Gusts are not realized instantaneously, but the intensity of the wind is a function of time. Some of the gust shapes considered in past and current airplane design practice are shown in Figure 23. The maximum incremental value the wind attains over steady state is termed the gust intensity. This shape $(1 - \cos\theta)$ is currently recommended when the response of the aircraft is being studied for a

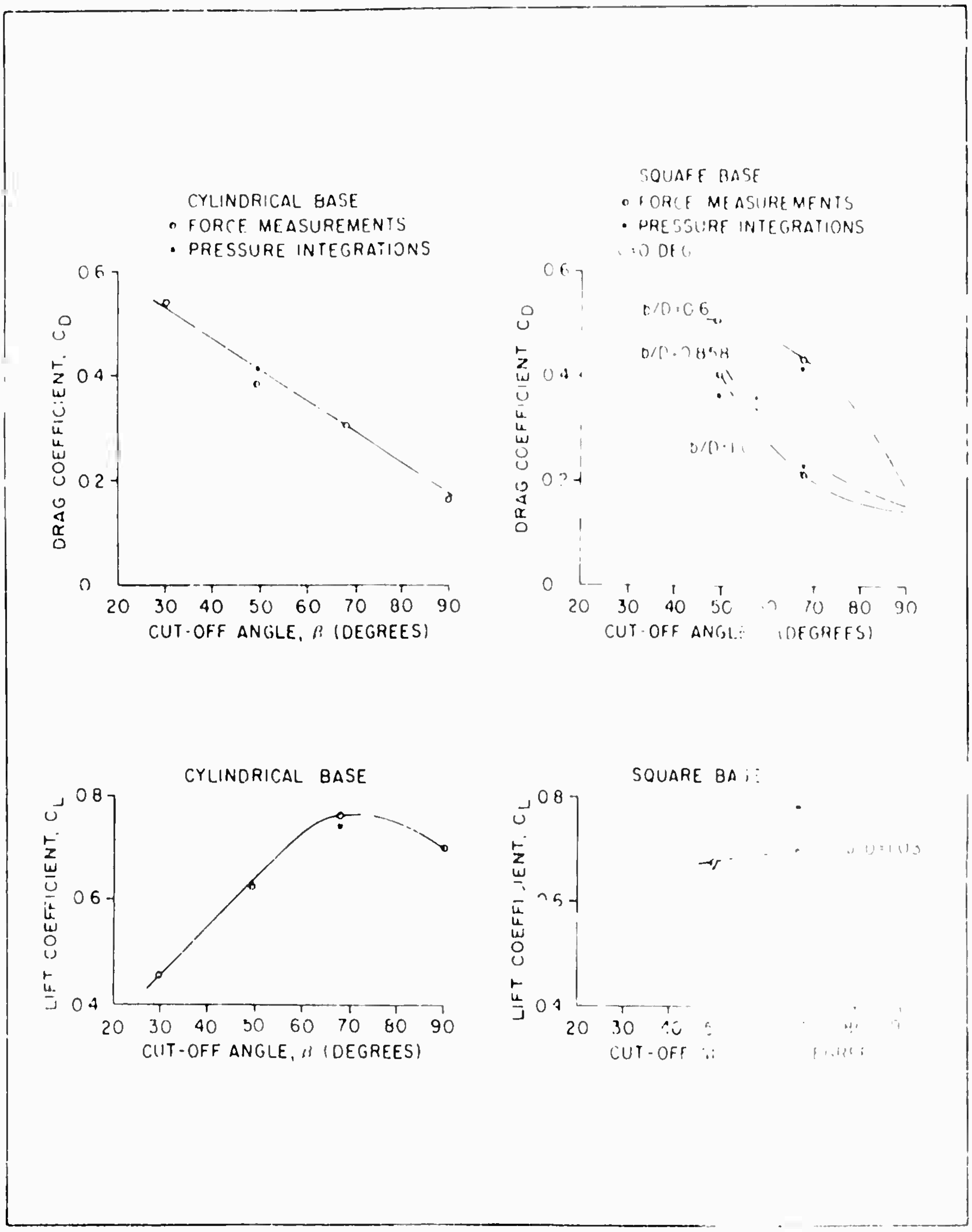

Figure 22 - Comparison of Force Measurements with Pressure Integrations

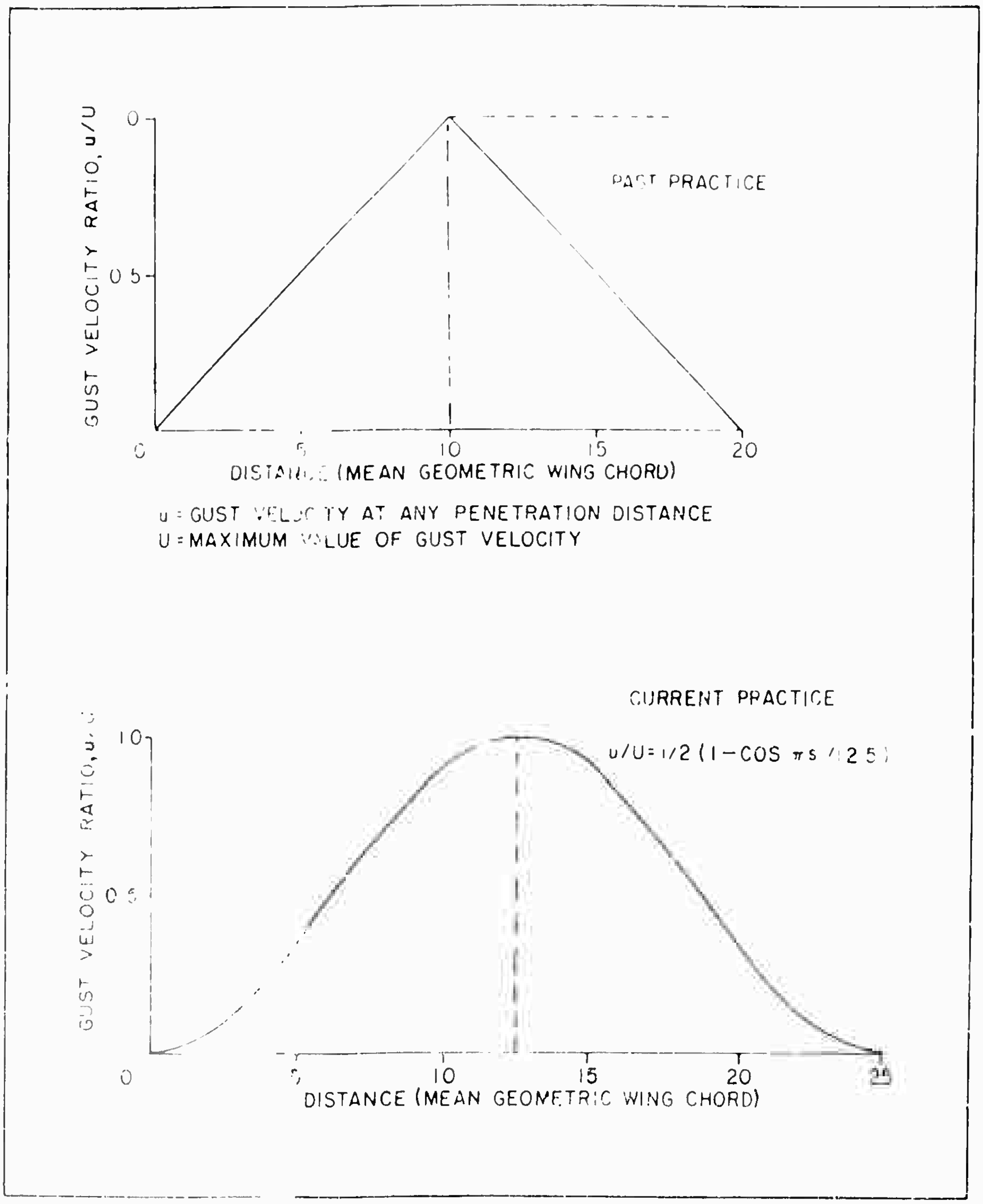

Figure 23 - Typical Gust Shapes Used in Airplane Design

discrete gust. The distance of the gust is measured in terms of the airplane wing chord - a relative but not finite measure.[8] This procedure has proved satisfactory for airplane design because the airplane in gust studies was used as a tool to measure the gust, and the wing chord was found to be the defining dimension of gust. But, since airplane gust geometry is not applicable to radome design, a finite description of gust geometry for this application must be formulated.

Once the gust geometry becomes definable, it will be possible for the aerodynamicist to determine reliably the loads on the radome. Such problems as this do not lend themselves easily to analytical methods and it has been deemed to be more practical to resort to the wind tunnel for such studies.

In addition to the probability of gust occurrence - a prime factor whereby the design-gust velocity is established for airplanes - another factor, the acceptable attrition rate for gust-critical designs, is significant in radome design. Airplane designers know a design for the severest gust ever encountered would impose an undue weight penalty on practically all aircraft series, since the probability of such a gust occurrence would be quite low. Therefore, an acceptable number of losses attributable to gust loading is established; this figure may be a loss number or it may be a gust level at which experience has shown the losses will be acceptable. The design of radomes might well be based on a similar philosophy in the interest of more efficient results.

The gust environment for radome design also could be defined by a method that allows for additional gust characteristics. Gusts are not discrete but

occur in chains of many intensities, shapes, and durations. Thus, a gust value may be determined for analytical purposes by means of a power spectral density method.

CONCLUSIONS

Although admittedly limited, the Goodyear Aircraft studies yielded considerable data on the effects of aerodynamic loads on hemispherical ground radomes. Certain conclusions generally applicable to radome design, although based solely on aerodynamic load considerations, can be drawn from this work as follows:

1. Radomes with cylindrical bases are preferable to those mounted on square bases.
2. If a square base must be used, better results can be obtained by orienting the flat side of the base to the prevailing winds.
3. A square base larger than the radome base circle is slightly preferable to decrease drag and overturning moment at the possible expense of an increase in lift.
4. Large radome cut-off angles are preferable because they ensure lower drag and overturning moment although some increase in lift results.
5. The negative surface pressure on the radome is higher with increases in cut-off angle.

The set of curves resulting from these extensive measurements of loads on various configurations have proved useful in radome design. It is hoped that data from future experiments will be offered for integration with the data presented herein to provide a better definition of the design curves.

The GAC studies also pointed up the need for more work in the area of defining the environment for more efficient radome design.

LIST OF REFERENCES

1. GER-8898: Wind-Tunnel Tests of Bell Radome and Supporting Buildings. Akron, Ohio, Goodyear Aircraft Corporation, Contract DA-30-064-ORD-1955, 22 July 1958.

2. GER-8839: Goodyear Aircraft Corporation Wind Tunnel Tests of R. C. A. Radome and Supporting Structure. Akron, Ohio, Goodyear Aircraft Corporation, 30 June 1958.

3. Experiments on a Sphere at Critical Reynolds Number. R and M No. 2023. London, England, Aeronautical Research Council.

4. Hoerner, S. F.: Fluid-Dynamic Drag. Midland Park, N. J., 1958.

5. Klemin, Alexander; Schaefer, Everett B.; and Beerer, Jr., J. G.: "Aerodynamics of the Perisphere and Trylon at World's Fair." Proceedings of American Society of Civil Engineers, May 1938.

6. Bird, Walter W.: Design Manual for Spherical Air Supported Radomes. Cornell Aeronautical Laboratory Report No. UB-909-D-2. Buffalo, N. Y., 15 March 1956.

7. Davenport, E. L · Wind Tunnel Test of the RCA Radome. University of Detroit-Aeronautical Laboratory Project 268. Detroit, Mich., June 1958.

8. Pratt, K. G.: A Revised Formula for the Calibration of Gust Loads. NACA Technical Note 2964, Washington, D. C., June 1953.

APPENDIX A - SUPPLEMENTAL PRESSURE MEASUREMENTS FOR RADOMES MOUNTED ON CYLINDRICAL AND SQUARE BASES

All measurements presented herein were made in the Goodyear Aircraft 43-by-61-in. wind tunnel at a Reynolds number of 2×10^6. Pressure distributions were measured with radomes mounted both on cylindrical and square bases on a ground plane and with various cut-off angles. The diameter of the radome for all tests was 13.5 in.; the wind speed was approximately 160 mph, the wind-tunnel turbulence factor was approximately 1.6.

The curves for radomes on cylindrical bases were made for radome cut-off angles of 30 and 67.7 deg (Figures A-1 through A-3). The curves for square-based radomes (Figures A-4 through A-20) cover the parameters shown below. Additional curves appear in the body of the report.

TABLE A-1 - PARAMETERS COVERED IN AERODYNAMIC MEASUREMENT OF SQUARE BASED RADOMES

Base size ratio, b/D	Cut-off angle, β (degrees)											
	49.2				57.2				67.7			
	Base orientation angle, ψ (degrees)											
	0	15	30	45	0	15	30	45	0	15	30	45
0.6	*	*	*	†	*	*	*	*	*	*	*	*
0.858	*	*	*	*	*	*	*	*	*	*	*	*
1.03	*	*	*	†	*	*	*	*	*	*	*	†

*Curves appear in Appendix A or B.

†Curves appear in body of report.

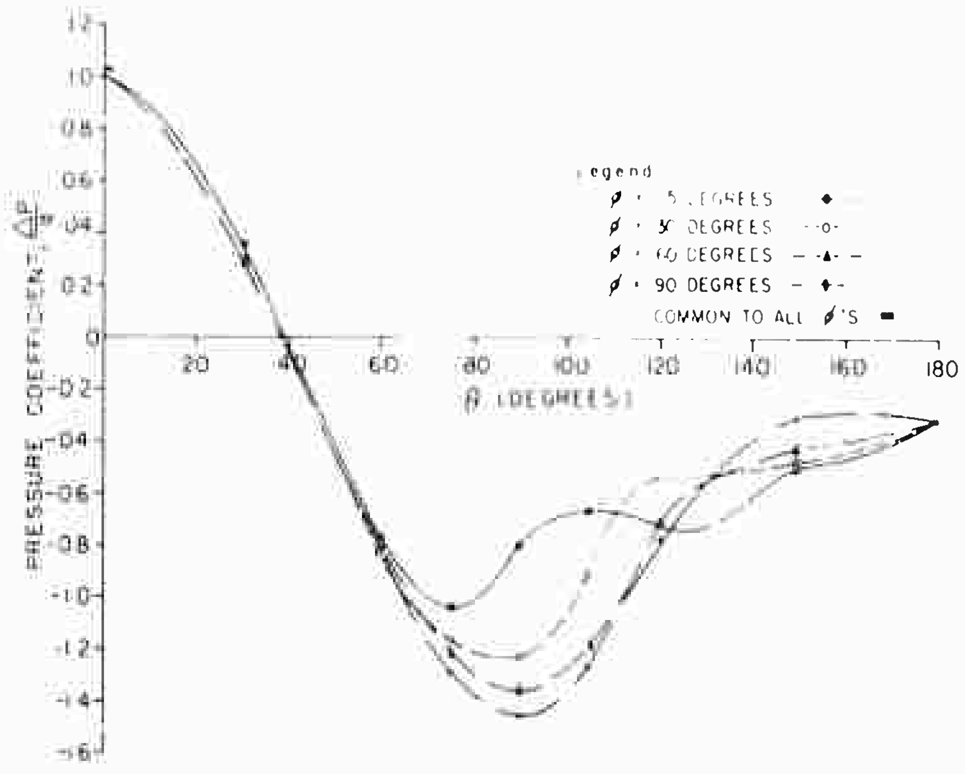

Figure A-1 - Pressure Distribution over Radome Mounted on Cylindrical Base (β = 90 Deg)

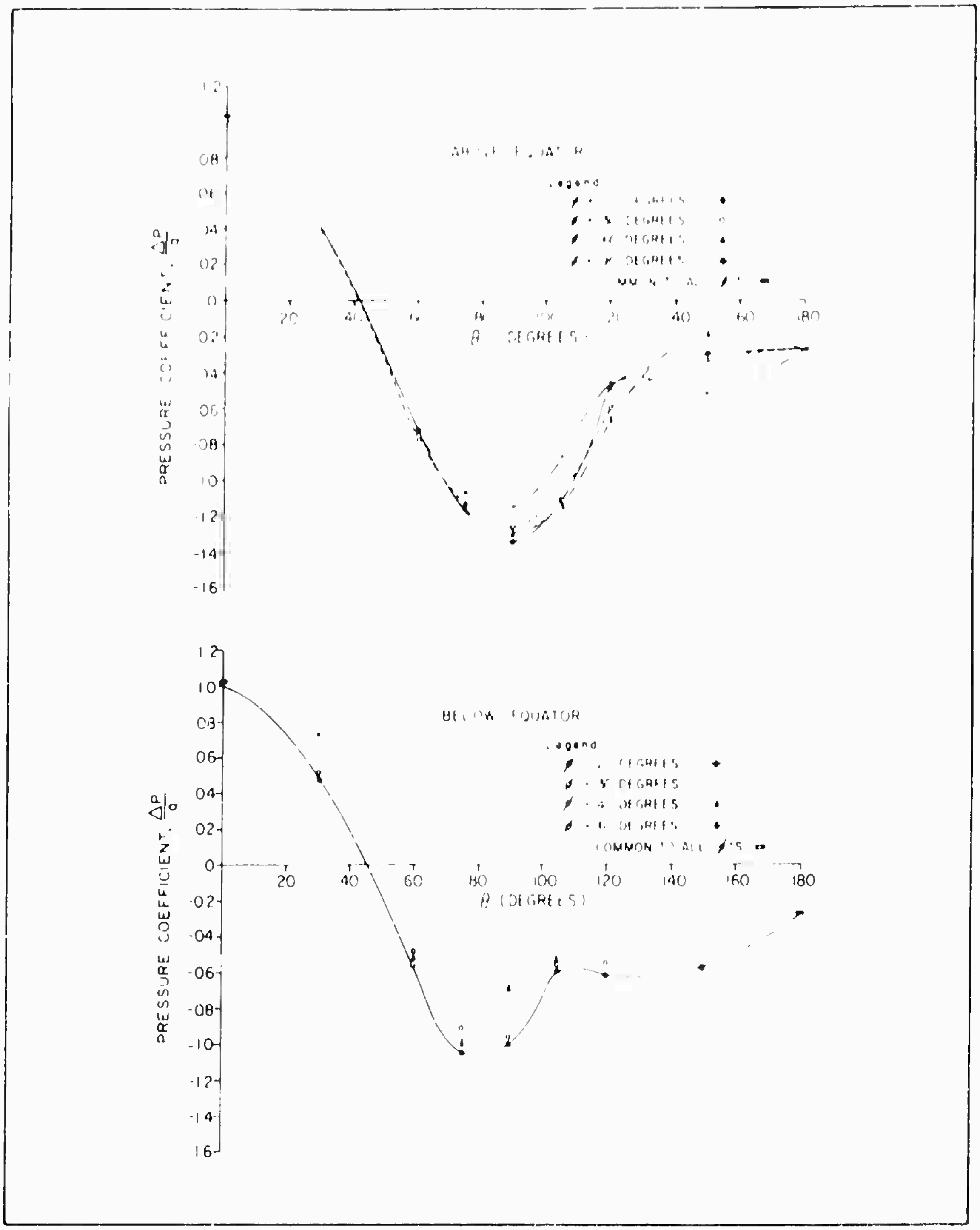

Figure A-2 - Pressure Distribution over Radome Mounted on Cylindrical Base (β = 30 Deg)

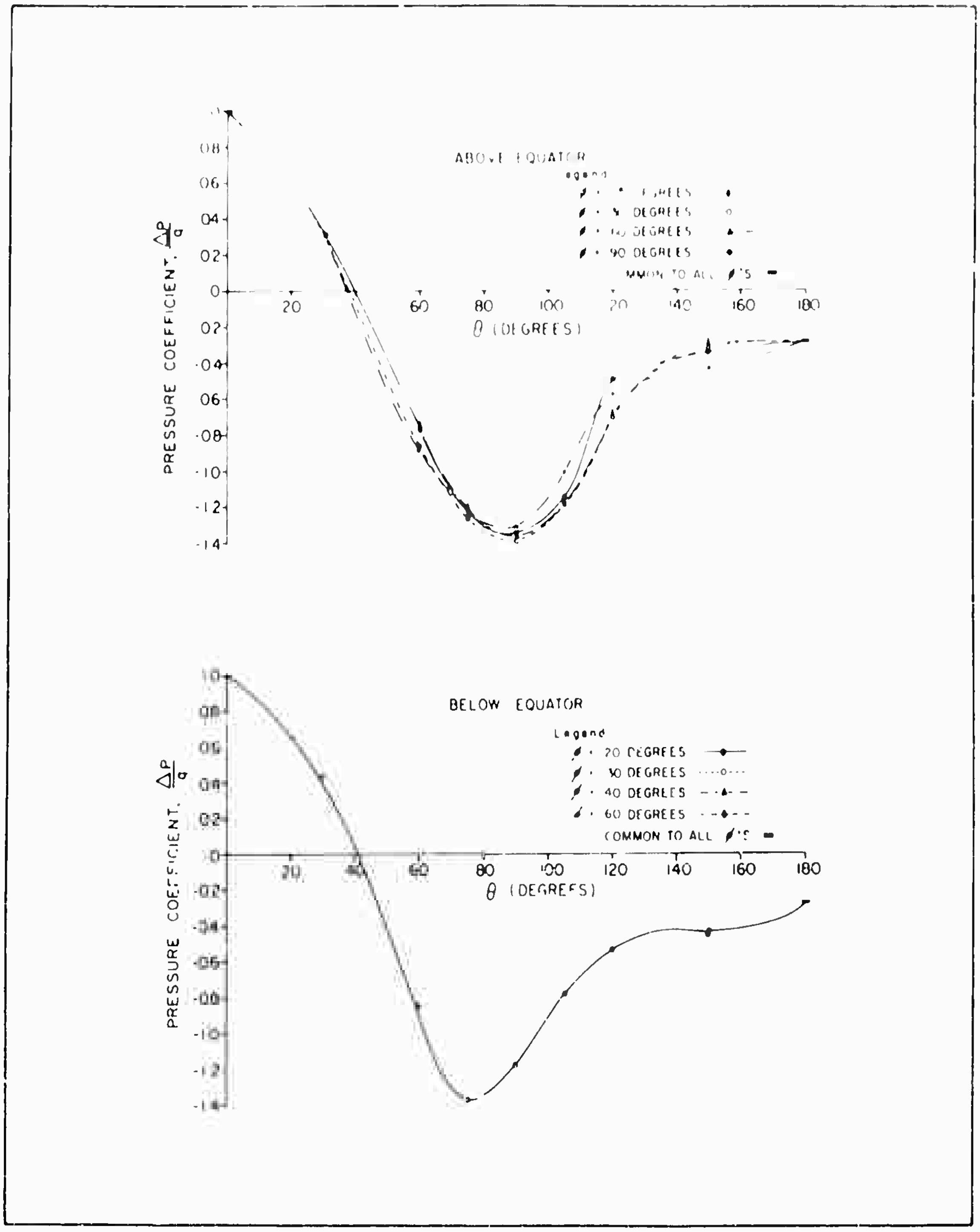

Figure A-3 - Pressure Distribution over Radome Mounted on Cylindrical Base (β = 67.7 Deg)

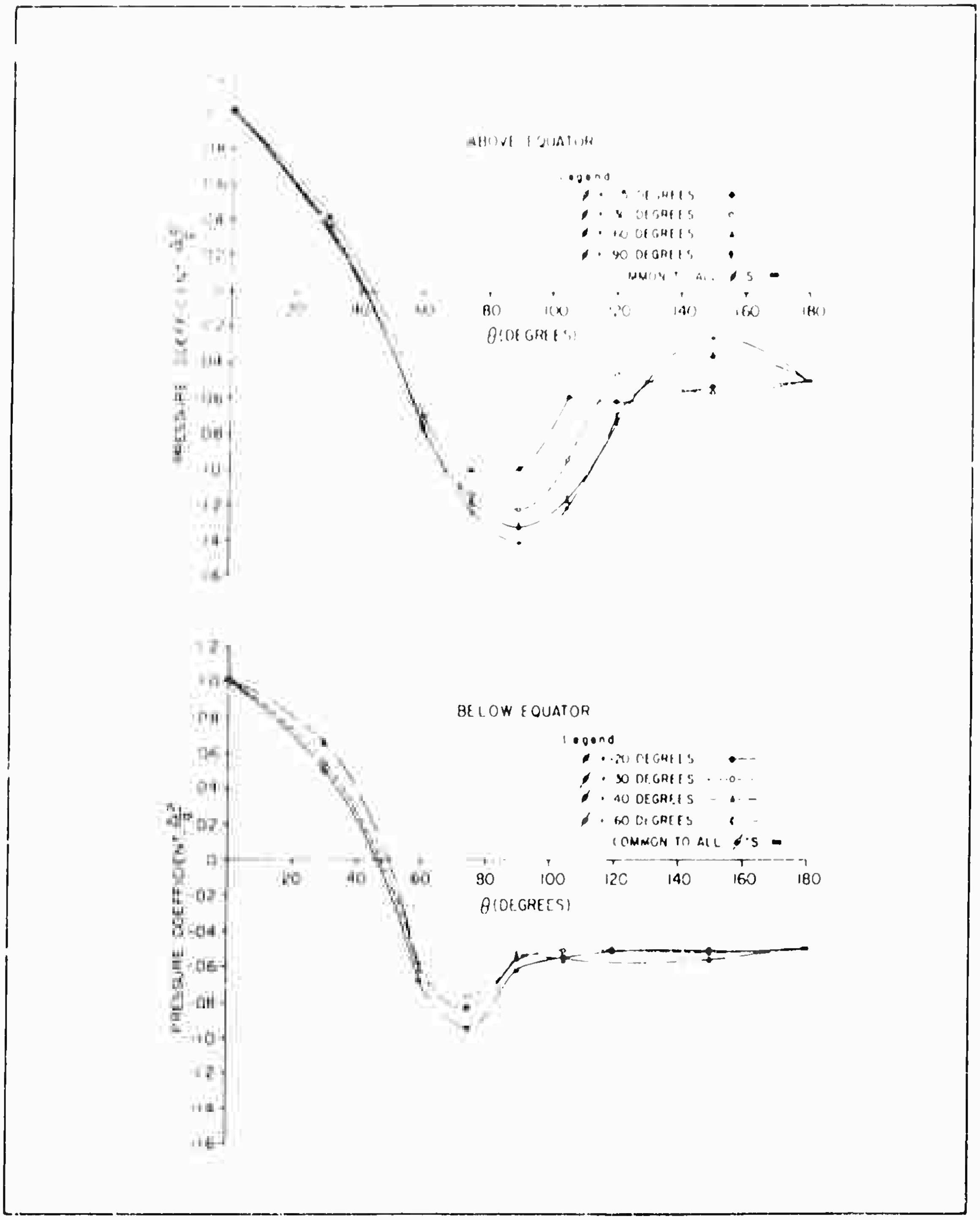

Figure A-4 - Pressure Distribution over Radome Mounted on Square Base
(β = 49.2 Deg, ψ = 0, b/D = 0.60)

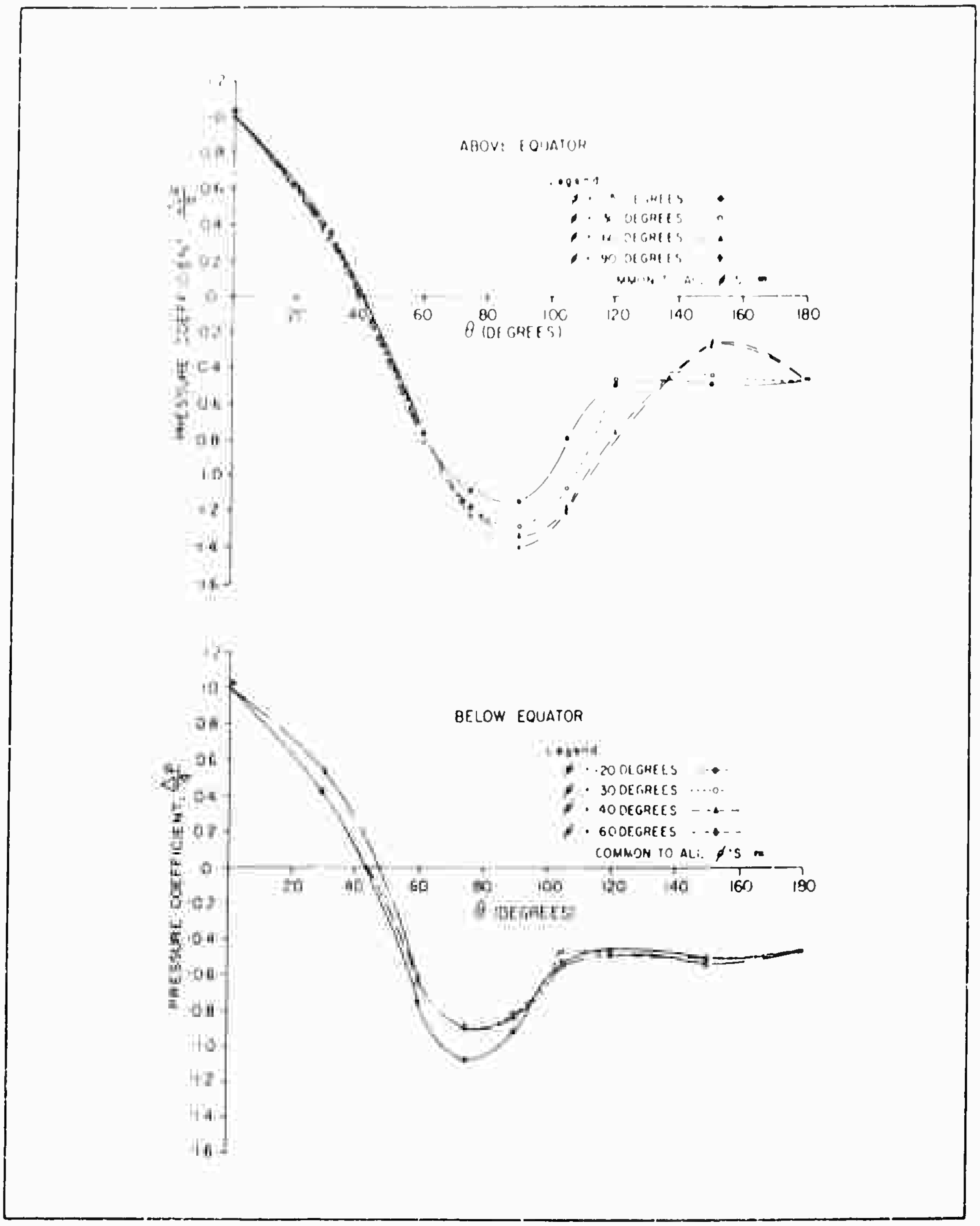

Figure A-5 - Pressure Distribution over Radome Mounted on Square Base (β = 49.2 Deg, ψ = 15 Deg, b/D = 0.60)

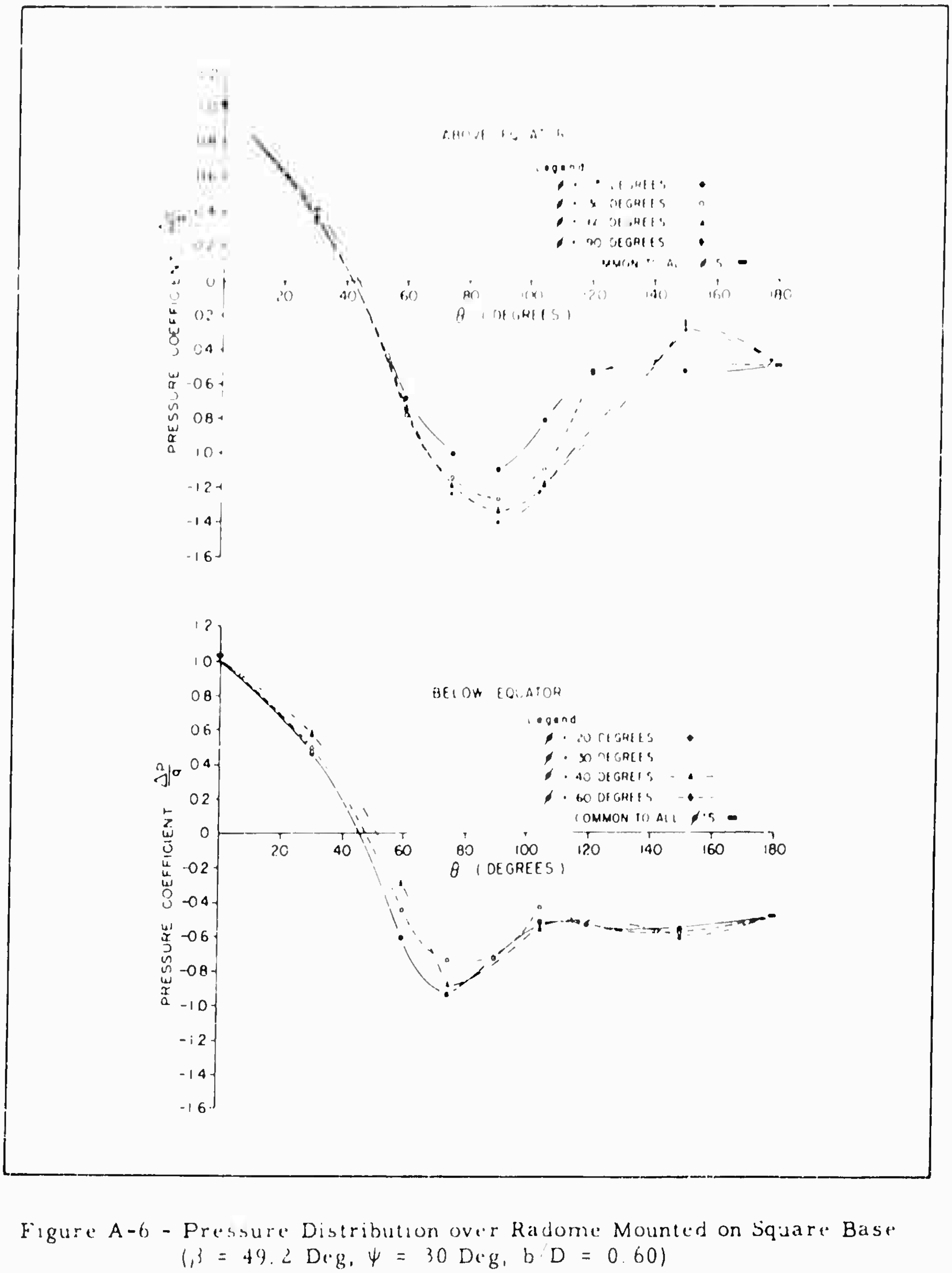

Figure A-6 - Pressure Distribution over Radome Mounted on Square Base (β = 49.2 Deg, ψ = 30 Deg, b/D = 0.60)

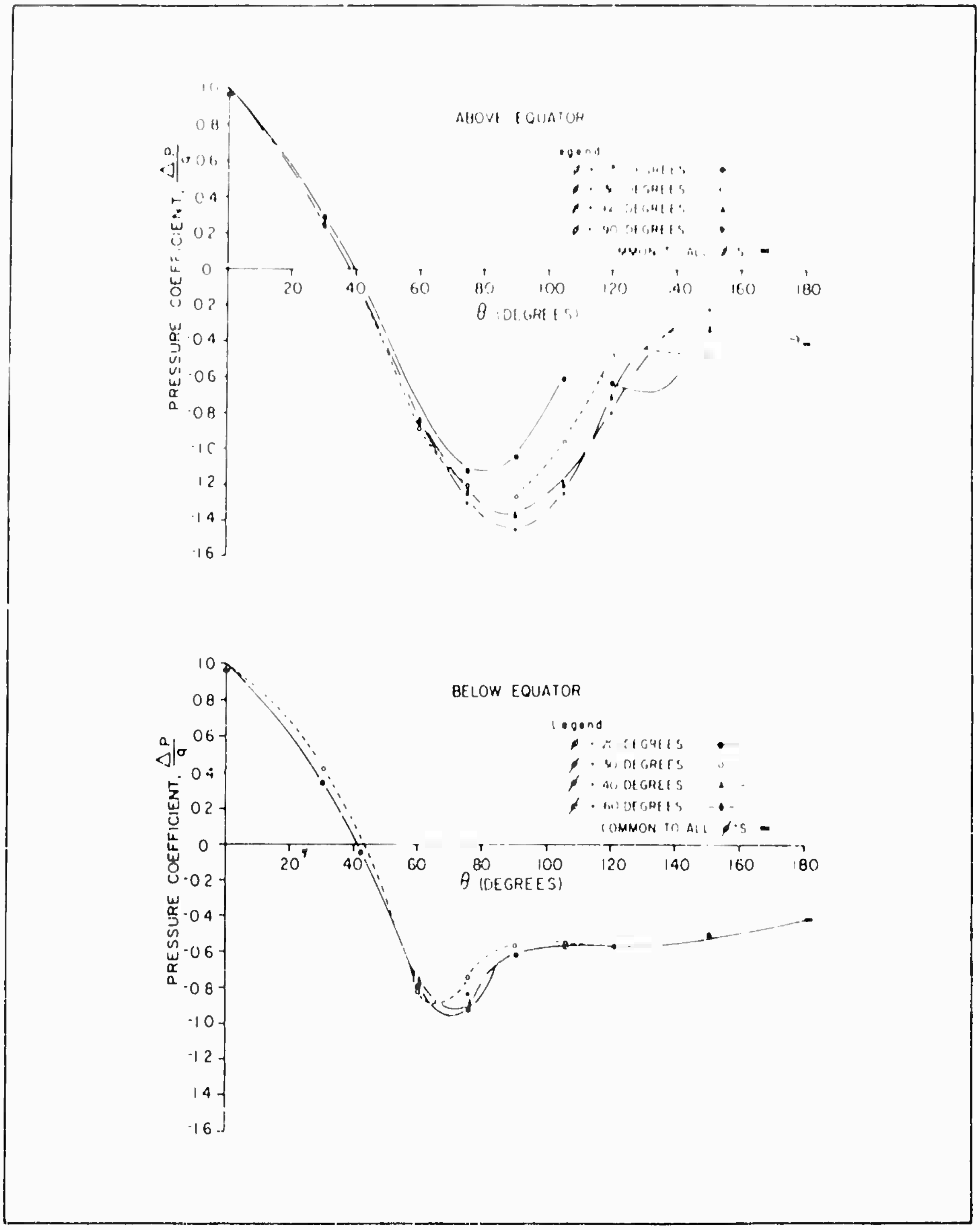

Figure A-7 - Pressure Distribution over Radome Mounted on Square Base (β = 49.2 Deg, ψ = 0, b D = 1.03)

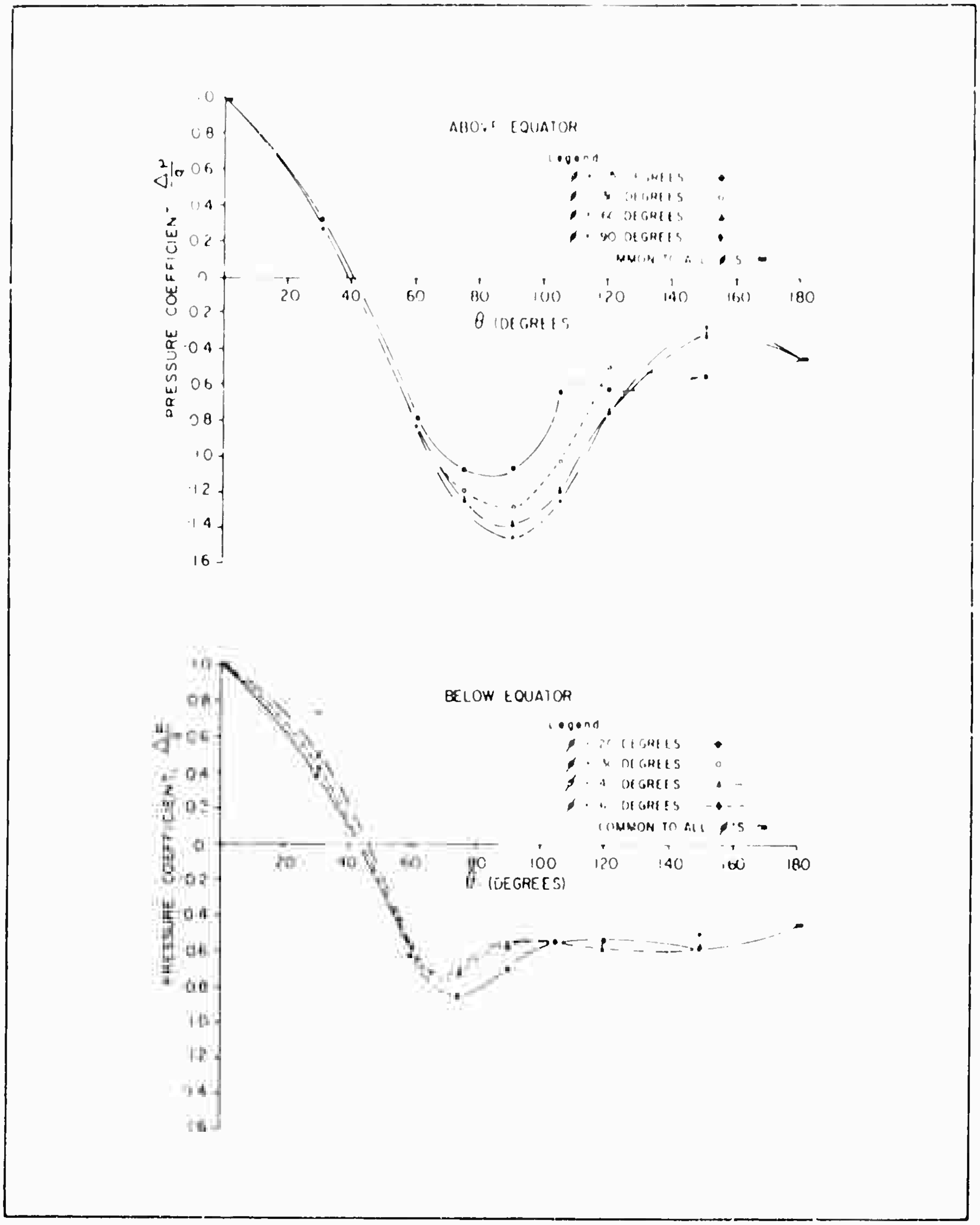

Figure A-8 - Pressure Distribution over Radome Mounted on Square Base (β = 49.2 Deg, ψ = 15 Deg, b/D = 1.03)

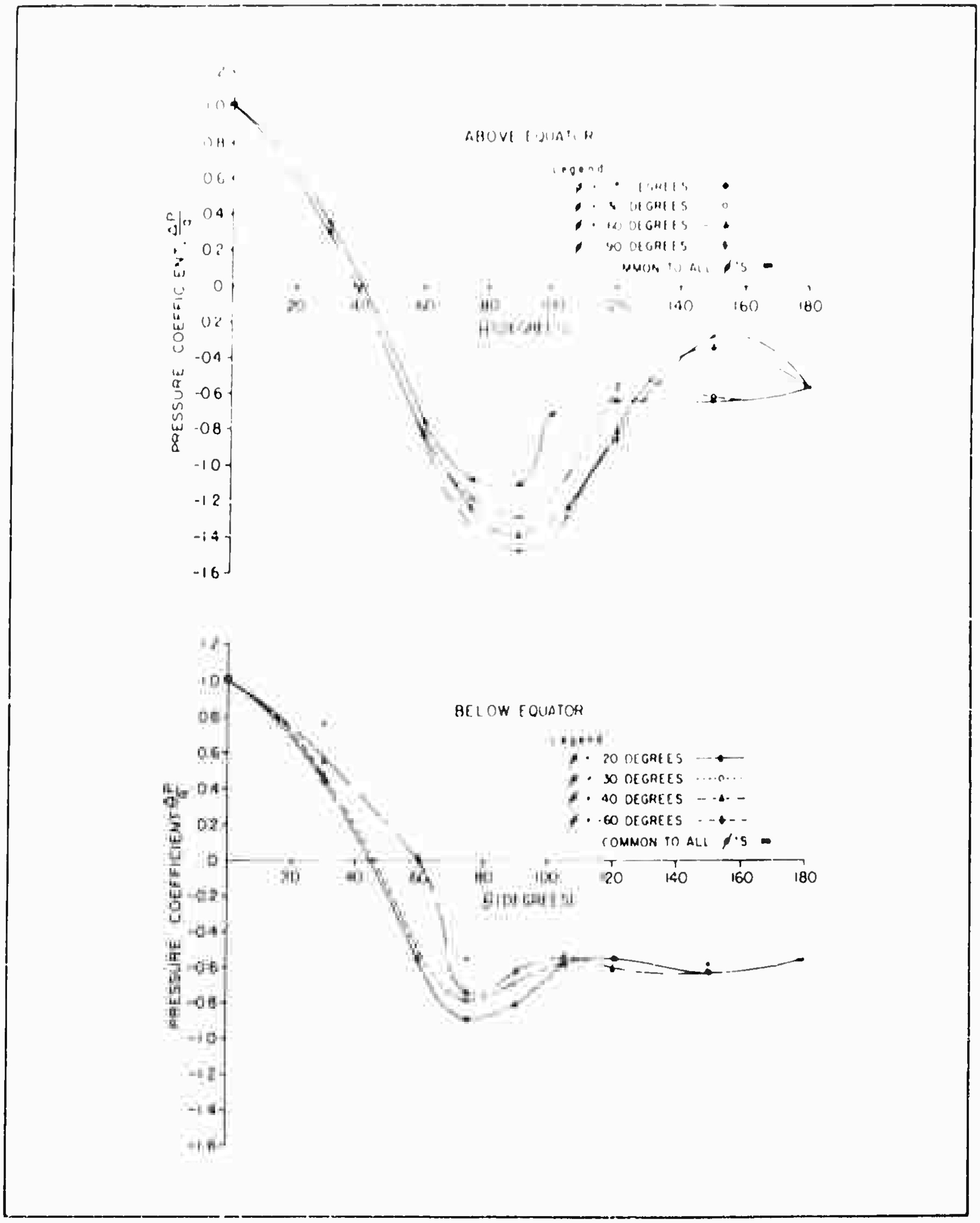

Figure A-9 - Pressure Distribution over Radome Mounted on Square Base
(β = 49.2 Deg, ψ = 30 Deg, b/D = 1.03)

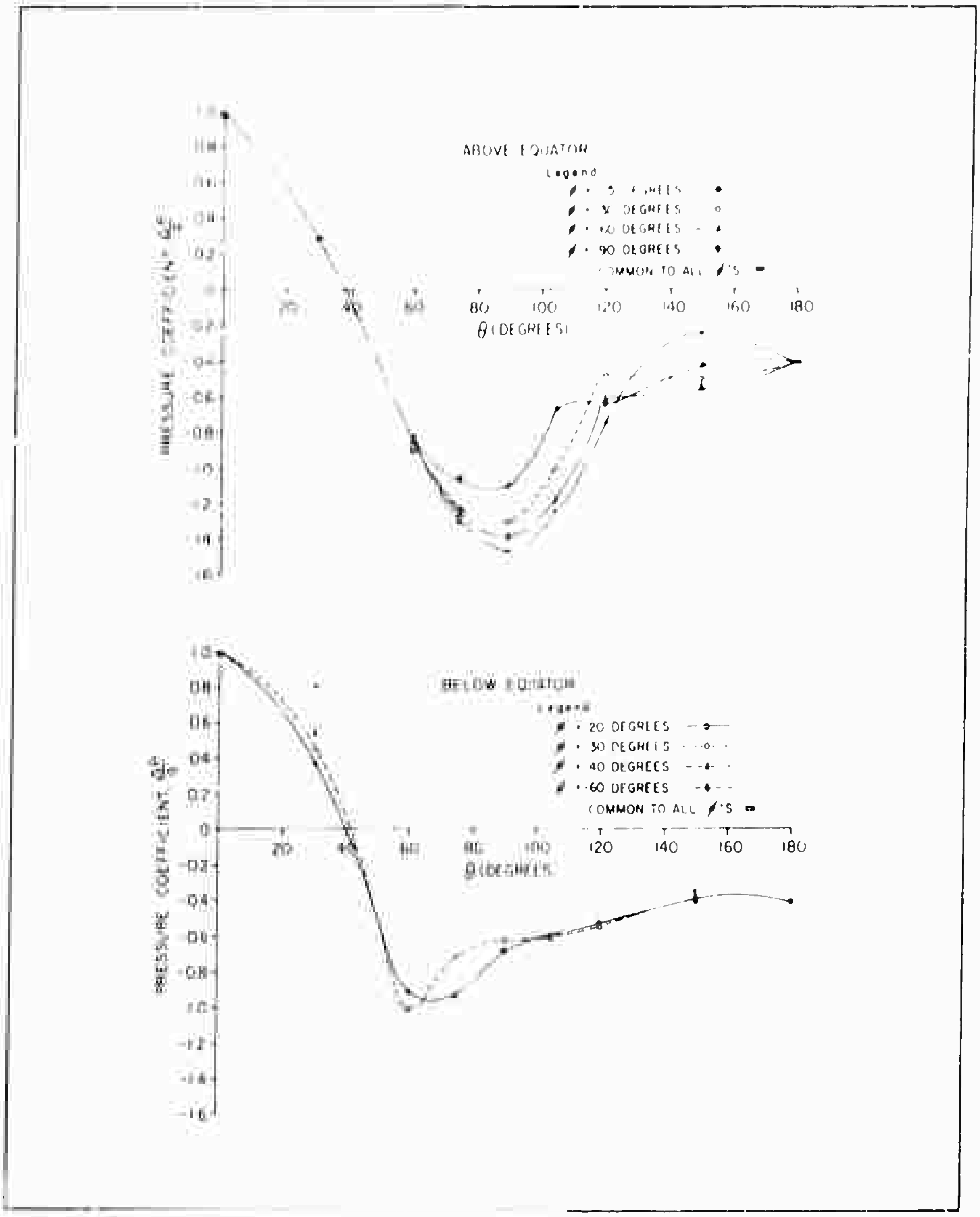

Figure A-10 - Pressure Distribution over Radome Mounted on Square Base (β = 57.2 Deg, ψ = 0, b/D = 0.858)

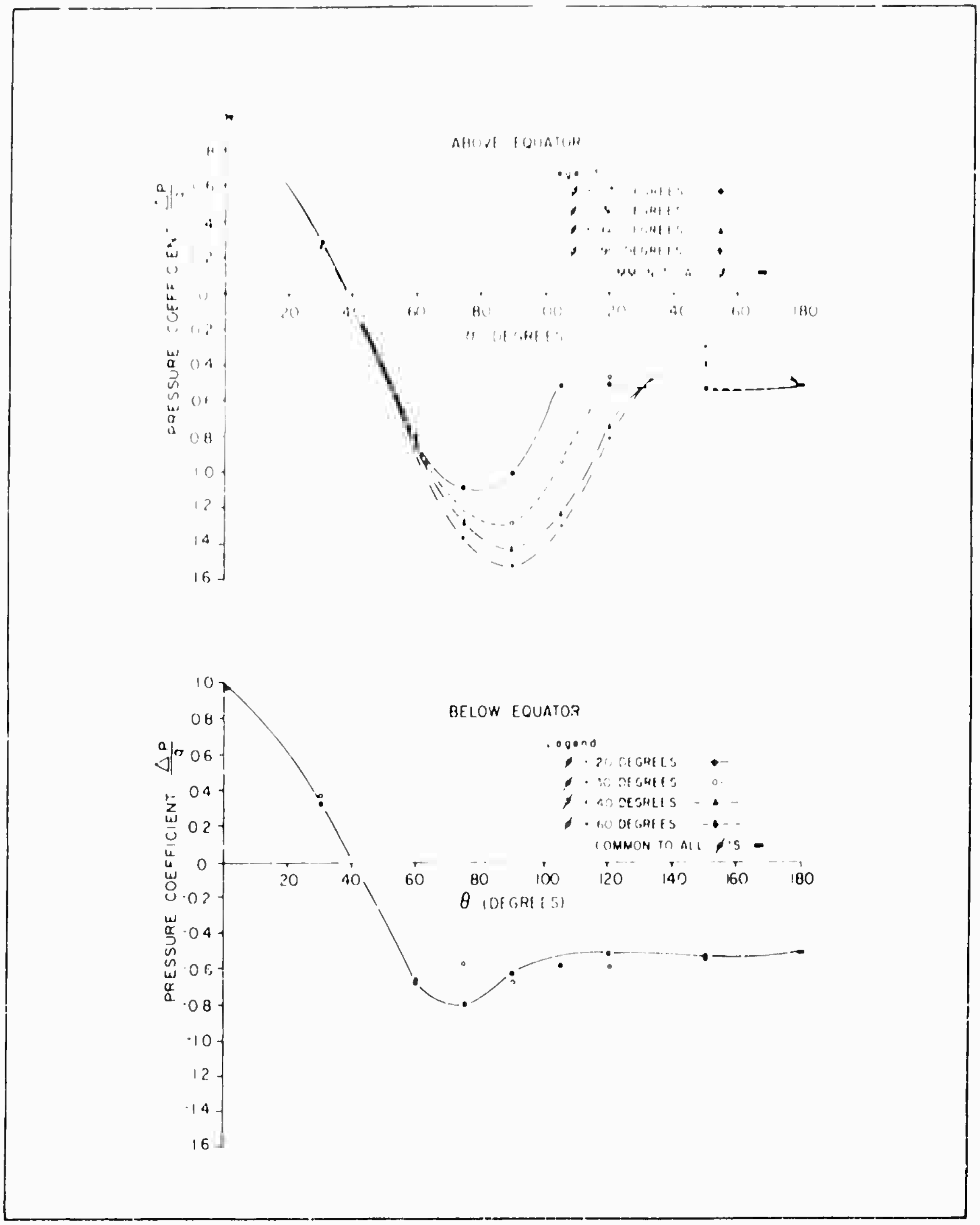

Figure A-11 - Pressure Distribution over Radome Mounted on Square Base (β = 57.2 Deg, ψ = 15 Deg, b/D = 0.858)

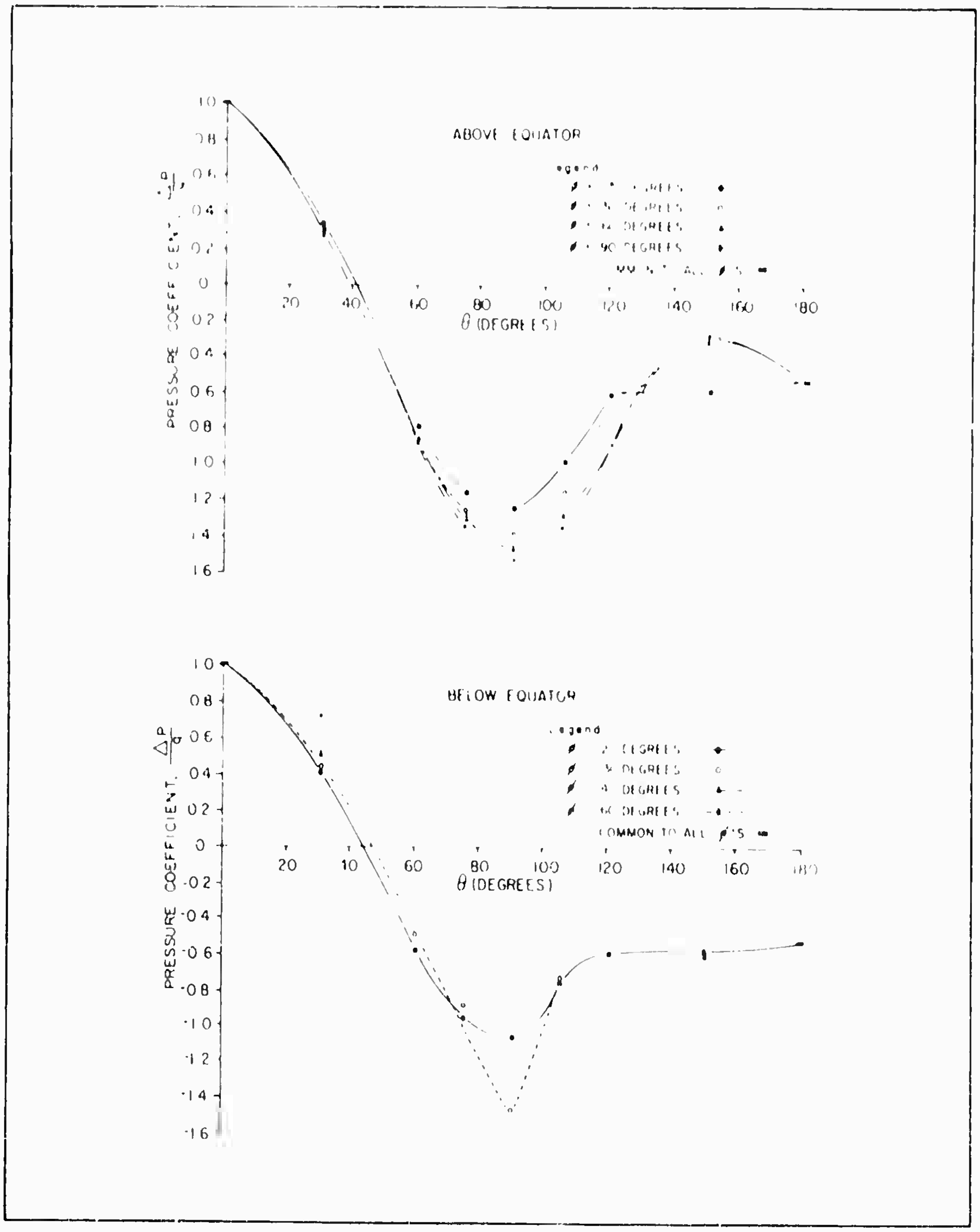

Figure A-12 - Pressure Distribution over Radome Mounted on Square Base
(β = 57.2 Deg, ψ = 30 Deg, b D = 0.858)

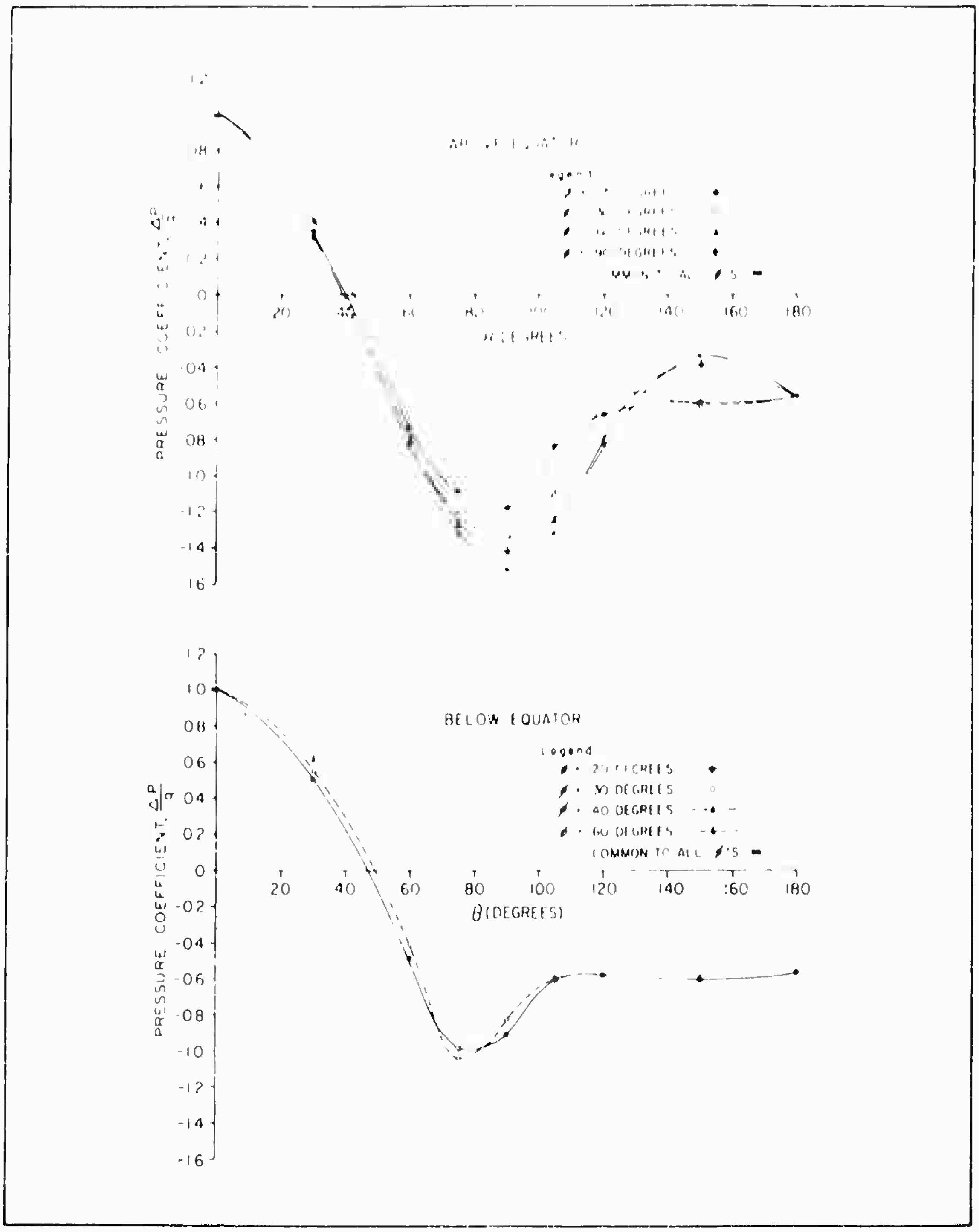

Figure A-13 - Pressure Distribution over Radome Mounted on Square Base
(β = 57.2 Deg, ψ = 45 Deg, b D = 0 858)

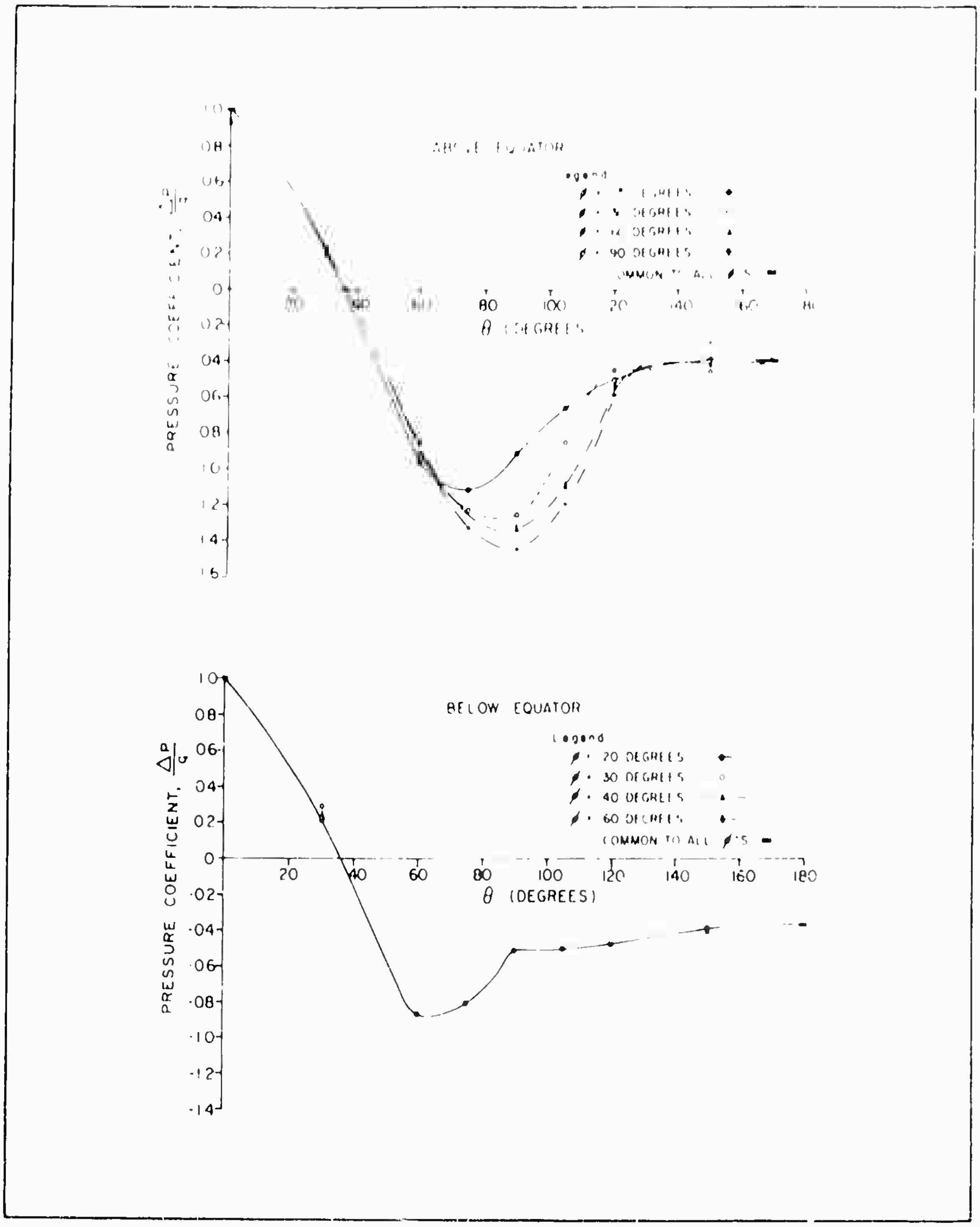

Figure A-14 - Pressure Distribution over Radome Mounted on Square Base (β = 67.7 Deg, ψ = 0, b/D = 1.03)

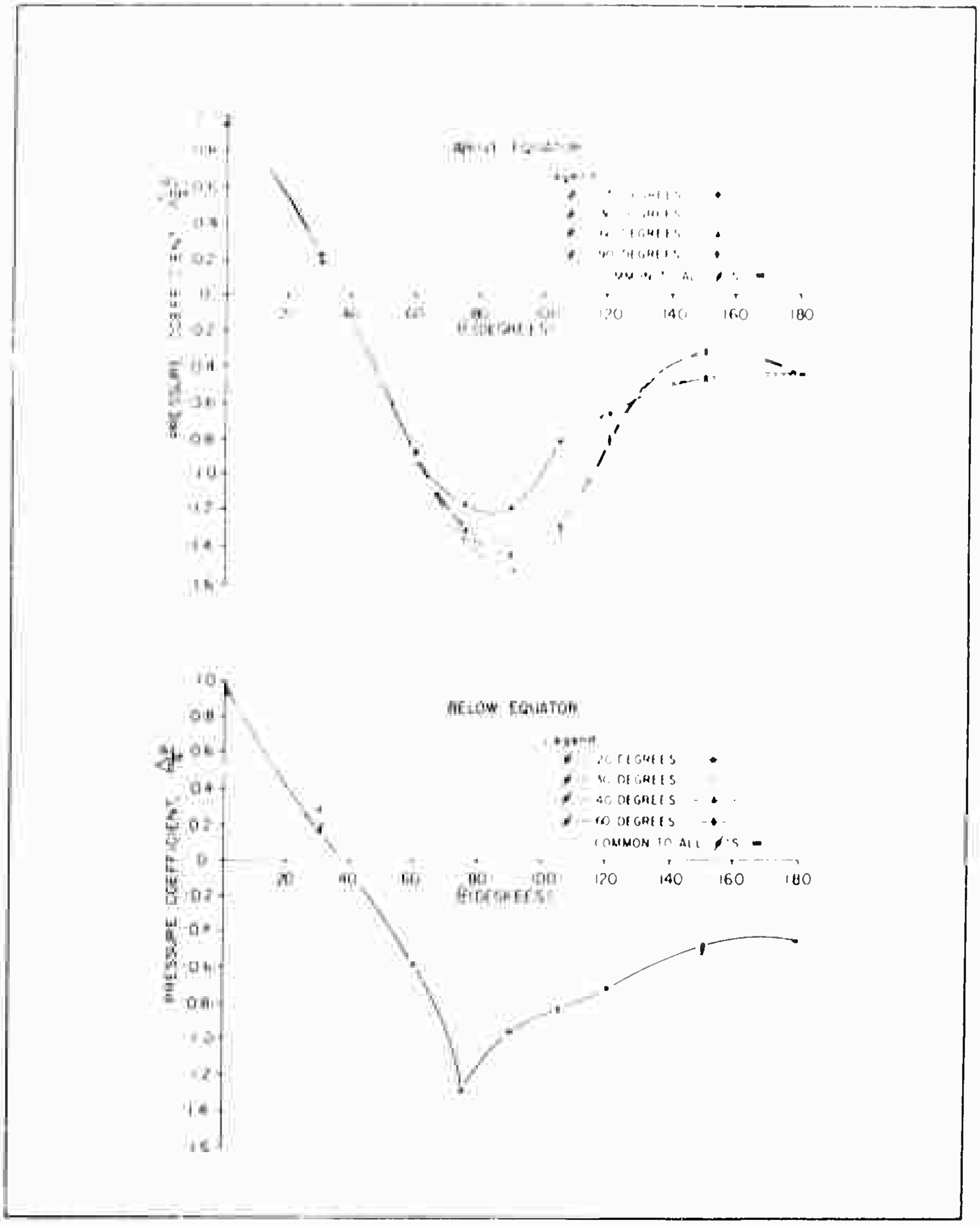

Figure A-15 - Pressure Distribution over Radome Mounted on Square Base
(β = 67.7 Deg, ψ = 15 Deg, b D = 1.03)

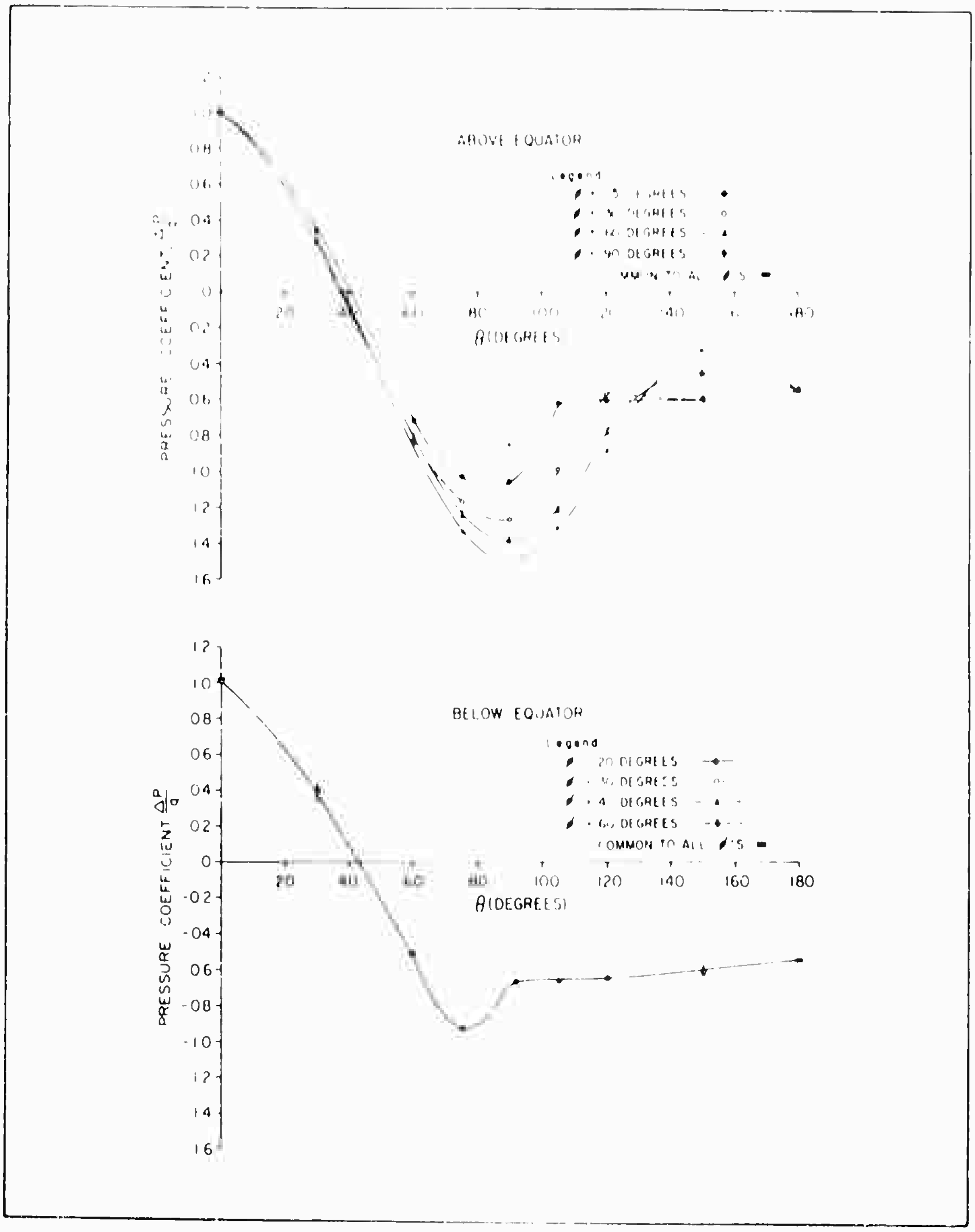

Figure A-16 - Pressure Distribution over Radome Mounted on Square Base (β = 67.7 Deg, ψ = 30 Deg, b D = 1.03)

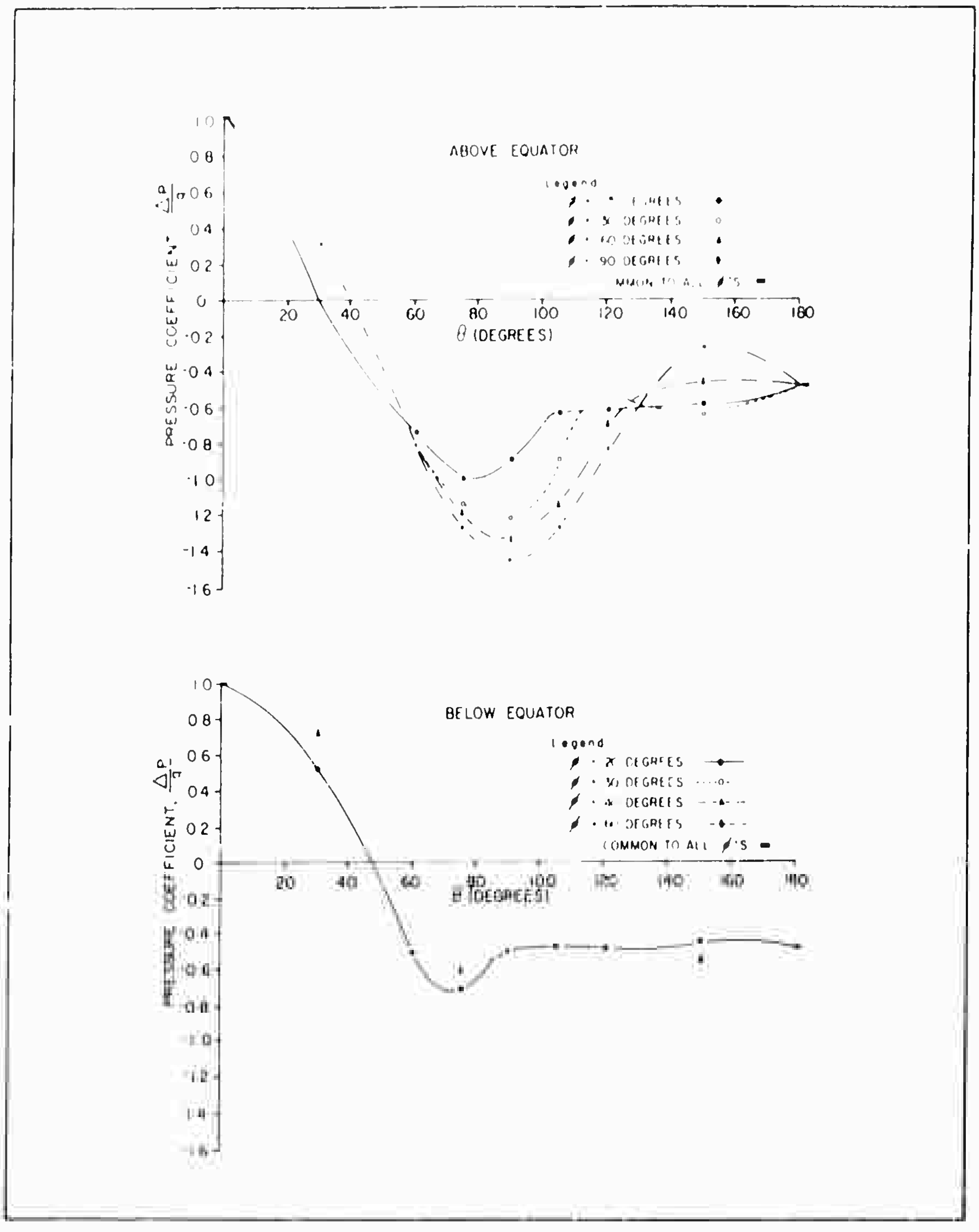

Figure A-17 - Pressure Distribution over Radome Mounted on Square Base
(β = 67.7 Deg, ψ = 0, b/D = 0.60)

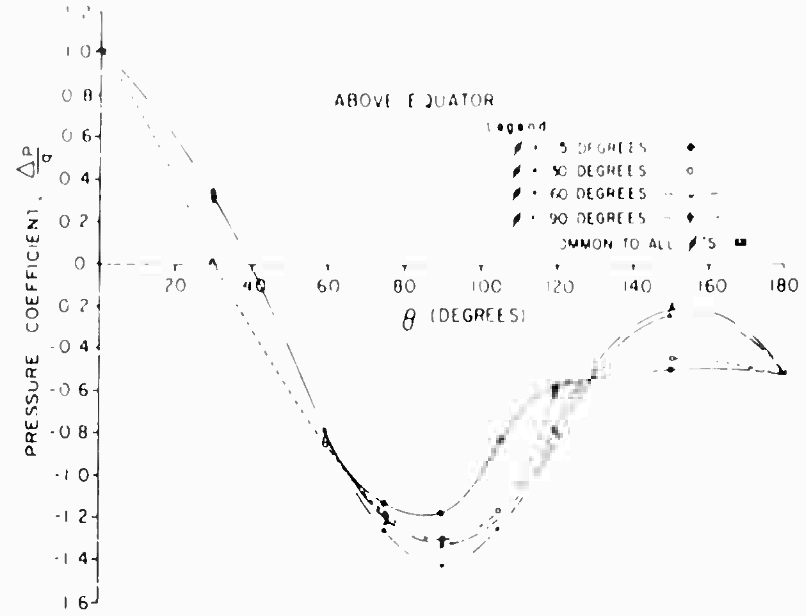

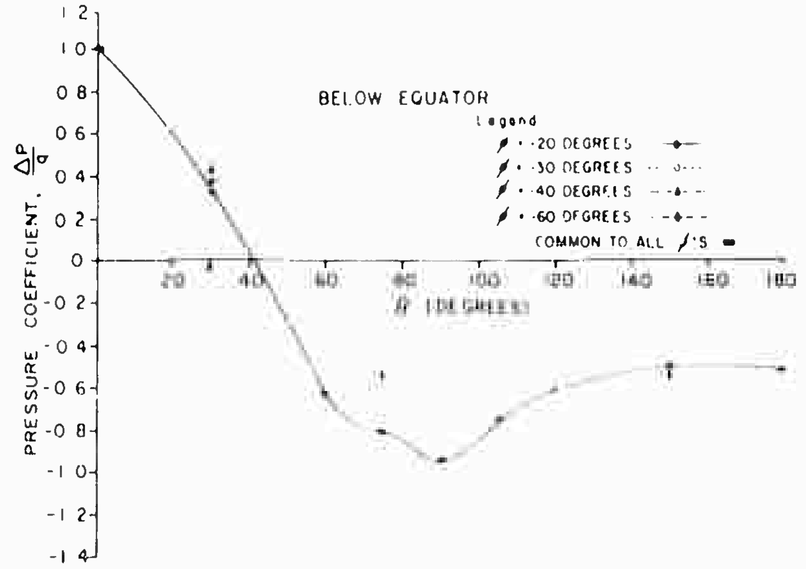

Figure A-18 - Pressure Distribution over Radome Mounted on Square Base (β = 67.7 Deg, ψ = 15 Deg, b/D = 0.60)

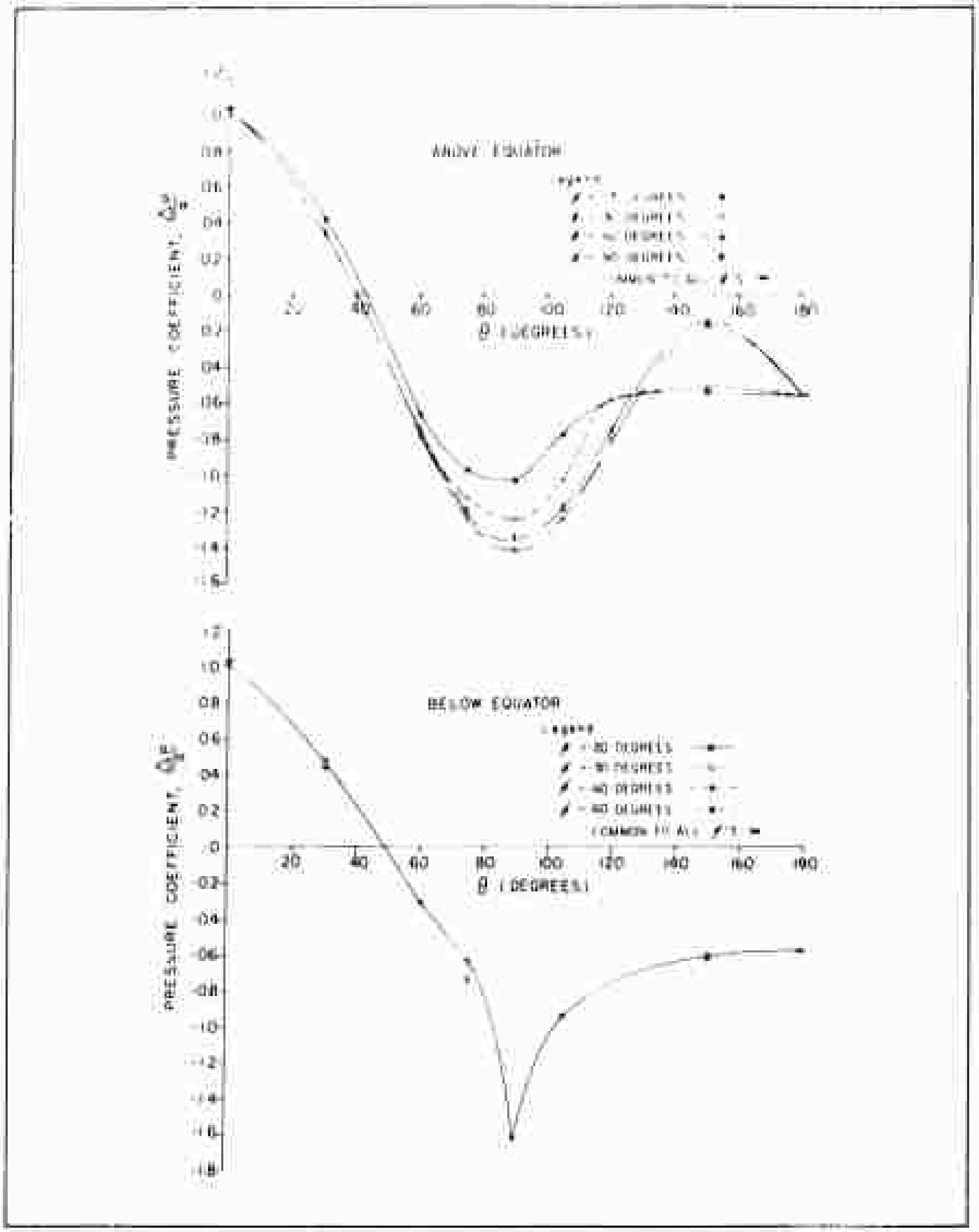

Figure A-19 - Pressure Distribution over Radome Mounted on Square Base
(β = 67.7 Deg, Ψ = 30 Deg, b/D = 0.60)

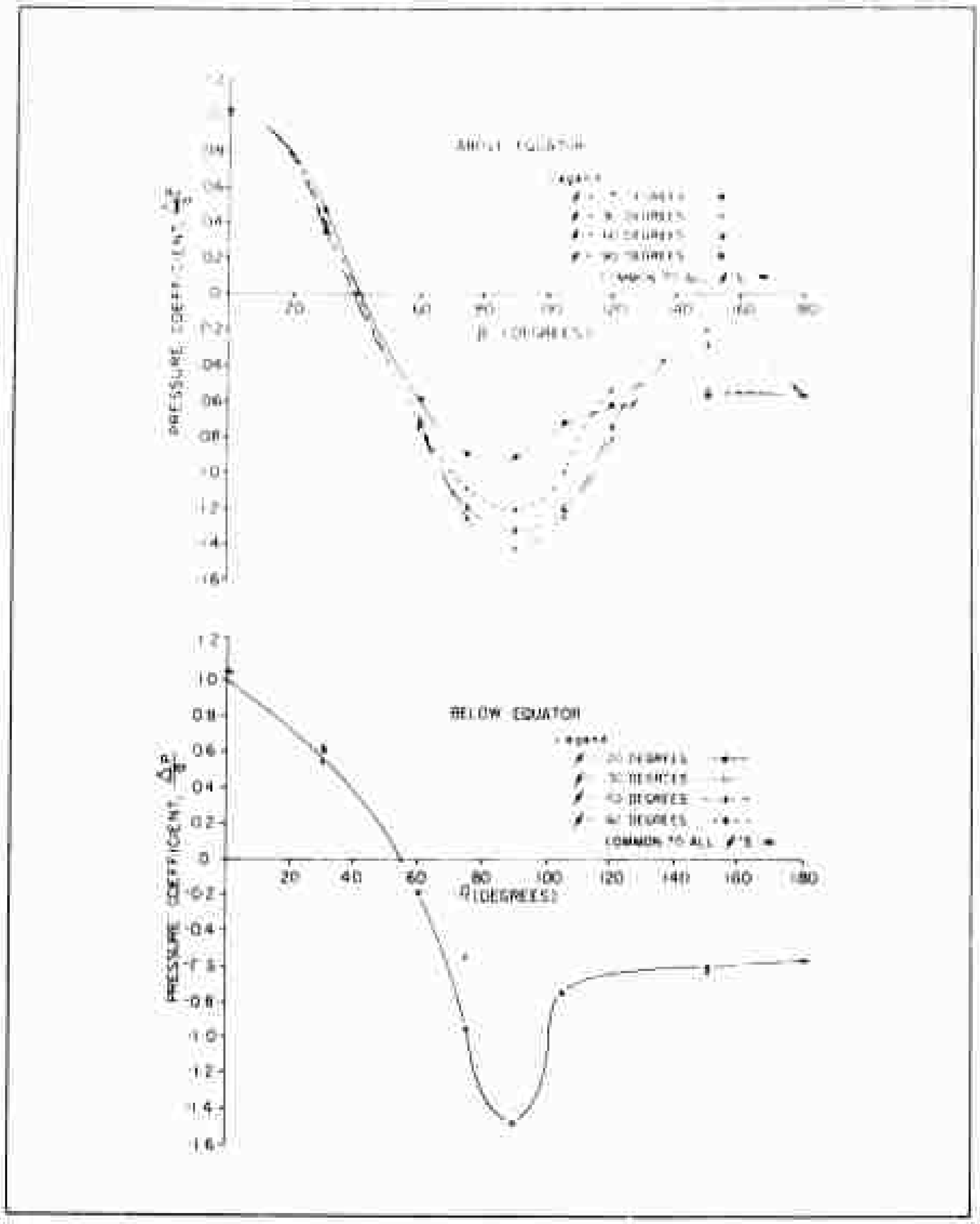

Figure A-20 - Pressure Distribution over Radome Mounted on Square Base (β = 67.7 Deg, ψ = 45 Deg, b/D = 0.60)

APPENDIX B - SUPPLEMENTAL FORCE MEASUREMENTS FOR RADOMES MOUNTED ON SQUARE BASES

As were the pressure distribution curves presented in Appendix A, the following force curves were evolved from measurements made of square - based radomes in the Goodyear Aircraft wind tunnel at a Reynolds number of 2×10^6. The wind tunnel balance system measured lift, drag, and pitching moment simultaneously. Tests were made for various cut-off angles and a ground plane was used in the test section. Again, the radome diameter was 13.5 in., the wind speed was approximately 160 mph, and the wind-tunnel turbulence factor was approximately 1.6.

Note that data for base orientation angles, ψ, of 0, 15, and 30 deg are covered for lift, drag, and pitching moment (Figures B-1 through B-9). Other curves for ψ = 45 deg are given in the body of the report.

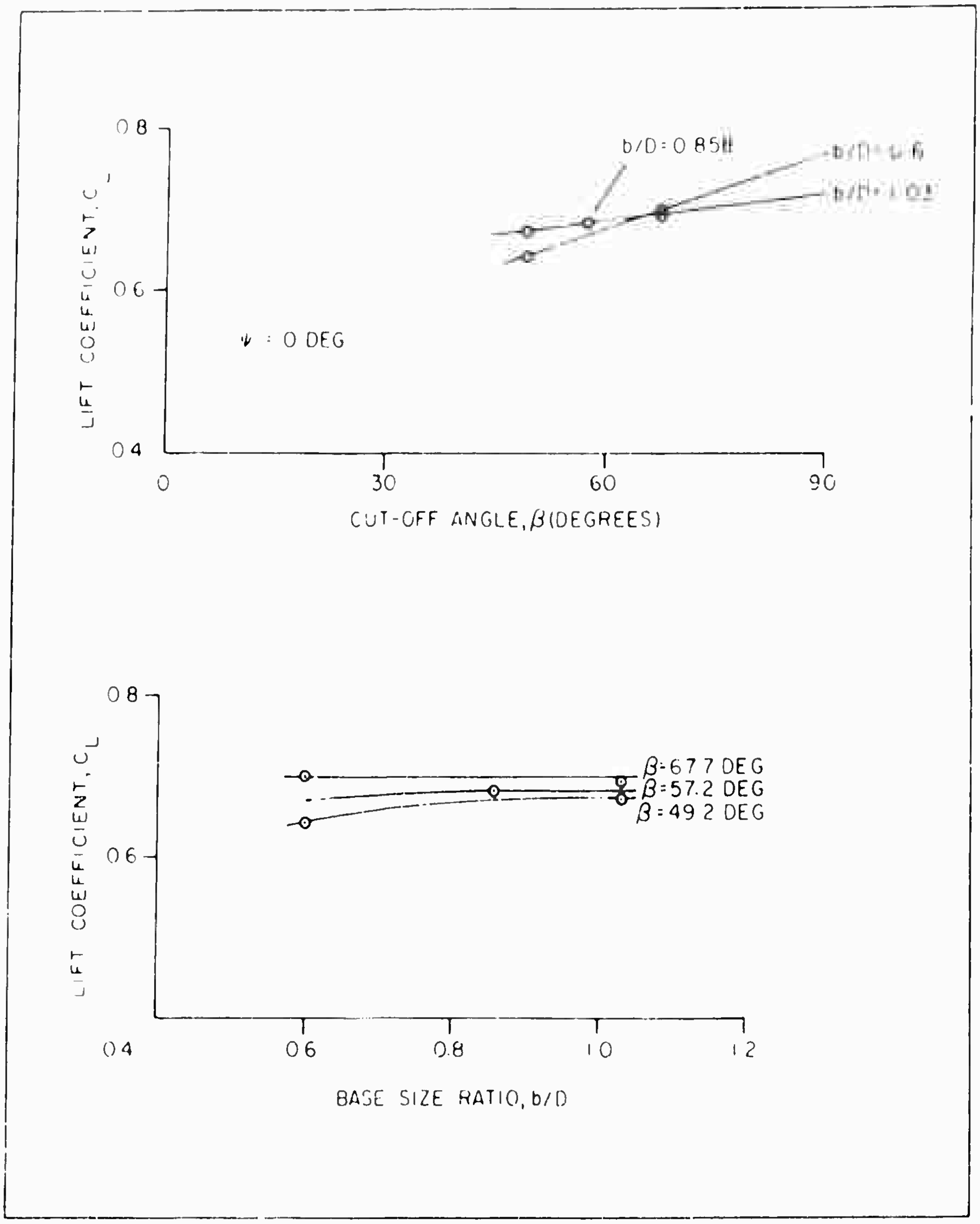

Figure B-1 - Lift Coefficient versus Cut-off Angle and Base Size Ratio
(Base Orientation Angle, ψ = 0 Deg)

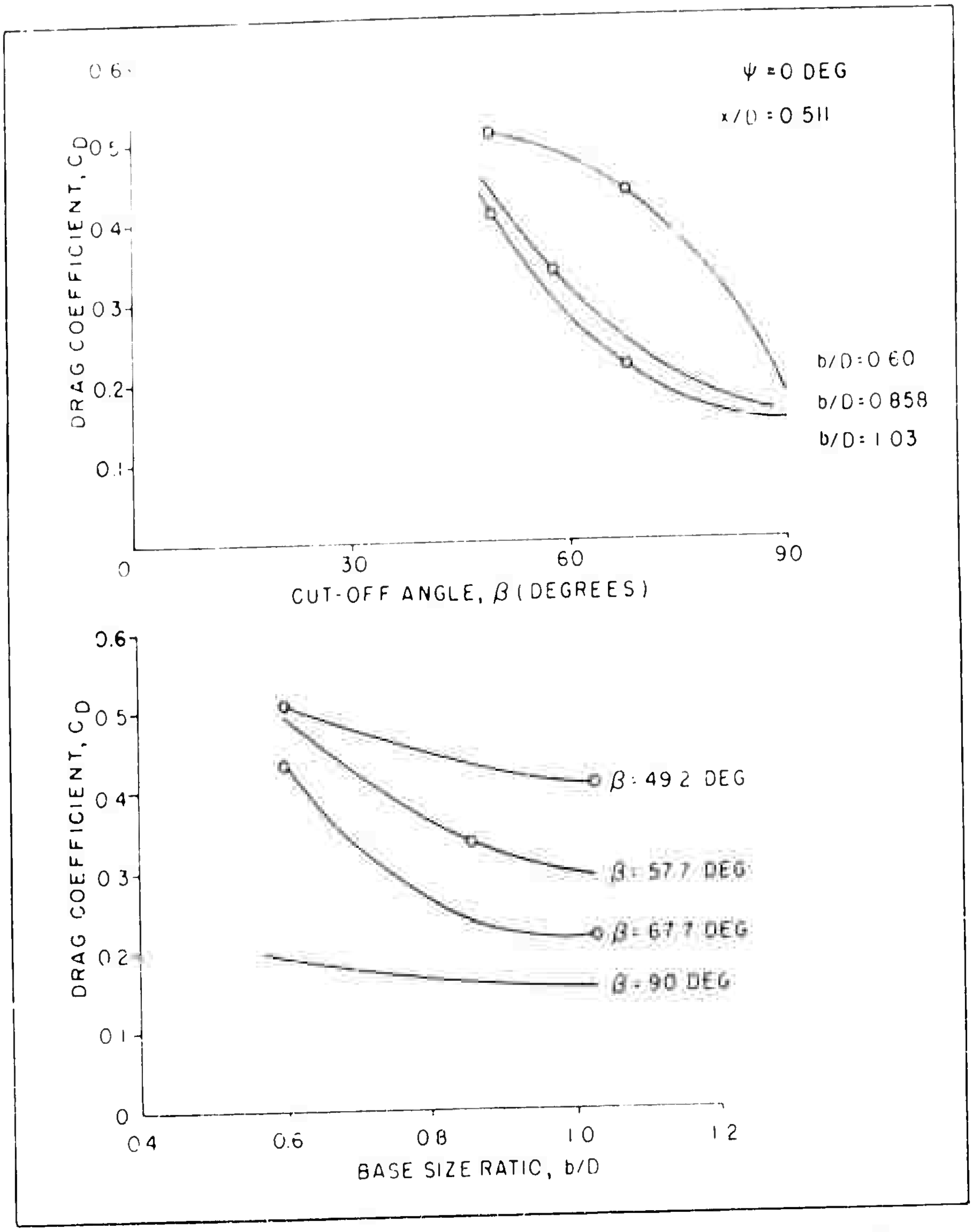

Figure B-2 - Drag Coefficient versus Cut-off Angle and Base Size Ratio (Base Orientation Angle, ψ = 0 Deg)

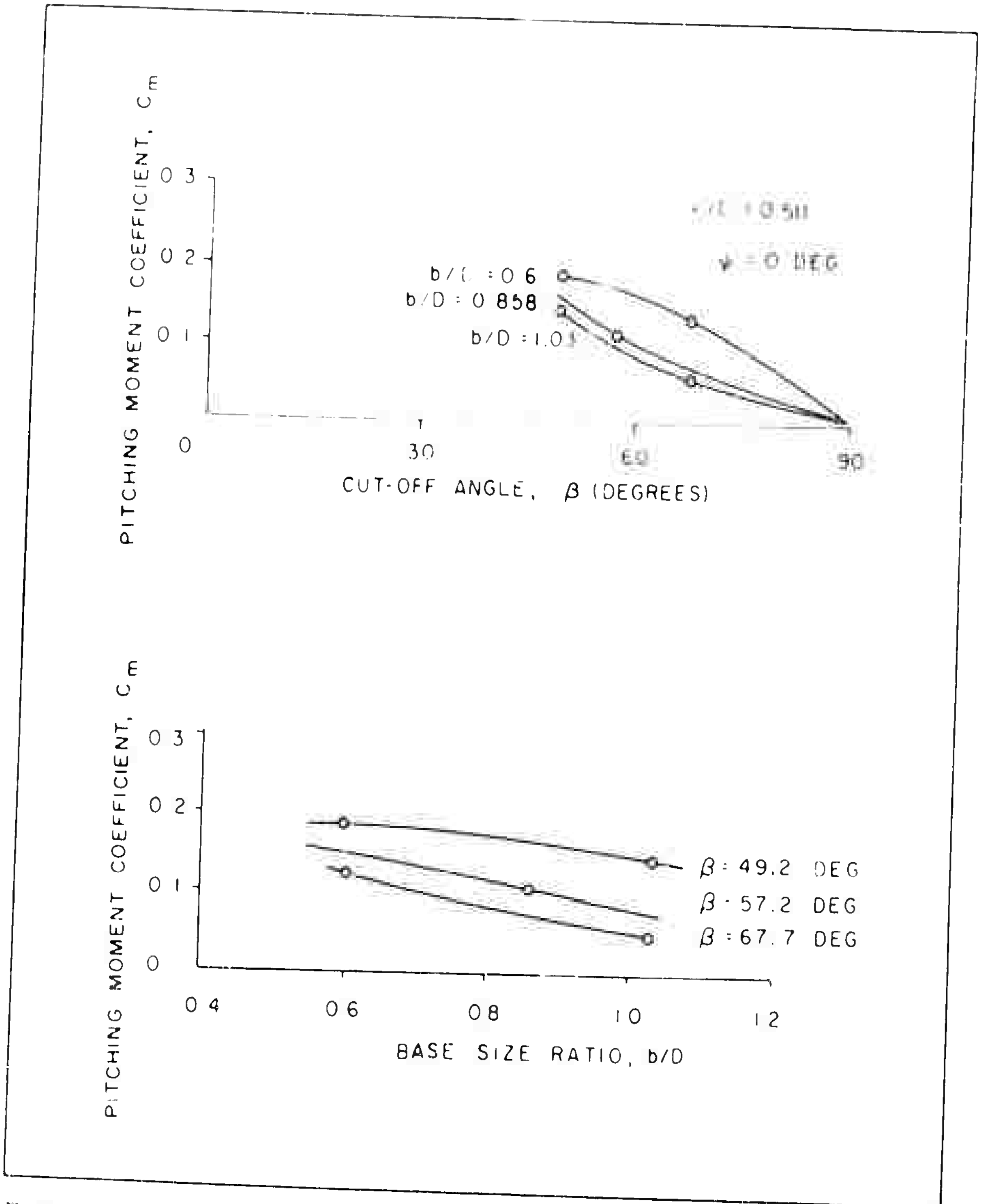

Figure B-3 - Pitching Moment Coefficient versus Cut-off Angle and Base Size Ratio (Base Orientation Angle, ψ = 0 Deg)

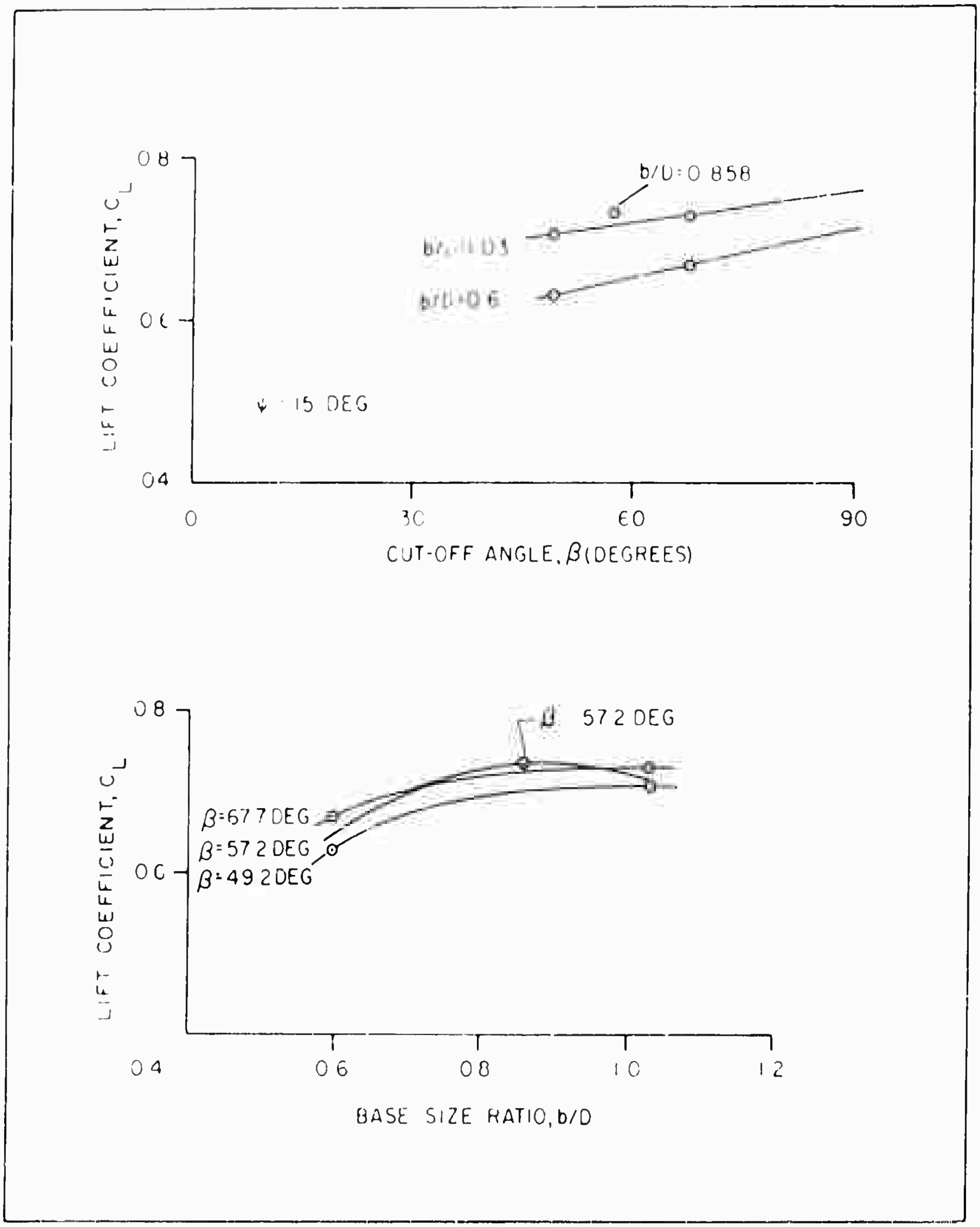

Figure B-4 - Lift Coefficient versus Cut-off Angle and Base Size Ratio (Base Orientation Angle, ψ = 15 Deg)

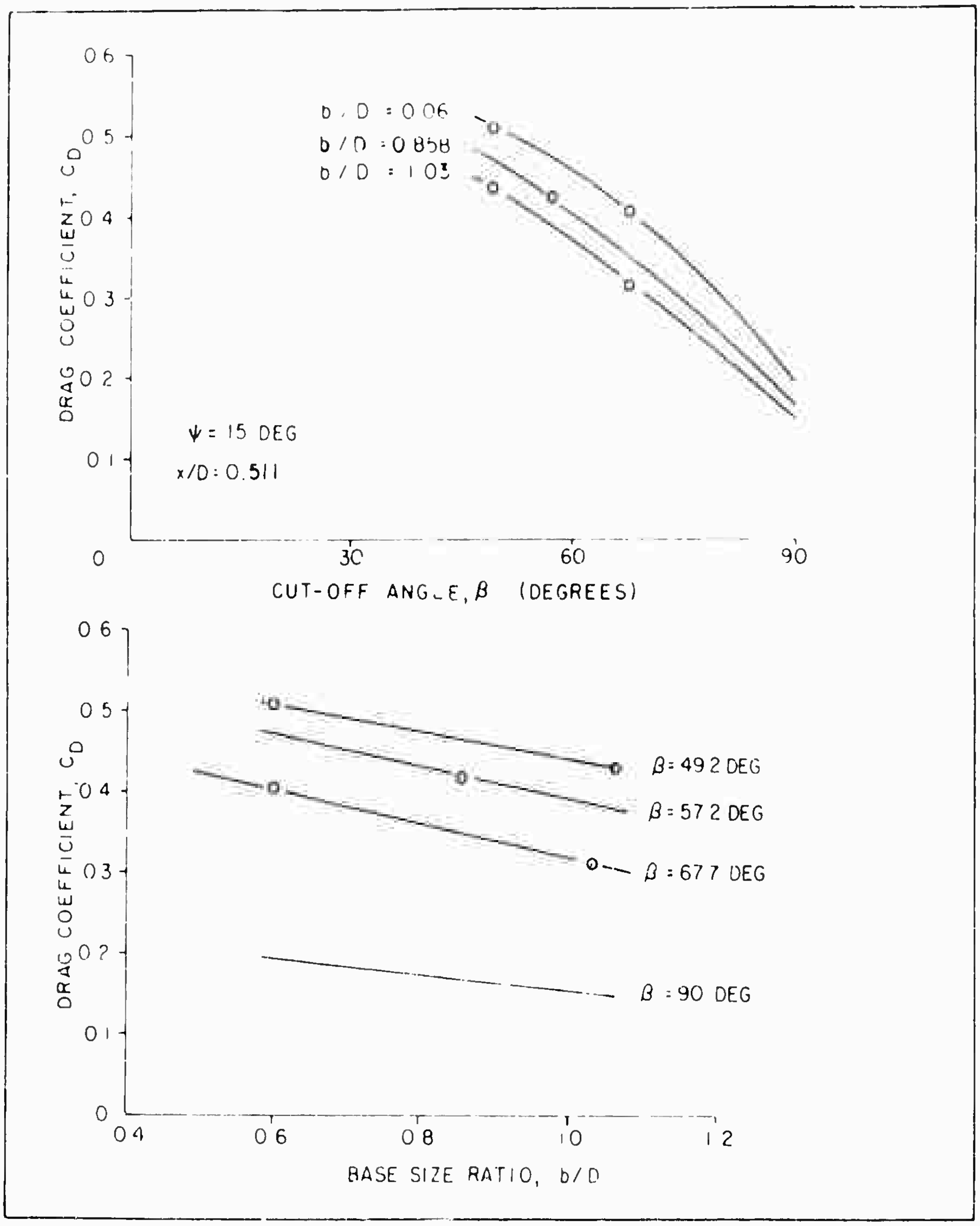

Figure B-5 - Drag Coefficient versus Cut-off Angle and Base Size Ratio (Base Orientation Angle, Ψ = 15 Deg)

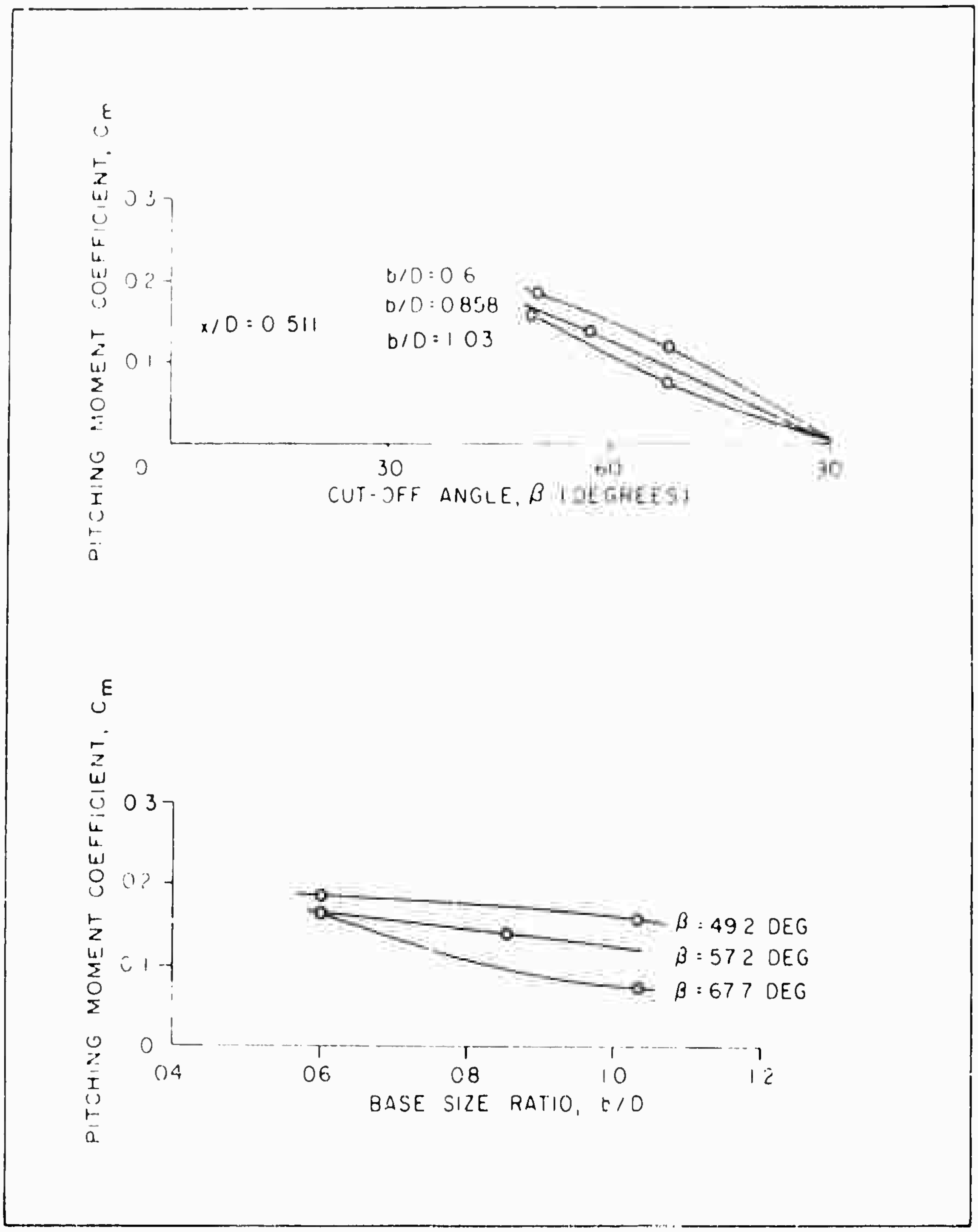

Figure B-6 - Pitching Moment Coefficient versus Cut-off Angle and Base Size Ratio (Base Orientation Angle, Ψ = 15 Deg)

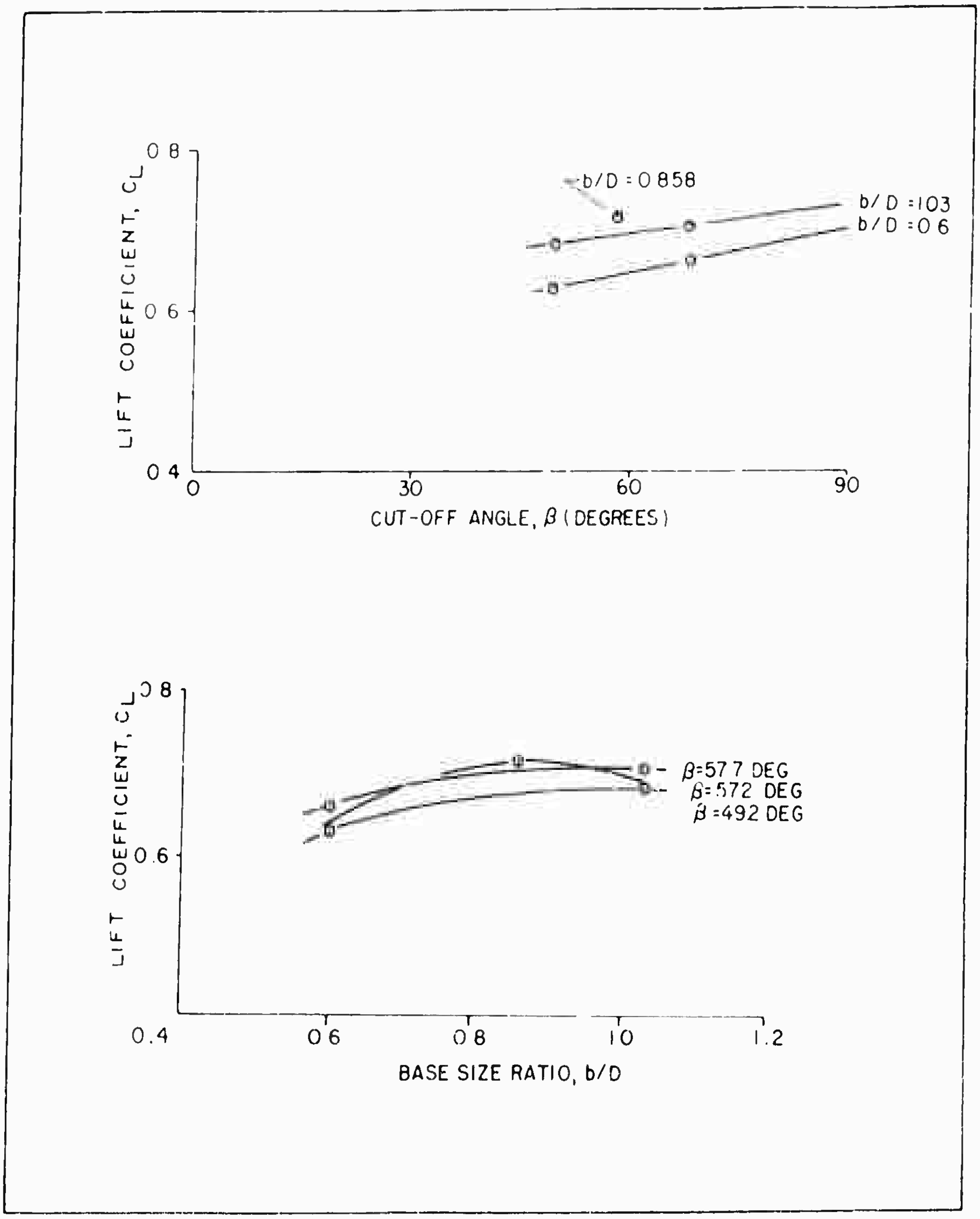

Figure B-7 - Lift Coefficient versus Cut-off Angle and Base Size Ratio (Base Orientation Angle, ψ = 30 Deg)

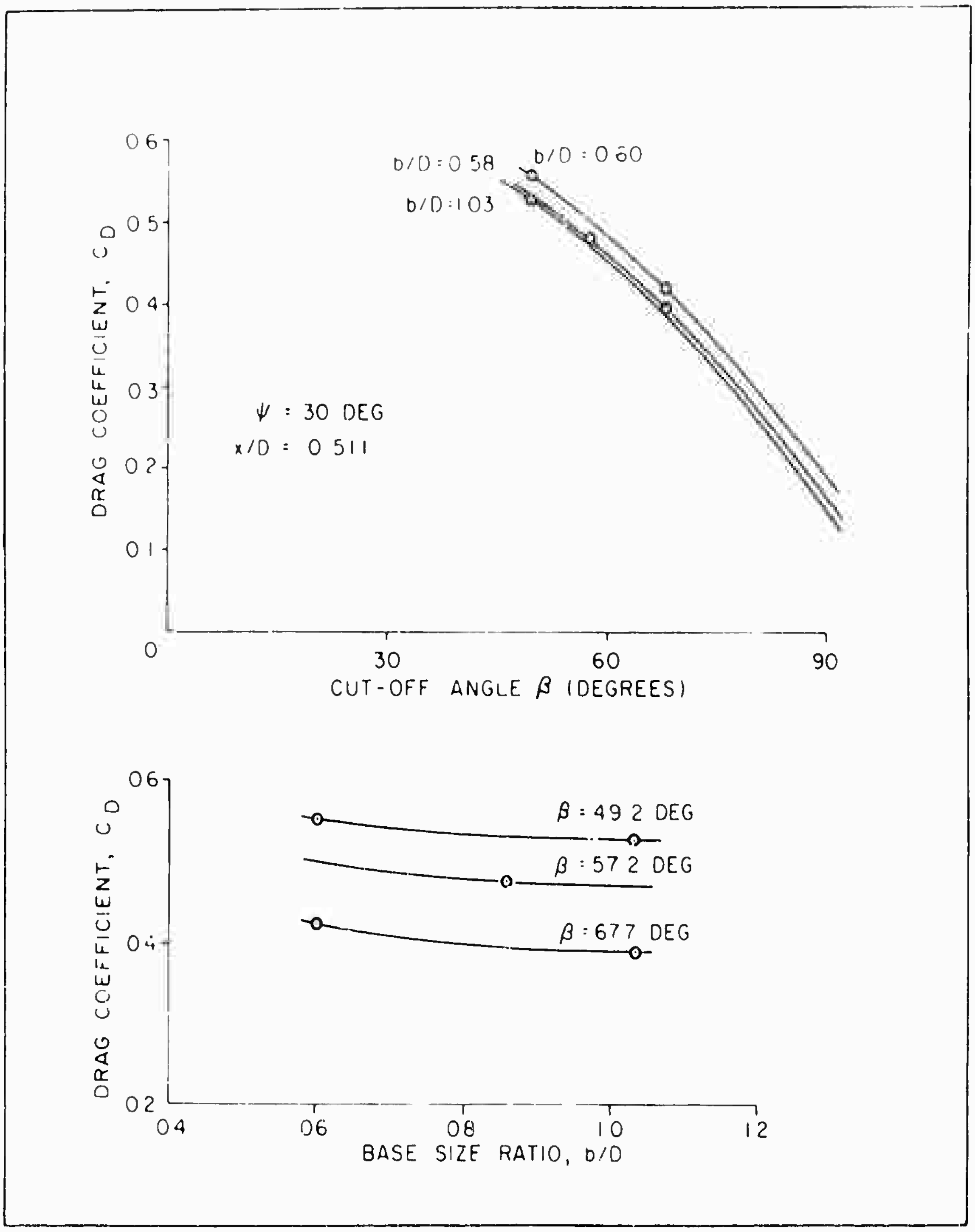

Figure B-8 - Drag Coefficient versus Cut-off Angle and Base Size Ratio (Base Orientation Angle, ψ = 30 Deg)

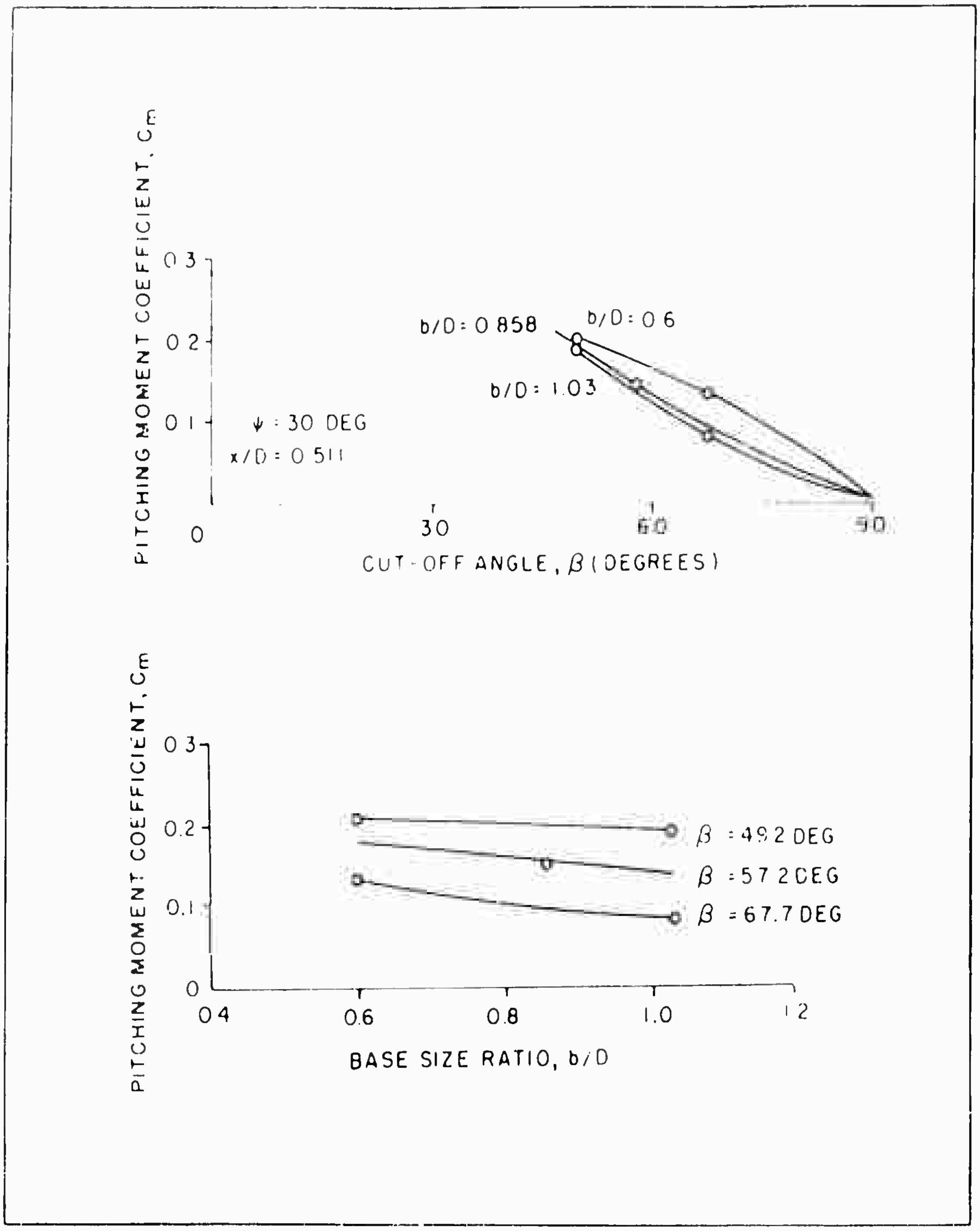

Figure B-9 - Pitching Moment Coefficient versus Cut-off Angle and Base Size Ratio (Base Orientation Angle, Ψ = 30 Deg)

STRESS DISTRIBUTION AND JUMP PHENOMENA IN SPHERICAL FRAMEWORKS UNDER PRESSURE LOADING[1,2]

by J. F. Besseling
Stanford University
Palo Alto, California

SUMMARY

In frameworks with all joints lying on a sphere and with small spherical angles between adjacent joints non-linear effects may play an important role if the loading consists of a non-uniform pressure distribution. The non-linear relation between load and displacements may even show a load maximum at which a jump phenomenon will occur. An analysis of the jump phenomenon shows that the critical load can only be calculated with sufficient accuracy after the linearized deformation problem of the complete structure has been solved. Though this involves the solution of a very large system of linear algebraic equations it is indicated how this is feasible by application of an iteration procedure on a digital computer. It is further shown how the actual pressure loading of the sphere may be approximated by concentrated loads at the joints.

---

[1] Lecture presented at the Symposium on Rigid Radomes conducted by the Lincoln Laboratory of the Massachusetts Institute of Technology in Cambridge, Massachusetts, September 8, 9 and 10, 1958.

[2] The author is indebted to Dr. M. Anliker for his critical and constructive review of the manuscript and for his willingness to give an oral presentation of the paper at the Symposium.

The research reported here was performed under subcontract to Lincoln Laboratory, a technical center operated by Massachusetts Institute of Technology with the joint support of the Army, Navy, and Air Force.

CONTENTS

NOTATION

A	Cross-sectional area of structural member. Also: Square matrix of coefficients of unknowns.
A_o	Column matrix with constant elements.
A_{ij}, A_{oi}	Submatrices.
B	Square matrix of coefficients of unknowns.
B_o	Column matrix with constant elements.
C, D, K	Matrices with constant elements.
E	Young's modulus.
$G(X), H(X)$	Column matrices with elements which are functions of the unknowns.
N	Number of structural members about a joint.
P	Radially directed compressive load.
S_n	Surface area of n^{th} triangle.
V	Total potential energy.
X	Column matrix of unknowns.
Y	Displacements at the base of two-tier framework.

j	Number of joints. Also as subscript referring to joint.
k	Number of upright members and base members in regular pyramid.
ℓ_n	Length of structural member.
n	Number of members. Also as subscript referring to member.
$(n,n+1)$	Angle between members n and $n + 1$.
p	External pressure.
p_j	Local value of external pressure at joint.
u_j, v_j	Tangential displacements of joint.
w_j	Radial displacement of joint.
α	Magnification factor, $\alpha = \sin\gamma^o/\sin\gamma$.
β	Ratio between compressive loads, $P_2 = \beta P_1$.
2γ	Spherical length of member.
γ^o	Superscript ^{o} indicates initial configuration.
ϵ	Strain.
λ_j	Load factor of joint.

1. Introduction

In some frameworks the stress distribution is very sensitive to small changes of the geometry and it is significantly affected by the deformations even when the stresses in the structural members are still far below the elastic limit. The equilibrium equations have to be written down for the deformed structure which leads to a non-linear relation between loads and displacements. A pyramidal framework with ideal joints under a central compressive load is a simple example of such a structure if the upright members make small angles with the base plane. The equations of equilibrium for the regular pyramid of Fig. 1 read

$$-kP_S\sin\gamma = P \quad ,$$

$$2k\sin(\pi/k)P_Z = P\cot\gamma, \tag{1.1}$$

where γ is the angle between the upright members and the base plane in the deformed structure. The structure is statically determinate for small central loads $P(\gamma \approx \gamma^0)$, but for loads of any magnitude the equilibrium equations do not suffice to determine the forces P_S in the k upright members and the forces P_Z in the k base members. The compatibility equation

$$\epsilon_S = (1 + \epsilon_Z)\cos\gamma^0/(\cos\gamma) - 1 \tag{1.2}$$

and the stress-strain relations

$$P_S/(EA_S) = \epsilon_S,$$

$$P_Z/(EA_Z) = \epsilon_Z, \tag{1.3}$$

are needed to make the load-deformation problem a determinate one.

[illegible] (1.2), (1.3) and (1.1) [illegible]

$$\frac{1}{EA_s} \quad [illegible] \qquad (1.4)$$

The condition for stability of the load-deformation process reads

$$\frac{dP}{d\gamma} > 0$$

and the limit of stability is reached at the load maximum determined by

$$\frac{dP}{d\gamma} = C(\cos^3\gamma - \cos\gamma^0) = 0$$

or

$$\gamma_{crit.} = \cos^{-1}(\cos\gamma^0)^{1/3} \qquad (1.5)$$

Hence the pyramidal framework of Fig. 1 collapses when under the action of a central compressive load the angles between the upright members and the base plane are reduced to a certain value. At the critical load the force in the upright members is increased above proportionality with respect to P by the factor

$$\alpha = \sin\gamma^0/\sin\gamma.$$

This factor may be significantly larger than 1 as is shown in Fig. 2, where the critical value of the factor [$\sin\gamma - \cos\gamma^0 \tg\gamma$] is plotted as a function of γ^0 and where the corresponding values of γ_{crit} and α are indicated. By substitution into equation (1.2) for ϵ_S

and ϵ_y the values of the strains at the elastic limit the largest value of γ can be determined at which the jump phenomenon will still occur in the elastic range. It is found that for aluminum alloys the value is never larger than [illegible] and for ordinary structural steel the initial angle must be even smaller than 4.[illegible].

In the spherical framework of Fig. [illegible], which is used for the construction of radomes, there are a large number of regular and irregular pyramids, which all have angles γ smaller than [illegible]°. Since the structure will be subjected to a non-uniform pressure distribution it was felt that non-linear effects described above with the possibility of the occurrence of a jump phenomenon should be considered in connection with the determination of the stress distribution. The investigation has been restricted so far to a framework with ideal joints, though it is realized that in particular the critical load with respect to the jump phenomenon may be increased appreciably by the rigidity of the joints in the actual structure. The conservative approach with the assumption of ideal joints presents already a formidable computational problem, however; it is felt that the influence of the rigidity of the joints should only be taken into account if the results of the computations deem it absolutely necessary. It is expected that after a quantitative analysis of the framework with ideal joints a qualitative investigation of this influence will suffice.

[illegible]. The Calculation of the Jump Phenomenon in Complex Frameworks

For frameworks more complex than the regular pyramid considered in section 1 an exact analysis of the load-deformation process proved to be no longer feasible.

Considerable simplification can be obtained if the strains for the individual members of the structure are expressed in terms of the tangential and radial displacements of the joints. The exact expression for the strain in a member in terms of the radial dis-displacements w_1, w_2, and the tangential displacements u_1, u_2, v_1, v_2 of

[illegible]

$$\epsilon = \left\{ 1 - [illegible] \right\}^{\frac{1}{2}} - 1$$

(2.1)

If ϵ is expanded into a series and if only quantities which are small of the first and second order are retained, the following expression for ϵ is found

$$\epsilon = -\sin\gamma^0 \frac{w_1 + w_2}{\ell} - \cos\gamma^0 \frac{u_1 + u_2}{\ell} + \frac{1}{2}\cos^2\gamma^0 \frac{(w_1 - w_2)^2}{\ell^2} + \left(\frac{v_1 - v_2}{\ell} \right)^2 \qquad (2.2a)$$

The quantities $\frac{w_1 - w_2}{\ell}$ and $\frac{v_1 - v_2}{\ell}$ represent rotations of the members. However since the stiffness of the structure against rotation about an axis perpendicular to the spherical surface is much larger than the stiffness against rotation about an axis tangent to the sphere it can be concluded that the term $\left(\frac{v_1 - v_2}{\ell} \right)^2$ may be neglected. Then the expression for ϵ reduces to

$$\epsilon = -\sin\gamma^0 \frac{w_1 + w_2}{\ell} - \cos\gamma^0 \frac{u_1 + u_2}{\ell} + \frac{1}{2}\cos^2\gamma^0 \left(\frac{w_1 - w_2}{\ell} \right)^2 \qquad (2.2)$$

According to the principle of minimum potential energy, equilibrium of the structure is characterized by a minimum of the total potential energy with respect to arbitrary variations of the displacements of the joints. If the pressure loading of the structure is represented by radially directed compressive loads P_j at the joints, the total potential energy can be written as

$$V = \frac{1}{2} \sum_n E A_n \ell_n \epsilon_n^2 - \sum_j P_j w_j . \qquad (2.3)$$

The variations in the strains ϵ_n in the structural members corresponding to given variations in the displacements of the joints follow from the relation (2.2).

First the principle of minimum potential energy has been applied to show that with expressions (...) for the strains a sufficient approximation is obtained for the load at which the jump phenomenon will occur. For a regular pyramid with a rigid base and k equal upright members loaded by a central compressive force the total potential energy according to (2.2) and (2.3) is given by

$$V = \frac{1}{2}\, kEA\ell\left[-\sin\gamma^{o}\frac{w}{\ell} + \frac{1}{2}\cos^2\gamma^{o}\left(\frac{w}{\ell}\right)^2\right]^2 - Pw. \qquad (2.4)$$

The condition for a minimum of V with respect to w : $\frac{dV}{dw} = 0$ leads to an expression for P and subsequently the load maximum can be determined. According to this analysis the critical value of P is given by

$$\left(\frac{P}{EA}\right)_{cr} = 0.193\, k\, \frac{\sin^3\gamma^{o}}{\cos^2\gamma^{o}} \qquad (2.5)$$

[illegible]

$$[illegible] \qquad (\; [illegible] \;)$$

In this case the difference between the value of the critical load according to the exact analysis (equations (1.4) and (1.5) with $A_2 \to \infty$) and according to ([illegible]) is less than 1% for an initial angle $\gamma = [illegible]^0$, which is a representative value for the structure under consideration. Hence the error introduced by considering only first and second order terms in the expression for the strains of the structural members is negligible.

In order to develop a method of calculation for complex spherical frameworks the two-tier framework of Fig. 5, taken from the framework of Fig. 3, has been considered with respect to the symmetrical jump phenomenon. The base structure was assumed rigid. For an exact analysis six types of displacements should be taken into account, as indicated in Fig. 5. A good approximation may be obtained, however, by putting $v_3 = 0$ and $u_3 = u_2$, $w_3 = w_2$. Furthermore the main purpose of the investigation was to develop a method of calculation rather than to arrive at a highly accurate solution for this particular case.

By the use of the geometrical data of Ref. 4 and equation (2.2) the strains in the individual members can be expressed in terms of the displacements w_1, w_2 and u_2. Application of the principle of minimum potential energy then leads to the following set of equations

$$\frac{P_1}{EA} = \sum \ell_n \, \epsilon_n \frac{\partial \epsilon_n}{\partial w_1} ,$$

$$\frac{9P_2}{EA} = \sum \ell_n \, \epsilon_n \frac{\partial \epsilon_n}{\partial w_2} , \qquad 0 = \sum \ell_n \, \epsilon_n \frac{\partial \epsilon_n}{\partial u_2} . \qquad (2.7)$$

[illegible] non-linear algebraic equations. The last equation is linear in w_3, however, and can be used to eliminate w_3 from the first and second equations. The result is two equations

$$\frac{P_1}{EA} = F_1(w_1,w_2), \quad \frac{P_2}{EA} = F_2(w_1,w_2) \qquad (2.8)$$

which give the loads P_1 and P_2 in terms of non-linear algebraic expressions in w_1 and w_2. If P_1 is taken as the load parameter, with $P_2/P_1 = \beta$ = constant, and w_1 as the deformation parameter, then the condition for a load maximum reads

$$\frac{d}{dw_1}\left(\frac{P_1}{EA}\right) = \frac{\partial F_1}{\partial w_1} + \frac{\partial F_1}{\partial w_2}\frac{\partial w_2}{\partial w_1} = 0 \quad ,$$

$$\frac{d}{dw_1}\left(\frac{\beta P_1}{EA}\right) = \frac{\partial F_2}{\partial w_1} + \frac{\partial F_2}{\partial w_2}\frac{\partial w_2}{\partial w_1} = 0 \quad ,$$

$$\frac{\beta P_1}{EA} - \frac{P_2}{EA} = \beta F_1(w_1,w_2) - F_2(w_1,w_2) = 0. \qquad (2.9)$$

These three equations are of the type

$$BX = B_0 + H(X), \qquad (2.10)$$

where B is the matrix of constant coefficients of the three unknowns X : w_1, w_2, $\frac{\partial w_2}{\partial w_1}$, and where B_0 and $H(X)$ represent the constant and non-linear terms respectively. It was found that a

solution of this non-linear system is possible by means of an iteration process characterized by

$$X^{k} = F^{-1}B_{0} + F^{-1}H(X^{k-1}) \qquad (2.11)$$

with the first approximation

$$X^{0} = F^{-1}B_{0}.$$

In the case of the two-tier framework of Fig. 5 for $P_2 = \frac{1}{3} P_1$ the following results were obtained after nine iteration steps

$$X = \begin{vmatrix} \dfrac{w_1}{\ell_1} \\[2ex] \dfrac{w_2}{\ell_1} \\[2ex] \dfrac{\partial w_2}{\partial w_1} \end{vmatrix} = \begin{vmatrix} 0.0262 \\[2ex] 0.0026 \\[2ex] -0.158 \end{vmatrix}, \quad \left(\frac{P_1}{EA}\right)_{cr} = 0.00113, \quad \frac{u_2}{\ell_1} = 0.00068. \qquad (2.12)$$

The upper part of the two-tier framework of Fig. 5 is a regular pyramid with k = 9. According to equations (1.4) and (1.5) the critical load for such a pyramid amounts to

$$\left(\frac{P_1}{EA}\right)_{cr} = 0.00140 \qquad (2.13)$$

if the base structure is rigid.

If the elasticity of the base members is taken into account,

but not the loads at the base joints and the members supporting the pyramid:

$$\left(\frac{P_i}{EA}\right)_{cr} = \frac{0.00140}{1 + \cos\gamma/(2\sin\frac{\pi}{4})} = 0.00057. \qquad (2.14)$$

It can be observed that a lower bound for the critical load in a complex framework of the type shown in Fig. 3 may be obtained by considering only pyramids with their base members, but this lower bound may differ from the actual value by a large factor according to the results given above.

Now some conclusions will be drawn upon which a proposal is based for the numerical analysis of the radome framework.

First it can be observed that the jump phenomenon, if it occurs, affects the stress distribution in the framework only locally. The difference between the loading of the surrounding structure when the local change in the initial geometry is neglected and the actual loading, can be expressed in terms of a self equilibrating load system which, by virtue of St. Venant's principle, affects the stress distribution only locally.

Furthermore the geometry of the framework under consideration makes it impossible that two adjacent joints jump simultaneously in the elastic range. The spherical angle between two adjacent joints is according to the data of Ref. 4 at least 10°. This implies as is shown in Fig. 6 that two adjacent joints are supported by members which make angles of at least 10° with the base plane. The influence of the interconnecting elastic member can be incorporated in the flexibility of the base structure. It has already been found that in the resulting pyramidal structure the angles between the upright members and the base plane should be less than 3° in case an aluminum alloy is used and less than 4.5° if the material is ordinary structural steel in order that the jump phenomenon will occur in the elastic range.

However situations of jumping of two joints with one joint moving outward in between these two will be possible under suitable loading conditions. Fig. 7 presents a highly simplified model which shows this type of jump phenomenon. Since the work required to move the middle joint outward is now furnished by the forces of two inward moving joints the critical load could be less than the load which will be found neglecting the jumping of the second joint.

This raises the question how it can be determined where the jump phenomenon is likely to occur and how many joints will be involved. Though no simple criterion can be given it should be realized that in the case of the jump phenomenon the displacements are functions of the loads with continuous derivatives (contrary to the case of classical elastic buckling). For sufficiently small loads the displacements are found from the solution of the linearized problem. If upon inspection of these displacements it is found that one or more joints start to move inward faster with increasing load than adjacent joints, then at these joints the jump phenomenon may eventually occur as the non-linearity of the equations tends to accentuate the differences in rate of growth of the displacements. This may also be concluded from expression (2.2) for the strain in a structural member. It is seen that in this expression non-linear effects such as the jump phenomenon depend solely on the differences between the radial displacements of the end points of a member.

Once the solution of the linearized deformation problem of the complete structure has been obtained from this solution the points can be determined where a local investigation of the jump phenomenon will be necessary.

The jump phenomenon for one joint can be calculated with sufficient accuracy by considering the pyramid of which it forms the top together with all members directly supporting this pyramid. This conclusion can be drawn from a comparison between the solution

of the linearized problem for the two-tier framework of Fig. [illegible] and the solution given above. It appears that at the critical load the actual values of the strains in the members supporting the pyramid differ at most 11.[illegible]% from the linear approximation. Since the change in geometry for these members at the critical load, given by $\frac{w}{\ell_1}$ = [illegible].002[illegible] and $\frac{u}{\ell_1}$ = 0.0006[illegible], is small the flexibility of the structure supporting a two-tier framework can be taken into account with sufficient accuracy by imposing on the joints at the base of the two-tier framework the displacements as they have been found as linear functions of the loads from the solution of the linearized deformation problem of the complete structure. The calculation procedure is then as follows:

Let the system of equations which is found by application of the principle of minimum potential energy with respect to variations of the displacements of all joints of the pyramid be given by

$$CX + G(X) + DY = C_0 P \tag{2.15}$$

In this equation C represents the matrix of coefficients of the linear terms containing the displacements X of the joints of the pyramid, G(X) represents the non-linear terms in X, and D represents the matrix of coefficients of the linear terms containing the displacements Y of the joints at the base of the two-tier framework. By means of the solution of the linearized deformation problem Y is expressed in terms of the loads by the relation

$$Y = KP \quad . \tag{2.16}$$

If (2.15) is substituted into (2.14) the following system of equations is found for X:

$$CX + G(X) = [C_0 - DK]P \tag{2.17}$$

Since the elements of DK will mean only a small correction of the elements C, an error of [illegible] or less in the forces in the structural members supporting the pyramid, and hence in the displacements Y, will result in a much smaller error in the critical load calculated from equations (.17).

The critical load with respect to the jump phenomenon can be calculated from the system of equations (..17) by the same method as was used above for the two-tier framework. It should be realized, however, that the computation of the critical load under actual load distributions will involve a much larger number of displacements as unknowns than need be taken into account in the highly simplified case considered above. Most likely the critical joint in the complete framework will not be the top of the two-tier framework considered above nor will the load distribution be of the symmetrical type. In general the computations should be performed on automatic digital computers.

The problem of the calculation of the critical load becomes even more complicated if from inspection of the solution of the linearized deformation problem a jump phenomenon can be expected involving two joints with one joint in between these two. In that case it will not be sufficient to consider a two-tier framework. However for a pressure distribution which shows no significant irregularities this possibility must be considered very improbable.

3. On the Solution of the Linearized Deformation Problem

The geometry of the spherical framework to be used for radomes has been obtained by taking the equilateral triangles of an icosahedron as a starting point for the triangulation of a sphere. In the domain of one equilateral triangle there are 19 joints contained in that particular triangle alone, 12 joints which are also contained in another triangle and 3 joints which belong to five triangles simultaneously. Hence the total number of joints in a

complete spherical framework would amount to

$$J = 20 \times 19 + \frac{20}{2} \times 12 + \frac{20}{5} \times 3 = 512.$$

In the same manner for the total number of structural members in the same framework is found

$$n = 20 \times 69 + \frac{20}{2} \times 15 = 1530.$$

In the actual radome structure, which has to be analysed, a horizontal plane cuts off the lower part of the sphere at some distance below the center. This plane contains supports for all structural members intersecting this plane. Thus the number of members and joints in the actual structure is significantly less than in the complete spherical framework considered above. Since, however, for a solution of the deformation problem and of the stress problem three displacements have to be determined at each joint, the system of equations for these displacements is very large and even the linearized problem can not be solved directly.

It is possible, however, by a suitable systemization to arrive at a system of equations which can be solved by an iteration procedure involving only matrix multiplications after one 39 x 39 matrix, two 18 x 18 matrices and some degenerate cases of these matrices have been inverted.

The systemization consists of an arrangement of the joints and corresponding structural members into three types of sub groups, which are shown in Fig. 8. Cross-coupling of two sub groups of a different kind is caused by the structural members of one of the substructures shown in Fig. 9, while two sub groups of the same type have no coupling terms in the resulting system of equations.

The solution of the linearized deformation problem is now

determined by a system of equations, which in symbolic form can be written as follows

$$\begin{vmatrix} A_{11} & A_{12} & A_{13} \\ A_{21} & A_{22} & A_{23} \\ A_{31} & A_{32} & A_{33} \end{vmatrix} \times \begin{vmatrix} X_1 \\ X_2 \\ X_3 \end{vmatrix} = \begin{vmatrix} A_{01} \\ A_{02} \\ A_{03} \end{vmatrix} \tag{3.1}$$

where the subscripts of the unknowns X refer to the displacements in the three subgroups of the joints. The matrices A_{11}, A_{22}, A_{33} can be inverted by computing the inverse of one 39 x 39 matrix (corresponding to subgroup I), of two 18 x 18 matrices (corresponding to subgroups II and III) and of some degenerate cases of these matrices. The solution of the complete system is then found by means of the following iteration procedure

$$X_1^n = A_{11}^{-1} [A_{01} - A_{12}X_2^{n-1} - A_{13}X_3^{n-1}]$$

$$X_2^n = A_{22}^{-1} [A_{02} - A_{21}X_1^n - A_{23}X_3^{n-1}]$$

$$X_3^n = A_{33}^{-1} [A_{03} - A_{31}X_1^n - A_{32}X_2^n] \tag{3.2}$$

where the 0^{th} approximation is given by

$$X_1^0 = A_{11}^{-1} A_{01}$$

$$X_2^0 = A_{22}^{-1} [A_{02} - A_{21}X_1^0]$$

$$X_3^0 = A_{33}^{-1} [A_{03} - A_{31}X_1^0 - A_{32}X_2^0]. \tag{3.3}$$

It can be observed that this method of solution is a particular form of a relaxation scheme suitable for automatic computers.

It should be realized that besides the computational time required to solve system (3.1) the calculation of the matrices A_{11} to A_{33} requires in itself a considerable computational effort. However, a computer program can be given for the latter computation also and by virtue of the systemization described above only one 39 x 39, two 39 x 18 and three 18 x 18 matrices need to be determined. Then the matrices A_{11} to A_{33} can be constructed.

The calculation of the elements of the column matrices A_{01}, A_{02}, A_{03} will be discussed next.

4. The Determination of the Loads at the Joints from the Pressure Distribution.

Since the spherical framework under consideration consists of a large number of relatively short members it is a sufficiently good approximation to represent the pressure loading as concentrated radially directed load at the joints. The pressure variation over one triangle will be small and hence the total pressure load on the triangle may be equally distributed over the three corner points. Since the spherical angles involved are small the loads at the corner points are approximately radially directed. If the pressure were constant over all triangles neighboring a particular joint then the total load at this joint would be given by (See Fig. 10).

$$P_j = \frac{1}{3} p \sum_N S_n = \frac{1}{6} p \sum_N \ell_n \ell_{n+1} \sin(n, n+1) \tag{4.1}$$

where N is the number of triangles neighboring the joint and $\ell_{N+1} \equiv \ell_1$.

If the pressure gradients are not very large, it will be a good approximation to the actual loading of the structure when the local value of p is substituted into (4.1). In that case it suffices to calculate the load factor

$$\lambda_j = \frac{1}{6} \sum_N \ell_n \ell_{n+1} \sin(n,n+1)$$

for all joints of the three subgroups of Fig. 5 in order to be able to write down the value of all elements of A_{01}, A_{02}, A_{03} (equations (3.1)) divided by the local pressure. When this is accomplished various pressure distributions can be considered by a simple multiplication of these values by the local pressure values.

In the case of the two-tier framework of Fig. 5 only three factors λ_j need to be determined. The loads at the joints 1, 2, 3 (See Fig. 5) follow from

$$\lambda_1 = P_1/p_1 = 26650 \text{ in}^2$$

$$\lambda_2 = P_2/p_2 = 20140 \text{ in}^2$$

$$\lambda_3 = P_3/p_3 = 15590 \text{ in}^2.$$

It is seen that a pressure distribution leading to $P_2 = P_3 = \frac{1}{3} P_1$, as considered above, would be far from a uniform distribution, but would have a pronounced maximum at the top of the two-tier framework, thus promoting the occurrence of the jump phenomenon.

5. Concluding Remarks

It is interesting to note the difference between classical

elastic buckling, where the relation between load and displacements suddenly changes from a linear one to a non-linear one when a certain load, namely the buckling load, is reached, and the jump phenomenon, where the non-linear relation between load and displacements shows a load maximum. Fig. 11 clearly shows the distinctive features of both phenomena.

The analysis of the nature of the jump phenomenon has shown that the calculation of the critical load for complex frameworks such as the radome structure is not feasible without a previous solution of the linearized deformation problem. The method of solution indicated for the latter problem is based on the use of automatic digital computers. Since the calculations have been put into matrix form an efficient use can be made of the standard programs of the computer.

Once the linearized deformation problem has been solved the strains and hence the forces in all structural members follow immediately, except in those regions where the linear approximation indicates that the non-linear terms may not be neglected. In those regions a local investigation suffices to determine the non-linear effects, the critical load with respect to a jump phenomenon included.

6. References

1. The Behavior of a Regular Space Framework with Ideal Joints under a Central Compressive Force, by J. F. Besseling.
2. A Method for the Calculation of the Stress Distribution and the Non-Linear Behavior Under Pressure Loading of a Space Framework with Ideal Joints Lying on a Sphere, by J. F. Besseling.
3. Evaluation and Application of the Theory of the Jump Phenomenon, by J. F. Besseling.
4. On Two Triangulations of the Sphere Meeting Specific Sides and Angles Requirements, by Parke Mathematical Laboratories' Staff.

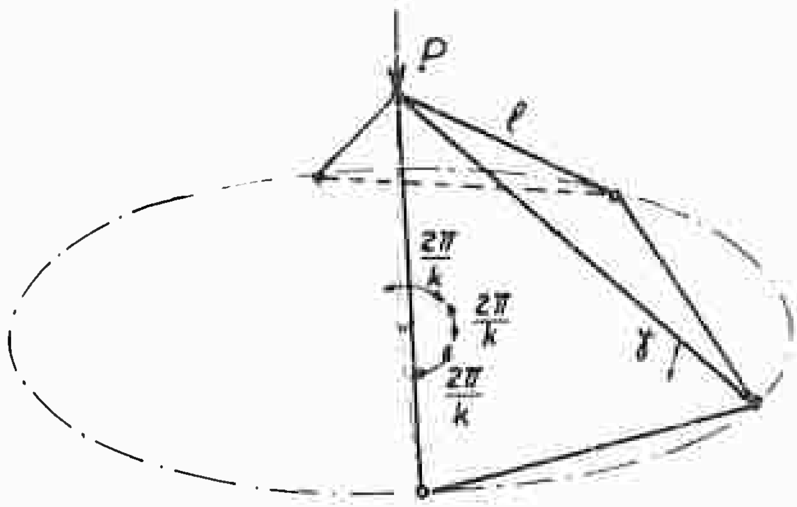

Fig. 1 - Geometry of regular pyramid.

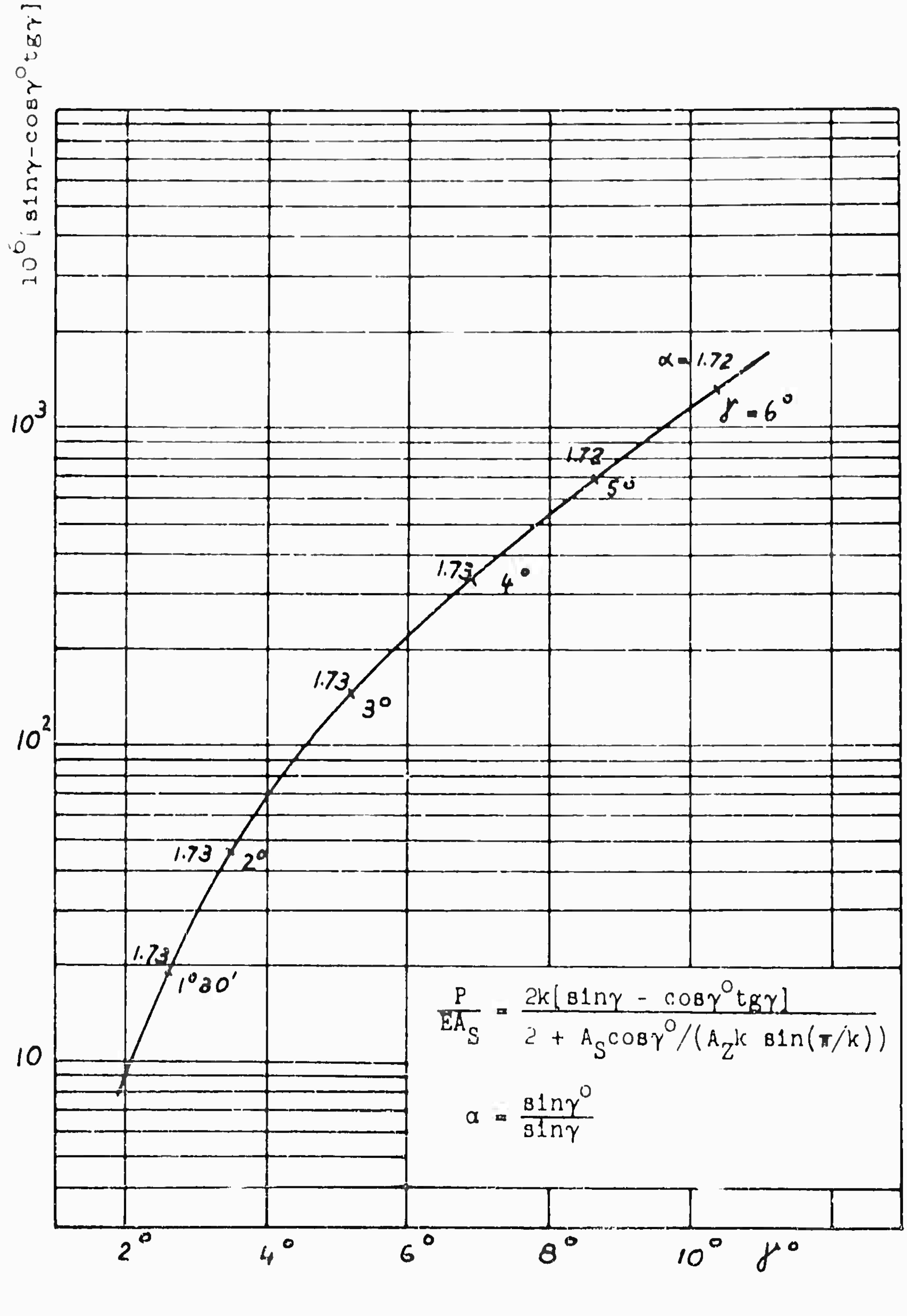

Fig. 2 - Graphical representation of the factor that determines the limit of stability of a regular pyramid under a central compressive force.

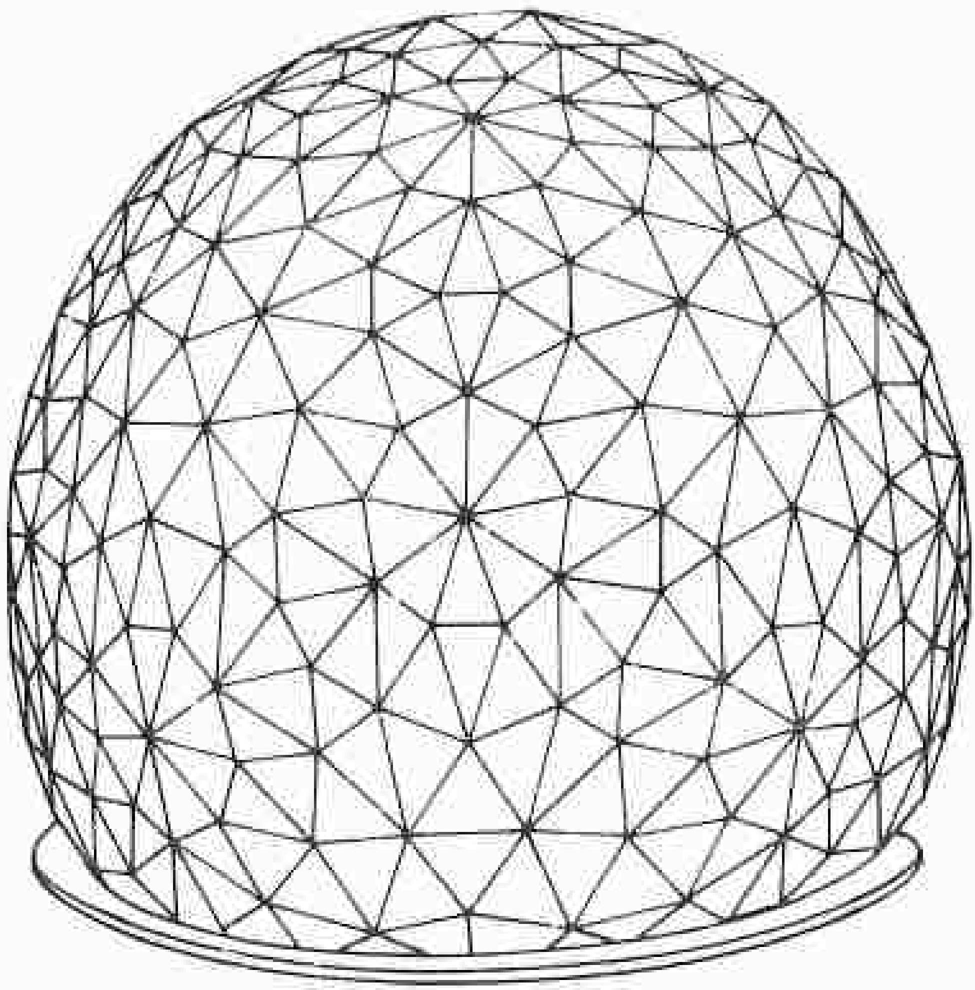

Fig. 3 - Radome structure.

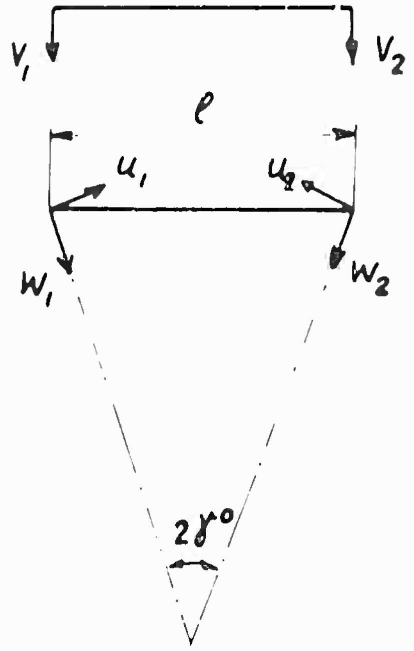

Fig. 4 - Geometry and displacements of endpoints of structural member.

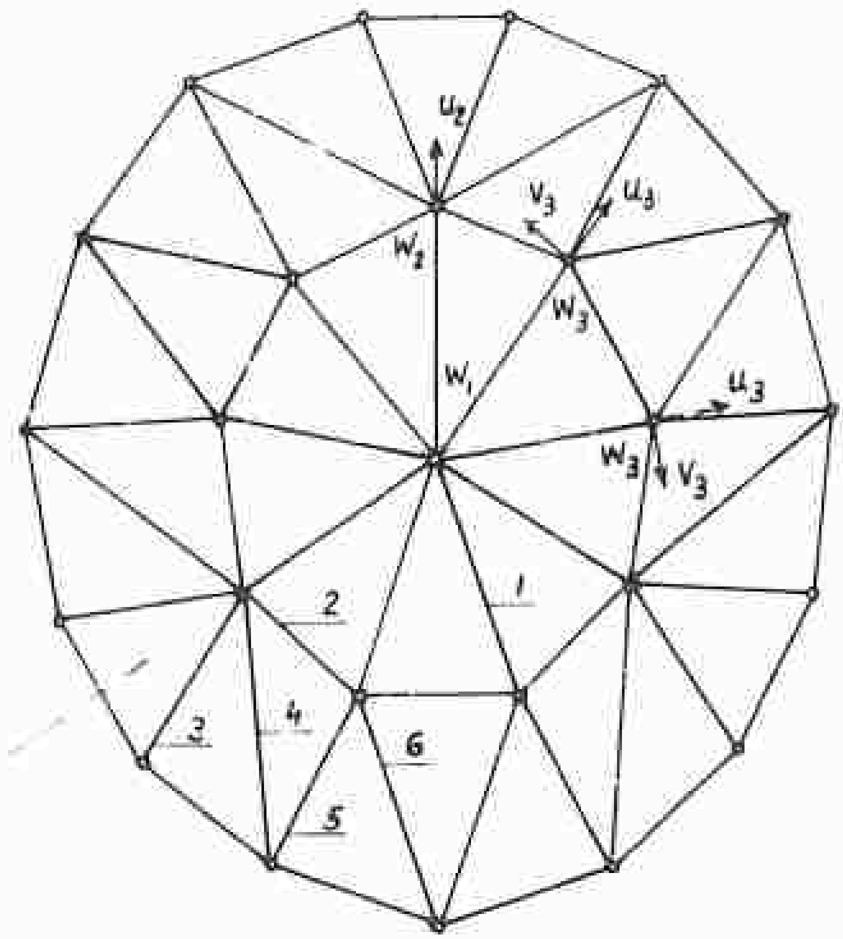

Fig. 5 - Two-tier framework with three axes of symmetry.

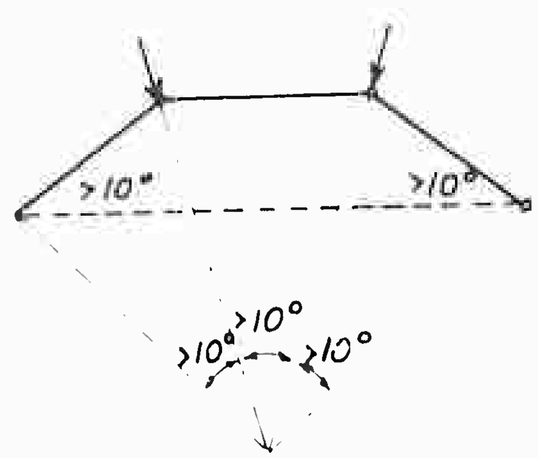

Fig. 6 - Model of support of two adjacent joints in spherical framework.

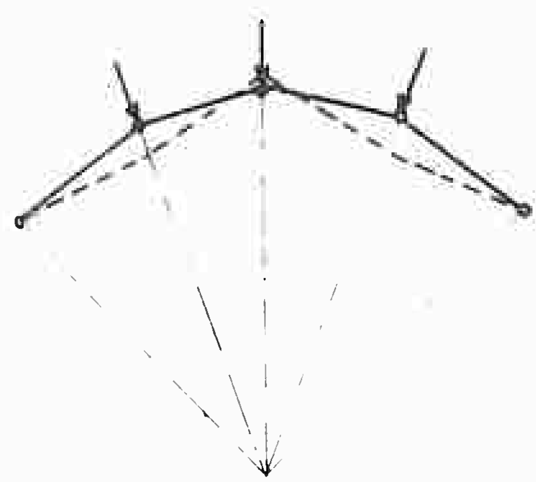

Fig. 7 - Model of jump phenomenon involving two joints which jump simultaneously.

I

II

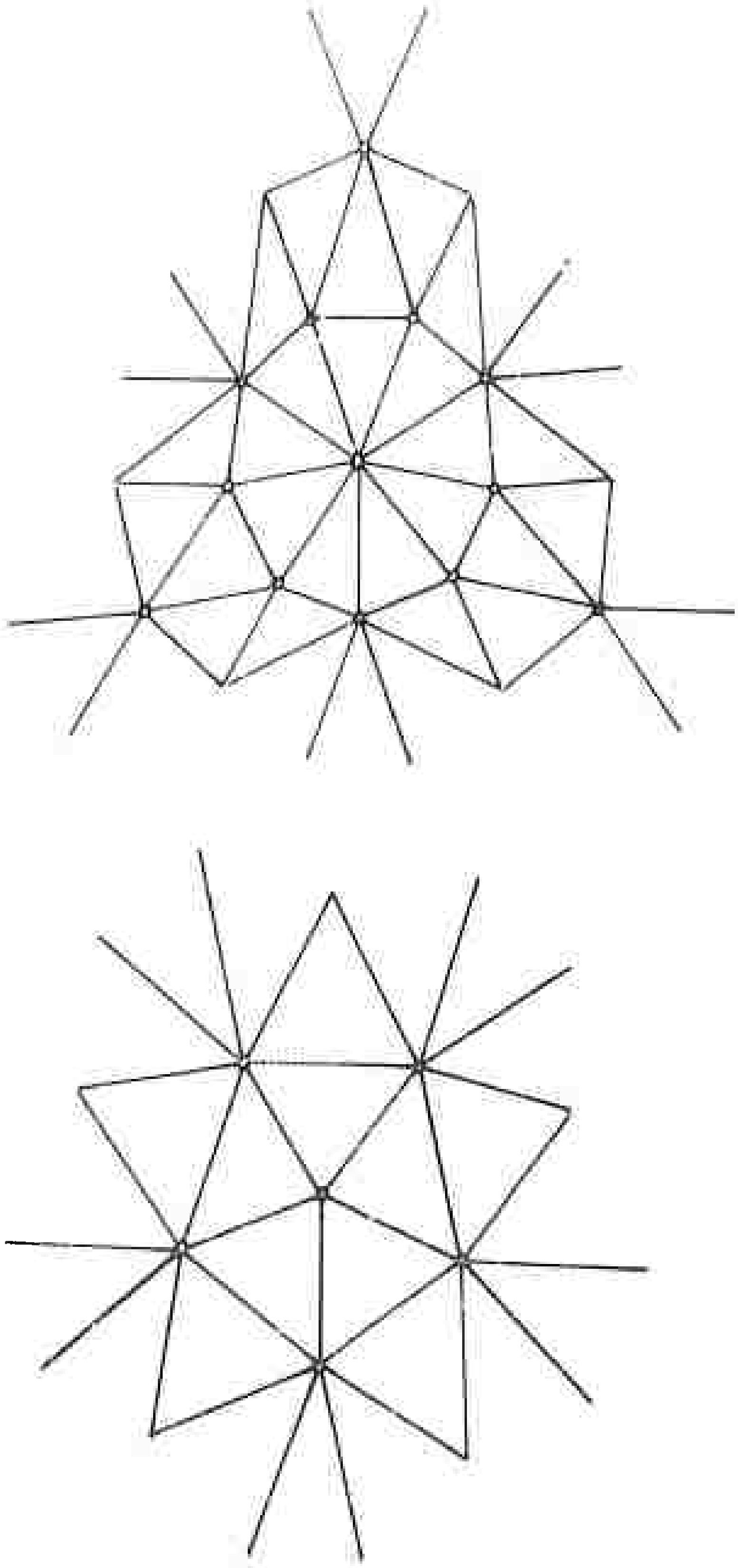

Fig. 5 - Subgroups in spherical framework.

III

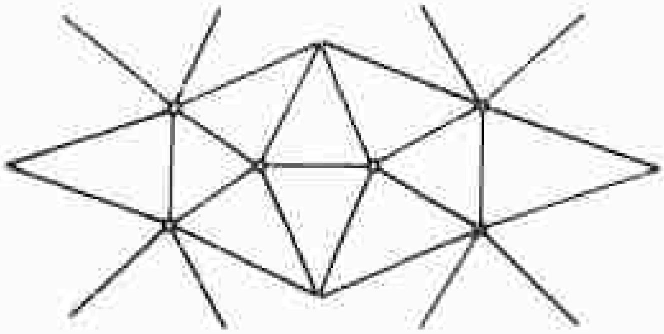

Fig. 8 - continued.

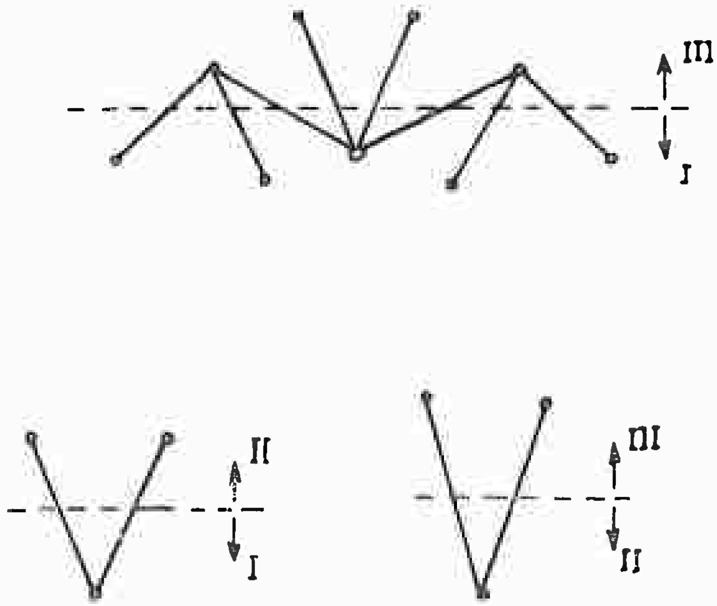

Fig. 9 - Substructures in spherical framework providing cross-coupling between subgroups of Fig. 8.

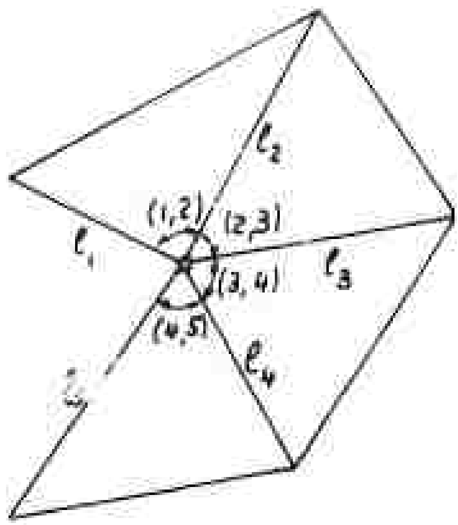

$$S_n = \frac{1}{2} \ell_n \ell_{n+1} \sin(n,n+1)$$

Fig. 10 - Geometry and surface area of triangles about a joint.

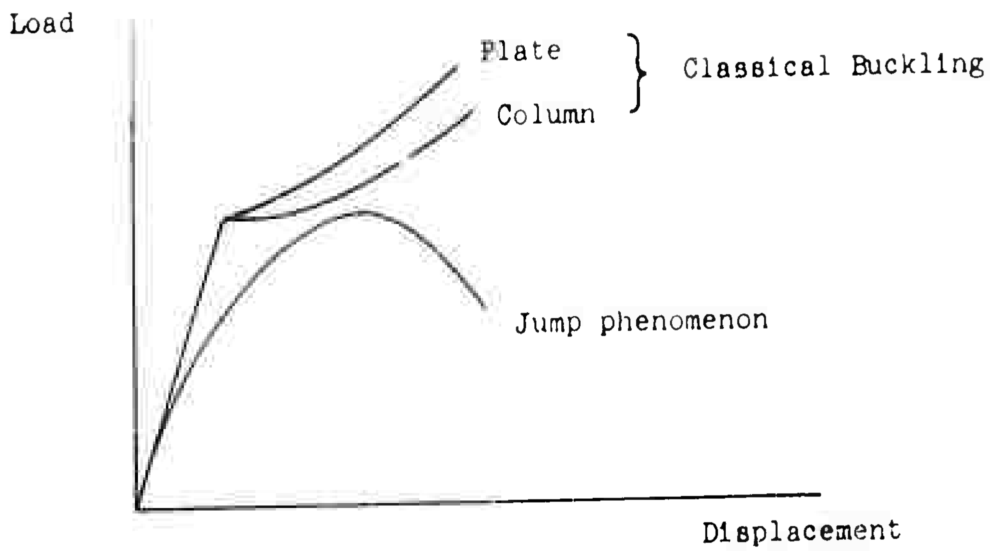

Fig. 11 - Typical load-displacement diagrams for classical buckling and for the jump phenomenon.

POLYESTER-POLYURETHANE FOAM AS A PRIMARY STRUCTURAL MATERIAL

T. C. Dauphiné

Hooker Chemical Corporation
Niagara Falls, New York

During the past few years, we have been experiencing a quiet revolution in structural materials, namely, the use of synthetic organic materials. It is noteworthy that some of the fastest progress in this direction has been stimulated by many of you attending this symposium, in the interest of obtaining electrically transparent, strong, and permanent shelters for radar. Thus we have progressed from the inflated non rigid radomes to the current concepts for rigid radomes involving a load bearing framework carrying electrically transparent fiberglass-plastic panels. Interest in the space-frame type of structure continues, as you know, with particular attention being given to requirements of high precision systems of large size. However, as requirements for extreme accuracy have become more important, designers have become more aware of the limitations of space-frame systems caused by the uneven energy absorbing and reflecting characteristics of the space frame itself. For this reason, increasing effort has been put forth to design radome structures which are as homogeneous as possible - that is, have completely uniform electrical and strength characteristics throughout the structure. In this regard, plastic foams, and particularly polyurethane foams, promise structures having the characteristics required by the ideal radome. They offer very low resistance to passage of the radar beam. Light in weight,

but with adequate strength and stiffness for self-supporting structures, they provide radomes of uniform wall thickness, without apparent joints or ribs to distort the radar beam. Consequently polyurethane foams are today being actively considered as structural materials for large radomes.

It is the purpose of this paper to discuss polyester-polyurethane foams as primary structural materials.

Before presenting the available data on structural properties of foams, I would like first to show you some typical foam structures, and then discuss briefly their chemical makeup.

A microscopic examination of a thin slice of low density (2 pcf) foam shows a random cellular structure (Fig. 1) reminiscent of a tiny space frame. This shows a Hooker 126, one-shot foam of closed cell structure, magnified 100 diameters. The bubble walls appear to be very thin, with relatively thick rod-like struts forming a three dimensional framework which apparently gives most of the structural strength to the foam.

For comparison is shown a similar magnification of an open cell, 1.7 pcf prepolymer Hooker foam (Fig. 2). The lower density correlates with the somewhat thinner ribs bounding the open cells.

As we go to higher polyurethane densities, as in Fig. 3 showing a 7.5 pcf Hooker 126, one-shot foam, you will note the bubbles become smaller, more spherical, and the space frame ribs become relatively more heavy.

By contrast Fig. 4 presents a 4.3 pcf Styrofoam showing a distinctly different structure. The ribs are quite delicate compared to those of the 7.5 pcf polyurethane, and the closed cells have multi-planar sides instead of being spherical.

Again going up the scale in density, Fig. 5 shows a 14 pcf Hooker [illegible], one-shot foam, again at 100 diameters magnification. Bubble size continues to be smaller, and they occur less frequently with larger volumes of solid resin between, as one would expect.

When we discuss structural foams, we generally mean foams of densities higher than 5 pcf. Consequently the structures shown in the last three figures are typical of the foams under consideration.

The history of organic foams is quite recent. As a class, they have had attention only in the last forty years. Until now there has been little incentive to use them as primary structural materials. Two factors have held them back in this respect. First, the lack of foams with sufficient toughness, strength,durability, and dimensional stability; second, the relatively high cost of such materials. At best the load bearing duties of foams in the past have been restricted to small-scale applications, mainly involving their use as cores or fillers in sandwich structures where loads on the foam were relatively small. It is primarily the advent of polyurethane foams in higher densities, coupled with the need for better radome structures, which has led to foams being seriously investigated as primary structural materials.

It might be helpful to talk a moment about organic foams in general, to put polyurethane foams in the proper perspective. Almost everything which is plastic can be foamed, by some technique.

Many flexible and semi-rigid foams are made through addition of chemical blowing agents to a plastic mass. These blowing agents have the property of decomposing above a certain temperature level to release gas bubbles which expand the plastic mass into a cellular structure. Many foamed rubbers and some

foamed vinyl plastics, are made in this way. This is an expensive approach, and is mostly limited to resilient foams.

Phenolic foams, which are about forty years old, are foamed partly by blowing agent, and partly by the liberation of water vapor during the polymerization reaction. Phenolic foams are rather brittle, odoriferous, corrosive if strong acids are used as catalysts, permeable to water and gas (in other words have open cell structure), but often have remarkable strength and outstanding fire resistance. Similarly urea formaldehyde can be made into foams by analogous techniques. However none of these foams have assumed commercial importance as structural material.

Another approach, which has been used both for resilient vinyl foams and rigid polyester foams, is that of the so-called "mechanical" foam made by beating a gas into a molten thermoplastic, or into an uncured catalyzed resin. The object is to create a stable froth or foam which will not settle in the time it takes for the resin to harden. This is potentially a very economical method, but is at present practical mainly for elastomeric vinyl foams.

Polystyrene foams have been made in two different ways. One technique produces a log of expanded polystyrene which may be cut into slabs and handled much like lumber. The principle is to expand molten polystyrene by first adding a volatile solvent which dissolves in the molten plastic, and which vaporizes on release of pressure to form a cellular structure. Such material must be aged to permit excess solvent to diffuse from the interior of the foam, before such foams attain good strength and dimensional stability.

An alternate approach is to dissolve a volatile hydrocarbon, such as liquid pentane, into small beads of molten polystyrene which is chilled, thereby hold-

ing a solid solution of the volatile hydrocarbon liquid. When such beads are heated, the volatile hydrocarbon held in a solid solution tends to vaporize and expand the bead to many times its original size. The beads should get hot enough to fuse together in the expanded state, thereby forming a light, strong structure. Basically this uses a volatile liquid as a blowing agent, its vapor pressure serving to expand the heated plastic into a foam.

Styrene foams are thermoplastic, and will melt at fairly low temperatures. They have no strength above 180°F. They have excellent electrical properties however, and have been of interest as core materials in smaller radomes, where fiberglass plastic skins may be used to take major structural loads, and protect them from the weather, since weathering properties are poor. Also they lack practical fire resistance desirable in large organic structures.

Polyurethane foams are of recent vintage, having been commercially available in this country only during the last three years. At present most polyurethane foam made is of the flexible type, and is in sharp competition with foam rubber. Rigid polyurethane foams are attracting wide developmental interest, however, for cores in structural panels, refrigeration insulation, flotation, as well as for radomes.

The chemistry of these foams is exceedingly complex, and I propose to show you only the basic essentials.

Polyester-polyurethane foams are based upon the reactions of diisocyanates with an alkyd resin containing a predominance of hydroxyl groups, with some carboxy groups.

Figure [illegible] shows the two commercial isomers of toluene diisocyanate, usually called TDI, which is the cheapest and most commonly used diisocyanate. The -NCO

groups are the reactive isocyanate groups. Note that there are two of them on this difunctional molecule, which permits the TDI to chain extend or cross link any two molecules with which it may react.

A polyester alkyd for flexible foams may be schematically represented (Fig. 7) as a linear combination of a dibasic acid, such as adipic acid, with a glycol, usually diethylene glycol. This gives a long chain mainly terminated by hydroxyl (OH) or with a few carboxy (-COOH) groups, both of which can react with the diisocyanate.

Similarly, a polyester alkyd for a rigid foam is shown in a simplified way in Fig. 8. The addition of a trifunctional triol such as glycerine leads to a three dimensional network structure, terminated by reactive hydroxyl and a few carboxyl groups. The higher molecular weight of the starting alkyd, plus its greater functionality, gives a higher softening, more rigid polymer after cross linking, in contrast to the rubbery polymer formed from the straight chain alkyd for flexible foams.

The most important isocyanate reactions, as far as foam formation is concerned, are listed in Fig. 9. Reaction A is between water and two -NCO radicals to form an urea linkage between two isocyanates, with the liberation of carbon dioxide gas. This is both a linking and blowing reaction, and water is customarily added in controlled quantities to act as a blowing agent in polyurethane foams.

Reaction B is the isocyanate reaction with an alcohol. This is a polymerization reaction through the so-called urethane linkage. No gas is formed, and it is this reaction which is predominant in the formation of a so-called "prepolymer", where all of the diisocyanate required for a foam is pre-reacted

[illegible]

[illegible] water ([illegible] agent) [illegible] foam.

Reaction C shows the reaction of an isocyanate with an acid or carboxy group to liberate carbon dioxide gas and form an amide linkage as shown.

Reaction D is the isocyanate reaction with an amine to form an urea linkage between molecules. Often organic amines are used in polyurethane foams, and serve as active catalysts.

In addition to the four reactions presented, the isocyanate group can react with the active hydrogen shown in the urea linkage, the urethane linkage, and the amide linkage, giving further cross linking, but liberating no gas.

Variations in foam properties may be obtained by influencing the various isocyanate reactions by adding catalysts, blowing agents such as water, and by control of alkyd specifications. The alkyd itself can vary through use of different glycols and triols, and different dibasic acids, as well as by different acid-polyol ratios to affect alkyd reactivity.

For instance, Hooker foams are unique in using chlorendic acid, trademarked HET Acid, in the alkyd portion. Fig. 10 shows its structure compared to adipic acid and phthalic acid, both of which are also used in other polyester alkyds for foams. This large heavy molecule, containing 55% of stable chlorine, contributes to fire resistance, stiffness, and strength at high temperatures.

Polyester-polyurethane rigid foams may be made by the one-shot technique, prepolymer technique, and semi-prepolymer techniques.

A one-shot foam is made by reacting all the diisocyanate with the polyester

[illegible]

A prepolymer technique involves [illegible] of the isocyanate with all of the polyester alkyd to produce an isocyanate terminated prepolymer with free isocyanate groups. This prepolymer is then reacted with water, catalyst, and surfactant at the time of foaming. This technique is not well adapted for rigid foams.

The semi-prepolymer technique has wider latitude for rigid foams. It reacts all of the diisocyanate with part of the polyester alkyd, to get a prepolymer with a high percentage of free isocyanate groups. At time of foaming this is reacted with the remainder of the alkyd, plus catalyst and blowing agent.

In all cases the mixing of the foaming ingredients results in a homogeneous liquid which is undergoing polymerization and blowing reactions simultaneously. These reactions generate heat, which raises the temperature to further speed the reactions and hasten gelation and foam rise, and helps cure the hardened foam. Some foams are self-curing, but others with less functionality may require oven curing to develop maximum properties.

I shall not attempt to describe the variety of equipment which may be used to make rigid polyurethane foams. Both batch and continuous systems are available, as well as equipment for spraying certain foams. Also, the problems of making foamed objects are not pertinent to this paper.

I hope this short review of the basic urethane foam chemistry has at least impressed upon you the complexity and variability of rigid urethane foam systems. Almost an infinite number of urethane foams can be made, each different, and it is very dangerous to make general statements regarding foam properties. The field is too new, and not sufficiently well organized, to

permit more than a presentation of specif[illegible] concerning [illegible] other [illegible]. Consequently, most of the data on structural properties which follow pertain to a Hooker 12[illegible], one-shot foam. Where possible, comparisons are made with other foams. Let me now introduce you to the structural performance of certain foams.

The reproducibility of structural properties in foams, as you may imagine, is poorer than that experienced with steel and other materials which may be made to closely controlled standards. The chemical foaming systems are very sensitive systems, being affected by the time of reaction, the amount of stirring, the probability factors in mixing, trace quantities of moisture and metallic or other impurities, so that to take a foaming system and get perfectly reproducible results seems to be very difficult. However with good control, foams can be made for which the structural properties are reproducible, and where variations from a given average are small for practical purposes.

Another factor is the direction in which strength is measured. In certain foaming systems, and for foams risen under nearly "free rise" conditions, the foam is often stronger in the direction of bubble rise. Needless to say, any good structural foam is such that this distinction is negligible. Directional effects may be substantially eliminated by using some pressure in the molds.

The figure (Fig. 11) shows a stress strain curve in compression for a Hooker 12[illegible], one-shot foam of 12.3 pcf. As you can see, we have a straight line relationship following Hooke's law, and at maximum stress reach a true yield point. This is a typical diagram for Hooker foams in compression. Some thermoplastic or semi-rigid foams do not show this type of diagram, but show a continuous curve to the right without a definite yield point. In these cases it is necessary to pick an arbitrary offset at which to measure yield point.

Fig. [illegible] shows how room temperature compressive strength increases with density for the Hooker 12[illegible], one-shot foams. This curve is fairly representative of a number of rigid polyester-polyurethane foams. Note that strength increases geometrically with density. By contrast the published values for polystyrene foams show equivalent strengths at [illegible] pcf, but much lower strengths, the order of 100 psi, at 10 pcf, with a linear strength - density relationship.

A comparison of room temperature compressive stiffness, or modulus, is presented in Fig. 13. Data are shown versus density for a Hooker 12[illegible], one-shot foam, and compared with data published by du Pont for typical polyester-polyurethane foams. For a given density, the Hooker foam shows a much higher modulus. This could possibly be explained by the high HET Acid content, and the fact that this system is thoroughly cured at about 250°F.

All materials lose strength as temperature is raised. Before urethane foams can be seriously considered as structural materials, we must know how they are affected by rise in temperature.

Fig. 14 demonstrates loss in compressive yield strength for an experimental Hooker 126, semi-prepolymer high heat distortion foam. Foam densities shown are for 2.4 pcf, 7.0 pcf, and 27.5 pcf. There is relatively little loss of strength out to 300°F, and 50% strength retention at 350 - 360°F. Above this temperature compressive yield falls off rapidly.

Plotted for comparison in the two lower foam densities are published data from du Pont on conventional polyester urethane foams. These are not high heat distortion foams and have 50% strength retention at about 220°F. The Hooker 126, one-shot foam has high temperature strength intermediate between the foams shown, with a 50% strength retention between 250°F and 275°F.

In the [illegible] of structural performance [illegible]

creep, or the flow with time of a material loaded below its elastic limit. Creep data are almost non-existent on plastic foams, and Fig. 15 shows information obtained at Hooker. Much more data on creep are desirable to define foam performance under load. Compressive creep at 158°F was measured at 25% of room temperature ultimate strength, which in this case corresponds to compressive yield strength. Curves are shown for 2 pcf Dylite expanded polystyrene beads, and a 12 pcf Hooker 13[illegible], one-shot. The Dylite carried 8.2 psi compressive load, and the Hooker foam carried a 28 psi load. Creep is shown as percent.

For Dylite creep was very rapid initially, going to 2% in only seven hours, and continuing at decreasing rate to [illegible]% at 285 hours. At this point the foam appeared to stabilize and had negligible additional creep for the duration of the test.

The Hooker foam gave significantly less creep, and at a much slower rate. At well over 1000 hours the creep was only 1.8%, or less than the creep of Dylite at seven hours.

As a qualitative measure of foam brittleness in compression, it is interesting to measure resiliency of foams. A foam cube is crushed beyond its yield point to 50% of original height, the load removed, and the recovery noted. Table 1 shows percent of original height regained immediately after load removal, and 24 hours later, for low, intermediate, and high density foams. In all cases immediate recovery is to 60 - 66% of original height, giving as high as 70% after 24 hours. A completely brittle material would stay at 50% with no recovery.

In considering materials of construction for cold buildings, the effect of low temperature upon structures must be known. Unfortunately we have been unable to find anyone who has studied foam properties at low temperature. This is important and should be done. However, in our laboratories we have obtained rather limited data on compressive yield strengths and resiliency at temperatures down to -[illegible]°F. The data we have indicate no falling off, and perhaps a modest rise, in both compressive yield and resiliency at low temperatures. However much more data are needed to confirm or deny this indication.

The ultimate test of a structural material is its ability to support itself and the functional loads imposed upon it. Fig. 16 shows a load bearing comparison between Hooker 12[illegible], one-shot foam and some conventional materials - brick masonry, concrete, limestone, marble - used in compression. The curve shows the column height required to cause compressive failure in the material. Allowable design loadings are of course much less.

The interesting fact is that foam, in an appropriate density, generally falls above the conventional materials shown in its self-supporting ability. Thus, while the structural properties of foams may not approach those of steel, concrete, and other materials on a pound per square inch basis, it is quite able to support itself in large structures because of its low density. It also appears to offer adequate reserve to handle the other functional loads required of a simple shelter.

Information on tensile properties of foams is more difficult to obtain than compressive data, and consequently I have less to present. Our testing equipment does not permit us to measure tensile load - deformation, but only ultimate tensile strength. This is shown on Fig. 17, versus foam density, for

[illegible] appeared to increase linearly with density, (at least [illegible] 3 pcf) [illegible] approach [illegible] psi for a 1½ pcf foam. However more recent data extending the curve to higher densities indicate the curve should become steeper as density increases.

Tensile creep at 150°F for 3 pcf Dylite and a 12 pcf Hooker 126, one-shot foam is shown in Fig. 18. Load on both foams is 50% of ultimate, being [illegible] psi for the Dylite, and 70 psi for the Hooker foam. The Dylite showed rapid creep to 2% in the first ten hours, went to 3% at 68 hours, and reached [illegible]% at 452 hours, where it held constant until the test was ended at [illegible] hours.

The polyurethane foam shows a positive creep of 0.5% in the first ten hours, and then began to show negative creep rate, possibly caused by shrinkage attending further curing at this temperature. At 30 hours the creep deformation was -0.7%, remaining constant to over 200 hours, and rising to -0.5% at 310 hours when the test was discontinued. Again, the rather striking difference between the thermoplastic Dylite and thermoset urethane is demonstrated. It is likely that longer time tests, which would be very desirable, would demonstrate even greater difference.

Shear strength is another property of foams which is difficult to measure, except at low densities. At densities above 8 pcf sample shear strength becomes high enough so that failure often comes not in shear, but at the adhesive line holding the sample in the test jig.

Fig. 19 shows shear strength versus density for the Hooker 126, one-shot foam at room temperature.

The flexural strength of Hooker 126, one-shot foam, with the load parallel to the direction of foam rise, is presented in Fig. 20. Sample size is

1" x 1" cross section with a 4 inch span. As in compression, flexural strength increases geometrically with foam density.

Flexural modulus, a measure of stiffness in bending, is presented in Fig. 21. Although the test is not directly comparable to that used for wood, foam flexural modulus is considerably under that for various woods. For instance balsa, at 8 pcf, has a flexural modulus of 420,000 psi, compared to only about 5000 psi for an 8 pcf foam.

Creep in bending is compared in Fig. 22 for 3 pcf Dylite and a 12 pcf Hooker 126, one-shot foam, both at 158°F. Specimens were 1" x 1" cross section and loaded at the midpoint of an 8 inch span to 25% of ultimate room temperature flexural strength. Load on Dylite is 22 psi, and on the polyurethane foam is 120 psi. Dylite takes an immediate deflection of 0.3 inches, going in 50 hours to a deflection of 0.8 inches. Thereafter creep at 158°F is relatively slow, going to 0.92 inches deflection at 720 hours. At this point temperature was raised to 176°F and deflection more than tripled to 3.5 inches at 768 hours.

The Hooker foam in 24 hours had a deflection of only 0.1 inch, which increased slightly to 0.13 inches at 720 hours. Increasing the temperature to 176°F raised deflection only to 0.16 inches at 768 hours.

If polyurethane foams are to be considered for structures, they must either have inherent weather resistance or be capable of being suitably protected. Certain polyurethane foams, particularly the older castor oil foams, had poor weather resistance, deteriorating badly on exposure to ultraviolet light and moisture. In our own laboratories we tested in the Atlas Weatherometer the Hooker 126, one-shot foam, of various densities, both

one at [illegible] end protected by Radalon. Radalon is a weather resistant and electrically transparent surface coating developed for radomes.

Results at 550 hours exposure are shown in Fig. 22. Although the raw foams have turned brown, none of the samples have changed weight due to erosion or moisture pickup. Original sample dimensions have been retained.

At this point the test was discontinued for the 5.7 pcf and 13.6 pcf foams, and the weathered samples were tested in compression and tension. No loss of physical strength had been caused by the accelerated weathering.

The weathering test was continued on the 2.5 pcf samples, Radalon coated and uncoated. Noticeable erosion began on the uncoated sample at about 1000 hours, with a somewhat sugary surface developing. The test has now run over 3500 hours, and the Radalon coated sample is still in excellent condition, although recently some deterioration of the Radalon coating has begun. From this data we would be confident that a suitable surface coating, such as Radalon, will give quite adequate weathering resistance to a foam structure.

At times it may be desirable to use inserts of other material imbedded in a foam. The thermal coefficient of linear expansion of most polyester-polyurethane foams, including Hooker 126, one-shot foams, is in the range of $2.0 - 3.5 \times 10^{-5}$ per ^{o}F, over a range from $-70^{o}F$ to $170^{o}F$. This is about double that for aluminum, and three to four times that for steel and stainless steel.

Polyester-polyurethane foams, in the higher density ranges we are discussing, have good dimensional stability, as indicated in the discussion of weathering. They are also unaffected by water and most organic solvents, and have high resistance to acids and alkalis. This inertness to various solvents

of the rigid polyurethane foams is superior to that of the thermoplastic foams such as the polystyrenes.

The electrical properties for Hooker 126, one-shot foam is given in Tables 2 and 3. This data was obtained from the Laboratory for Insulation Research at M.I.T.

More recent information indicates that Hooker semi-prepolymer foams also fall in this range, which is fairly typical of polyester-polyurethane foams. Since in particular heat cured polyurethane foam shapes can be made without any appreciable "skin", or high density resin layer on the surface, these good electrical properties can be fully realized in practice.

In the consideration of foams as structural materials, mention should be made of fatigue and impact properties. Unfortunately no reliable data exist that we know of on either fatigue or impact. As interest in polyurethane foams for structural purposes grows, definitive data will have to be obtained. Experience to date does not indicate that polyurethane foams are deficient in these properties for the fixed structures considered.

The fire hazards of foam structures deserve most careful consideration since the thermoplastic foams (except vinyls) and most polyurethane foams are

[illegible] ... material. The cellular nature of foam surfaces can give [illegible] high surface areas per square foot of projected surface, with attendant high rates of flamespread.

It is possible to give conventional polyester-polyurethane foams self-extinguishing properties by incorporating snuffing agents such as tris chlorethyl phosphate. These are also plasticizers, and seriously weaken the foam, particularly at above room temperature.

The Hooker polyurethane foams obtain built-in fire resistance through use of the stable, highly chlorinated chlorendic acid in the polyester molecule. This gives permanent fire resistance of a high degree, increasing with foam density, and actually gives improved foam strength and stiffness.

The measurement of practical fire resistance in foams is not well defined. It is obvious that simple "match" tests and other small scale comparative tests do not measure real fire hazards of structural materials. The Underwriter's Laboratory has developed methods and much data for rating the real hazards of building materials. In the long run foams that are intended for large structures, and particularly those housing personnel, will have to be rated with more conventional materials by tests such as the Underwriters' Wall Test and Tunnel Test. At present this kind of information is not available.

In summary, we have presented a very brief discussion of polyester-polyurethane foams, their chemistry, and their structural properties, with particular emphasis on polyurethane foams based on chlorendic acid. We have noted the complexity of this field, and the need for identifying and

[illegible] the physical properties of foams of different [illegible] higher [illegible], much more, and better [illegible] before we can deal with f[illegible] as structural materials as we now can deal with metals.

In closing, I wish to acknowledge the help of the Hooker Plastics Laboratory, and in particular that of Dr F Roltschek and Dr B C Schoepfle, under whose supervision most of the structural data were obtained.

And last, I thank Lincoln Laboratory for the privilege of appearing at this symposium.

<u>REFERENCES</u>

"Properties of Rigid and Semi-Rigid Urethane Foams"

By Dr E Tufts, Elastomer Chemicals Department
E I du Pont de Nemours & Company, Wilmington, Del.
August 1957

"Engineering Materials Handbook"
By Charles L Mantell, Editor
McGraw Hill Book Company, New York
1958

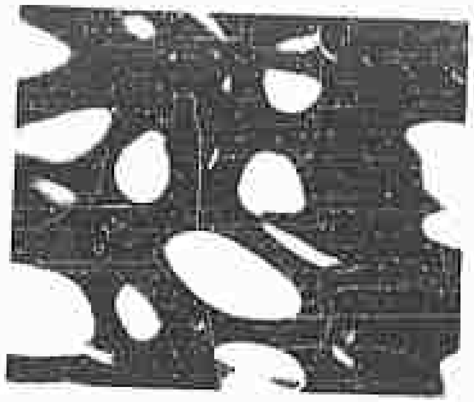

[illegible]

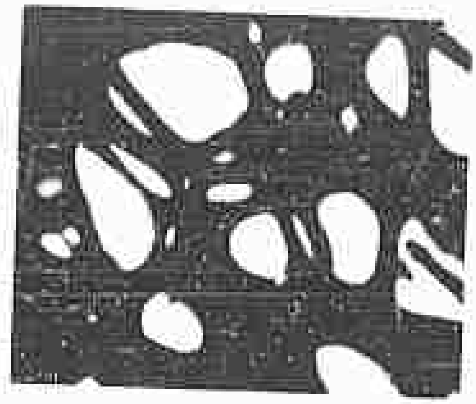

[illegible]

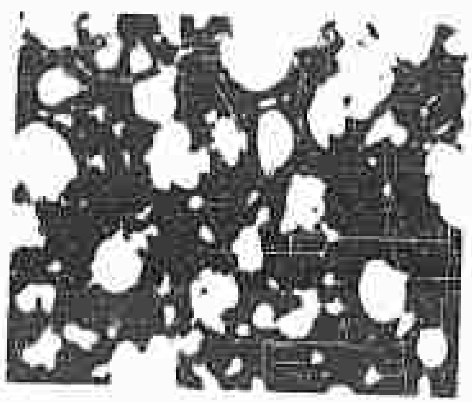

[illegible]

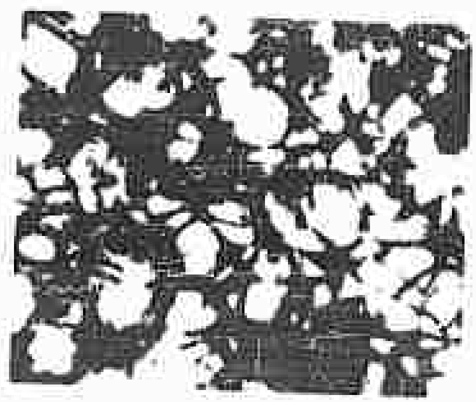

[illegible]

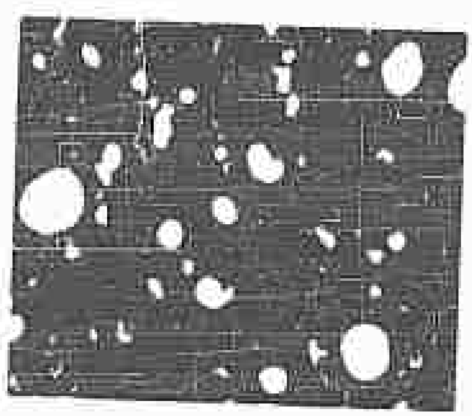

[illegible]

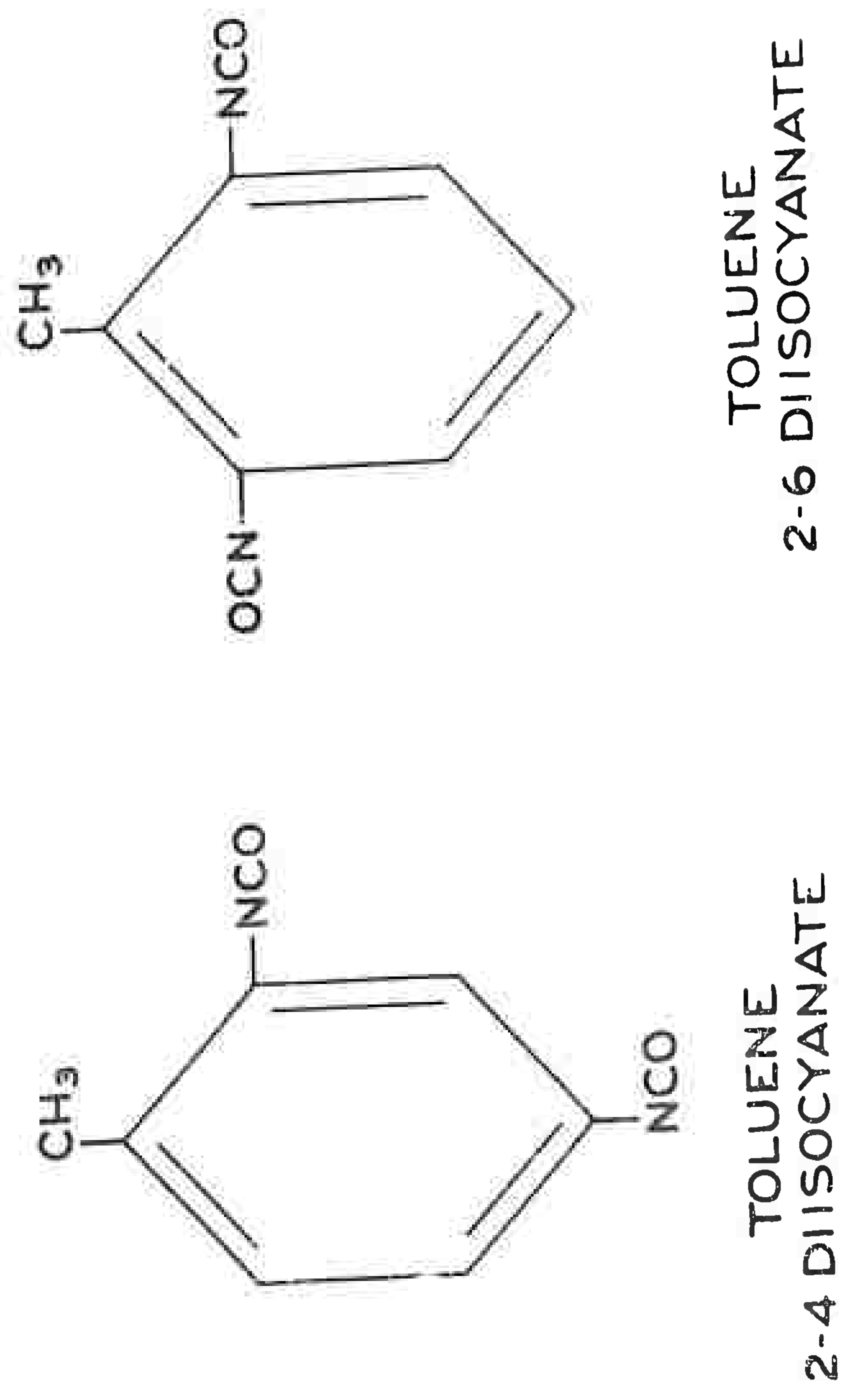
CH3
NCO
OCN
TOLUENE
2-6 DIISOCYANATE
CH3
NCO
NCO
TOLUENE
2-4 DIISOCYANATE

Figure 6

POLYESTER ALKYD - FLEXIBLE FOAM

HOOC — A — G — A — G — A — G — OH

WHERE A = ACID, DIBASIC - USUALLY ADIPIC ACID

G = GLYCOL - DIFUNCTIONAL - OFTEN DIETHYLENE GLYCOL

FIGURE 7

POLYESTER ALKYD - RIGID FOAM

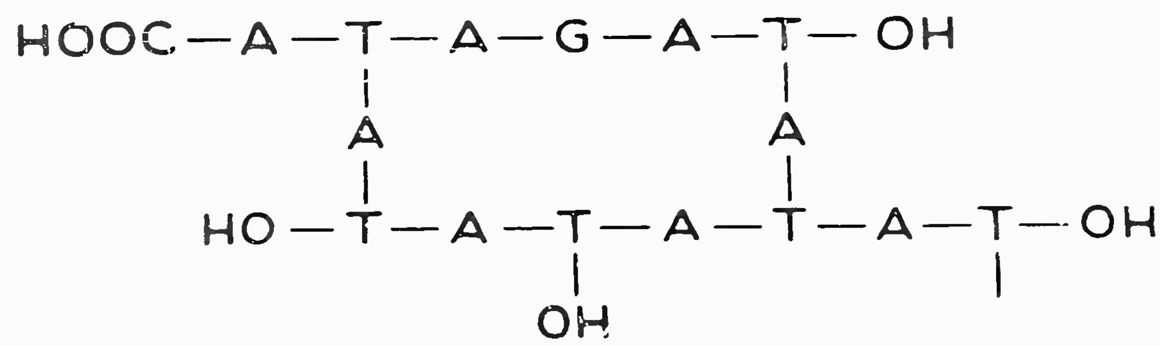

WHERE A = ACID, DIBASIC

G = GLYCOL-DIFUNCTIONAL

T = TRIOL-TRIFUNCTIONAL-
USUALLY GLYCERINE OR
TRIMETHYLOL PROPANE, ETC.

Figure 8

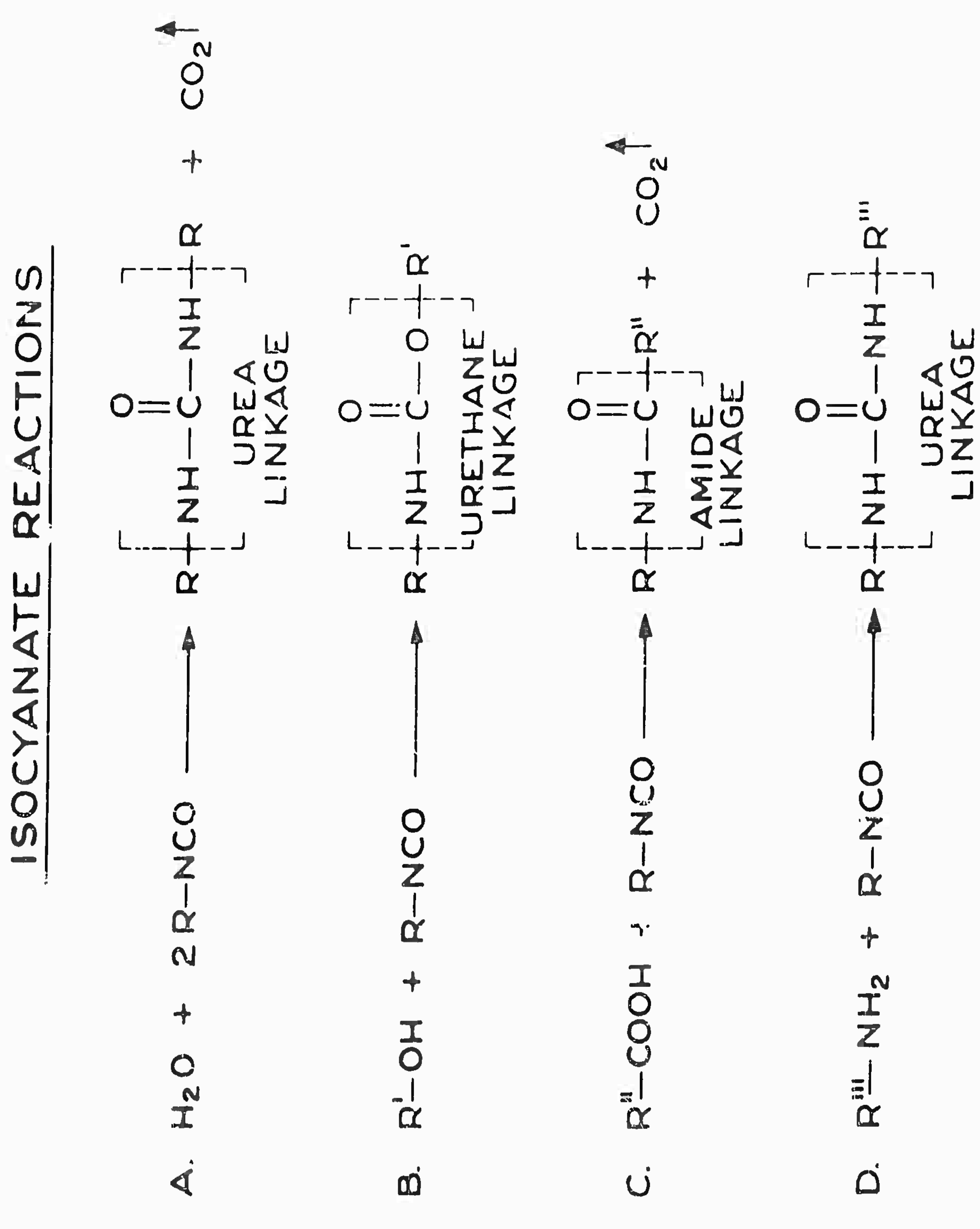
ISOCYANATE REACTIONS
A. H_2O + 2R–NCO → R–NH–C(=O)–NH–R + CO_2↑
UREA LINKAGE
B. R'–OH + R–NCO → R–NH–C(=O)–O–R'
URETHANE LINKAGE
C. R''–COOH + R–NCO → R–NH–C(=O)–R'' + CO_2↑
AMIDE LINKAGE
D. R'''–NH_2 + R–NCO → R–NH–C(=O)–NH–R'''
UREA LINKAGE

Figure 9

DIBASIC ACIDS

HOOC—CH_2—CH_2—CH_2—CH_2—COOH   ADIPIC ACID

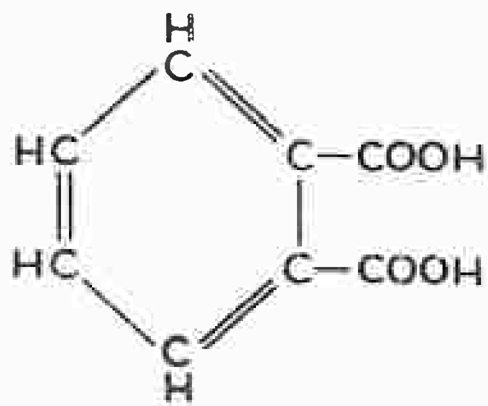

PHTHALIC ACID

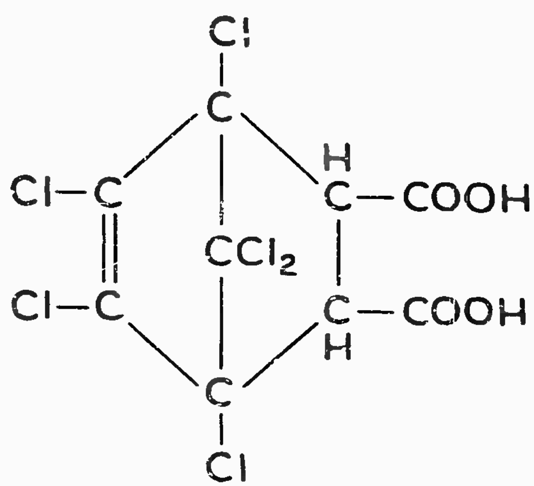

CHLORENDIC ACID
OR
"HET" ACID

Figure 10

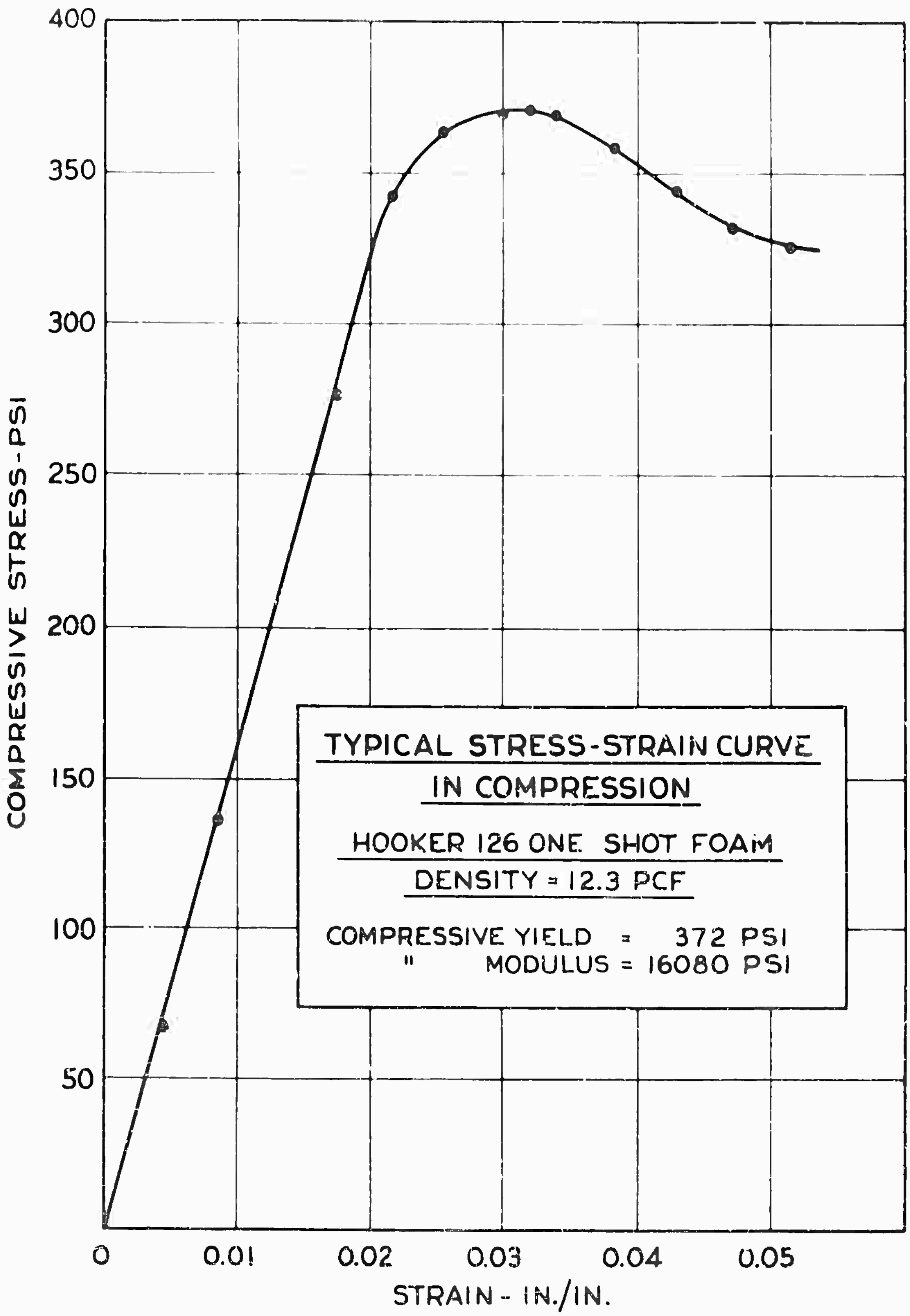

TYPICAL STRESS-STRAIN CURVE
IN COMPRESSION
HOOKER 126 ONE SHOT FOAM
DENSITY = 12.3 PCF
COMPRESSIVE YIELD = 372 PSI
" MODULUS = 16080 PSI
COMPRESSIVE STRESS - PSI
400
350
300
250
200
150
100
50
0
0.01
0.02
0.03
0.04
0.05
STRAIN - IN./IN.

Figure 11

HOOKER 126 FOAM - ONE SHOT
COMPRESSIVE STRENGTH AT YIELD POINT VS. DENSITY
(LOAD PARALLEL OR PERPENDICULAR TO RISE)
TEMPERATURE = 73.4°F.

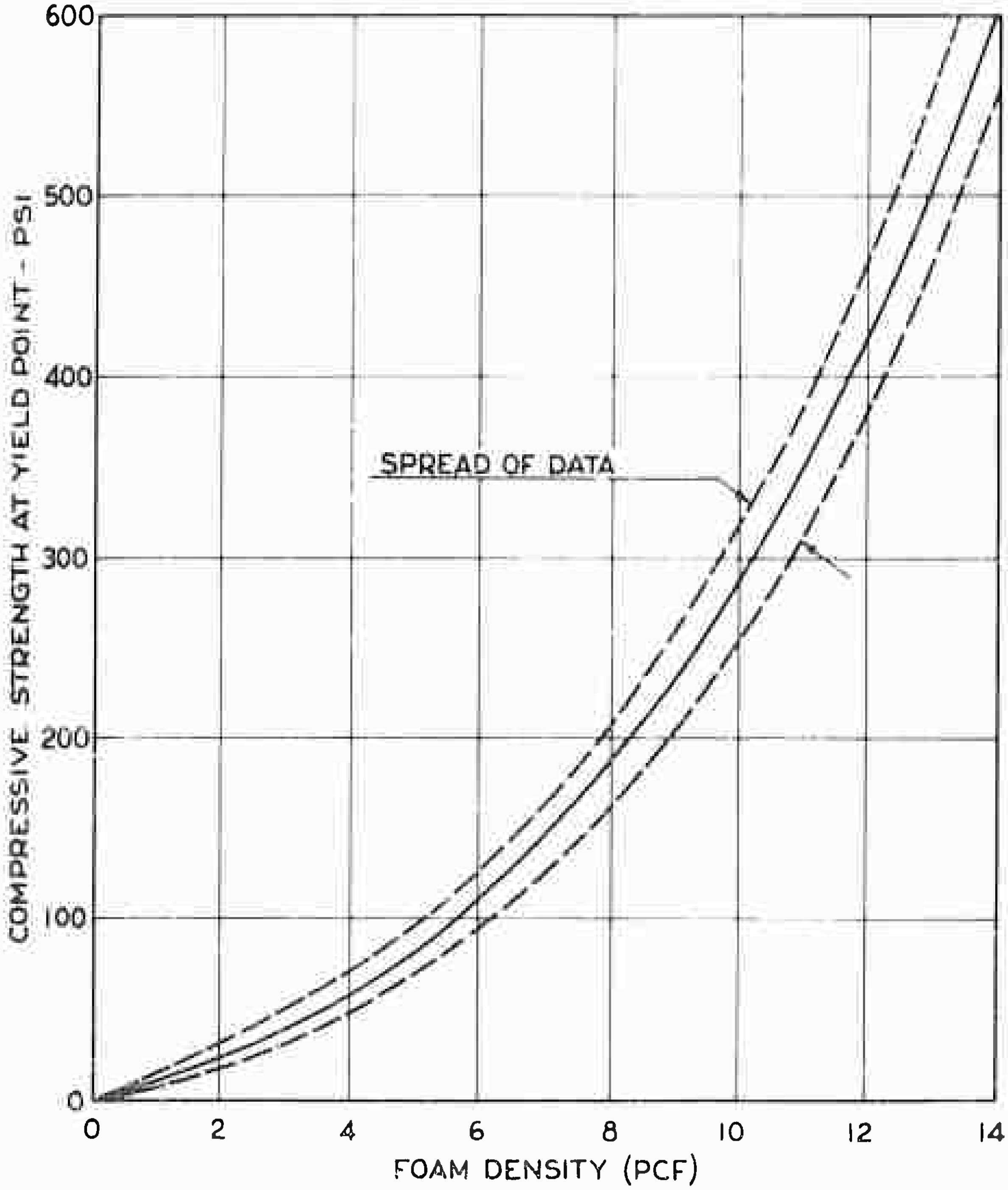

Figure 12

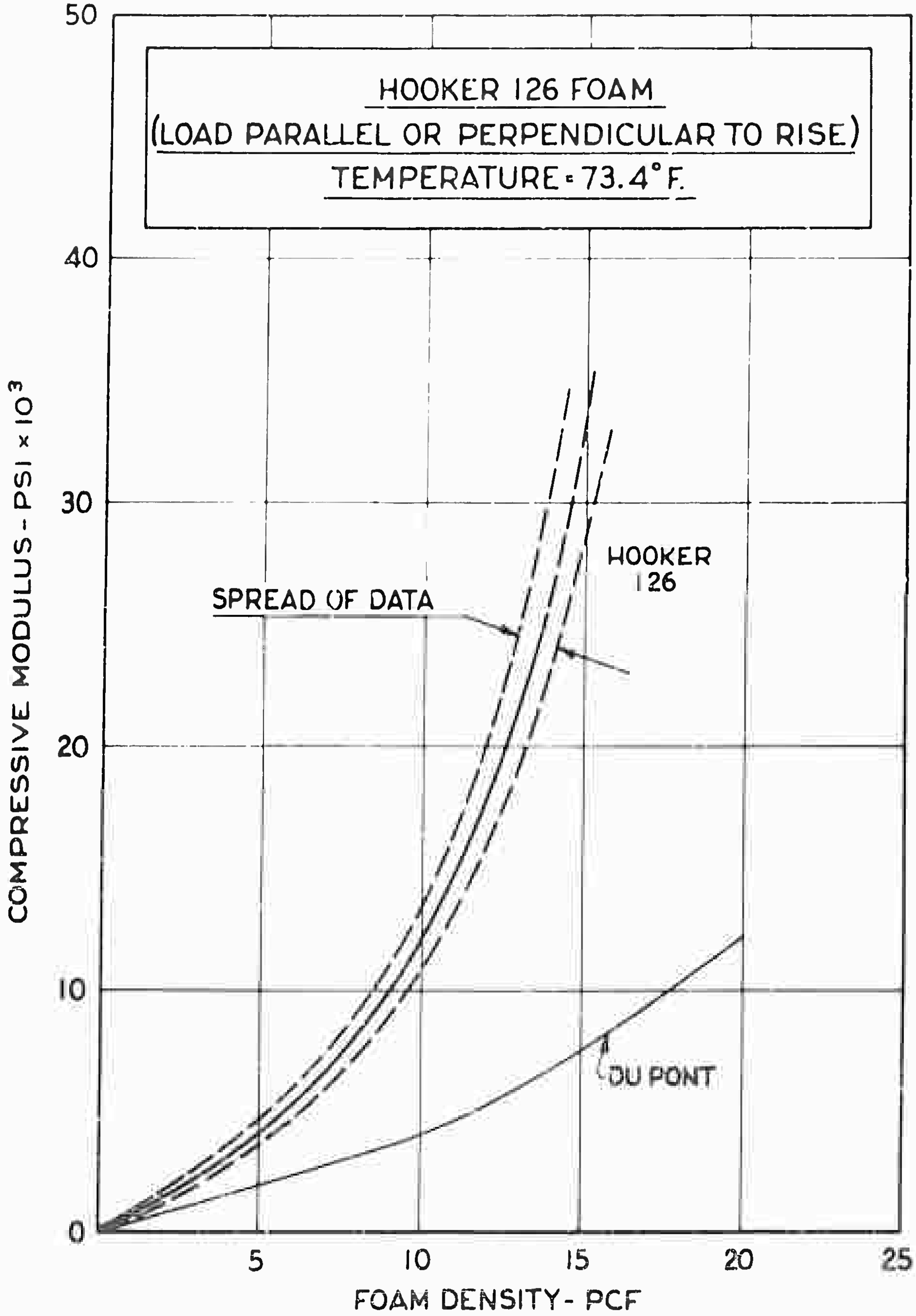
HOOKER 126 FOAM
(LOAD PARALLEL OR PERPENDICULAR TO RISE)
TEMPERATURE = 73.4°F.
SPREAD OF DATA
HOOKER 126
DU PONT
COMPRESSIVE MODULUS - PSI × 10³
FOAM DENSITY - PCF
0
10
20
30
40
50
5
10
15
20
25

Figure 13

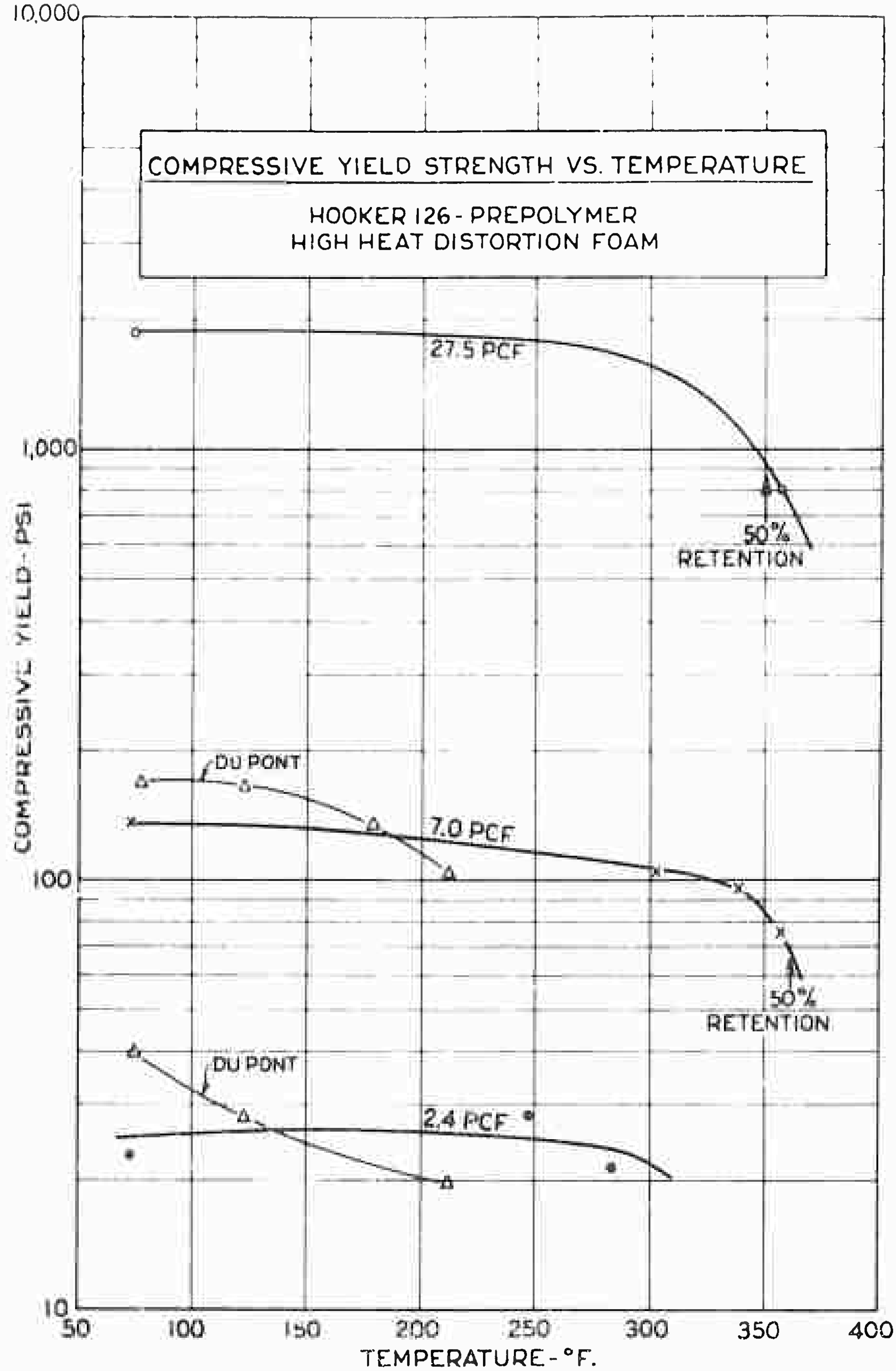
COMPRESSIVE YIELD STRENGTH VS. TEMPERATURE
HOOKER 126 - PREPOLYMER
HIGH HEAT DISTORTION FOAM
10,000
1,000
100
10
COMPRESSIVE YIELD - PSI
27.5 PCF
50%
RETENTION
DU PONT
7.0 PCF
50%
RETENTION
DU PONT
2.4 PCF
50
100
150
200
250
300
350
400
TEMPERATURE - °F.

Figure 14

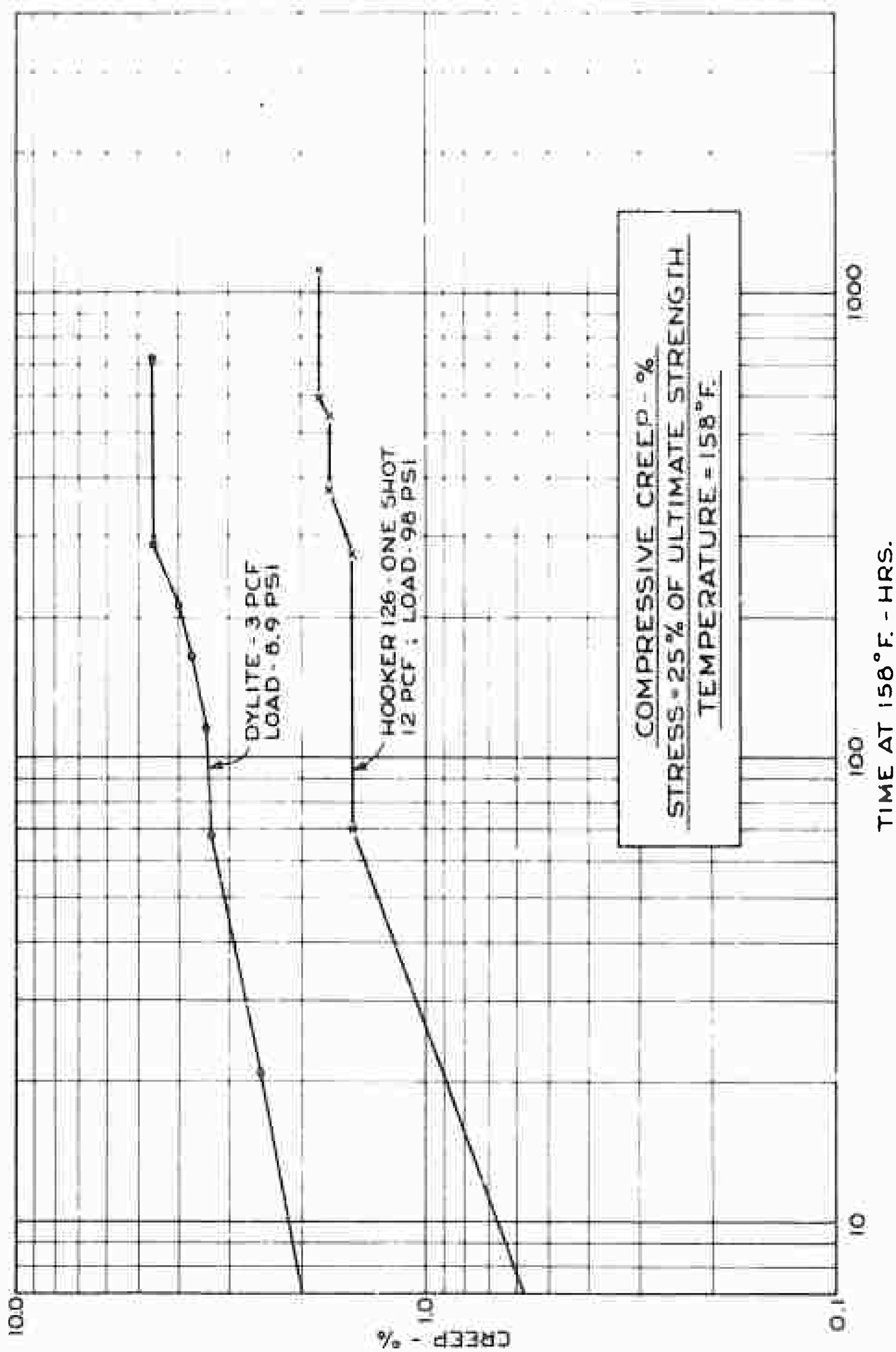
COMPRESSIVE CREEP - %
STRESS = 25% OF ULTIMATE STRENGTH
TEMPERATURE = 158°F.
DYLITE - 3 PCF
LOAD - 6.9 PSI
HOOKER 126 - ONE SHOT
12 PCF ; LOAD - 98 PSI
CREEP - %
10.0
1.0
0.1
10
100
1000
TIME AT 158°F. - HRS.

Figure 15

RESILIENCE OF HOOKER 126 - ONE SHOT FOAMS VS. DENSITY

INITIAL COMPRESSION - 50% OF ORIGINAL HEIGHT

FOAM DENSITY	% OF ORIGINAL HT. IMMEDIATELY AFTER LOAD REMOVED	% OF ORIGINAL HT. 24 HOURS AFTER LOAD REMOVED
2-4 PCF	59 - 66%	66 - 70%
8-9 PCF	62 - 66.5%	63.5-70%
12-13 PCF	63.5-65.5%	69.2-70.2%

TABLE I

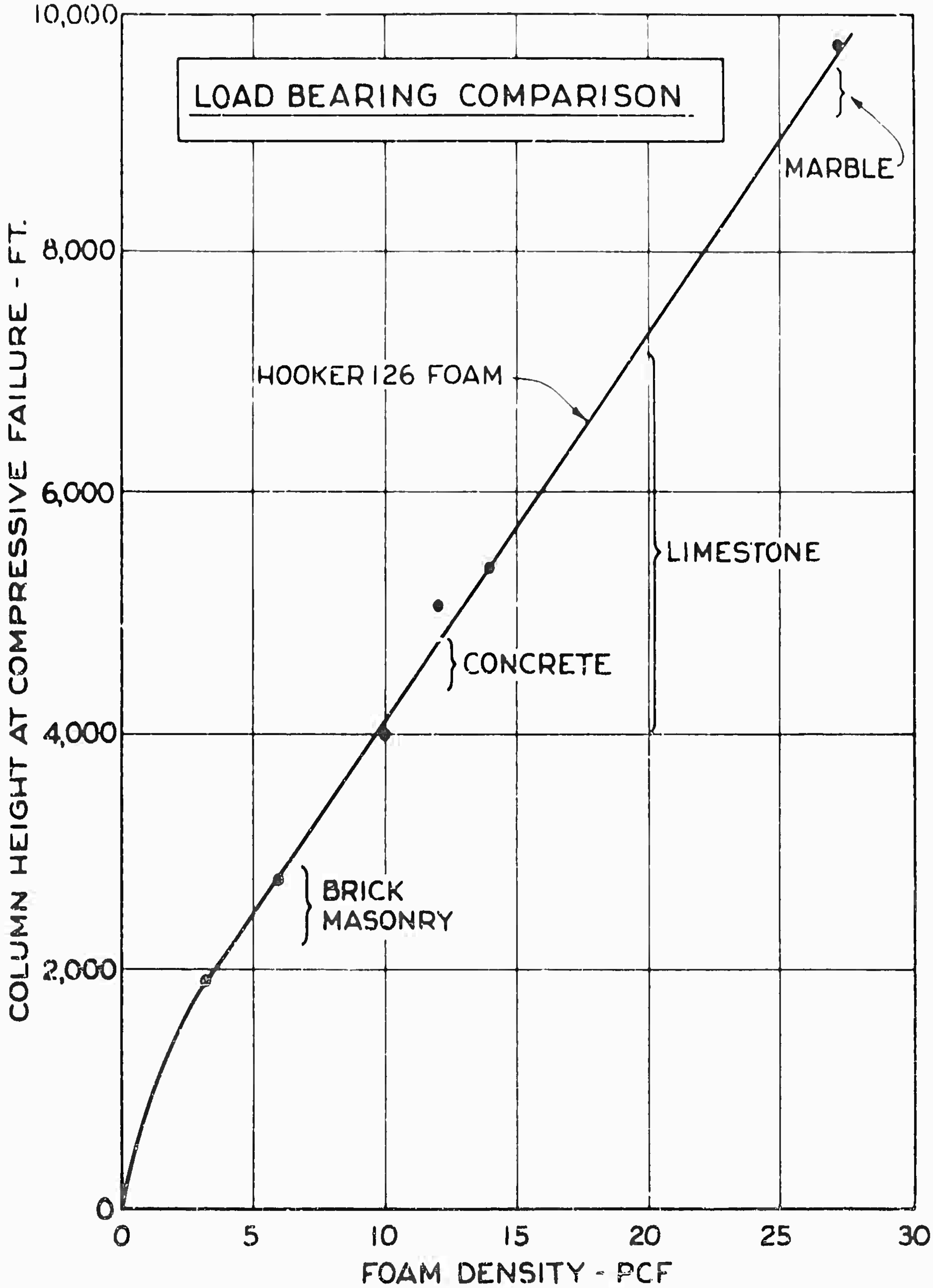
LOAD BEARING COMPARISON
MARBLE
HOOKER 126 FOAM
LIMESTONE
CONCRETE
BRICK
MASONRY
COLUMN HEIGHT AT COMPRESSIVE FAILURE - FT.
10,000
8,000
6,000
4,000
2,000
0
0
5
10
15
20
25
30
FOAM DENSITY - PCF

Figure 16

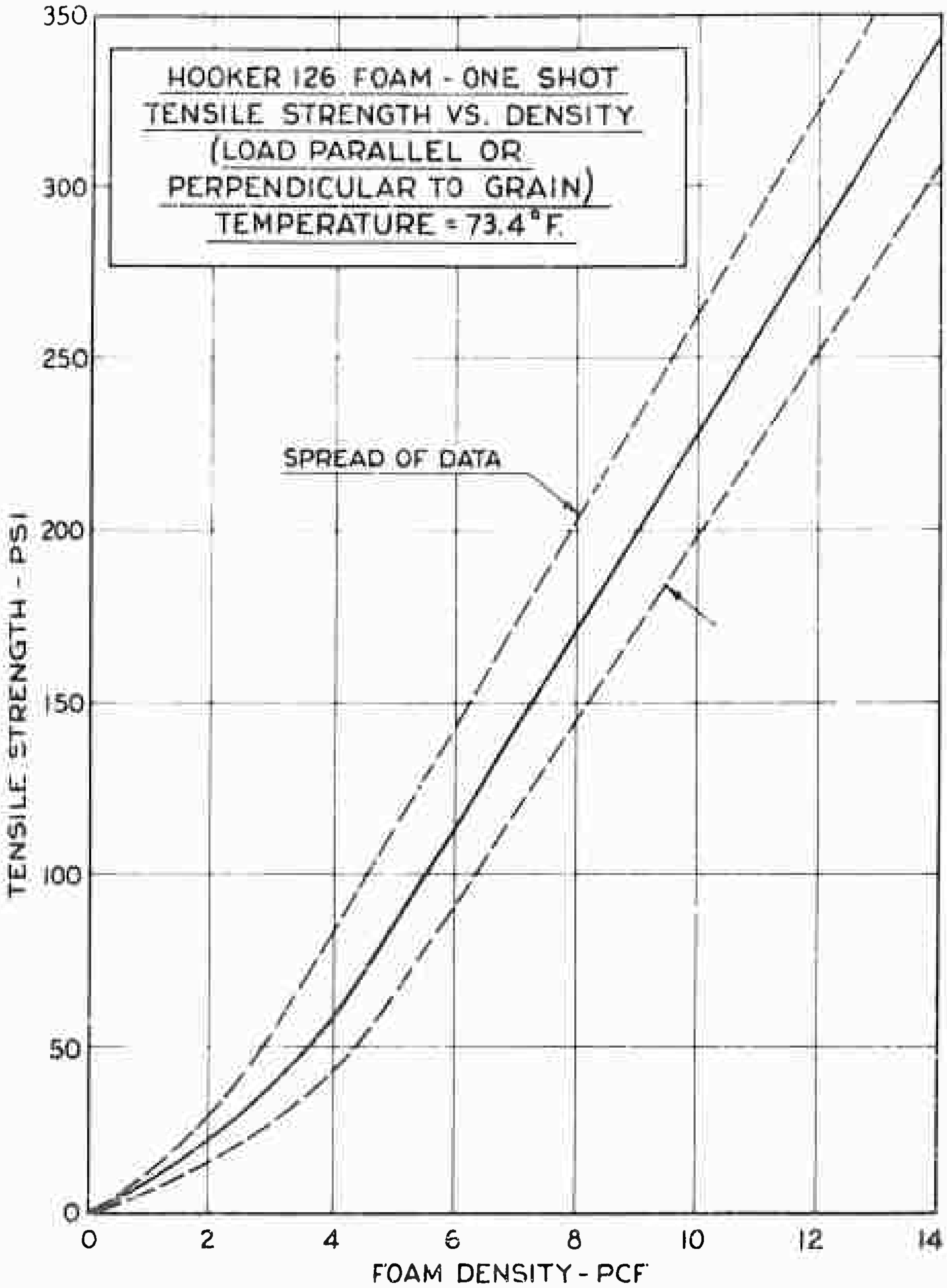
HOOKER 126 FOAM - ONE SHOT
TENSILE STRENGTH VS. DENSITY
(LOAD PARALLEL OR
PERPENDICULAR TO GRAIN)
TEMPERATURE = 73.4°F
SPREAD OF DATA
TENSILE STRENGTH - PSI
0
50
100
150
200
250
300
350
0
2
4
6
8
10
12
14
FOAM DENSITY - PCF

Figure 17

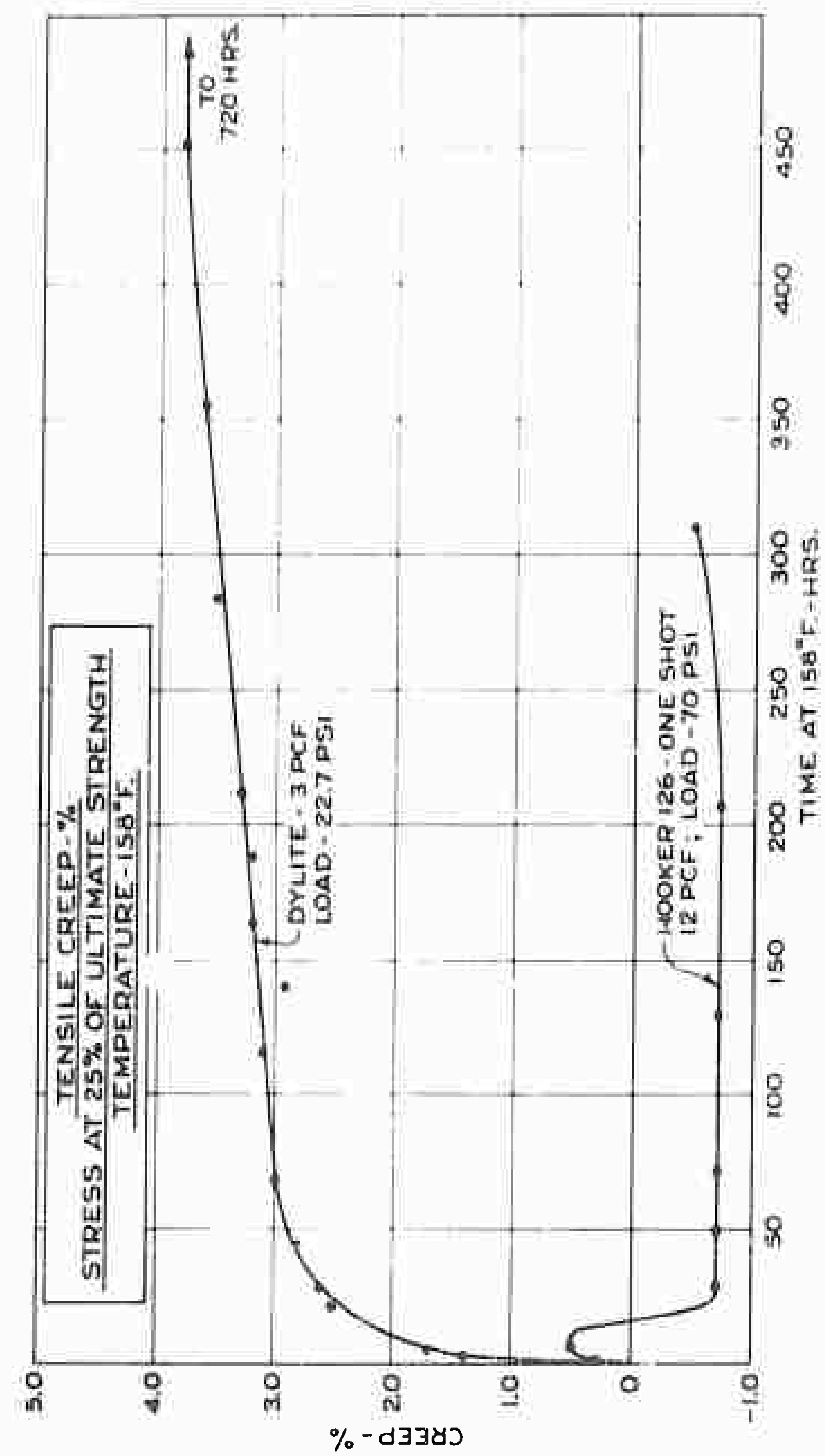
TENSILE CREEP-%
STRESS AT 25% OF ULTIMATE STRENGTH
TEMPERATURE-158°F.
TO 720 HRS.
DYLITE - 3 PCF
LOAD - 22.7 PSI
HOOKER 126 - ONE SHOT
12 PCF ; LOAD - 70 PSI
CREEP - %
5.0
4.0
3.0
2.0
1.0
0
-1.0
50
100
150
200
250
300
350
400
450
TIME AT 158°F. - HRS.

Figure 18

HOOKER 126 FOAM - ONE SHOT
SHEAR STRENGTH VS. DENSITY
LOAD PARALLEL OR PERPENDICULAR TO RISE
TEMPERATURE - 73.4° F.

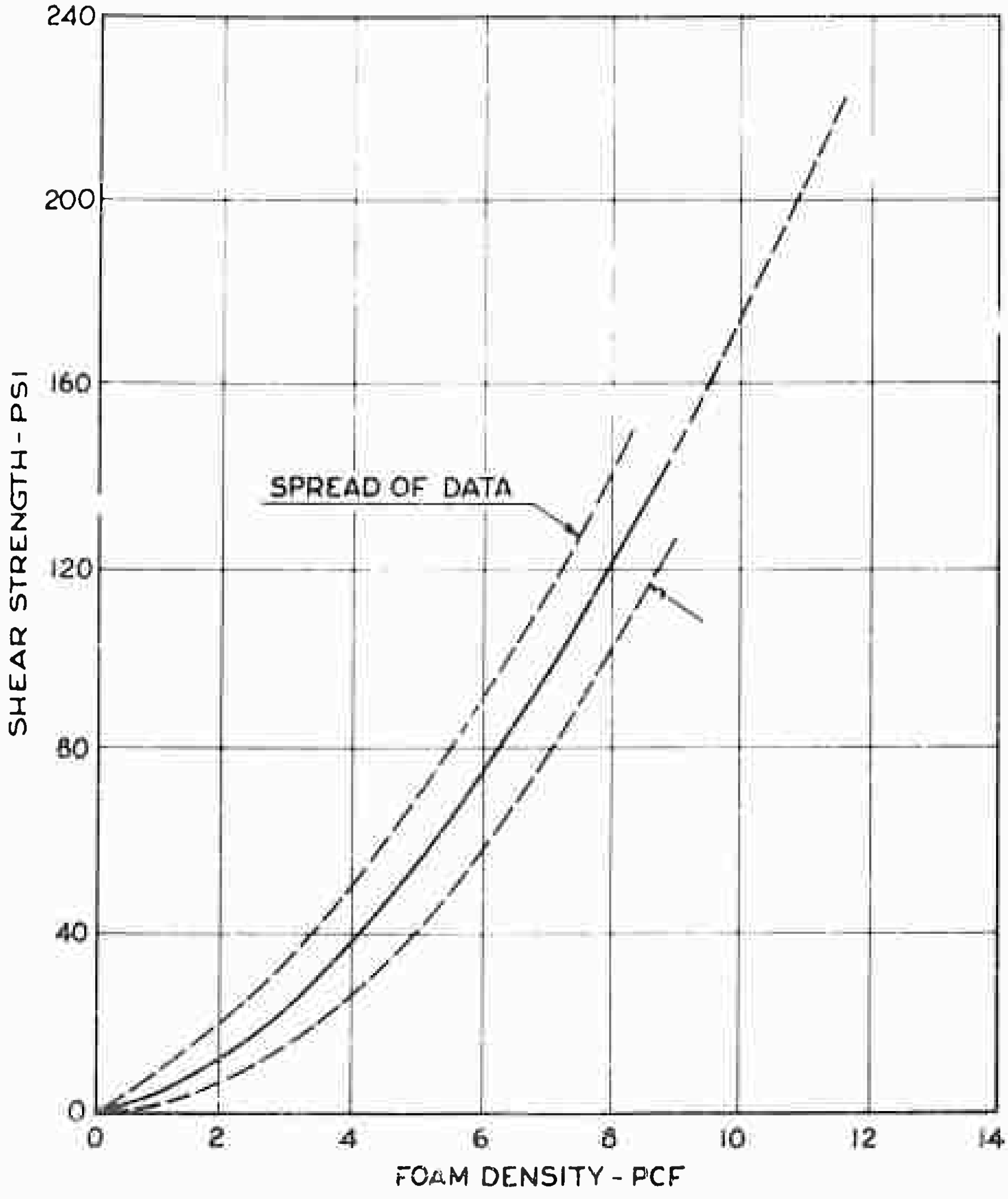

Figure 1y

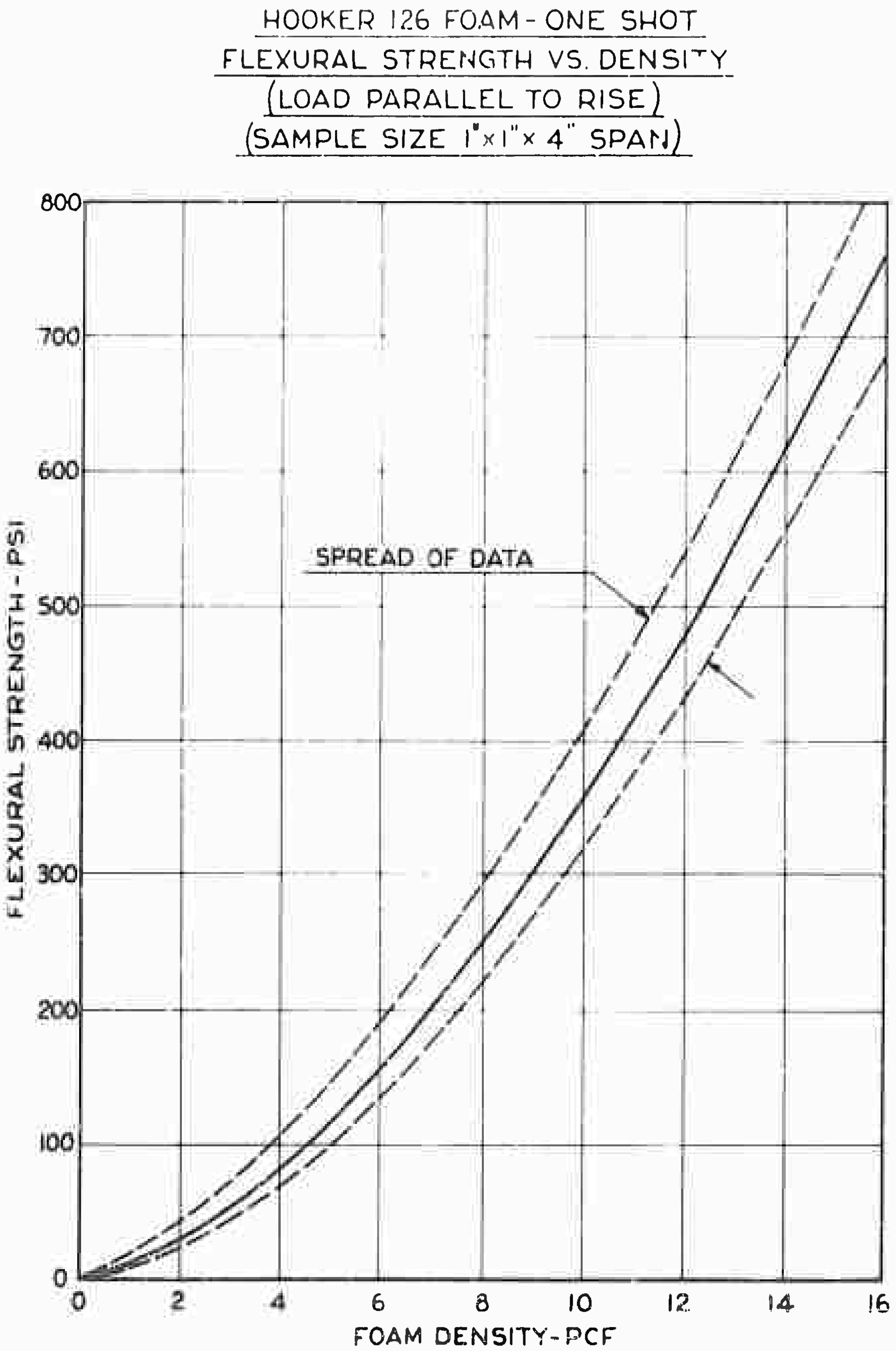
HOOKER 126 FOAM - ONE SHOT
FLEXURAL STRENGTH VS. DENSITY
(LOAD PARALLEL TO RISE)
(SAMPLE SIZE 1"x1"x 4" SPAN)
SPREAD OF DATA
FLEXURAL STRENGTH - PSI
FOAM DENSITY - PCF
0
100
200
300
400
500
600
700
800
2
4
6
8
10
12
14
16

Figure 20

HOOKER 126 FOAM - ONE SHOT
FLEXURAL MODULUS VS. DENSITY
LOAD PARALLEL TO RISE
SAMPLE 1"×1"×4" SPAN

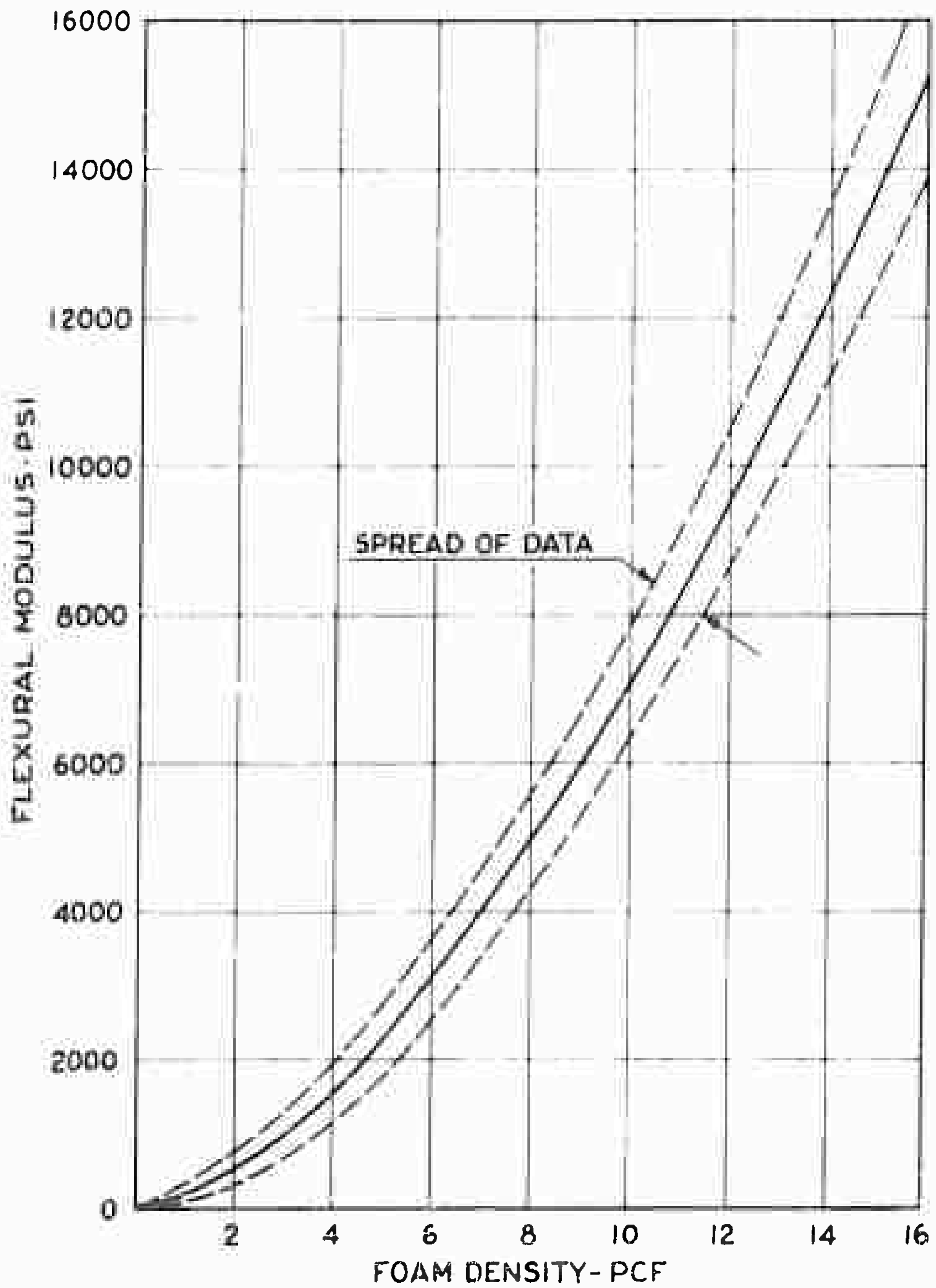

Figure 21

DEFLECTION OF 1" x 1" SPECIMENS AT MID-POINT OF 8" SPAN
FLEXURAL STRESS EQUIVALENT TO 25% OF ULTIMATE STRENGTH

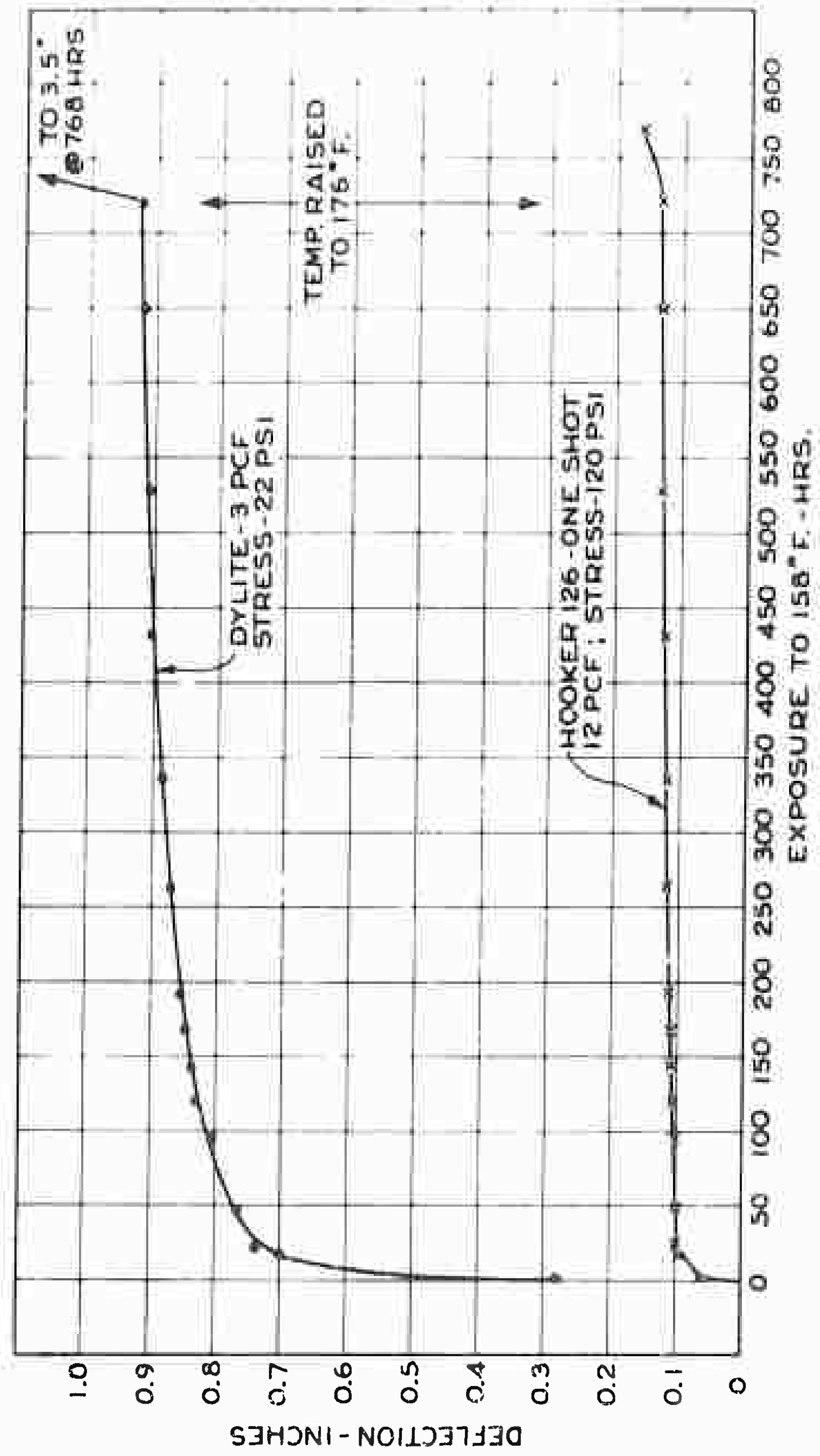

Figure 22

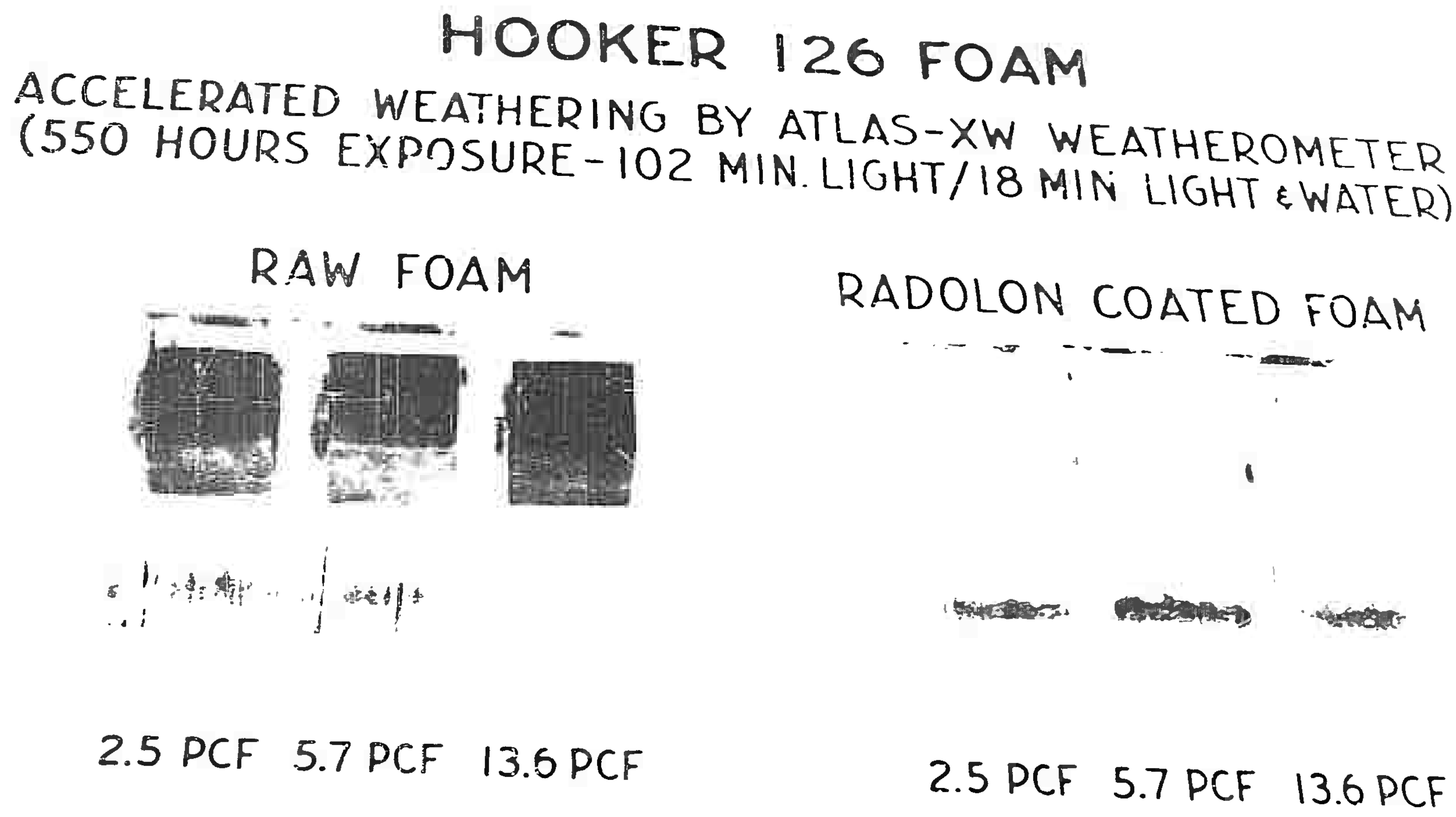
HOOKER 126 FOAM
ACCELERATED WEATHERING BY ATLAS-XW WEATHEROMETER
(550 HOURS EXPOSURE-102 MIN. LIGHT/18 MIN LIGHT & WATER)
RAW FOAM
RADOLON COATED FOAM
2.5 PCF 5.7 PCF 13.6 PCF
2.5 PCF 5.7 PCF 13.6 PCF

Figure 23

DENSITY (lb/ft^3) (HOOKER 126 FOAM)	8500 Mcps Tan δ	8500 Mcps ∈	3000 Mcps Tan δ	3000 Mcps ∈	1000 Mcps Tan δ	1000 Mcps ∈
2.5	0.00065	1.040	0.00053	1.040	0.00038	1.[illegible]4
6.7	0.00162	1.100	0.00159	1.1[illegible]	0.00159	1.[illegible]
13.6	0.0026	1.24 ±0.015	0.0029	1.24	0.0026	1.2[illegible]
	10,000 Mcps Tan δ	10,000 Mcps ∈	3000 Mcps Tan δ	3000 Mcps ∈	1000 Mcps Tan δ	1000 Mcps ∈
POLYETHYLENE (ALATHON)	0.0004	2.25	0.0003	2.25	<0.0004	2.25
POLYTETRAFLUOROETHYLENE (TEFLON)	0.00037	2.08	0.00015	2.1	<0.0002	2.1
POLYSTYRENE (SHEET STOCK)	0.00043	2.54	0.00033	2.55	<0.0007	2.56
STYROFOAM 103.7	0.00015	1.03	0.0001	1.03	<0.0002	1.03

TABLE II POLYURETHANE FOAM – DIELECTRIC DATA @ 1000, 3000 & 8500 Mcps

DENSITY (lb / ft³) (Hooker 126 Foam)		24,000 Mcps						
		ϵ_1			ϵ_2			Tan δ
		PARALLEL TO FOAM RISE			PERPENDICULAR TO FOAM RISE			*
Measured	Nominal	FACE 1	FACE 2	AVG	FACE 1	FACE 2	AVG.	
10.25	12.5				1.180	1.179	1.180	
10.29	12.5				1.179	1.180	1.180	.0024
10.38	12.5	1.179	1.179	1.179				
10.09	12.5	1.178	1.174	1.176				
24.81	25.8				1.439	1.443	1.441	.0048
26.38	25.8				1.457	—	1.457	
25.32	25.8	1.442	1.444	1.443				
24.45	25.8	1.399	1.428	1.414				
33.18	33.0				1.592	1.591	1.592	
32.69	33.0				1.578	1.575	1.577	
33.08	33.0	1.612	1.623	1.618				
34.34	33.0	1.603	1.616	1.610				.0063

* LOSS TANGENTS WITHIN EACH GROUP ARE WITHIN 5% OF VALUES SHOWN.

TABLE III RIGID POLYURETHANE FOAM — DIELECTRIC DATA @ 24,000 Mcps (EFFECT OF SPECIMEN ORIENTATION WITH FOAM RISE DIRECTION).

NUCLEAR THERMAL AND RADIATION EFFECTS ON RADOME MATERIALS

H. S. Schwartz
Wright Air Development Center
Wright Patterson Air Force Base, Dayton, Ohio

ABSTRACT

The effect of simulated nuclear thermal radiant energy environment on conventional and heat resistant radome laminate materials of polyester, TAC polyester, epoxy, silicone, and phenolic glass fabric base construction was evaluated by dynamic mechanical property tests and visual observation. The effect of nuclear gamma radiation on laminate and sandwich materials was evaluated by mechanical and electrical property tests after and during irradiation.

INTRODUCTION

The utilization of nuclear energy for destructive purposes, such as nuclear weapons, and for constructive purposes, such as power reactors, introduces new exposure environments which must be considered by materials and systems engineers. The information presented herein shows the effect of exposure environment on the materials properties, as compared to reference properties of unexposed materials. It is intended that the data will provide information on the environmental limitations for materials and on the selection of appropriate materials.

The materials evaluated were conventional polymeric type radome materials, such as glass fabric base plastic laminates, alkyd-isocyanate foam core, foam core plastic sandwich, white reflective coatings, and rain erosion resistant coatings.

One exposure environment was thermal radiant energy having spectral energy distribution simulating the actual conditions (assumed to be 6000°K) and having parameters of intensity and time over a square wave pulse. The exposure environment representing nuclear power reactors was gamma radiation, rather than a mixed gamma and neutron flux which actually occurs. However, the physical and electrical changes in structural plastics which result from gamma radiation and fast neutron irradiation are quite similar on the basis of energy absorbed, and, therefore, a radiation effects program performed in a gamma field reflects the behavior of a material exposed to a mixed radiation environment. Time of exposure was the variable parameter for the gamma radiation environment.

A. Thermal Radiation Evaluation

In conducting the laboratory program to evaluate plastic laminates and surface coatings under simulated environmental conditions of high intensity thermal radiation, the independent variables, test parameters, and evaluation criteria were established to provide data which would be useful, not only for aircraft radomes, but also for other related applications, such as ground radomes.

The independent variables were material construction and thickness, and tensile stress levels in per cent of ultimate tensile strength. Variable parameters were reinforcement orientation, laminating resin, surface coatings, and radiant energy intensity. The evaluation criteria were mechanical and physical degradation, expressed in time and quantity of radiation required to cause failure or damage of mechanically stressed and unstressed specimens.

All thermal radiation tests were conducted at the facilities of the Materials Laboratory, Directorate of Laboratories, Wright Air Development Center, Wright-Patterson Air Force Base, Ohio.

The primary objective of this program was to determine the effects of high intensity thermal radiation on the mechanical properties of plastic sandwich materials of the types used in aircraft radomes.

It was apparent that the outer skin of the plastic sandwich, being the exposed surface, was a critical sandwich component (the skin-to-core bond also can be critical), and therefore, it was decided to conduct tests on thin plastic laminates about 0.035-0.040 inch thick,

representative of laminate skins used in aircraft radomes. The materials tested were all typical glass-fabric base plastic laminates differing principally in the laminating resin used. The laminates, designated according to resin, consisted of a conventional polyester (Polylite 8000), a heat-resistant phenolic (CTL-91LD), a silicone (DC-2106), a triallyl-cyanurate polyester (Vibrin 135), and a heat-resistant epoxy (X-131, now known as Epon 1310).

The polyester laminate was evaluated in three different forms: "as received"; surface to be exposed coating with a rain-erosion resistant coating (designated as Polylite 8000-1); and, surface to be exposed coated with a white thermally reflective coating applied over the rain-erosion coating (designated as Polylite 8000-2). (The two suffix designations were used for reference purposes and are not manufacturer's designations). In addition, a series of tests were run on specimens of each material painted black to evaluate strength under equivalent heat absorption; the use of the black paint was merely a test expedient. The materials evaluated were not necessarily formulated or constructed to withstand the extremely severe environmental test conditions to which they were subjected and therefore any data reported on them should not be construed as reflecting on their quality or performance under normal conditions.

The polyester laminates were made with Style 112 glass fabric and the others with Style 181 glass fabric. A description of the laminates, including component materials and fabrication procedure, is given in Table I. A description of the coatings used on the Polylite 8000 and of a white rain erosion coating evaluated for absorption and degradation is given in Table II.

1. Mechanical Property Tests

Ultimate tensile strength was selected as the mechanical property criterion for determining the resistance of the materials to degradation by thermal radiation. The size and configuration of the tensile test specimens were in accordance with Federal Specification L-P-406b, "Plastics, Organic: General Specifications, Test Methods", Method 1011, Type 2, which specifies a gauge section 1/4 inch wide and 2 1/4 inches long. For the initial series of tests, the specimens were machined with their longitudinal axis parallel to the fabric warp. This is common practice in determining design data on plastic laminates. However, in thermal radiation tests, resin degradation was partially masked by the continuity of the load bearing capability of the glass fabric. Therefore, subsequent tests were made on specimens having their longitudinal axis at 45 degrees to the warp, so the resin and resin-to-glass bond supported the load.

The test procedure used for each material was follows: A room temperature, ultimate tensile strength control value was determined by testing five random specimens from the same panel and averaging the test values. The control tensile strength data are shown in Table III. The remaining specimens were randomly arranged into groups of five specimens each, each group to be irradiated under stress with a stress level within the range of 20 to 60% of ultimate, at increments of 10% stress. Tensile stress was applied by a Cal-Tester, an electric motor driven hydraulic test machine, which applies load in the horizontal direction. A photograph of the radiant energy source is shown in Figure 1, and a photograph of the Cal-Tester in operation is shown in Figure 2. For each material, two series of

tests were conducted, one at an intensity of 25 cal./cm^2-second, and the other at 10 cal./cm^2-second. For a given series of tests on a material, the radiation intensity was held constant, and the time required to cause ultimate tensile failure at a particular stress level was determined. In this manner, plots of "time required to cause failure" versus "stress level, percent of control ultimate" were obtained. The effect of radiation intensity on total incident energy (intensity multiplied by time of exposure) required to cause failure for different stress levels is shown in similar plots. These data obtained are presented graphically in Figures 3 and 4 for "parallel-to-warp" specimens and Figure 5 for "45 degree to warp" specimens. In addition, Figure 6 shows failure time versus absolute stresses for "45 degree to warp" specimens. In addition, 45° to warp tensile specimens were painted black to equalize energy absorption, and the failure time was determined at 30% pre-stress, using three radiation intensities, 1, 5 and 10 cal./cm^2-second. The results are shown in bar graph form in Figure 7. The time required to cause ultimate failure was determined experimentally in the following manner: For a given group of five specimens (at a particular stress level), one specimen was selected to be exposed for an arbitrary time period, say five seconds. Depending on whether the specimen failed or did not fail, the exposure time was respectively decreased or increased until about 5% of the representative time separated the failure time from the no-failure time. The two closest failure, no-failure times were then averaged to yield the representative failure time for the particular stress level.

2. Visual Degradation Tests

The threshold level in terms of time and total incident energy required for visual degradation of the materials was determined experimentally by a method similar to that described above. In addition to the laminates, a white rain erosion resistant coating of the neoprene type (Gates KV-9431) was also evaluated.

The laminate specimens were one inch in diameter and were placed in a special wedge type specimen holder, so that the specimen was supported at only two points on its edge, to minimize heat transfer from the specimen to the holder.

Tests were conducted at radiation intensities of 10 cal./cm^2-second and 25 cal./cm^2-second. Evaluation criteria were: (1) first visible discoloration or degradation, (2) charring, and (3) ignition or delamination. Data were taken in terms of time required to cause degradation and were converted to total incident energy values by multiplying by radiation intensity. Test results are shown in Table IV.

3. Determination of Absorptivity of Radiant Energy From a 6000°K Black Body

The determination of absorptivity for all test materials, including the coated Polylite 8000 and the KV-9431 white rain erosion coating, was computed from experimentally determined spectral values of reflectance and transmittance over the region of 0.4 to 2.0 microns, and the theoretical curve of spectral energy distribution from a 6000°K black body, which closely approximates the carbon arc source.

A graphical illustration of the method of calculation is shown in Figure 20.

The energy below 0.4 microns and above 2.0 microns was not included in the absorptivity computations because of difficulty in obtaining spectral reflectance data in these regions. Fortunately, the energy outside these limits is very small compared to the total energy emitted by the carbon arc source, and therefore the absorptivity data are considered valid for engineering purposes.

Values of integrated normal incidence absorptivity computed for the materials are shown in Table V. Spectral values of reflectance and transmittance for the test materials are shown in Figures 8 through 19.

4. Radar Transmission Through Coated Laminates

The radar transmission coefficient at 9375 megacycles, phase delay, and surface resistivity for 0.050" thick glass fabric base polyester laminates coated with KV-9431 white rain erosion coating was determined directly after application, after 3 months weathering, and after 6 months weathering. Results are shown in Table VI.

5. Radiant Energy Equipment

The radiant energy source was a Mitchell Process Projector utilizing a carbon arc. A photograph of the source is shown in Figure 1. The power supply for the arc was a 30 KW direct current generator with variable resistors to adjust the current between 150 and 225 amperes. The radiant energy beam was focused through two sets of quartz lenses. The maximum uniform intensity obtained was 25 cal./cm^2-second over a spot one inch in diameter. For tests at lower intensities, the radiant energy beam was attenuated to the desired value by interposing screens between the lenses, by reducing the current, or a combination of both.

Two sets of shutters were used to control the exposure duration. The first shutter, called the "douser", was a water-cooled copper plate operated by a rotary solenoid switch. This shutter, placed between the arc source and the first lens system, was the "coarse" control and opened first, followed by the opening of the second shutter, which accurately controlled the exposure duration to $\pm$0.05 seconds. The second shutter, placed between the two lens system, consisted of blades rotatable in opposite directions to a maximum of 90 degrees. The shutter control apparatus was an electronic timing circuit whose central control was a digital type preset counter which was used to set the time period during which the shutters remained open. In operation, the desired time interval was obtained by setting the counter on a certain digital combination, and pressing a starter switch. The shutter blades then automatically opened and closed at the correct time. The timing cycle was such that an essentially "square wave" pattern of intensity versus time was achieved.

The radiometer used to determine the radiant energy intensity received by the test specimen was a water-cooled calorimeter type obtained from the U. S. Naval Radiological Defense Laboratory in San Francisco, California. It consisted of a blackened copper disc energy receiver with a thermocouple connected to the back surface of the disc. The disc was inclosed in a housing in which cooling water was circulated in contact with the back of the disc.

6. Test Results and Conclusions

a. The results of tensile strength tests on laminate specimens at 45 degrees to the warp give a better indication of resin strength degradation than do tensile strength tests parallel to the warp.

b. For uncoated materials, tested in tension at 45° to the warp, using pre-stresses at various percentages of the room temperature strength of the material, the following results were noted: (1) The DC-2106 silicone and the X-131 epoxy had the highest failure time, with the X-131 being better than the DC-2106 at the higher pre-stresses; and (2) On the basis of absolute stress, the X-131 laminate was better mechanically than the other materials tested.

c. For the materials painted black (to produce equal energy absorption), tested at 45° to the warp, at 1, 5 and 10 cal./cm^2-second, and stressed at 30% of the control strength, the following results were obtained: (1) At 1 cal./cm^2-second, the DC-2106, CTL-91LD, and Vibrin 135 materials had very close to the same failure times, respectively 4.8, 4.6 and 4.7 seconds. The X-131 was slightly lower, 4.0 seconds and Polylite 8000 much lower, 1.7 seconds; (2) At 5 cal./cm^2-second, the CTL-91LD and DC-2106 had the highest failure time, 4.2 and 3.9 seconds respectively. The Vibrin 135 was somewhat lower, 3.3 seconds, and the X-131 dropped sharply to 1.5 seconds; (3) At 10 cal./cm^2-second, the CTL-91LD material had the highest failure time; and (4) The results indicate that the relative merits of the materials depend considerably on the rate of energy input.

d. The data from visual degradation tests indicate that the incident energy required to cause visually observable degradation depends more on energy absorption properties than on mechanical strength at high temperatures, except to a certain extent for the DC-2106 silicone material.

B. Nuclear Radiation Evaluation

The materials properties used as criteria in evaluating effects of nuclear radiation were mechanical properties consisting of ultimate strength

and modulus of elasticity and electrical properties consisting of dielectric constant and loss tangent at 8.5 KMC.

Three evaluation phases were conducted as follows:

Phase One - Specimens were exposed at normal temperature in the spent fuel gamma facility at the Materials Testing Reactor, National Reactor Testing Station, Idaho Falls, Idaho. Following exposure to a specified radiation dosage, the specimens were removed from the exposure and tested for the appropriate property.

Phase Two - Specimens for electrical property tests were exposed to gamma radiation from a Cobalt 60 source, and the dielectric constant and loss tangent at 8.5 KMC were monitored during the exposure period.

Phase Three - Specimens for mechanical property tests were exposed up to 200 hours at 500°F and simultaneously to gamma radiation from a Cobalt 60 source, followed by mechanical testing at 500°F.

1. Materials Evaluated

The materials evaluated were 1/8 inch thick glass-fabric base plastic laminates having polyester, heat-resistant polyester, phenolic, epoxy, and silicone resin binders; sandwich construction consisting of glass-fabric reinforced polyester resin laminate faces and alkyd-isocyanate foam core; and alkyd isocyanate foam core without face material. A description of the component materials and fabrication procedures as reported by the manufacturers are given in Table VII.

2. Evaluation Program - Phase 1

a. Radiation Source and Exposure Conditions - The gamma facility at the MTR is a rack at the bottom of a water canal 20 feet deep

around which is placed spent fuel elements from the reactor. The gamma flux in this facility is extremely variable ranging between 3×10^7 r/hr to 5×10^5 r/hr depending on the length of time the fuel elements have been out of the reactor. The average gamma energy is estimated to be in the range of 0.7 to 1.2 Mev.

The laminate samples included in this phase of the study were exposed to radiation dosages of 6.2×10^7, 7.9×10^7, 2.94×10^8, and 9.48×10^8 roentgens. The foam sandwich samples were exposed to radiation dosages of 6×10^7, 8.2×10^7, 3×10^8, and 1×10^9 roentgens. Mechanical tests were performed on control (no exposure) samples and samples exposed to each of the above dosages.

b. Mechanical Property Tests - The following tests were run on each of the laminate materials; ultimate flexural strength, ultimate tensile strength, ultimate compressive strength, and flexural modulus of elasticity. These properties were also determined on samples which were irradiated and then immersed in boiling water for two hours. For those laminates made with heat-resistant resins, additional tests were made at 500°F after exposure to this temperature for 1/2 hour and 200 hours.

Tensile specimens were 3/4-inch wide and 9-inches long and corresponded to the Type II specimen under Method 1011 of Federal Specification L-P-406b, "Plastics, Organic; General Specifications, Test Methods". The specimens were tested using Templin tension grips, with a testing machine head speed of 0.2 inch per minute.

Compression specimens were 1/2-inch wide and 3 1/8-inches long, and were restrained from buckling by means of a supporting jig as

described in Method 1021 of Federal Specification L-P-406b. Load was applied at a testing machine head speed of 0.05 inch per minute.

Flexural specimens were 1-inch wide and 4-inches long. These specimens were tested flatwise by center loading over a span of 2 inches. Load was applied at a testing machine head speed of 0.025 inch per minute and load deflection data were obtained.

The foam sandwich material was subjected to two tests; ultimate flexural strength and flatwise compressive strength. The flexural specimens were 1 1/2-inches wide and 4-inches long. These samples were tested flatwise by center loading over a three inch span. Load was applied at a testing machine head speed of 0.05 inch per minute and maximum load was determined.

The foam sandwich compression specimens were 2 inches by 2 inches and the load was applied in the flatwise direction at a head speed of 0.01 inch per minute. The compressive strength at 10% strain was determined.

The data obtained on the laminate specimens and foam sandwich specimens are presented in Tables VIII and IX respectively.

c. Discussion of Results of Mechanical Property Tests - Analysis of the data on the glass fabric reinforced plastic samples reveals that the mechanical properties of only one sample material is adversely affected by gamma irradiation to a dosage of 9.48×10^8 roentgens. The Epon 1001 laminate material reaches a radiation threshold at 6×10^7r and the mechanical properties of this material fall off very rapidly when this dosage is exceeded. Irradiation increases the strength of the Vibrin 135 laminate when tested at 500°F after being subjected to 500°F for 1/2 hour. However, this increase was not present after 200 hours conditioning at 500°F.

Within the statistical limits of the test results, the mechanical properties of the rest of the materials can be represented by straight horizontal lines, showing no appreciable radiation damage.

The foam sandwich samples showed no reduction in mechanical properties at dosages up to 1×10^9 roentgens.

d. Electrical Property Tests -

(1) Samples - The test specimens used in this series of tests were cylindrical laminates and foam samples 1.000± .002 inch in diameter. Triplicate cylindrical specimens of polyester, heat resistant polyester and alkyd-diisocyanate foam were prepared 0.400, 0.450, and 0.500 inches thick. The dielectric constant and loss tangent were determined on control (no exposure) specimens and on specimens irradiated to dosages of 3.0×10^8 and 1.0×10^9 roentgens at the MTR gamma facility.

(2) Test Equipment - Measurements of microwave dielectric constant and loss tangent were made with a modified microwave dielectrometer, Model #1, manufactured by the Central Research Laboratories, Inc., Redwing, Minnesota. This instrument consists of a slotted circular wave guide equipped with a precision positioning probe type pickup, a probe output amplifier and a square wave modulated klystron capable of oscillating at 8.5 kilomegacycles per second.

(3) Results - The data obtained from this series of tests are presented in Table I. At first, it would appear that there is a slight affect on the dielectric constant and loss tangent due to radiation. The dielectric constant and loss tangent, however, are inverse functions of resin content and when this parameter is considered, it appears that the effect may be a result of varying resin content. In any case, however, it

can be concluded that there is no significant change of electrical properties as a function of radiation dosage.

3. Electrical Property Evaluation Program - Phase 2

a. Radiation Source and Exposure - The 1500 curie Cobalt 60 source located at Wright Air Development Center was used in this study. The available flux in this facility was 4.3×10^5 r/hr with an average gamma energy of 1.25 Mev. Exposures up to approximately 5.0×10^7 roentgens were made.

b. Materials and Property Evaluated - The materials evaluated were Selectron 5003 polyester, Epon 1001/Plyophen 5023 epoxy-phenolic, Epon 1001 epoxy, Epon 828 epoxy, Vibin 135 triallyl-cyanurate polyester, and CTL-911D phenolic. The evaluation property was dielectric constant at 8.5 KMC.

c. Results - The primary purpose of these dynamic electrical tests was to determine if the ion buildup in these materials during irradiation would cause a significant change in their electrical properties. The results show conclusively that the presence of a high intensity gamma flux does not alter these characteristics. Graphs of dielectric constant versus exposure, roentgens show essentially a horizontal straight line.

4. Elevated Temperature Irradiation - Phase 3

a. Radiation Source and Exposure - The 1500 curie Cobalt 60 source at WADC was used in conjunction with an electrical resistance type furnace operating at 500°F. Flexural and compression specimens were placed inside the furnace and exposed simultaneously to 500°F and a gamma flux of 5×10^5 roentgen/hr for periods of 50, 100, and 200 hours. Control specimens

were exposed at room temperature without irradiation and at room temperature with irradiation for 200 hours, and at 500°F for 50, 100, and 200 hours without irradiation.

b. Test Materials and Test Procedures - The test materials were 1/8 inch glass fabric base laminates made with CTL-91LD phenolic, X-131 (now Epon 1310) epoxy, and DC-2104 silicone resins. A detailed description of the materials and cure cycle is given in Table XI. The CTL-91LD and DC-2104 materials were evaluated for ultimate flexural strength and flexural modulus of elasticity, and the X-131 material for ultimate compressive strength only. All of the test specimens which were exposed to the concurrent radiation and high temperature environment were tested at 500°F.

C. Test Results

The test results for control specimens and irradiated 500°F exposed specimens are shown in Table XI. The most significant results noted are, that for the CTL-91LD phenolic, the mechanical properties at 500°F after simultaneous radiation and 500°F exposure were considerably higher than after 500°F without irradiation. This effect is most pronounced, comparatively, after 100 hours exposure.

In general, for the X-131 and DC-2104 materials, there was little difference in the mechanical properties of non-irradiated and irradiated 500°F exposed specimens. However, for the DC-2104, after 200 hours exposure at 500°F, the irradiated specimens had only about 70% of the strength of the non-irradiated specimens. For the X-131 material exposed to 500°F, the irradiated specimens were slightly stronger than the non-irradiated specimens after 100 hours and 200 hours exposure.

SUMMARY

Structural plastic materials have been used extensively in recent years for a variety of applications and under a wide range of environments. Current and projected applications include additional environmental conditions such as intense thermal and nuclear energy exposures. In order to determine the usefulness of structural materials under such conditions, extensive materials evaluation is required. Then, as materials deficiencies are found, new materials can be developed to include improved properties. In the evaluation studies presented, reinforced plastic materials have shown outstanding properties which should be extremely useful in many types of advanced applications including those applications in which high intensity energies are imposed on the structural materials.

TABLE I

DESCRIPTION OF TEST MATERIALS

Test Material Variable	Polylite 8000 (Note 1)	CTL-91LD	DC-2106	Vibrin 135	X-131
	TEST MATERIAL DESIGNATED ACCORDING TO LAMINATING RESIN				
A. Component Materials					
Glass Fabric Desig.	#112	#181	#181	#181	#181
Fabric Finish	Volan A	Volan A	Heat Cleaned	[illegible]	Volan A
Number of Plies	8	4	4	4	-
Fabric Layup	Parallel	Parallel	Parallel	Parallel	Parallel
Catalyst	Benzoyl Peroxide	———	———	Benzoyl Peroxide 1.0% by wt.	BF_3-400, 1% by wt.
Resin Content, Avg.%, by wt.	40.0	28.0	31.0	40.0 ± 1.5	———
Resin Supplier	Reichhold Chemicals	American Reinforced Sales	Dow Corning	Naugatuck Chemical Company	Shell Development Company
B. Cure Cycle					
Pressure, psi	30	200	40	25	Contact 9.5 min; 100 psi 50.5 min.
Temperature (°F)	190	260	350	158 176 194 ALLOWED TO COOL IN PRESS	330°F 60 min total ALLOWED TO COOL IN PRESS
Time at Cure Temp., min.	90	30	30	60 60 120	
Postcure Cycle	None	24 hrs each at 250°, 300°, 350°	10 hrs each at 195 -485°F plus 12 hrs at 485°F	60 min. each at: 300, 400, 420, 440, 460, 480°F followed by 3 hrs at 500°F	3 hrs at 400°F
C. Test Panels					
Quantity Used	3	10	2	2	2
Panel Size	24" x 24"	10" x 10"	24" x 24"	23" x 23"	18" x 24"
Nominal Thickness, in.	0.035	0.038	0.039	0.040	0.035

Note 1 - Polylite 8000-1 and Polylite 8000-2 are Polylite 8000 coated respectively with (1) rain erosion coating (2) white thermally reflective coating applied over the rain erosion coating. A description of the coatings and their method of application is given in Table II.

TABLE II

DESCRIPTION OF COATINGS

Property or Variable	COATINGS APPLIED TO POLYLITE 8000: Rain Erosion Coating	COATINGS APPLIED TO POLYLITE 8000: Thermally Reflective White Coating	WHITE RAIN EROSION RESISTANT COATING
Manufacturer Designation	23-56S	PV-100 with B-100 Topcoat	KV-9431
Manufacturer	Goodyear Tire & Rubber Company, Akron, Ohio	Vita-Var Corp. Newark, N. J.	Gates Engineering Company Wilmington, Delaware
Chemical Type	Neoprene	Silicone-Alkyd	Neoprene with Titanium Dioxide Filler
Prime Coat	Bostik 1007	Rain Erosion Coating 23-56S	Gaco KT 6006-[illegible]
Thickness of Prime Coat, inches	0.0015	0.009	0.003
Total Coating Thickness, inches	0.009	0.017	0.013-0.015
Remarks	Prime coat brushed on, dried, followed by required number of spray coats of rain erosion coating to attain 0.009" total thickness. Coating allowed to dry 30 days prior to test so that normal darkening would occur.	Light coat of shellac applied over rain erosion coating to prevent "bleeding" of rain erosion coating into white coating to be subsequently applied. White coating (PV-100) sprayed on followed by spray coat of B-100 clear coating.	Solvent wiped laminate with toluene or heptane, followed by light sanding and solvent wipe. Prime coat brushed on, allowed to dry, and top coat brushed on in sufficient application to achieve desired thickness.

TABLE III

ULTIMATE TENSILE STRENGTH CONTROL VALUES FOR LAMINATES

Material Designation		Ultimate Tensile Strength, psi* Parallel to Warp	At 45° to Warp
Polylite 8000.	Panel A	24,800	17,300
	Panel B	27,800	19,900
	Panel C	33,800	
CTL-91LD		41,600	24,630
DC-2106:	Panel A	30,800	—
	Panel B	32,500	—
	Panel C	—	9920
Vibrin 135		—	17,960
X-131	A	—	19,200
	B	—	21,200

*Average of five tests

TABLE IV

CRITICAL ENERGY OF LAMINATES USING VISUAL OBSERVATION AS CRITERIA

Material Designation	ENERGY, Cal./cm^2 AT SPECIFIED RADIATION INTENSITY (Cal./cm^2-second)											
	DISCOLORATION				SCORCH		CHAR		IGNITION	
	10 Incident	25 Incident	10 Absorbed	25 Absorbed	10	25	10	25	10	25
					INCIDENT ENERGY					
Polylite 8000	50	25	14.0	7.0	90	100	—	—	150	150
DC-2106	30	25	16.0	13.5	90	75	120	150	—	—
CTL-911D	40	2.5	34.0	2.1	—	—	60	25	—	62.5
Vibrin 135	40	37.5	21.2	19.8	42	40	50	42.5	—	77.5
E-131	40	30.0	25.2	18.9	50	32.5	60	40	70	[illegible]
KV-9431 Coating*	18	—	2.6	—	—	—	24	—	—	—

*White Rain Erosion Resistant Coating Applied Over Glass Fabric Base Polyester Laminate

TABLE V

ABSORPTIVITY FROM A 6000°K BLACK BODY REPRESENTING CARBON ARC SOURCE

MATERIAL	ABSORPTIVITY
Polylite 8000	0.279
Polylite 8000-1 (Note 1)	0.728
Polylite 8000-2 (Note 1)	0.118
DC-2106	0.549 0.527 0.538 Average
CTL-91LD	0.863 0.838 0.850 Average
Vibrin 135	0.529
X-131	0.631
KV-9431 Coating: Normal Conditioning	0.145
After 6 months outdoor weathering	0.209

Note 1 - Absorptivities of coated Polyester materials are for the coated surfaces.

TABLE VI

RADAR TRANSMISSION PROPERTIES FOR POLYESTER LAMINATE [illegible] WITH EY-9471 WHITE COATING

Incidence Angle	UNCOATED PANEL		AFTER COATING WITH EY-9471							
			UNWEATHERED			AFTER 3 MOS. WEATH.		AFTER 6 MOS. WEATH.		
	Absolute Trans., %	Phase Delay, Degrees	Relative Trans., %	Phase Delay Degrees	Surface Resistivity, Ohms	Relative Trans., %	Phase Delay, Degrees	Relative Trans., %	Phase Delay, Degrees	Surface Resistivity Ohms
0°	86.0	21.0	92.[illegible]	25.7		92.1	26.4	93.6	25.[illegible]	
20°	86.5	30.9	92.3	22.9	[illegible] 10^9	94.0	25.0	94.0	25.9	186 x 10^9 ± 17 x 10^9
30°	88.5	20.5	94.7	25.1		96.0	26.4	96.0	25.5	

TABLE [illegible]

[illegible] MATERIALS [illegible]

[illegible]	[illegible]	[illegible]	[illegible]	[illegible]	[illegible]	[illegible]	[illegible]	[illegible]	[illegible]	[illegible]	Specific Gravity
[illegible]	[illegible] Polyester	[illegible] Peroxide	181-Glass Fabric	[illegible]						[illegible].26	1.82
[illegible]	[illegible] Polyester			[illegible]	[illegible]	[illegible]				3.62	1.97
[illegible]	Epoxy	[illegible]		[illegible]	[illegible]				[illegible]	30.42	1.88
[illegible]	Epoxy	Dicyandi-amide	"		[illegible]5					36.75	1.81
[illegible]	Epoxy-Phenolic	Dicyandi-amide	"	"	[illegible]	[illegible]			[illegible]	29.82	1.71
CTL	Phenolic	None	"	"	2[illegible]	[illegible]		[illegible]	36 36 24	28.92	1.96
[illegible]	Epoxy	BF_3-400	"	"	310 310	[illegible] [illegible]	[illegible] 100	[illegible]0	3	34.5	—
[illegible]	Silicone	DC XY-5	"	None	3[illegible]5	[illegible]	30	480	150	30.0	1.88
[illegible] P-[illegible]	Polyester	Benzoyl Peroxide	"	Volan &	2[illegible]	[illegible]	15	NONE		37.4	1.80
[illegible]	"	"	"	136	250	70	14	NONE		34.36	1.85
[illegible]	"	"	"	"	225	20	[illegible]	NONE		35.7	1.82
Lockfoam [illegible]	Polyurethane				120	30		250	2	10#/ft³ Density	
Lockfoam [illegible] Glass Fabric Laminate Faced Sandwich	Polyurethane				120	30		250	2	" " "	

TABLE VIII MECHANICAL PROPERTIES OF GLASS FABRIC REINFORCED PLASTIC LAMINATES AFTER IRRADIATION.

Exposure	Material	Room Temp. Flexural	Flexural Modulus	[illegible] at 500°F	Room Temp. Tensile	Tensile [illegible]	Tensile [illegible] at [illegible]	[illegible]	Room Temp. [illegible]	[illegible]	[illegible]	[illegible]	[illegible]	[illegible]	[illegible]
CONTROL [illegible]	[illegible] POLYESTER	[illegible]	[illegible]	—	[illegible]	[illegible]	—	—	[illegible]	[illegible]	—	—	[illegible]	[illegible]	[illegible]
CONTROL [illegible]	[illegible]	[illegible]	[illegible]	[illegible]	—	—	—	—	[illegible]	[illegible]	[illegible]	[illegible]	[illegible]	[illegible]	[illegible]
CONTROL [illegible]	[illegible] PHENOLIC	[illegible]	[illegible]	[illegible]	[illegible]	[illegible]	[illegible]	—	[illegible]	[illegible]	[illegible]	[illegible]	[illegible]	[illegible]	[illegible]
CONTROL [illegible]	[illegible]	[illegible]	[illegible]	[illegible]	[illegible]	[illegible]	[illegible]	[illegible]	[illegible]	[illegible]	[illegible]	[illegible]	[illegible]	[illegible]	[illegible]
CONTROL [illegible]	[illegible]	[illegible]	[illegible]	—	[illegible]	[illegible]	—	—	[illegible]	[illegible]	—	—	[illegible]	[illegible]	[illegible]
CONTROL [illegible]	[illegible]	[illegible]	[illegible]	—	[illegible]	[illegible]	—	—	[illegible]	[illegible]	—	—	[illegible]	[illegible]	[illegible]
CONTROL [illegible]	[illegible] POLYESTER	[illegible]	[illegible]	[illegible]	[illegible]	[illegible]	—	—	[illegible]	[illegible]	[illegible]	[illegible]	[illegible]	[illegible]	[illegible]
CONTROL [illegible]	[illegible] POLYESTER	[illegible]	[illegible]	[illegible]	[illegible]	[illegible]	—	—	[illegible]	[illegible]	[illegible]	[illegible]	[illegible]	[illegible]	[illegible]
CONTROL [illegible]	[illegible]	[illegible]	[illegible]	—	—	—	—	—	[illegible]	[illegible]	—	—	[illegible]	[illegible]	[illegible]

THE VALUES IN THIS TABLE REPRESENT THE AVERAGE VALUE OF FIVE SPECIMENS IN 10^3 PSI. THE STANDARD DEVIATION IN 10^3 PSI WITH THE EXCEPTION OF THE FLEXURAL MODULUS, WHICH IS IN 10^6 PSI.
EXPOSURE IS IN ROENTGENS

TABLE IX

MECHANICAL PROPERTIES OF ALKYD-ISOCYANATE FOAM SANDWICH AFTER EXPOSURE AT VARIOUS RADIATION LEVELS

EXPOSURE, ROENTGENS	NO. OF SPECIMENS	ULTIMATE FLEXURAL STRENGTH, LBS/IN. WIDTH		NO. OF SPECIMENS	FLATWISE COMPRESSIVE STRENGTH PSI AT 10% STRAIN	
		RANGE	AVERAGE		RANGE	AVERAGE
0	3	319–320	320	2	168–186	177
6×10^7	3	328–356	344	3	180–205	193
8.2×10^7	3	321–335	330	3	182–197	189
3×10^8	3	321–336	328	3	174–194	184
1×10^9	3	303–358	324	3	189–200	196

TABLE X

DIELECTRIC CONSTANT AND LOSS TANGENT AT 8.5 KMC/s OF FOUR MATERIALS
BEFORE AND AFTER EXPOSURE TO GAMMA RADIATION

SAMPLE IDENTIFICATION	SAMPLE NO.	DIELECTRIC CONSTANT	LOSS TANGENT	RESIN CONTENT	WT. IN GRAMS	SPECIFIC GRAVITY	CONDITION
Selectron 5003-Laminate	1	4.055	.0097	39.83	9.0030	1.746	25°C, Control
	2	4.113	.0120	39.93	10.1770	1.756	
	3	4.129	.0125	39.49	11.2911	1.755	
Selectron 5003 Laminate	4	4.058	.0109	40.25	8.9468	1.739	25°C, 3 x 10^8 Exposure
	5	4.156	.0131	39.86	10.1640	1.759	
	6	4.155	.0124	39.45	11.3137	1.749	
Selectron 5003 Laminate	7	4.292	.0159	37.61	9.4280	1.841	25°C, 1 x 10^9 Exposure
	8	4.363	.0115	36.98	10.7201	1.858	
	9	4.386	.0114	36.89	11.8918	1.856	
Laminac 4202 Laminate	1	4.237	.0110	37.67	9.4557	1.835	25°C, Control
	2	4.305	.0127	37.19	10.6017	1.831	
	3	4.285	.0134	37.09	11.8868	1.846	
Laminac 4202 Laminate	4	4.280	.0113	36.32	9.4612	1.846	25°C, 3 x 10^8 Exposure
	5	4.297	.0123	37.42	10.6807	1.851	
	6	4.352	.0107	37.01	11.9249	1.860	
Laminac 4202 Laminate	7	4.455	.0165	37.37	9.5881	1.867	25°C, 1 x 10^9 Exposure
	8	4.426	.0133	37.40	10.6996	1.851	
	9	4.453	.0148	36.99	11.7938	1.843	
Alkyd-Isocyanate Foam	1	1.188	.0019	——	0.7517	0.1459	25°C, Control
	2	1.191	.0023	——	0.8499	0.1468	
	3	1.182	.0008	——	0.9724	0.1512	
Alkyd-Isocyanate Foam	4	1.218	.0040	——	0.8405	0.1632	25°C, 3 x 10^8 Exposure
	5	1.203	.0031	——	0.8647	0.1500	
	6	1.201	.0031	——	0.9579	0.1497	
Alkyd-Isocyanate Foam	7	1.208	.0038	——	0.7898	0.1532	25°C, 1 x 10^9 Exposure
	8	1.207	.0044	——	0.8995	0.1553	
	9	1.208	.0040	——	0.9976	0.1552	
Vibrin 135 Laminate	1	4.325	.0130	37.06	9.5262	1.853	25°C, Control
	2	4.338	.0145	37.74	10.7031	1.850	
	3	4.381	.0142	37.00	11.9644	1.860	
Vibrin 135 Laminate	4	4.461	.0173	37.58	9.5664	1.860	25°C, 3 x 10^8 Exposure
	5	4.434	.0175	37.83	10.7094	1.852	
	6	4.464	.0143	37.64	11.9547	1.863	
Vibrin 135	7	4.086	.0109	39.83	8.9787	1.746	25°C, 1 x 10^9 Exposure
	8	4.111	.0136	37.99	10.1844	1.761	
	9	4.250	.0127	39.13	11.3069	1.749	

TABLE XI

MECHANICAL PROPERTIES OF IRRADIATED AND NON-IRRADIATED LAMINATES
EXPOSED AND TESTED AT 500°F

Material Designation	Test Property	Radiation Dosage, Roentgens	Exposure & Test Temp, °F	Exposure Time, hrs	Ultimate Strength psi	Modulus of Elasticity psi x 10^6
CTL-91LD	Flexure	None	Room	None	84,525	4.22
		1 x 10^8	Room	200	84,040	4.35
		None	500	50	27,300	3.14
		2.5 x 10^7	500	50	55,020	3.46
		None	500	100	17,660	2.62
		5.0 x 10^7	500	100	47,015	3.61
		None	500	200	12,330	2.13
		1 x 10^8	500	200	15,645	2.41
DC-2104	Flexure	None	Room	None	31,760	3.06
		1 x 10^8	Room	200	31,460	2.94
		None	500	50	12,390	1.90
		2.5 x 10^7	500	50	13,625	2.0
		None	500	100	13,410	2.0
		5.0 x 10^7	500	100	11,720	2.0
		None	500	200	14,060	2.0
		1.0 x 10^8	500	200	9,860	1.9
X-131 (BF_3-400 Catalyst)	Compression	None	Room	None	46,680	——
		1 x 10^8	Room	200	46,660	——
		None	500	50	3,700	——
		2.5 x 10^7	500	50	3,780	——
		None	500	100	4,090	——
		5.0 x 10^7	500	100	5,490	——
		None	500	200	4,720	——
		1.0 x 10^8	500	200	6,360	——

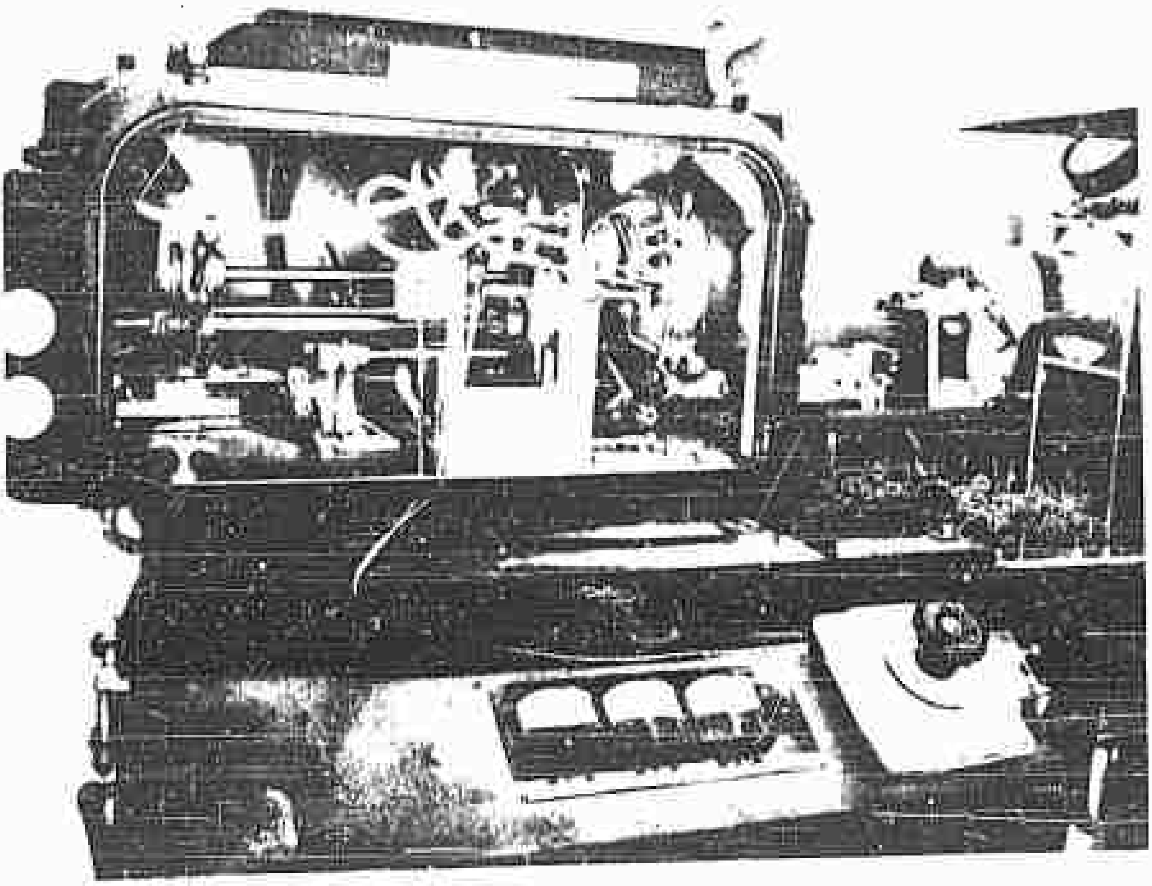

Figure 1 - Mitchell Carbon Arc Projector Radiant Energy Source

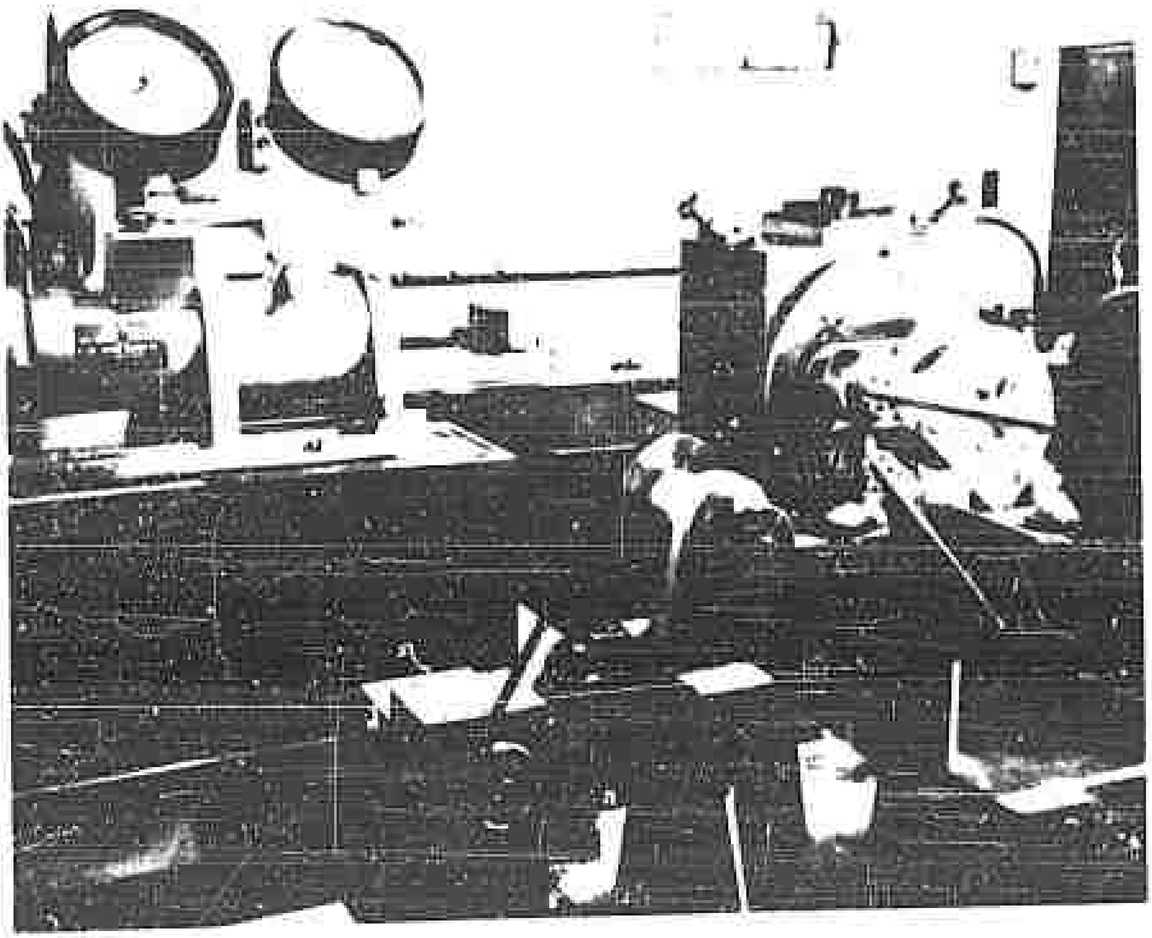

Figure 2 - Cal-Tester with Tensile Specimen Under Load

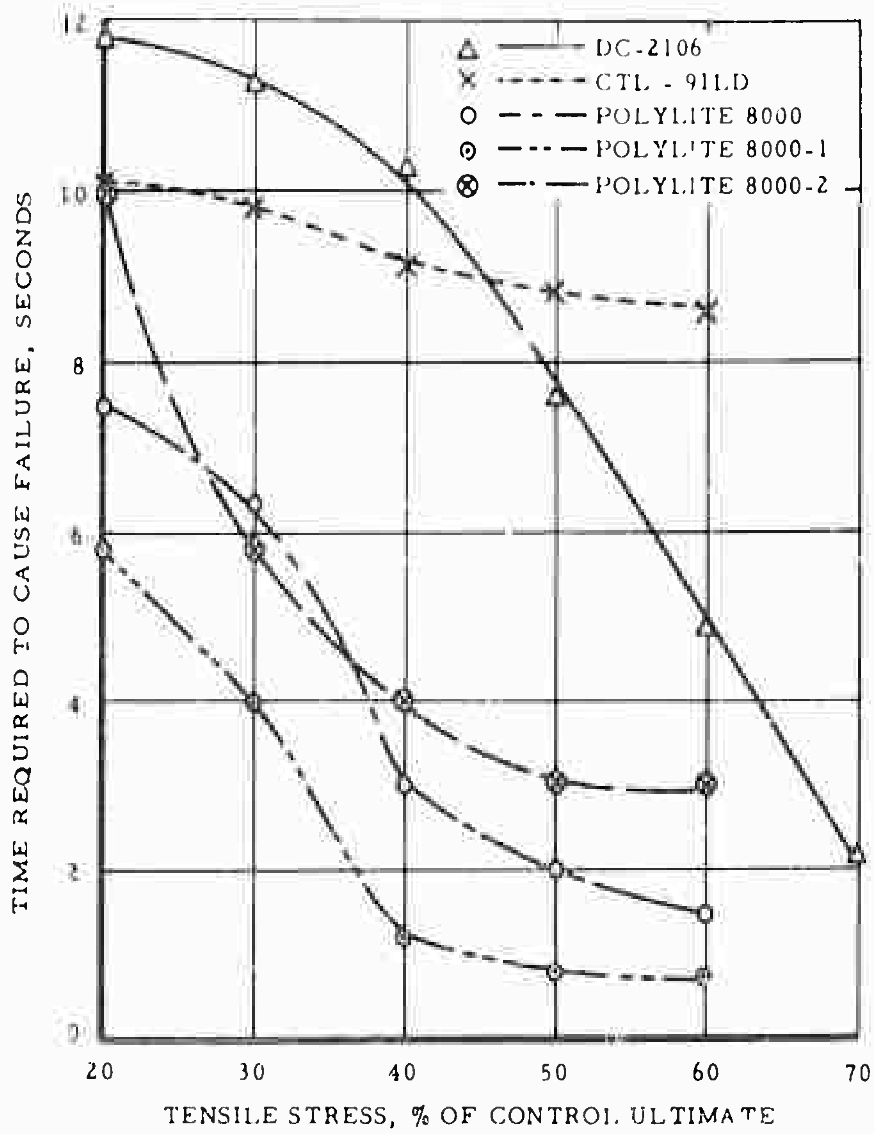

FIGURE 3 FAILURE TIME VS. PER CENT STRESS AT 10 CAL/CM^2/SEC

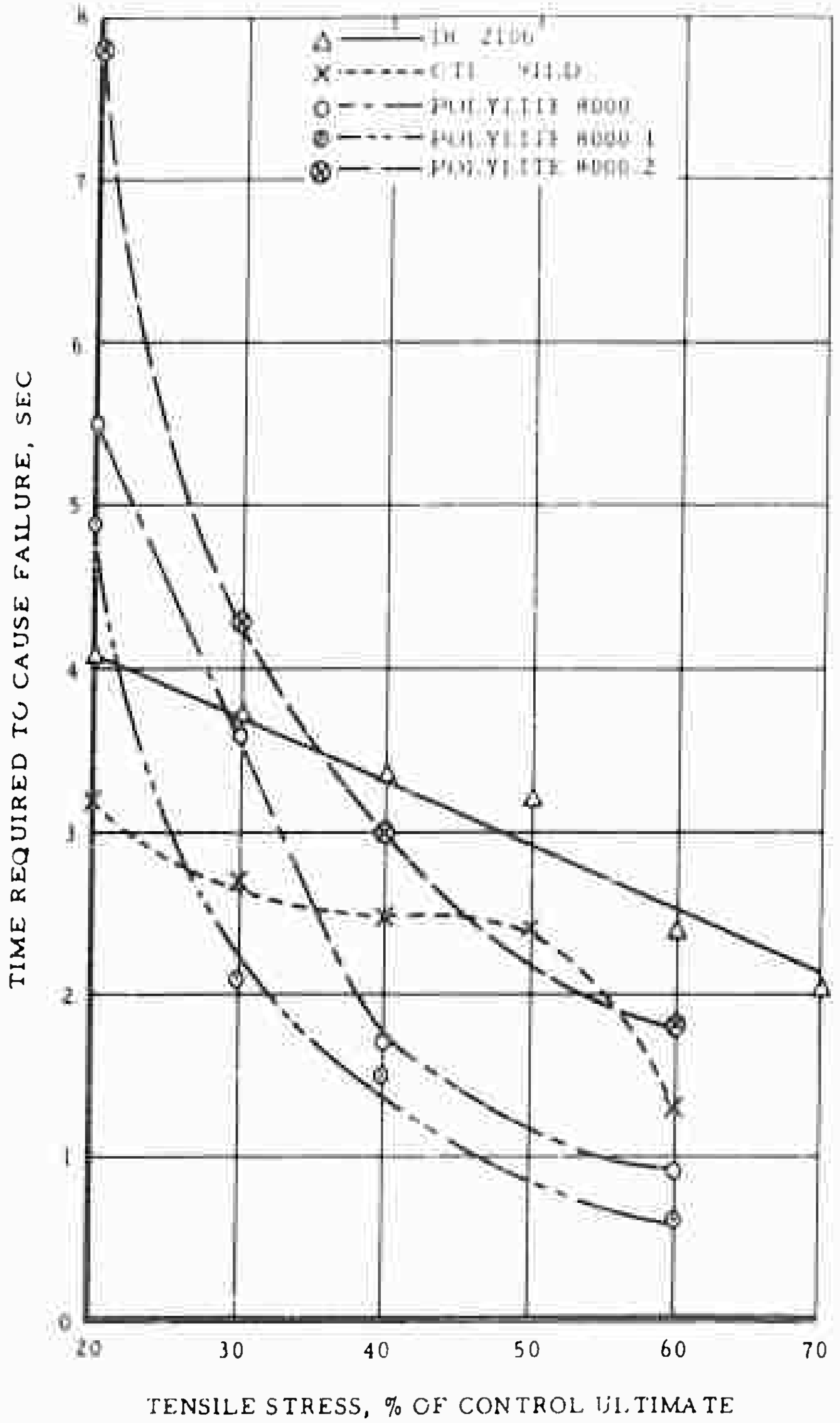

FIGURE 4 FAILURE TIME VS. PER CENT STRESS AT 25 CAL/CM^2/SEC

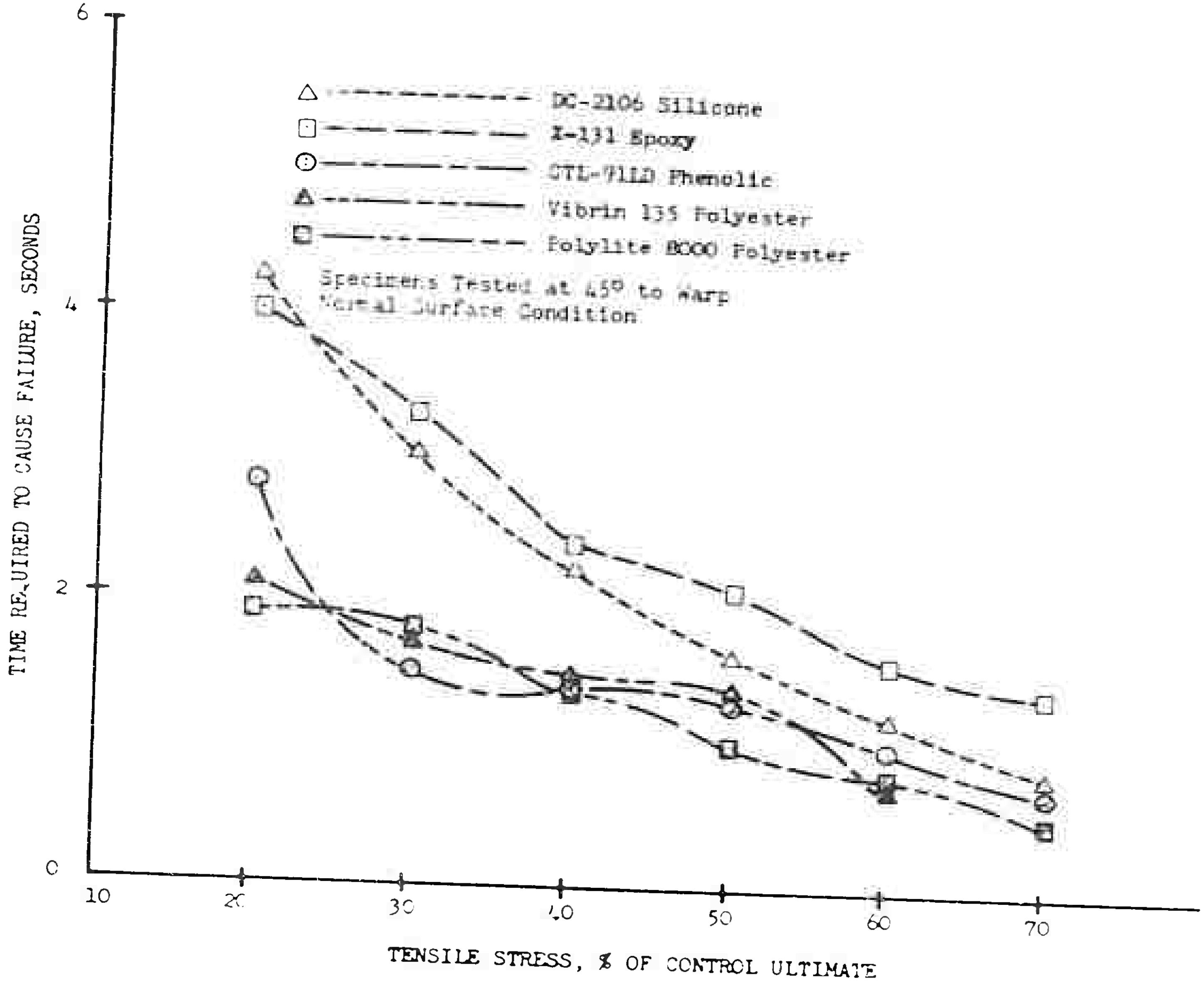

Figure 5 - Failure Time Versus Percent Tensile Stress at 10 CAL/CM^2-SEC Incident Energy

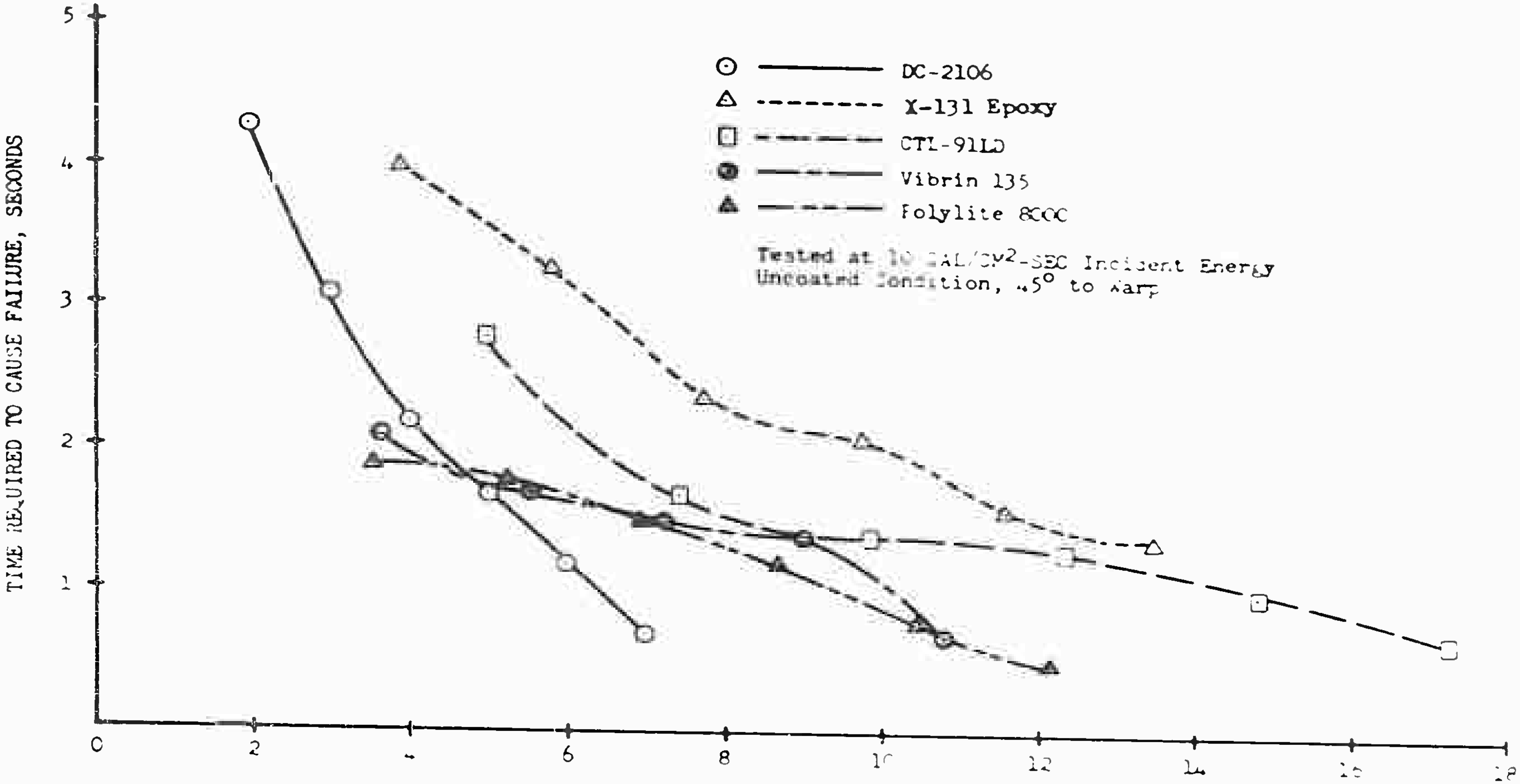

Figure 6 - TENSILE STRESS, PSI X 10^{-3}
(Loaded at 45 Degrees to Warp Direction)

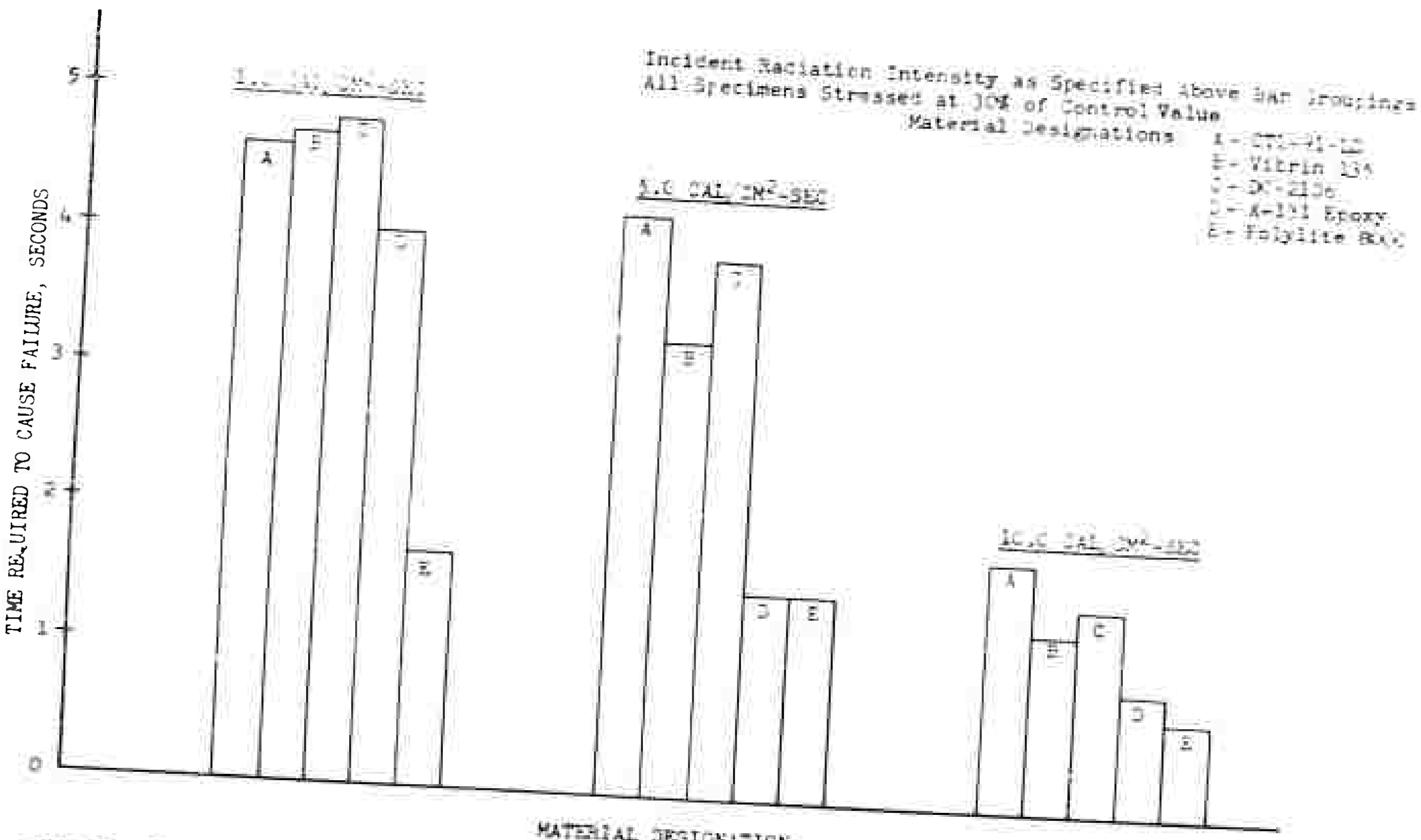

Figure 7 – Failure Time for Black Painted Tensile Specimens Loaded at 45° to Warp

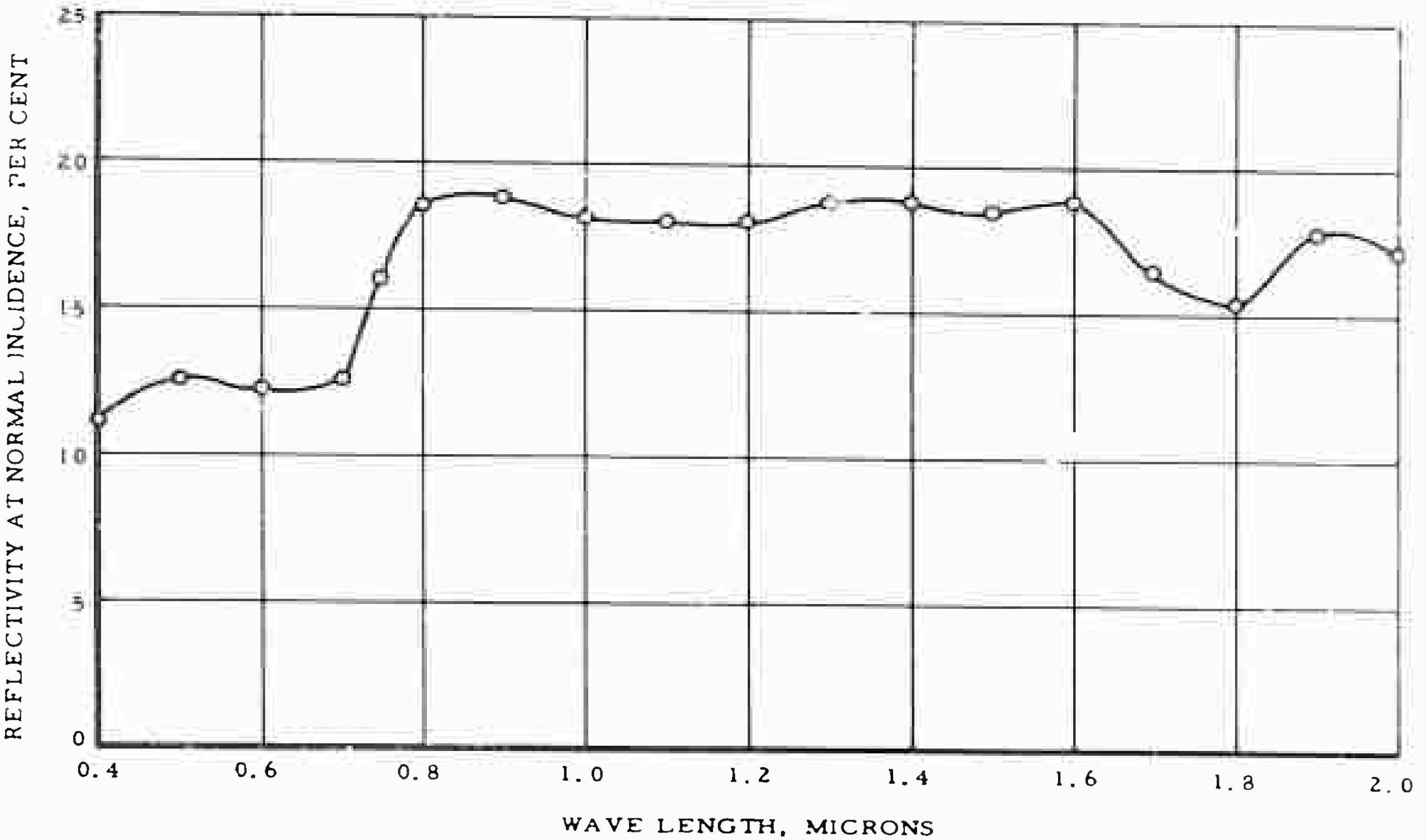

FIGURE 8 - SPECTRAL REFLECTIVITY OF POLYLITE 8000

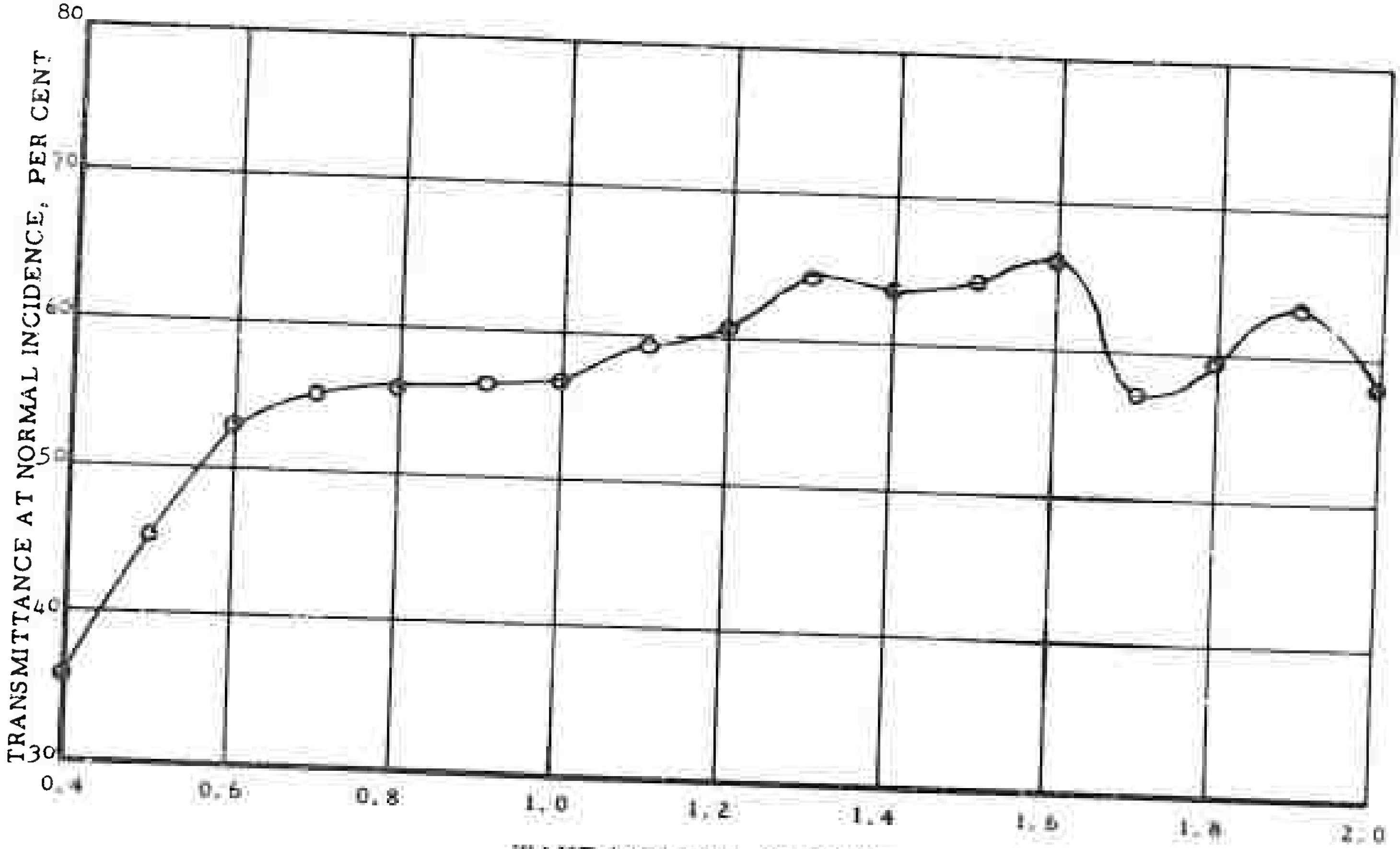

FIGURE 9 - SPECTRAL TRANSMISSIVITY OF POLYLITE 8000

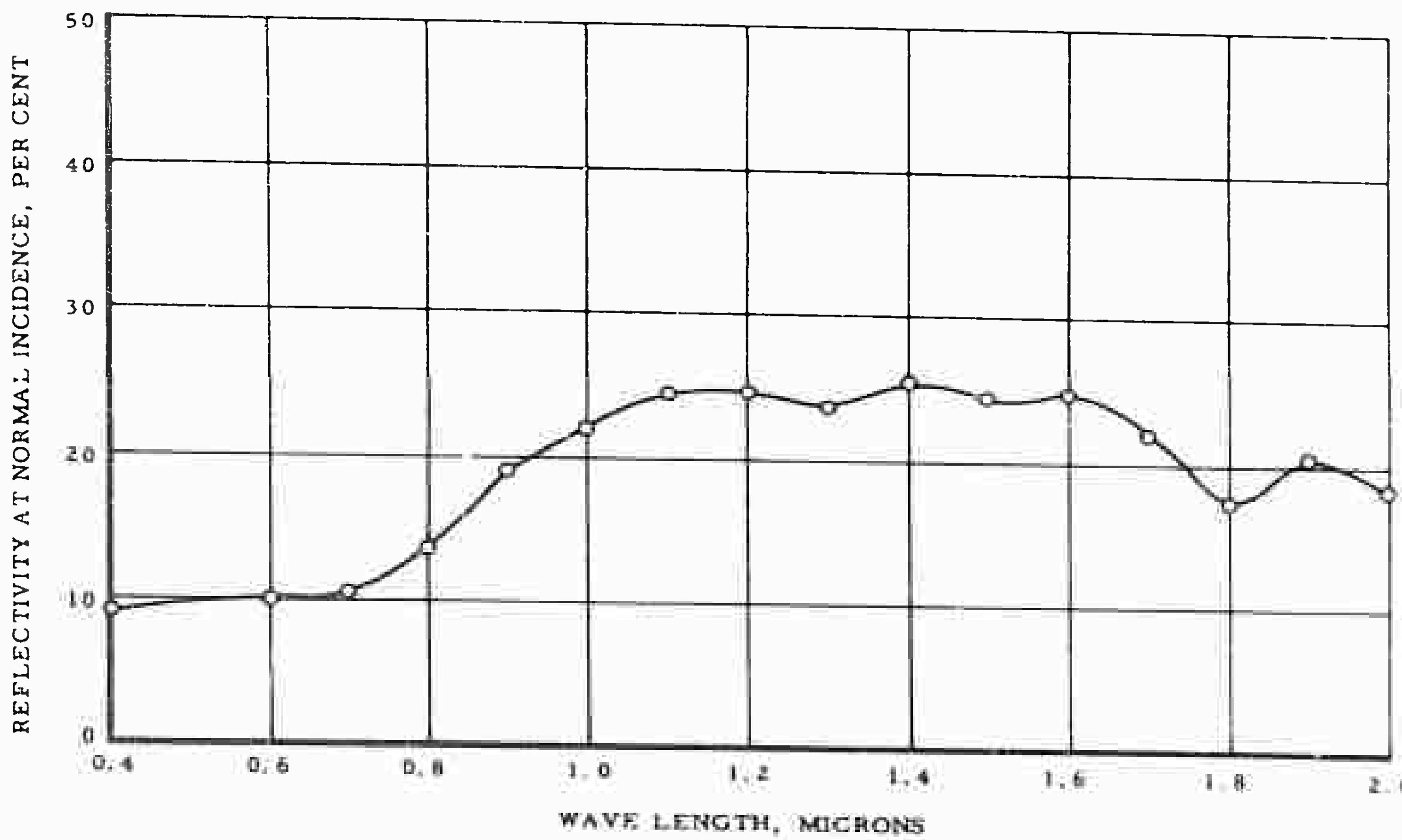

FIGURE 10 - SPECTRAL REFLECTIVITY OF POLYLITE 8000-1

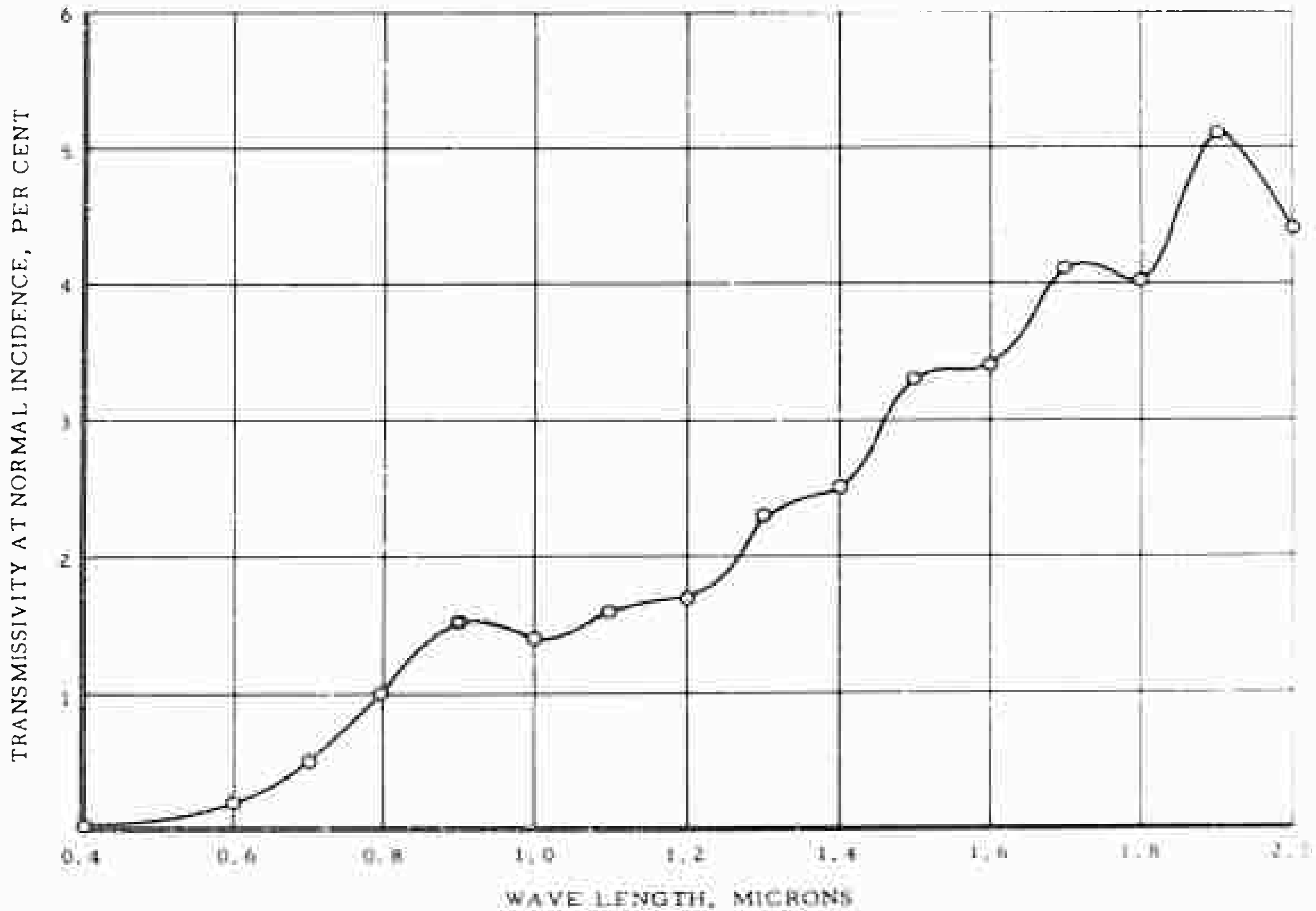

FIGURE 11 - SPECTRAL TRANSMISSIVITY OF POLYLITE 8000-1

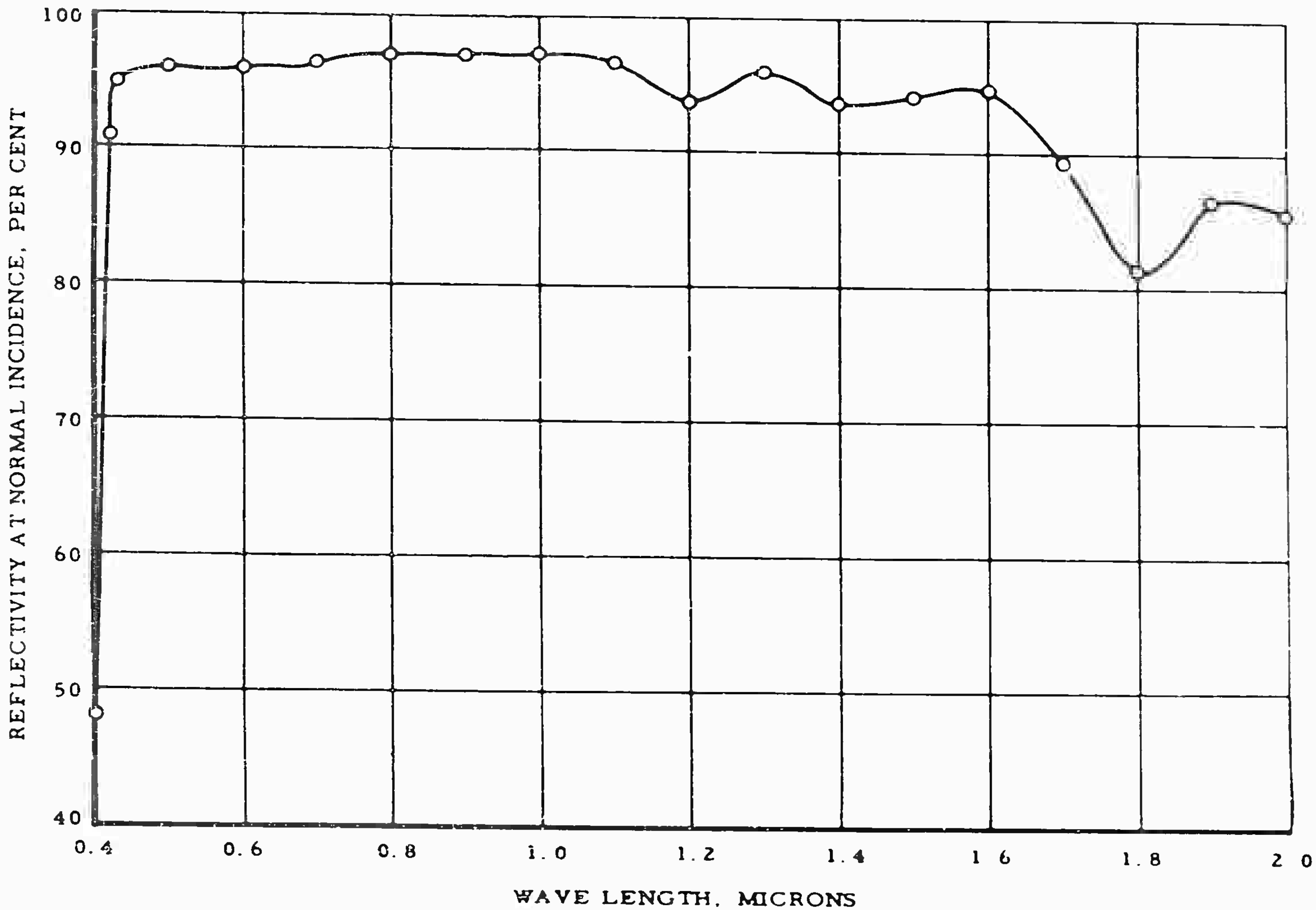

FIGURE 12 - SPECTRAL REFLECTIVITY OF POLYLITE 8000-2

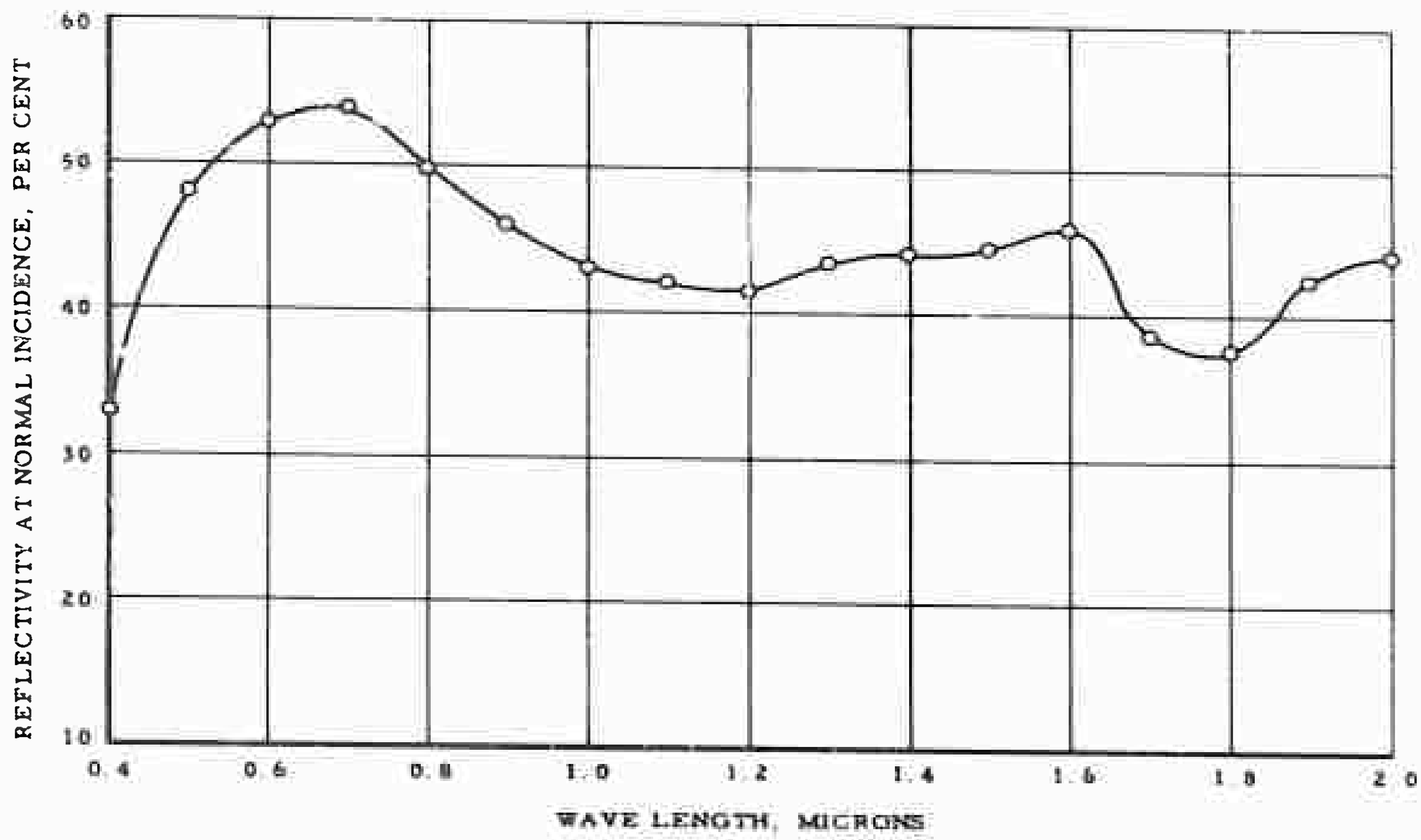

FIGURE 13 - SPECTRAL REFLECTIVITY OF DC-2106

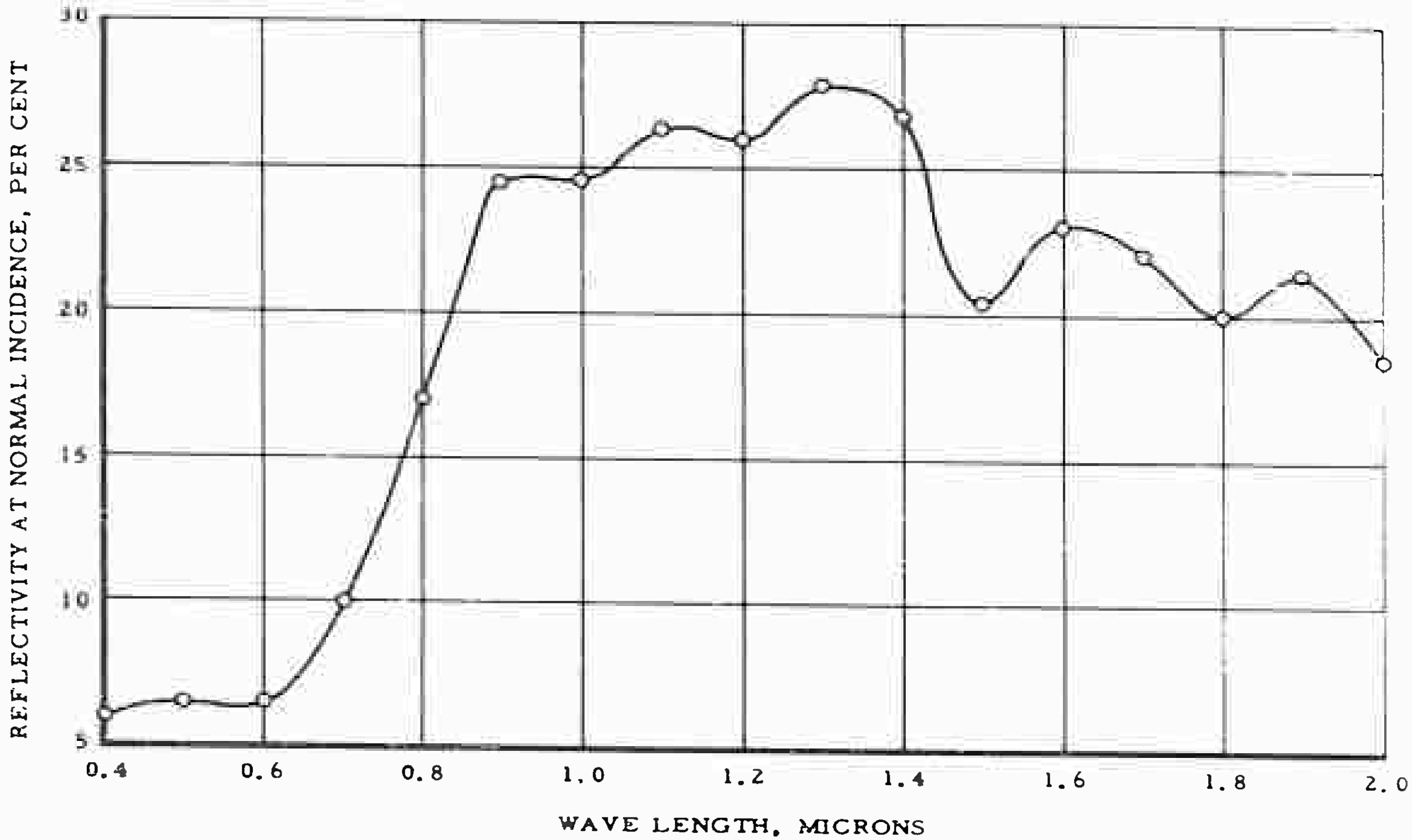

FIGURE 14 - SPECTRAL REFLECTIVITY OF CTL - 91LD

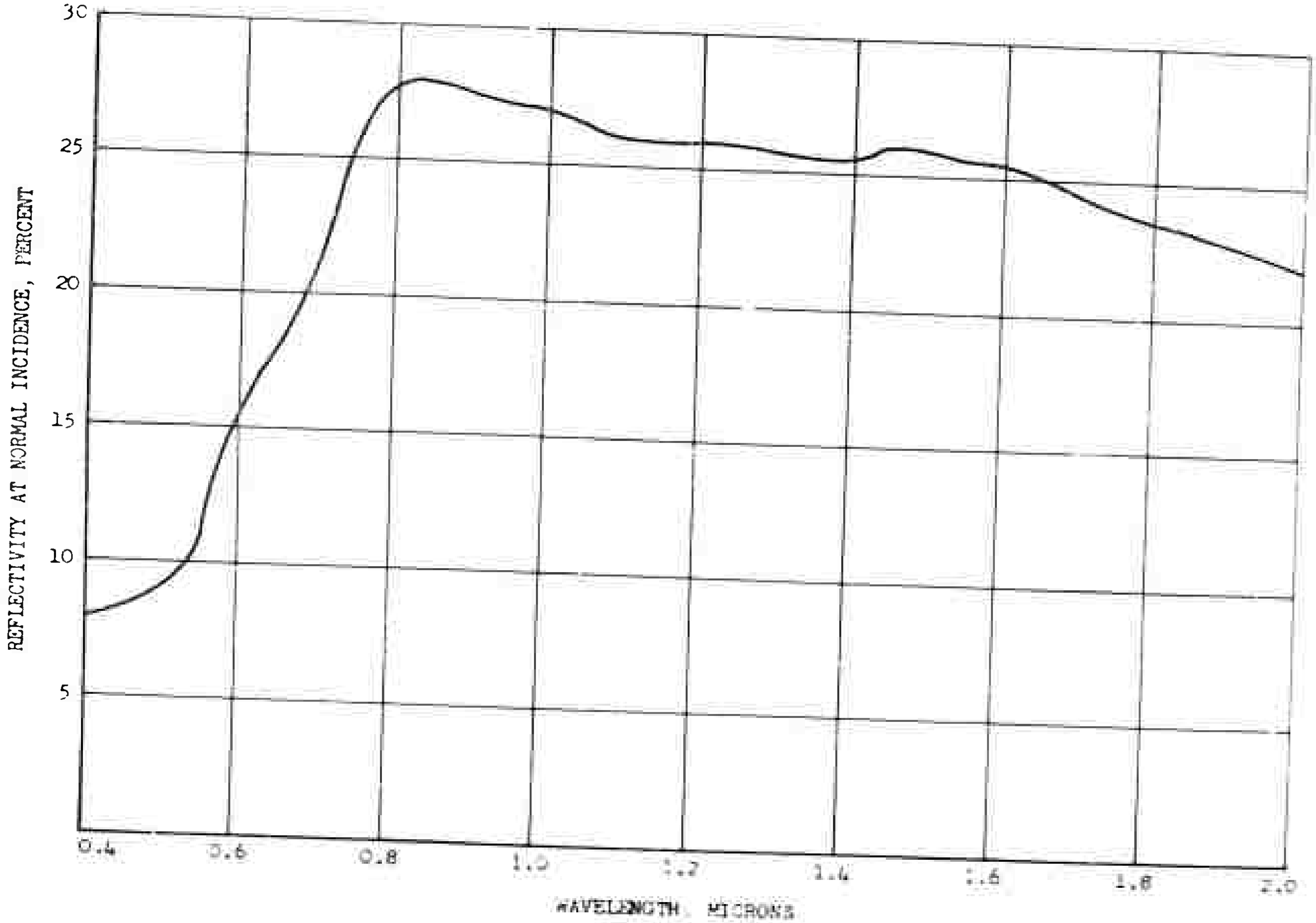

FIGURE 15 - Spectral Reflectivity of X-131 Laminate

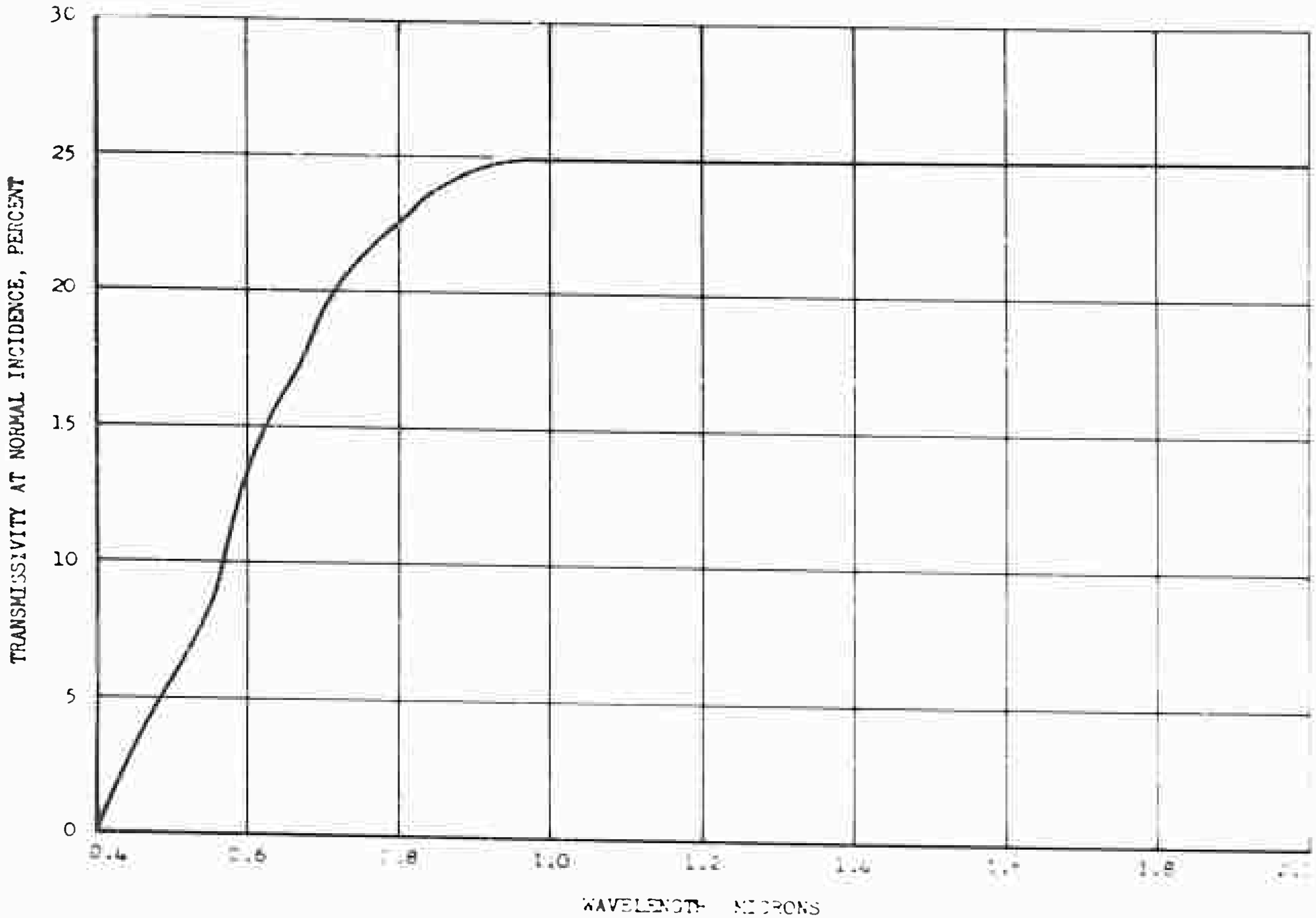

FIGURE 16 - Spectral Transmissivity of X-131 Laminate

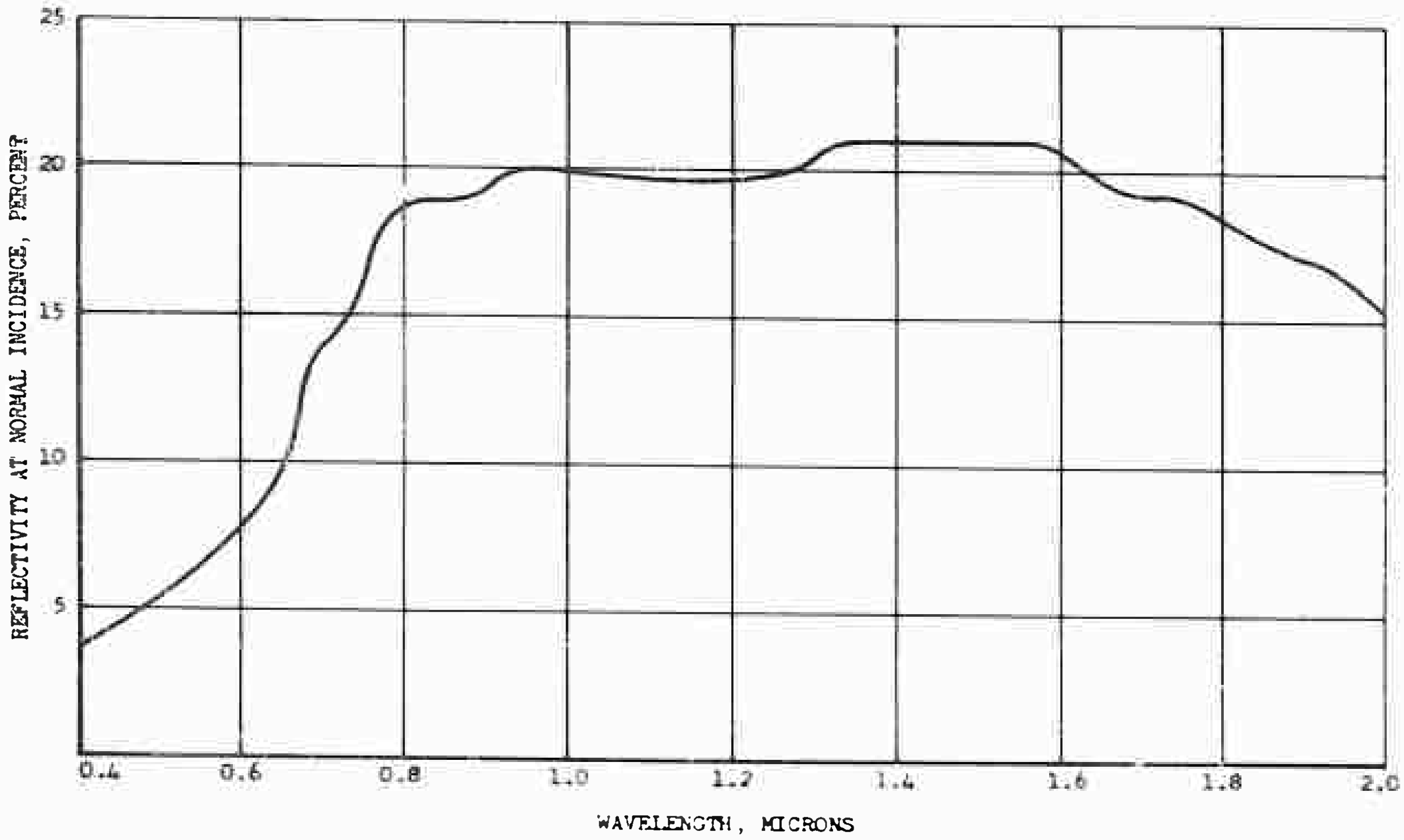

FIGURE 17 - Spectral Reflectivity of Vibrin 135 Laminate

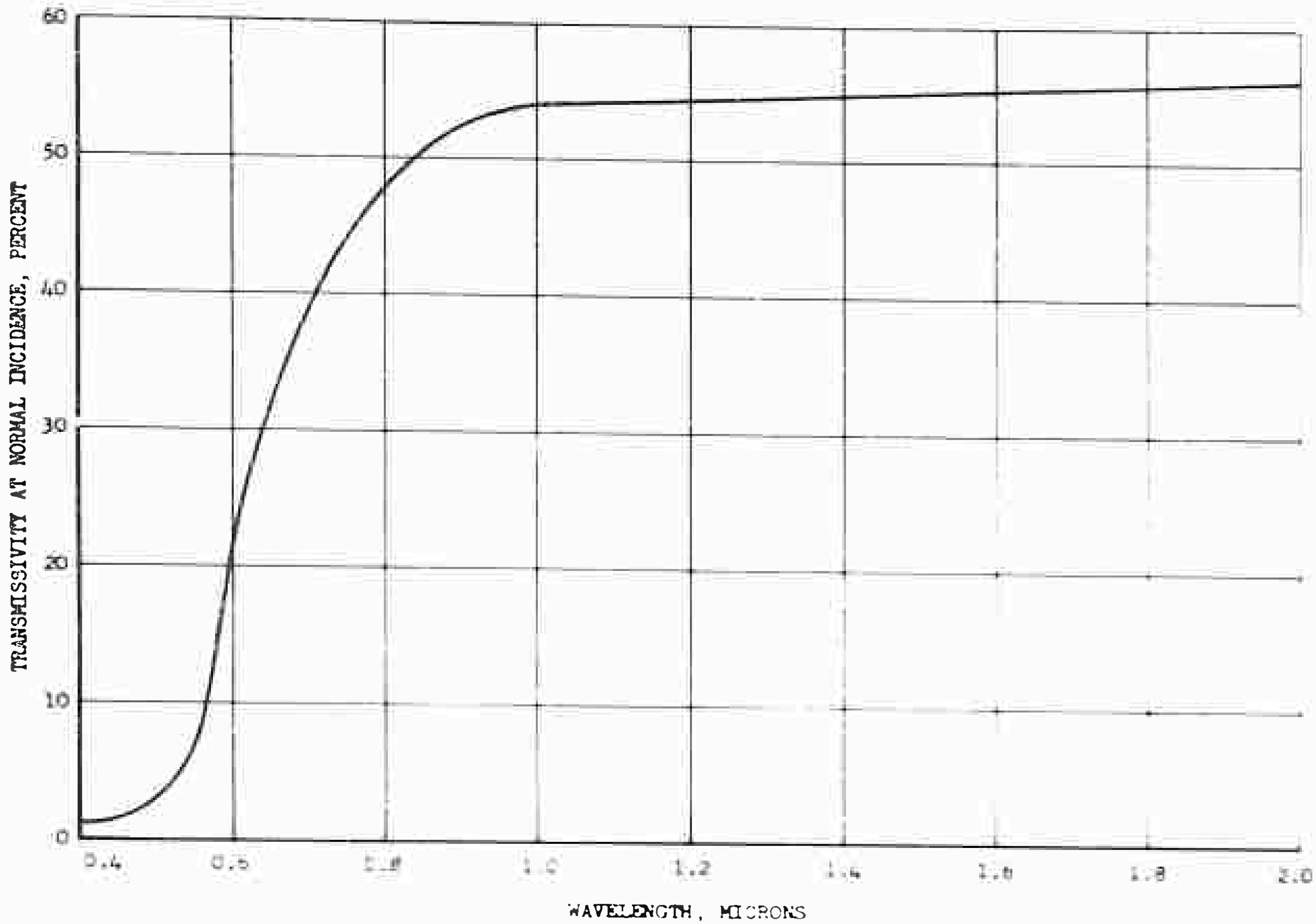

FIGURE 18 - Spectral Transmissivity of Vibrin 135 Laminate

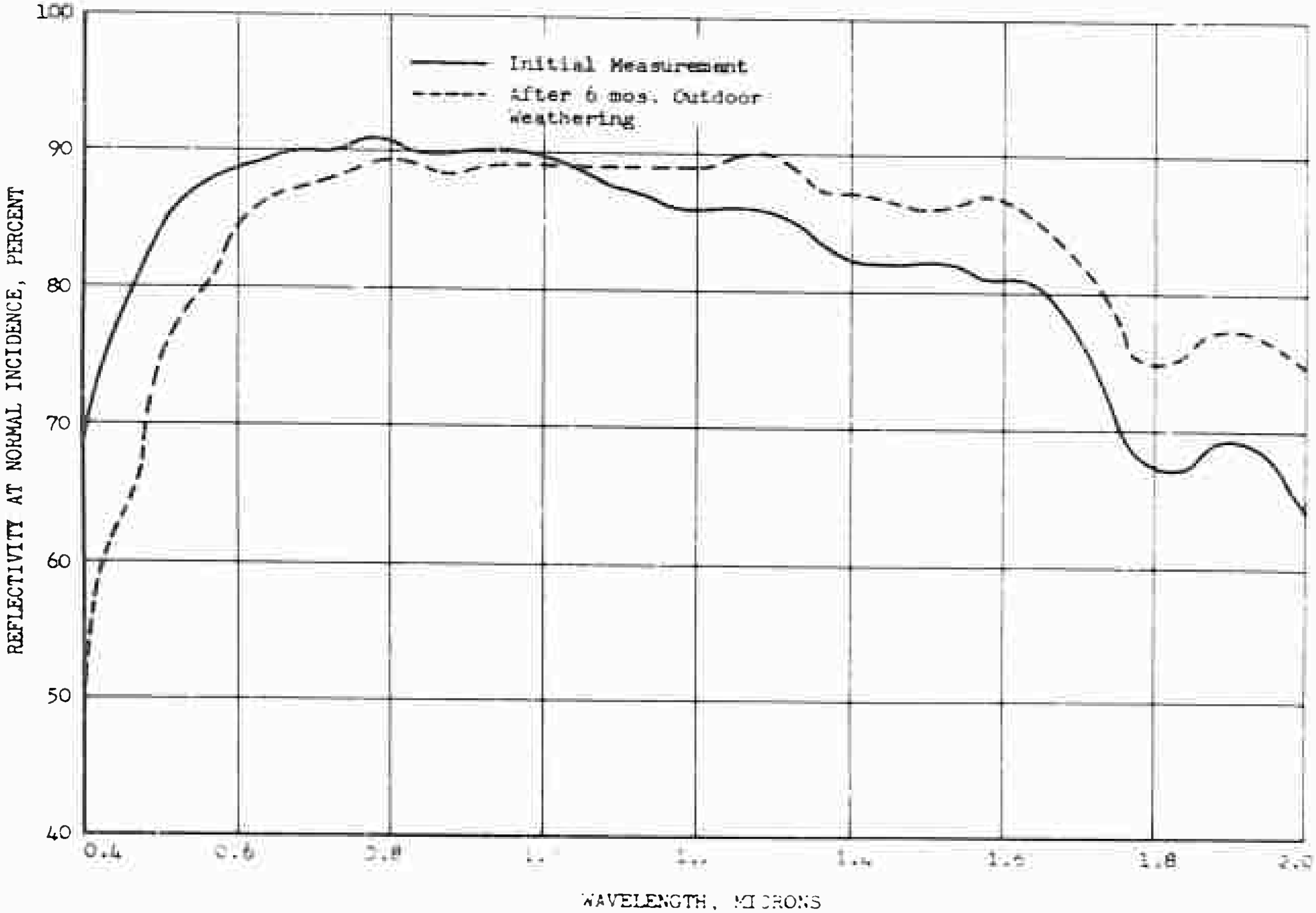

FIGURE 19 - Spectral Reflectivity of KV-9431 White Rain Erosion Coating

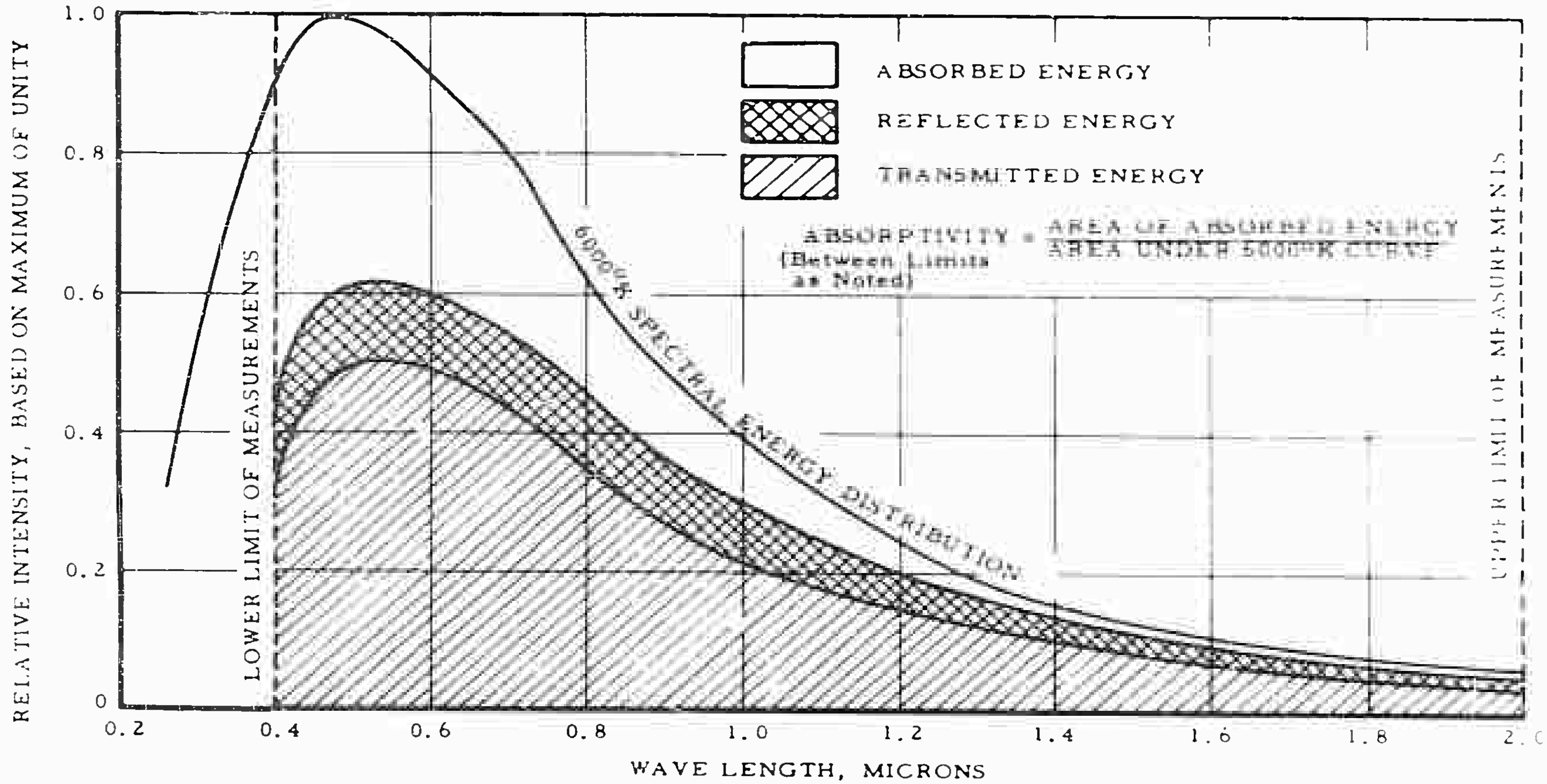

FIGURE 20 - GRAPHICAL PRESENTATION OF ABSORPTIVITY OF POLYLITE 8000 (UNCOATED)

[illegible][1]

By

[illegible], Engineer
and
[illegible], Engineer

Forest Products Laboratory,[2] Forest Service
U. S. Department of Agriculture
Madison, Wisconsin

Abstract

Work on the fatigue, creep, and weathering characteristics of reinforced plastics has been conducted at the Forest Products Laboratory in cooperation with Department of Defense Agencies. Fatigue properties of typical laminates under axial loading were determined in a direct stress fatigue machine operating at 900 cycles per minute. Unnotched and notched specimens were tested, usually at zero mean stress. Creep and creep rupture data in tension, flexure, and Johnson shear include data on specimens that have been loaded for periods up to 4 years. Effects of outdoor exposure on the strength and electrical properties of 10 different glass-fabric laminates have been evaluated. Four of the laminates were made with polyester resins and two with epoxy resins. Laminates were exposed at five different outdoor exposure sites for periods up to 3 years.

This paper summarizes the results of work that the Laboratory has done in these three fields of investigation.

---

[1] For presentation at Symposium on Rigid Radomes, September 8, 9, and 10, at Massachusetts Institute of Technology, Cambridge, Mass.

[2] Maintained at Madison, Wis., in cooperation with the University of Wisconsin.

Introduction

For about [illegible] years, the Forest Products Laboratory has conducted research on reinforced plastics in cooperation with agencies of the Department of Defense. Most of the work has been related to the establishment of design criteria, particularly for military applications. Other work has pertained to such factors as evaluation of materials, processes, test methods, and environmental conditions.

In this paper is reviewed some of the information that has been obtained at the Laboratory on fatigue, creep, and weathering characteristics of reinforced plastics. Most of the information on fatigue and creep is contained in published reports; the final report on weathering characteristics is now being processed. A list of applicable publications is presented under Literature Cited.

Fatigue

Fatigue data were obtained on several types of reinforced plastics tested under axial loading; specimens tested were dumbbell shaped (fig. 1). Stress was applied at 900 cycles per minute and usually at zero mean stress. Both unnotched and notched specimens were tested, the notch being a 1/8-inch-diameter hole drilled through the thickness at the net section. The specimens were tested under normal conditions and many also while wet. Some tests were also made of heat-resistant laminates both under normal conditions

and at elevated temperatures. Details of the test procedures, materials evaluated, and the final results are described in the report [illegible].

Polyester laminates reinforced with parallel plies of [illegible] fabric and cross-laminated plies of [illegible] fabric were tested ([illegible])[1] in fatigue parallel to the warp direction. All of the S-N curves were of similar shape and magnitude, indicating that the type of reinforcement had but little effect on fatigue strength. A polyester-mat laminate, as expected, had lower fatigue strength values than the polyester laminates reinforced with glass fabric. After [illegible] million repetitions of stress, however, the fatigue strength of all polyester laminates was about one-fourth of the static tensile strength (fig. [illegible]).

An epoxy laminate reinforced with [illegible] glass fabric had higher fatigue strength values than a comparable polyester laminate, particularly after 10,000 or more repetitions of loading. Furthermore, the fatigue strength after 10 million repetitions of stress was about 35 or 40 percent of the static tensile strength. This might be expected, because fatigue strength at zero mean stress is influenced by both the tensile and compressive strength of the material; compressive strength of epoxy laminates is generally appreciably higher than that of comparable polyester laminates.

In all laminates tested parallel or perpendicular to the warp direction, an endurance limit was not reached at 10 million

---

[1]Underlined numbers in parentheses refer to literature cited at the end of this report.

[illegible] when tested at angles to the warp, the fatigue characteristics were quite different and an endurance limit may have been reached at [illegible]° loading ([illegible]).

Notching generally reduces fatigue strength. For a [illegible]-inch-diameter hole, the fatigue strength at [illegible]° loading is about 10 to [illegible] percent less than that of unnotched material. At angles to the warp, there is some overlapping of S-N curves for unnotched and notched specimens, indicating a varying and lesser effect of stress concentration at angles to the warp (fig. 3). Although the small hole generally affects fatigue strength by only a few percent, recent data (9) have shown that a shallow Izod cut at the edge of a specimen reduced the fatigue strength to about one-half that of an unnotched specimen. Further work needs to be done to determine the effects of different types of notches on the fatigue properties.

Type of resin affects the fatigue properties (fig. 4), and data from typical laminates reinforced with 181 glass fabric are presented in reference (3). At 10 million cycles, however, the fatigue strength of all but the epoxy laminate was about one-fourth of the corresponding static tensile strength. Reference (3) also presents data on the effect of temperature and on tests at mean stresses other than zero.

Data from fatigue tests of epoxy laminates reinforced with continuous unwoven glass fibers and with 181 glass fabric, as well as from tests of asbestos-mat phenolic laminates, have recently been completed and will be presented in reference (14). Large

differences in strength between laminates were evident from static strength tests of specimens loaded parallel to the reinforcing fibers. The fatigue-strength values of the same materials after [illegible] million cycles, however, had a much smaller spread than the static-strength data. The epoxy laminate reinforced with parallel layers of continuous unwoven glass fibers was more sensitive to stress risers than the other materials tested. At [illegible]° and [illegible]° loading (fig. 5), the epoxy laminate reinforced with cross plies of unwoven continuous glass fibers had fatigue-strength values that were generally higher than those of the 181-glass-fabric epoxy laminate; at 45° loading, the glass-fabric laminate was superior.

Creep Properties

Creep properties will be mentioned only briefly in this paper, and the three referenced reports (4, 5, 6) will be useful in obtaining further details. Reference (6) presents tensile data for a typical polyester and epoxy laminate loaded at 0° and 45° for periods up to 1,000 hours. Mathematical relationships are presented for both strain-time and stress rupture. Similar mathematical relationships are presented in reference (5), which includes data on creep and stress-rupture characteristics of seven glass-fiber-reinforced laminates tested in tension, flexure, and shear for periods up to [illegible] years.

As is well known, tensile creep at room temperature parallel or perpendicular to the warp of glass-fabric laminates is small. Strain at failure for polyester and epoxy laminates is usually

about 10 to 20 percent higher than the initial strain, even after 10,000 hours. Since initial deformations are generally in the range of 1/2 to 1-3/4 percent, the additional deformation due to creep is usually so small as to be negligible. For mat laminates, however, strain at failure may be almost twice the initial strain, although initial strain at a comparable proportion of the static strength is much lower than for glass-fabric laminates. In flexure, final strain is a somewhat larger percentage of the initial strain than in tension.

Although tensile creep parallel and perpendicular to the warp of glass-fabric laminates is small, data (6) show that creep at 45° to the warp may be substantial (fig. 6). Even at 100 hours, the strain may be 2 or 3 times the initial strain.

Load-carrying capacity, or creep rupture, is markedly affected by the load and period under load and must be considered in many designs. Curves relating stress to the logarithim of time are approximately straight lines from 1 to 10,000 hours (fig. 7). Some data are available to 30,000 hours, but they are not enough to establish a "knee," or endurance limit, in the stress-time relationship. Tests of seven laminates tested for periods up to 30,000 hours (5) show that the tensile, flexural, and shear strength are not less than about 50 and 35 percent of the corresponding control strength for dry and wet conditions, respectively.

[illegible]

F[illegible] different glass fabric base [illegible] laminates made with five different laminating resins were exposed to various environmental conditions for periods up to [illegible] years. Laminates were exposed outdoors at Alaska, Panama, New Mexico, Florida, and Wisconsin, and were also stored in a room conditioned at [illegible]° F. and [illegible] percent relative humidity. After completion of the exposure period, tensile, compressive, and flexural strength properties and certain electrical properties were determined from tests made at the Laboratory.

All of the panels were parallel laminated of 181 glass fabric and were about [illegible] inch thick. The fabric finish used with each resin was varied so that fabric finish and resin were compatible. Two panels, about [illegible] inch thick and 36 inches square, were fabricated for most of the laminates.

Five general types of resins were used to make the laminated panels. Types and names of resins were: (1) polyester--Selectron 5003, Selectron 5003 with room temperature setting catalyst system, Plaskon 911-II, and Dryply 81; (2) epoxy--Epon 828 with Curing Agent D and Epon 1001 with 4 percent of dicyandiamide; (3) heat-resistant polyester--PDL-7-669 and Vibrin X-1047; (4) silicone--DC 2104; and (5) heat-resistant phenolic--Bakelite BV 17085. The details of the fabrication methods are described in the basic report (17). Each laminated panel was cut up into 9- by 12-inch subpanels, and the subpanels were exposed to various conditions. Subpanels subjected to outdoor exposure were mounted on racks and their faces were tilted upward at an angle of 45° from the horizontal, facing south.

Tension, compression, and flexural tests were made of each material after normal conditioning. Flexural tests were also made after the material had been conditioned for at least [illegible] months at 100° F. and near 100 percent relative humidity. A few flexural specimens of the heat-resistant laminates were tested at [illegible]° F. after 1/2 hour at that temperature.

Three electrical test specimens, each a disk 1 inch in diameter and the thickness of the laminate, were prepared from subpanels that had been exposed for 1 year and 3 years. The faces of each disk were not machined or altered in any way, and hence one face was generally rough because of the weathering effects. Tests were made by the shorted line waveguide method at a frequency of 8,530 megacycles. The disks were tested in pairs, pressed together tightly with no adhesive between them. Average electrical properties from tests of three pairs of disks were computed and averaged and are recorded as the test values for that material (table 1) (16).

Data from tests of the laminates weathered for periods of up to 3 years indicate substantial variations between properties depending upon factors such as exposure and materials. Detailed comparisons of strength and electrical properties must be made from data in the report (16). Table 2 presents a summary of the apparent effects of weathering on the strength properties of the different materials (16).

The appearance of the panels after 3 years' exposure varies greatly. It was observed that the greatest erosion occurred at the Florida (salt air) site. Laminates made with the heat-resistant polyester resins had the poorest resistance to erosion, while the

[illegible] the laminates [illegible] evidence of erosion. Photographs were made of extra-compressed specimens cut from near the center of each outpanel, and these were of help in visualizing the change in appearance that took place during various periods of outdoor exposure at different sites.

It should be remembered that the particular combination of resin, curing agent, fabric finish, laminating procedure, and other related factors that were employed was not intended to produce laminates with optimum strength or electrical properties. Nevertheless, the laminates were made with materials and by procedures that were in use at that time (1953), and in that respect may be considered as representative laminates. In this presentation it is not possible to discuss detailed comparisons of individual strength and electrical properties; such comparisons must be made from a detailed study of the report (figs. 8, 9).

A few general conclusions follow, but it should be remembered that there are often exceptions to these general conclusions:

1. The salt-air exposure at the Florida site was the most severe with respect to erosion of the surface resin and degradation in strength and electrical properties.

2. Three months' and 1 year's exposure under jungle conditions at Panama had less effect on strength properties than did similar periods of exposure at the other sites. Data after 3 years' exposure of laminates at Panama were not obtained, but 3 years' exposure at Alaska had less effect on strength properties than did similar periods of exposure at New Mexico, Florida, or Wisconsin.

3. Er[illegible] [illegible] surface re[illegible] [illegible] weathering [illegible] Barcol hardness, as might be expected. Laminates in which the resin was crazed or cracked decreased in hardness with continued weathering.

4. Exposure of laminates at normal conditions for periods [illegible] had little effect on the strength or electrical [illegible]

5. The heat-resistant polyester laminates had poorer resistance to weathering than any of the other laminates tested.

6. In all laminates, outdoor exposure usually had the least deleterious effect on dry compressive strength and the greatest effect on wet flexural strength. Wet flexural properties decreased more with weathering than did the flexural properties after normal conditioning.

7. Electrical properties of dry-conditioned specimens were affected only slightly by weathering. Properties of wet-conditioned specimens were poorer after weathering, particularly when glass fibers were exposed by erosion of the surface resin.

Resistance of Foams and Cores to Adverse Conditions

Limited data on the effects of adverse conditions on sandwich constructions and on certain types of cores used in sandwich constructions are presented in references (7, 8, 10, 11, 12, and 13). The results of tests and behavior of structural sandwiches having facings of plywood, hardboard, cement-asbestos board, and porcelain-enameled, steel-faced hardboard on cores of resin-treated paper are discussed in reference (10). Information on cores of

alkyl-isocyanate and waffle-type glass fiber and on honeycomb constructions made of paper, cotton fabric, glass fabric, and aluminum is presented in references (7) and (1[illegible]). Other published and unpublished data obtained at the Laboratory show that paper honeycomb cores can be made that have good impact resistance, good compressive strength, and good shear strength whether dry or wet, and excellent resistance to water migration.

Literature Cited

1. Boller, K. H.

1952. Fatigue Tests of Glass-Fabric-Base Laminates Subjected to Axial Loading. Forest Products Laboratory Report No. 1823.

2. ____________

1954. Supplement to Fatigue of Glass-Fabric-Base Laminates Subjected to Axial Loading. Forest Products Laboratory Report No. 1823-A.

3. ____________

1955. Fatigue Properties of Various Glass-Fiber-Reinforced Plastic Laminates. WADC TR 55-389.

4. ____________

1953. Stress-Rupture Tests of a Glass-Fabric-Base Plastic Laminate. Forest Products Laboratory Report No. 1839.

5. ____________

1958. Effect of Long-Term Loading on Glass-Reinforced Plastic Laminates. Forest Products Laboratory Report No. 2039 (Revised).

6. ____________

1957. Tensile Stress-Rupture and Creep Characteristics of Two Glass-Fabric-Base Plastic Laminates. Forest Products Laboratory Report No. 1863.

7. Heebink, B. G., Kommers, W. J., and Mohaupt, A. A.

[illegible]. Durability of Low-Density Core Materials and Sandwich Panels of the Aircraft Type as Determined by Laboratory Tests and Exposure to the Weather. Forest Products Laboratory Report No. 1573-B.

8. Jenkinson, P. M., and Kuenzi, E. W.

1957. Properties of Alkyd-Isocyanate Foamed-In-Place Core. WADC TR 57-182.

9. Kimball, K. E.

1958. Supplement to Fatigue Tests of Glass-Fabric-Base Laminates Subjected to Axial Loading (Effect of Notches) Forest Products Laboratory Report No. 1823-C. (Will be available for distribution about October 1, 1958.)

10. Kuenzi, E. W., and Wood, L. W.

1958. Durability Tests of Structural Sandwich (To be printed by ASTM. Presented at Symposium on Durability in Structures at Boston, Mass., June 1958).

11. Seidl, R. J., Kuenzi, E. W., Fahey, D. J., and Moses, C. S.

1951. Paper Honeycomb Cores for Structural Building Panels. Forest Products Laboratory Report No. 1796.

12. Setterholm, V. C., Heebink, B. G., and Kuenzi, E. W.

1955. Durability of Low-Density Sandwich Panels of the Aircraft Type as Determined by Laboratory Tests and Exposure to Weather. Forest Products Laboratory Report No. 1573-C.

13. ______________ and Kuenzi, E. W.

1956. Effect of Moisture Sorption on Weight and Dimensional Stability of Alkyd-Isocyanate Foam Core. WADC TR 56-86.

14. Stevens, G. H., and Boller, K. H.

Effect of Type of Reinforcement on Fatigue Properties of Plastic Laminates. WADC TR ______ (In preparation).

15. Werren, Fred

1956. Supplement to Fatigue Tests of Glass-Fabric-Base Laminates Subjected to Axial Loading. Forest Products Laboratory Report No. 1823-B.

16. ______________

Weathering of Glass-Fabric-Base Plastic Laminates. WADC TR 55-319, Supplement 1. (In preparation).

17. ______________ and Heebink, B. G.

1956. Weathering of Glass-Fabric-Base Plastic Laminates. WADC TR 55-319.

Table [illegible] Electrical properties [illegible]

Fabric finish	Resin	Exposure site	Properties after 1 year: Panel No.	Dielectric constant: Dry	Dielectric constant: Wet	Loss tangent: Dry	Loss tangent: Wet	Properties after 5 years: Panel No.	Dielectric constant: Dry	Dielectric constant: Wet	Loss tangent: Dry	Loss tangent: Wet
Garan RB-49	Selectron 5003	Alaska	301-L	4.333	4.385	0.0124	0.0148	302-M	4.331	4.491	0.0113	0.0259
		Panama	301-K	4.316	4.337	.0130	.0147					
		New Mexico	301-J	4.324	4.378	.0127	.0133	302-O	4.252	4.303	.0104	.0331
		Florida	301-I	4.265	4.451	.0123	.0281	302-P	4.247	4.807	.0116	.0373
		Madison	301-H	4.392	4.401	.0124	.0142	302-T	4.282	4.363	.0114	.0182
		Normal	302-U	4.313	4.334	.0124	.0136	302-V	4.297	4.323	.0113	.0138
	Plaskon 911-11	Alaska	303-L	4.447	4.507	.0124	.0208	304-M	4.371	4.433	.0214	.0240
		Panama	303-K	4.452	4.498	.0224	.0230					
		New Mexico	303-J	4.406	4.446	.0197	.0217	304-O	4.341	4.329	.0176	.0353
		Florida	303-I	4.306	4.624	.0171	.0273	304-P	4.255	5.004	.0236	.0646
		Madison	303-H	4.304	4.364	.0173	.0221	304-T	4.409	4.323	.0224	.0291
		Normal	304-U	4.397	4.434	.0193	.0204	304-V	4.348	4.417	.0212	.0221
	FDL-7-669	Alaska	309-L	4.640	5.673	.0310	.0940	310-M	4.659	6.113	.0374	.1239
		Panama	309-K	4.695	5.652	.0313	.0818					
		New Mexico	309-J	4.674	5.795	.0282	.0874	310-O	4.605	6.273	.0319	.1295
		Florida	309-I	4.742	6.328	.0311	.1182	310-P	4.592	7.607	.0388	.2186
		Madison	309-H	4.673	5.780	.0313	.0847	310-T	4.648	6.710	.0349	.1593
		Normal	310-U	4.571	5.709	.0265	.0901	310-V	4.601	5.716	.0288	.0872
	Vibrin X-1047	Alaska	313-L	4.736	5.584	.0234	.0730	314-M	4.815	5.900	.0295	.1067
		Panama	313-K	4.765	5.462	.0240	.0654					
		New Mexico	313-J	4.809	5.738	.0211	.0815	314-O	4.664	6.220	.0295	.1343
		Florida	313-I	4.855	6.329	.0253	.1139	314-P	4.705	7.680	.0322	.2169
		Madison	313-H	4.827	5.902	.0226	.0930	314-T	4.739	6.196	.0284	.1231
		Normal	314-U	4.859	5.493	.0179	.0533	314-V	4.826	5.392	.0201	.0533
Volan A	Epon 1001	Alaska	319-L	4.579	4.605	.0252	.0225	320-M	4.533	4.677	.0213	.0349
		Panama	319-K	4.528	4.565	.0276	.0265					
		New Mexico	319-J	4.505	4.551	.0264	.0272	320-O	4.502	4.713	.0210	.0385
		Florida	319-I	4.506	4.488	.0195	.0346	320-P	4.557	5.273	.0229	.0780
		Madison	319-H	4.447	4.492	.0209	.0254	320-T	4.504	4.710	.0231	.0360
		Normal	320-U	4.382	4.419	.0206	.0215	320-V	4.486	4.530	.0239	.0246
Garan RB-49	Dryply 81	Alaska	321-L	4.308	4.394	.0181	.0260	322-M	4.276	4.608	.0183	.0447
		Panama	321-K	4.294	4.397	.0206	.0304					
		New Mexico	321-J	4.297	4.412	.0186	.0304	322-O	4.169	4.388	.0180	.0370
		Florida	321-I	4.300	4.698	.0160	.0544	322-P	4.199	5.295	.0208	.1103
		Madison	321-H	4.304	4.409	.0200	.0267	322-T	4.253	4.785	.0188	.0389
		Normal	322-U	4.347	4.403	.0204	.0236	322-V	4.314	4.385	.0195	.0231
Volan A	Epon 828	Alaska	326-L	4.322	4.340	.0164	.0182	327-M	4.382	4.452	.0168	.0209
		Panama	326-K	4.266	4.286	.0181	.0198					
		New Mexico	326-J	4.172	4.202	.0171	.0188	327-O	4.218	4.339	.0158	.0257
		Florida	326-I	4.211	4.243	.0187	.0221	327-P	4.245	4.370	.0176	.0433
		Madison	326-H	4.272	4.293	.0181	.0195	327-T	4.266	4.378	.0162	.0246
		Normal	327-U	4.340	4.358	.0165	.0185	327-V	4.271	4.306	.0170	.0176
Heat cleaned	D.C. 2104 silicone	Alaska	331-L	3.840	4.137	.00835	.0333	332-M	3.770	4.088	.00865	.0357
		Panama	331-K	3.833	4.193	.00847	.0320					
		New Mexico	331-J	3.804	4.183	.00830	.0348	332-O	4.011	4.433	.00892	.0393
		Florida	331-I	3.706	4.304	.00846	.0480	332-P	3.993	4.403	.00899	.0386
		Madison	331-H	3.927	4.206	.00823	.0332	332-T	4.162	4.496	.01017	.0330
		Normal	332-U	3.703	4.030	.00819	.0338	332-V	3.833	4.098	.00893	.0293
Garan RB-49	Selectron 5003 (room-temp. setting)	Alaska	336-L	4.241	4.278	.0108	.0144	336-M	4.203	4.258	.0123	.0154
		Panama	337-K	4.217	4.233	.0120	.0152					
		New Mexico	338-J	4.178	4.204	.0117	.0148	338-O	4.092	4.246	.0120	.0269
		Florida	339-I	4.293	4.354	.0112	.0187	339-P	4.229	4.559	.0107	.0418
		Madison	341-H	4.259	4.279	.0108	.0124	341-T	4.148	4.203	.0125	.0188
		Normal	340-U	4.232	4.255	.0104	.0138	340-V	4.261	4.281	.0113	.0127
Volan A	Bakelite BV 17085	Alaska	347-L	4.796	4.852	.0456	.0465	348-M	4.938	5.049	.0474	.0545
		Panama	347-K	4.679	4.785	.0473	.0471					
		New Mexico	347-J	4.955	4.980	.0451	.0470	348-O	4.800	4.951	.0452	.0641
		Florida	347-I	4.932	4.961	.0474	.0479	348-P	4.910	5.434	.0447	.0830
		Madison	347-H	4.839	4.874	.0441	.0461	348-T	4.840	4.985	.0425	.0532
		Normal	349-U	4.773	4.850	.0464	.0462	349-V	4.998	5.039	.0434	.0505

Table 2.--Summary of apparent effects of exposure on strength properties of plastic laminates

Strength [illegible]	Kind of test	General effect of [illegible] exposure on strength	General effect of [illegible] exposure on strength	[illegible]	[illegible]	[illegible]	[illegible]	[illegible]	[illegible]
[illegible] RESIN WITH 181 [illegible]-FINISHED GLASS FABRIC									
Tension	N	None	Increase at [illegible] months, then decrease	[illegible]	[illegible]	Low High	[illegible]	New Mex[illegible] Florida	[illegible]
Compression	N	Increase	Increase [illegible] year, then some decrease	[illegible]	[illegible]	Low High	[illegible]	Florida & Alaska [illegible]	[illegible]
Flexure	N	Slight increase after [illegible] years	Increase at [illegible] months and [illegible] year, then decrease	[illegible]	[illegible]	Low High	[illegible]	New Mex[illegible] Alaska	[illegible]
Flexure	W	Very slight increase	Increase at [illegible] months, decrease at [illegible] years	[illegible]	[illegible]	Low High	[illegible]	Florida Alaska	[illegible]
[illegible] RESIN WITH 181 [illegible]-FINISHED GLASS FABRIC									
Tension	N	None	Slight increase at [illegible] months, then decrease	[illegible]	[illegible]	Low High	[illegible]	Florida [illegible]	[illegible]
Compression	N	Increase	Increase at [illegible] months and 1 year, then some decrease	[illegible]	[illegible]	Low High	[illegible]	Florida New Mex[illegible]	[illegible]
Flexure	N	None	No change or slight increase at [illegible] months, then decrease	[illegible]	[illegible]	Low High	[illegible]	Florida & New Mex[illegible] Alaska	[illegible]
Flexure	W	None	No change or slight decrease at [illegible] months, then decrease	[illegible]		Low High	[illegible]	New Mex[illegible] Alaska	[illegible]
[illegible] RESIN WITH 181 [illegible]-FINISHED GLASS FABRIC									
Tension	N	Slight decrease	No change at [illegible] months, then decrease	[illegible]	[illegible]	Low High	[illegible]	Florida Alaska	[illegible]
Compression	N	Slight increase	Increase at [illegible] months, then pronounced decrease	[illegible]	[illegible]	Low High	[illegible]	Florida Alaska	[illegible]
Flexure	N	Slight decrease	Progressive decrease with added exposure	[illegible]	[illegible]	Low High	[illegible]	Florida Alaska	[illegible]
Flexure	W	Decrease	Progressive decrease with added exposure	[illegible]	[illegible]	Low High	[illegible] [illegible]	Florida Alaska	[illegible]
Flexure	500	Increase	Little change at [illegible] months and some decrease at 1 year. Then pronounced decrease	10.0	[illegible]	Low High	[illegible]	Florida Alaska	[illegible]
VIBRIN [illegible] RESIN WITH 181 [illegible]-FINISHED GLASS FABRIC									
Tension	N	Little change to [illegible] year, then decrease	Some decrease at [illegible] months; then pronounced decrease	35.0	[illegible]	Low High	[illegible]	New Mexico Alaska	[illegible]
Compression	N	Increase	Increase at [illegible] months, then decrease	[illegible]	[illegible]	Low High	[illegible] [illegible]	Florida & Wisconsin Alaska	[illegible]
Flexure	N	Slight decrease	Progressive decrease with added exposure	[illegible]	[illegible]	Low High	[illegible]	New Mexico Alaska	[illegible]
Flexure	W	Slight decrease	Progressive decrease with added exposure	[illegible]	[illegible]	Low High	[illegible]	New Mexico Alaska	[illegible]
Flexure	500	Slight decrease	Little change at [illegible] months; then decrease	[illegible]	[illegible]	Low High	[illegible] 18.8	New Mexico Alaska	[illegible]

(Sheet 1 of 3)

Table [illegible].--Summary of apparent effects of exposure on strength properties of plastic laminates (Continued)

Strength in --	Kind of test[2]	General effect of normal exposure on strength	General effect of outdoor exposure on strength	[illegible] strength requirement per spec [illegible]	Comparative effects of 3 years weathering: Control[3]		Weathered[4]		Range from control[3]
					Strength	Order	Strength	Site	
(1)	(2)	(3)	(4)	(5)	(6)	(7)	(8)	(9)	(10)
				1,000 p.s.i.	1,000 p.s.i.		1,000 p.s.i.		Percent
					EPON [illegible] RESIN WITH [illegible] A-FINISHED GLASS FABRIC				
Tension	N	About same at 3 months then slight decrease	[illegible] decrease at 3 months, then further decrease	[illegible]	[illegible]	Low High	[illegible] [illegible]	Florida Wisconsin	[illegible] [illegible]
Compression	N	Increase at 3 months, then decrease	Marked increase at 3 months and 1 year, then decrease	[illegible]	[illegible]	Low High	[illegible] [illegible]	Florida New Mexico	[illegible] [illegible]
Flexure	N	Same at 3 months, then decrease	Little change at 3 months, then increase	[illegible]	[illegible]	Low High	[illegible] [illegible]	Florida Alaska	[illegible] [illegible]
Flexure	W	Same at 3 months, then decrease	Slight decrease at 3 months, then marked decrease	[illegible]	[illegible]	Low High	[illegible] [illegible]	Wisconsin Alaska	[illegible] - 2[illegible]
					[illegible] 81 LAMINATED WITH 181 GARAN-FINISHED GLASS FABRIC				
Tension	N	Slight increase	Marked increase at 3 months, then slight decrease	[illegible]	58.2	Low High	41.1 4[illegible].5	Florida Alaska	+ [illegible] + 2[illegible]
Compression	N	Increase	Marked increase at 3 months then little change	[illegible]	33.[illegible]	Low High	46.[illegible] [illegible].8	Florida New Mexico	+ [illegible] + [illegible]
Flexure	N	Increase	Marked increase to 1 year, then some decrease	[illegible]	[illegible]	Low High	48.6 64.2	Florida Alaska	[illegible] + [illegible]
Flexure	W	Increase to 1 year, then decrease	Marked increase to 1 year, then some decrease	[illegible]	[illegible]	Low High	40.[illegible] 45.8	Florida Alaska	- 2[illegible] + [illegible]
					EPON 828 RESIN WITH 181 VOLAN A-FINISHED GLASS FABRIC				
Tension	N	Slight increase	About same or increase at 3 months, then some decrease	[illegible]	48.[illegible]	Low High	43.7 51.4	Florida Alaska	- [illegible] + [illegible]
Compression	N	Increase	Some increase effects erratic	50.0	44.1	Low High	47.6 49.3	Florida New Mexico	+ 8 + 12
Flexure	N	Slight increase at 3 months, then decrease	About same or decrease at 3 months; decrease at 3 years	70.0	63.3	Low High	52.4 63.4	Florida Alaska	- 17 0
Flexure	W	Some increase at 3 months, then decrease	Increase at 3 months, then decrease	65.0	40.[illegible]	Low High	37.4 42.8	Florida Alaska	- 8 + [illegible]
					DC 2106 RESIN WITH 181 HEAT-CLEANED GLASS FABRIC				
Tension	W	None to 1 year; then slight decrease	A general decrease, when thickness variations are considered	30.0	34.6	Low High	26.7 31.6	Alaska Wisconsin	- 2[illegible] - [illegible]
Compression	N	Progressive increase	Increase at 3 months, some decrease after 1 year	18.0	14.2	Low High	15.2 16.1	Wisconsin Florida	+ [illegible] + 13
Flexure	N	Slight increase	Very little effect	35.0	27.3	Low High	27.6 28.2	Alaska Wisconsin	+ 1 + [illegible]
Flexure	W	None	Minor increase at 3 months, slight decrease at 3 years	30.0	26.2	Low High	24.8 25.9	New Mexico Wisconsin	- 5 - 1
Flexure	500	Same	Very slight increase	15.0	11.1	Low High	11.2 11.7	Wisconsin Florida	+ 1 + 5

(Sheet 2 of 5)

Table 2.--Summary of apparent effects of exposure on strength properties of plastic laminates (continued)

Strength in --	Kind of test[1]	General effect of normal exposure on strength	General effect of outdoor exposure on strength	Initial strength requirement per specification[2]	Control[3] Strength	Control[3] Order	Weathered[4] Strength	Weathered[4] Site	Change from control[5]
(1)	(2)	(3)	(4)	(5)	(6)	(7)	(8)	(9)	(10)
				1,000 p.s.i.	1,000 p.s.i.		1,000 p.s.i.		Percent
[illegible] FROM [illegible] RESIN ROOM-TEMPERATURE-SETTING, WITH 181 [illegible]-FINISHED GLASS FABRIC									
Tension	N	None	Slight increase at [illegible] months then slight decrease	[illegible]	[illegible]	Low	[illegible]	Wisconsin	[illegible]
						High	[illegible]	Florida	[illegible]
Compression	N	Progressive increase	Large increase [illegible] year, then slight decrease	[illegible]	[illegible]	Low	[illegible]	Florida	[illegible]
						High	[illegible]	Wisconsin	[illegible]
Flexure	N	Slight increase	Slight increase [illegible] months or 1 year, then decrease	[illegible]	[illegible]	Low	[illegible]	New Mexico	[illegible]
						High	[illegible]	Alaska & Wisconsin	[illegible]
Flexure	W	Progressive decrease	Progressive decrease with additional exposure	[illegible]	[illegible]	Low	[illegible]	New Mexico	[illegible]
						High	[illegible]	Alaska	[illegible]
BAKELITE [illegible] RESIN WITH 181 VOLAN A FINISHED GLASS FABRIC									
Tension	N	Increase	Little change	[illegible]	[illegible]	Low	[illegible]	Florida	[illegible]
						High	[illegible]	Alaska	[illegible]
Compression	N	Progressive increase	Irregular but gradual increase	[illegible]	[illegible]	Low	[illegible]	Wisconsin	[illegible]
						High	[illegible]	Alaska & New Mexico	[illegible]
Flexure	N	Tend to increase	Inconsistent, except trend to decrease at Florida	[illegible]	[illegible]	Low	[illegible]	Florida	[illegible]
						High	[illegible]	Alaska	[illegible]
Flexure	W	Slight increase	Small inconsistent changes, except trend to decrease at Florida	[illegible]	[illegible]	Low	[illegible]	Florida	[illegible]
						High	[illegible]	New Mexico	[illegible]
Flexure	500	Little change	Increase	[illegible]	11.2	Low	12.[illegible]	New Mexico	[illegible]
						High	14.[illegible]	Alaska	[illegible]

[1] N denotes strength test after normal conditioning, W denotes wet test after about [illegible] months conditioning at [illegible]° F. and [illegible] percent relative humidity, 500 denotes strength test after 1/2 hour at 500° F.

[2] Strength values from applicable military specifications, but wet conditioning procedure used was more severe than that specified in specification. Refer to MIL-P-7575, MIL-P-9274, MIL-P-9300, MIL-P-[illegible], and MIL-P-[illegible].

[3] Control subpanels that were cut from same panel as the subpanels weathered for 5 years, except that control values for room-temperature-setting Selectron are an average of all control subpanels.

[4] Columns show the exposure sites in which the widest differences occurred in each strength property and the corresponding strength values after weathering laminates for 5 years.

[5] Percentage decrease or increase of extreme strength values after weathering laminates for 5 years compared to the corresponding control value.

(Sheet 3 of 3)

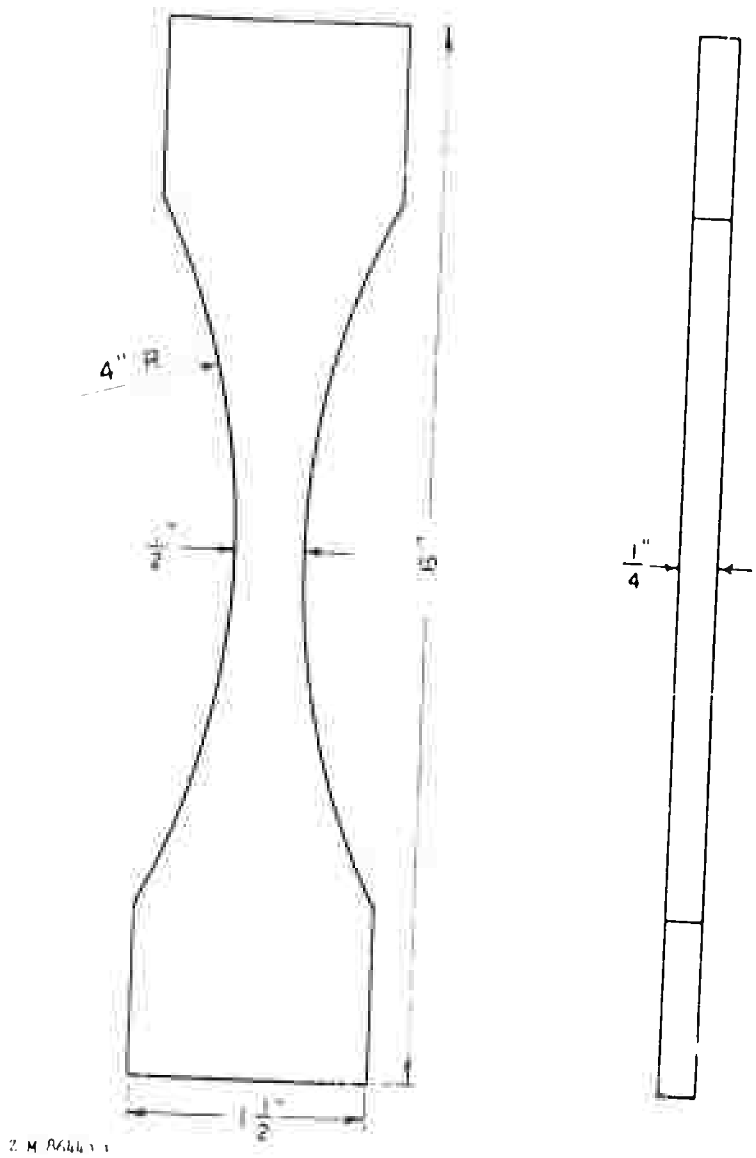

Figure 1.--Unnotched fatigue specimen of the type used in axial fatigue tests.

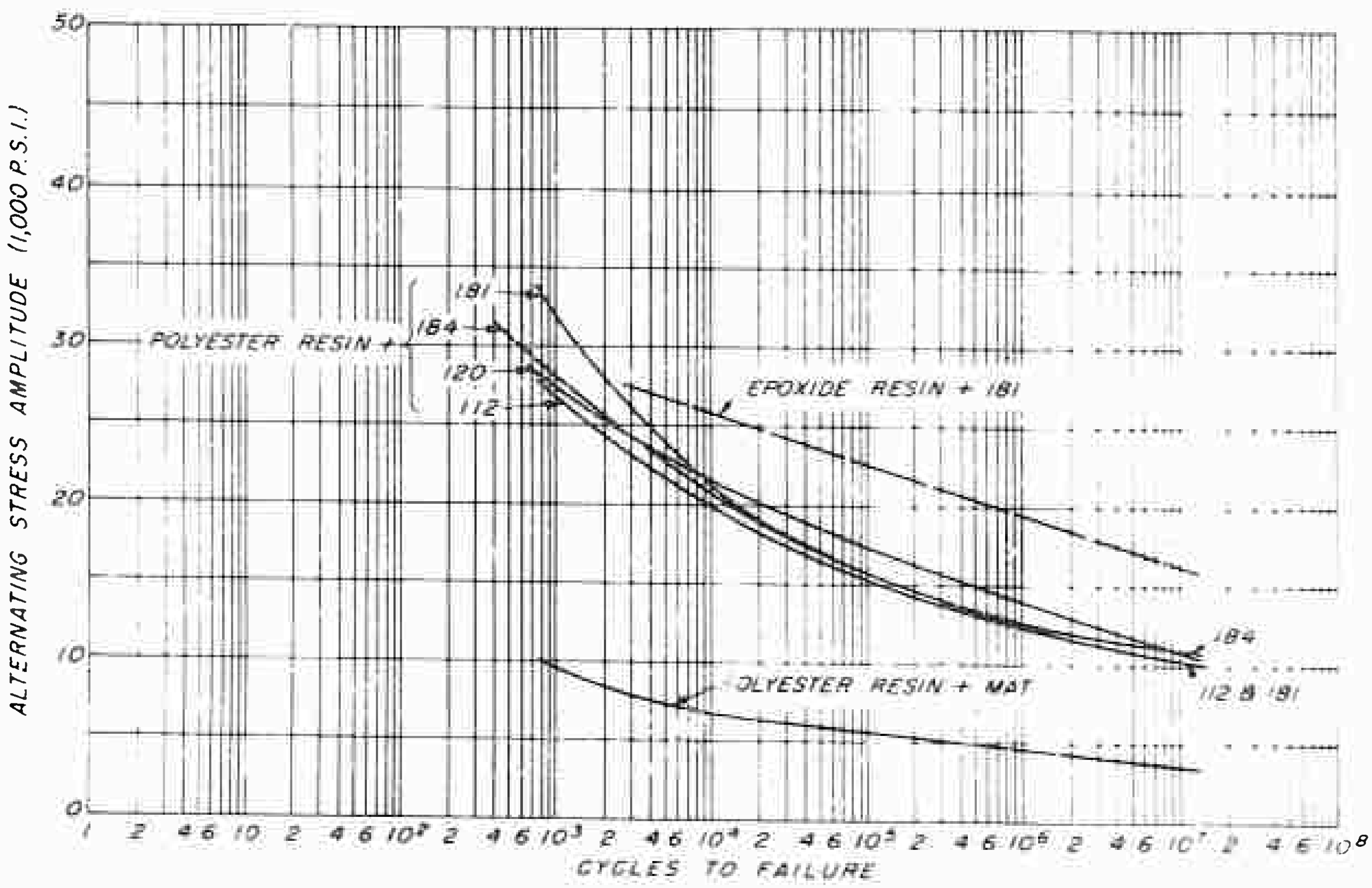

Figure 2.--S-N curves of unnotched specimens of laminates reinforced with various glass fabrics and a glass mat. Tests made parallel to the warp, under normal conditions, and at zero mean stress.

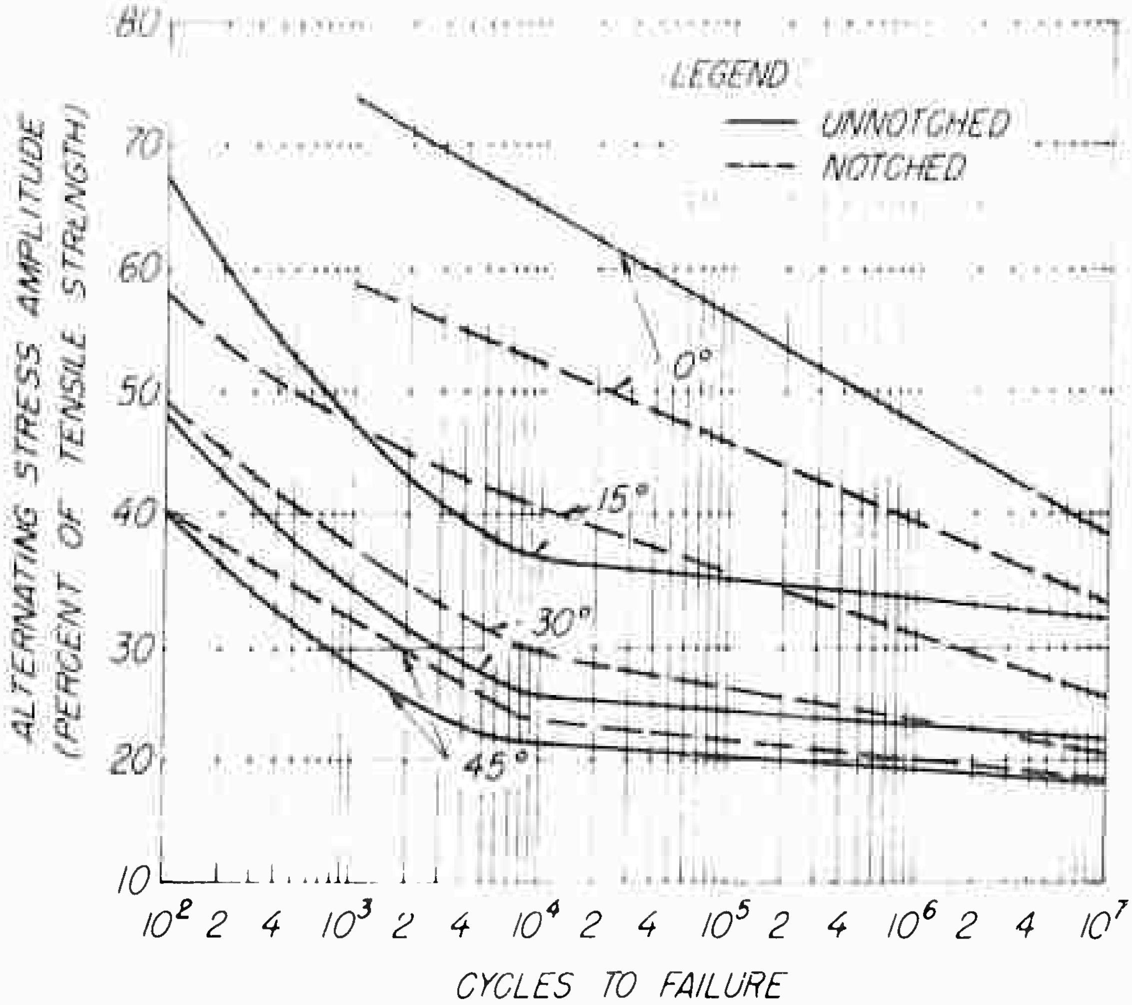

Figure 3.--S-N curves for parallel laminate made of 181 glass fabric and an epoxy resin. Tests made at different angles to the warp, under normal conditions, and at zero mean stress.

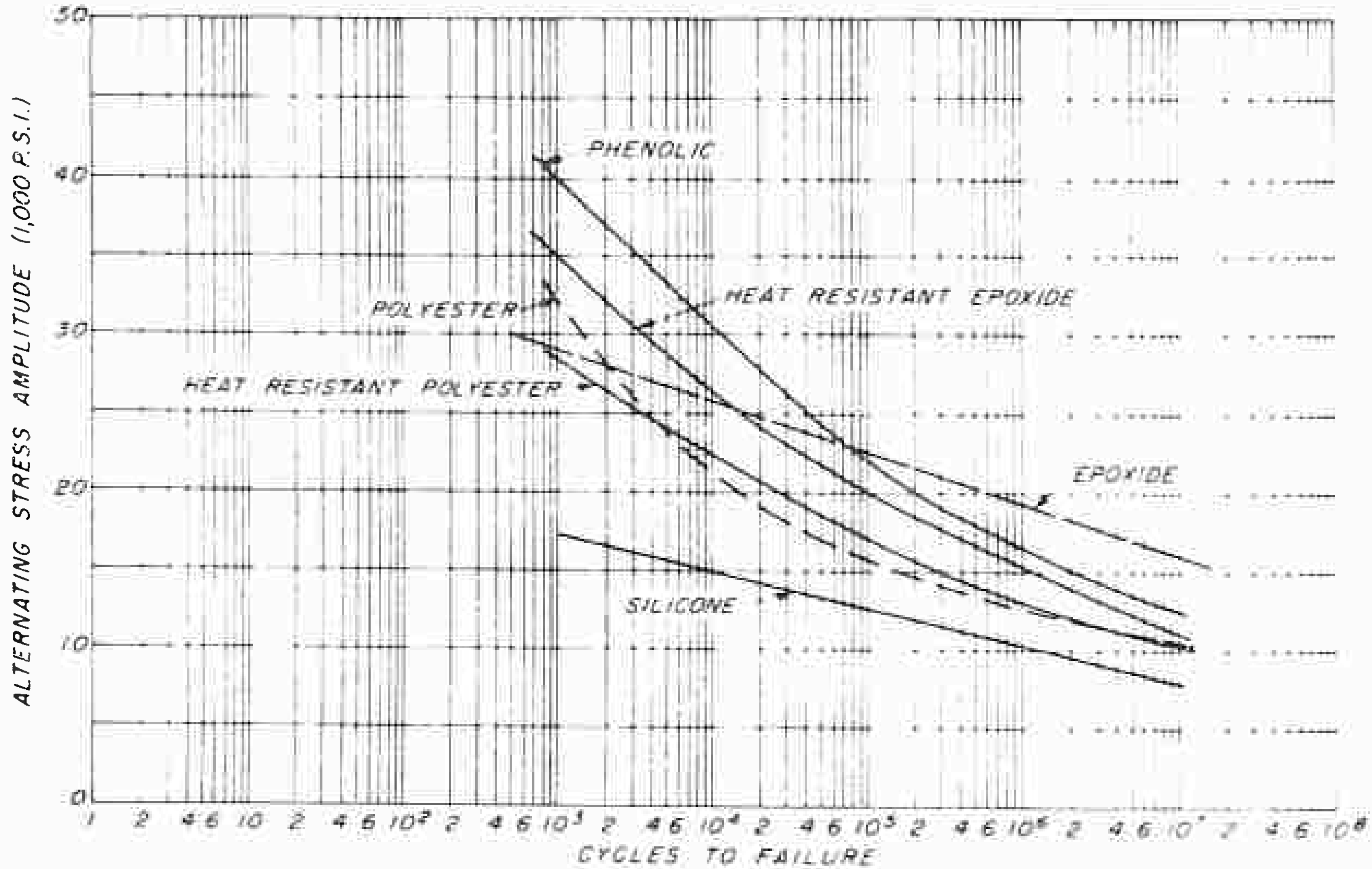

Figure 4.--S-N curves of unnotched specimens of laminates made with 181 glass fabric and different types of resins. Tests made parallel to the warp, under normal conditions, and at zero mean stress.

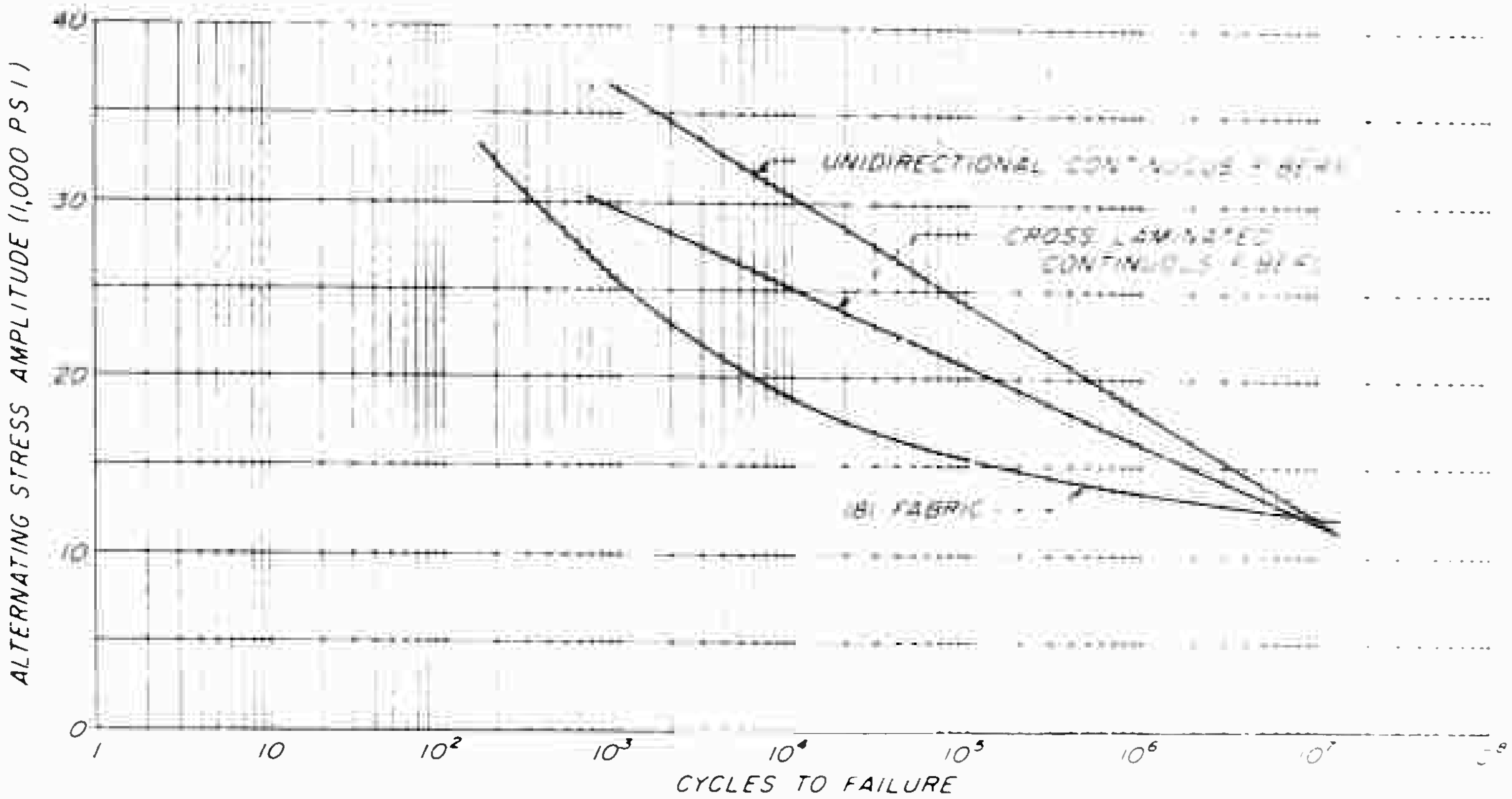

Figure 5.--S-N curves of unnotched specimens of laminates made with epoxy resin and glass fabric or unwoven glass fibers. Tests made parallel to the major fiber direction, at 1[illegible]° F. and 100 percent relative humidity, and at zero mean stress.

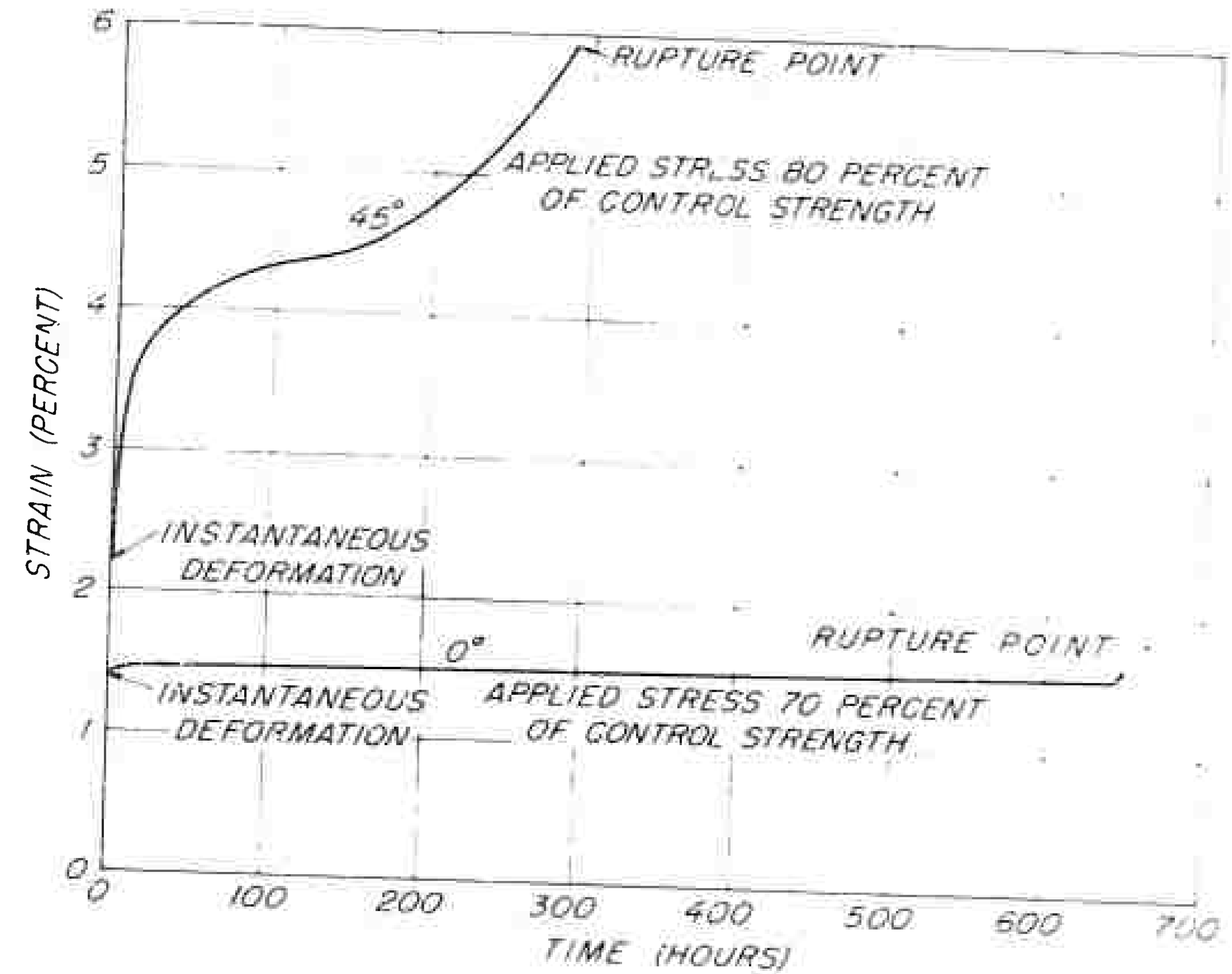

Figure 6.--Typical strain-time curves for a 181-epoxy laminate at normal conditions, tested in tension at 0° and 45° to the warp direction.

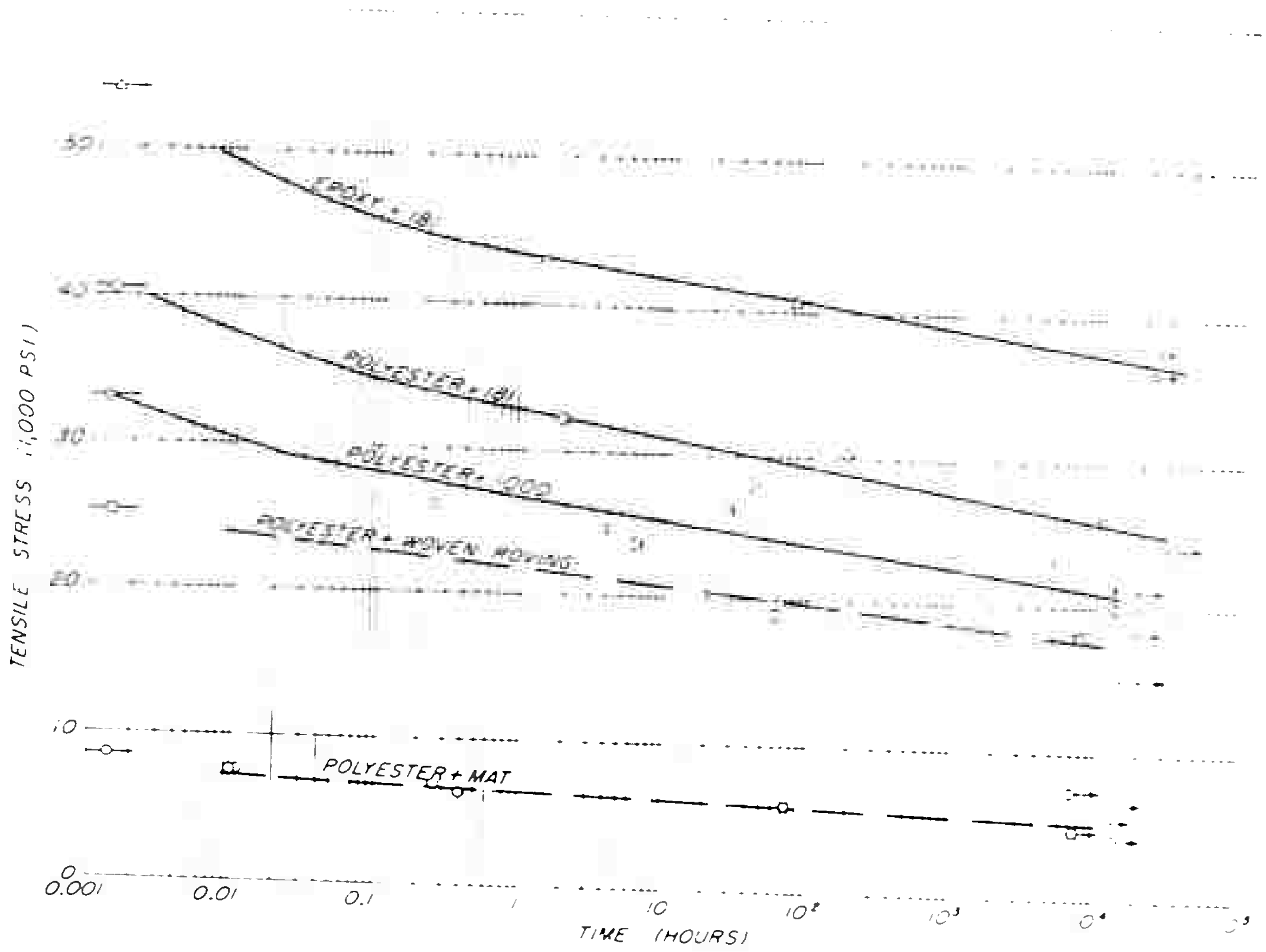

Figure 7.--Tensile stress-rupture curves of glass reinforced plastic laminates tested at normal conditions.

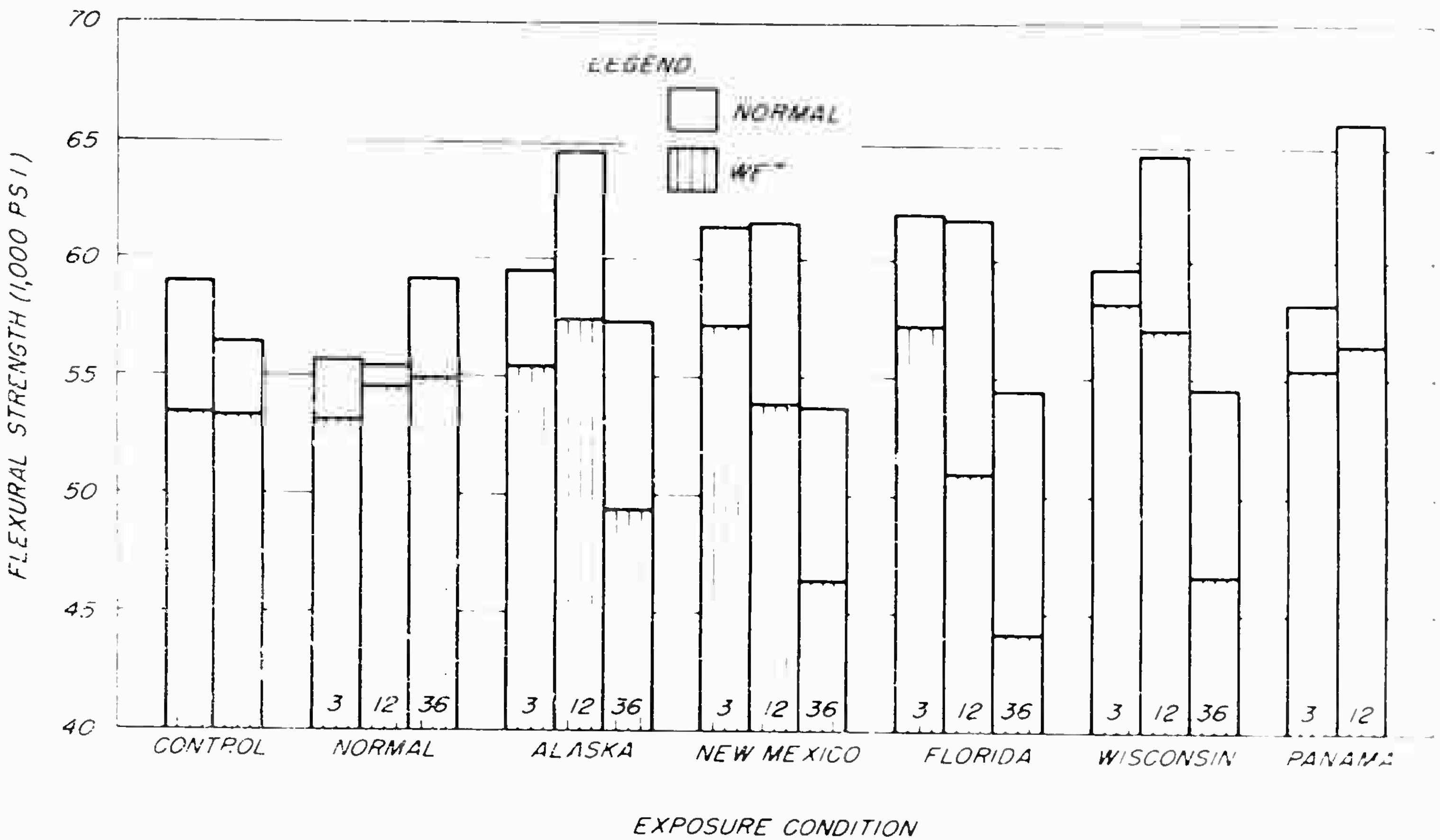

Figure 8.--Flexural strength of Selectron 5003 laminates reinforced with 181-Garan glass fabric. Except for controls, tests were made after 3, 12, and 36 months' exposure of subpanels.

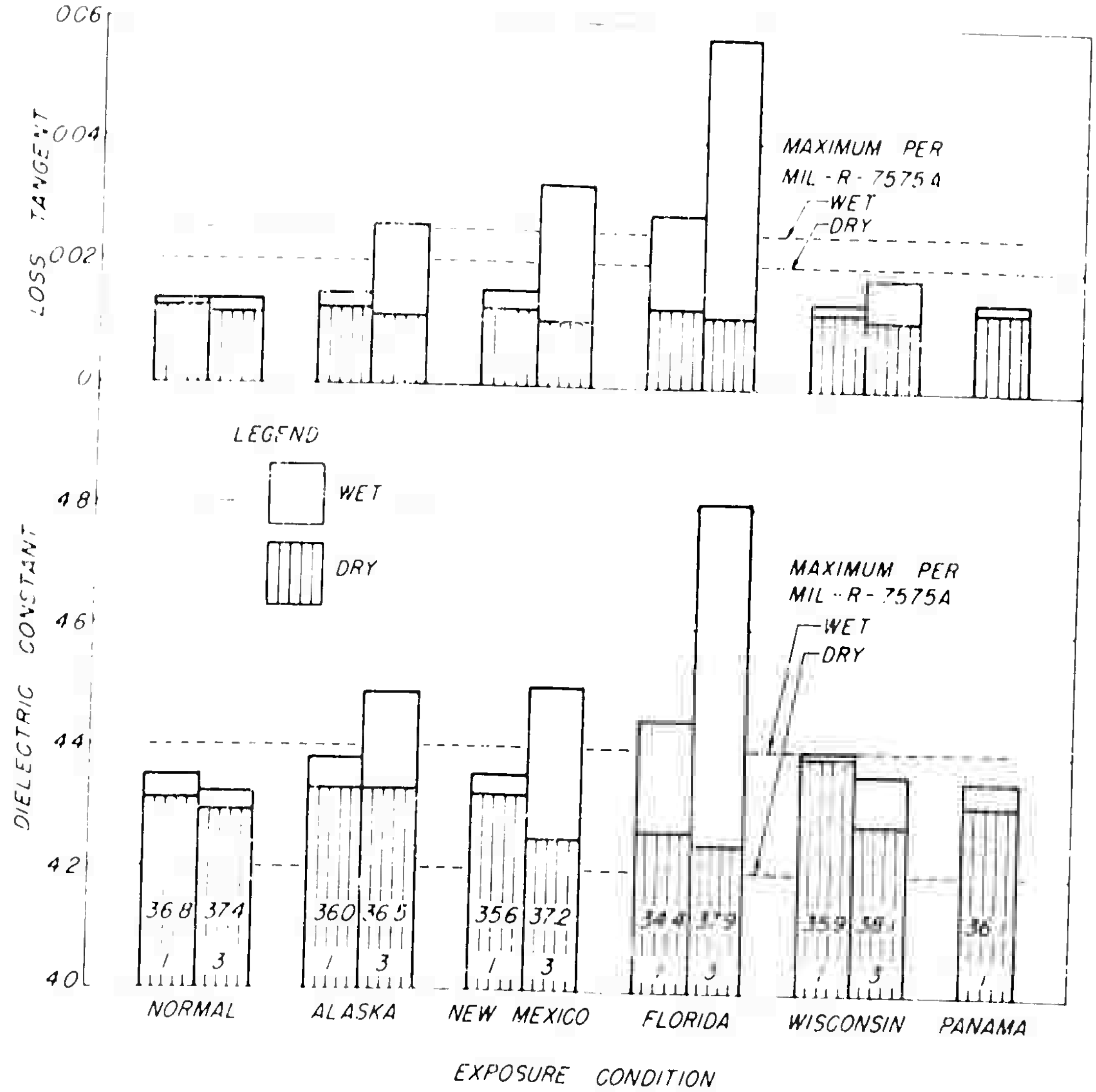

Figure 9.--Electrical properties of Selectron 5003 laminates reinforced with 181-Garan glass fabric. Tests were made after 1 year and 3 years' exposure. Figures on bars show percent of resin content and years of exposure.

HIGH SPEED TESTING OF STRUCTURAL FOAMS AND REINFORCED LAMINATES

Ross H. Supnik (1)
Melvin Silberberg

Plas-Tech Equipment Corporation
Waltham, Mass.

INTRODUCTION

During the past few years in testing laboratories throughout the country there has been growing concern over the effects of rate of loading on the mechanical properties of materials. Polymeric sub[illegible] are particularly rate sensitive, and some plastic materials be[illegible] substantially different manner when subjected to shock l[illegible] [illegible] several thousand inches per minute than when subjected [illegible] conventional loading rates of [illegible] inches per minute. Inform[illegible] as to which materials are rate sensitive and to what degree [illegible] extremely important in designing structures which may be subjected [illegible] shock loading conditions in actual use.

Test equipment has recently been developed [illegible] to measure the strength properties of materials shock loaded by means [illegible] the rapid release of compressed gas. Published papers on this subj[illegible] have already presented data on the dynamic tensile properties of [illegible] thermoplastic materials (1-5).[2] In general, modulus of elasticity [illegible] tensile strength are greater while strain at fracture is lower than the [illegible] observed in slow speed, static tests. You are all familiar with the [illegible] behavior of putty. When load is a[illegible] slowly, it draws out like taffy, [illegible] when struck with a hammer it shatters like glass. It becomes apparent th[illegible] that if a radome member is de[illegible] on the basis of static data and if [illegible] dynamic strength

properties are significantly lower than those under static loading, difficulties may be incurred unless an adequate safety factor is incorporated in the design of the structure. The object of this paper is to compare the mechanical properties measured under dynamic conditions with those measured under static conditions for polyester polyurethane foams and for structural laminates in order to determine the validity of the safety factors which are currently being used in the design of rigid radomes.

TEST EQUIPMENT

The Instron Tensile Tester(3) Model TT-C with X-Y recorder and strain gage pre-amplifier was used to obtain static data, while the Plastechon High Speed Tester(4) was used to measure dynamic properties.

The Plastechon is a universal testing machine in which the load is applied to the test specimen by the action of an air cylinder. Loading rates of 2000-10,000 in./min. are obtained depending on the gas pressure used and the modulus of elasticity of the material being tested. The stress-strain pattern is measured electronically on an oscilloscope, and a permanent record is obtained with a Polaroid Land Camera.

A V-bar extensometer of the strain gage type was used with both testing machines to measure strain in tensile and compression tests.

---

(1) Plas-Tech Equipment Corporation, Waltham, Mass.

(2) Numbers in parentheses refer to References listed in the Bibliography.

(3) Manufactured by Instron Engineering Corporation, Canton, Mass.

(4) Manufactured by Plas-Tech Equipment Corporation, Waltham, Mass.

The extensometer was mounted directly [illegible] was recorded as the Y axis of the stress-strain [illegible] the extensometer was checked both before and after [illegible] the unit on a special fixture and [illegible] the [illegible] produced by the motion of a micrometer head.

For strain measurements in flexure, the crosshead travel of the machine was used. On the Plastechon this was obtained with a [illegible] Linear Variable Differential Transformer.[5] This unit consists of a shielded cylindrical coil of wire and a permanently magnetized iron rod. As the rod moves through the coil, lines of flux are cut, and the resultant signal is amplified and transmitted to the oscilloscope as a beam deflection. A calibration curve of beam deflection vs platen travel was obtained prior to testing and checked immediately thereafter.

TEST METHODS

Tests on the laminates were run in accordance with Federal Specification L-P-406, while those on the foam were run in accordance with the Tentative Methods of Test for Rigid Cellular Materials proposed by the Society of the Plastics Industry. Specimen sizes were altered in some cases to allow for load and weight limitations in the equipment,[6] but in each test the same specimen size was used for both static and

---

(5) Manufactured by The Sanborn Company, Waltham, Mass.

(6) Test specimens used for compression tests in foam were 7/8x7/8x7/8 in. instead of 2x2x2 in. because of the high loads required by high density materials.
Test specimens for compression tests on laminates were ½x1/8x2½ in. instead of ½x1/8x3½ in. to minimize weight requirements [illegible] in dynamic tests.

ading for a direct comparison. Flexural tests on foam were run on 1x1x-4 in. specimens with a 2-in. span since no standard flex test for foam exists at the present time. Tests performed ... the results obtained are demonstrated in the following figures:

Figure ... is a photograph of the Plastechon High Speed Tester. ... the sample is placed in suitable grips and it is mounted ... the two platens. The top is stationary, while the bottom is ... through a coupling to the shaft of an air cylinder. When the ... the bottom platen is forced downward loading the sample

... marizes the tests on structural foams. Tensile, ... ression tests were run on foams of each of three ... o, ... and 30. Tensile and Flexural tests were run ... direction of foaming, while compression tests were run ... perpendicular to and parallel to the direction of foaming ... represent averages of 3, 4 or 5 tests as indicated in paren... trends can be noted from these averages. However, ... of individual test specimens varied within and between ... this compilation of averages could be somewhat mislead... figures demonstrate these properties as a function of ... individual test specimens.

In Figure 3 is ... modulus vs density. Little difference exists between ... mic values for densities up to 10 lb/ft^3. As density ... , little change is noted in the

dynamic modulus, while the static modulus continues to climb and to a different order of magnitude.

Tensile strength and elongation at break are plotted vs foam density in Figure 4. Tensile strength increases as density increases, with lower values observed in dynamic tests than in static tests for densities greater than 10. Elongation decreases markedly as density increases from 6 to 12 in static tests, while in dynamic tests not much difference in elongation is noted as density increases. Above 12 lb/ft^3 elongation in dynamic tests is greater than that in static tests.

Compressive modulus vs density (see Figure 5) shows the same type of pattern as does tensile modulus vs density. Above a density of 15 lb/ft^3 dynamic modulus is lower than the static modulus. The rate of change of dynamic modulus with density is small, while the static modulus increases quite rapidly. Compressive stress at 2 percent strain plotted vs density in the next figure shows the same relationship, (see Figure 6).

Flexural results indicate a reversal in this pattern. Here the dynamic modulus is <u>higher</u> than the static modulus for all densities, and rate of change of dynamic modulus increases markedly above a density of 28. (See Figures 7 and 8) This is not observed in static tests, although for densities greater than 31, this may occur.

Flexural strength and deflection at break are plotted vs density in Figure 8. No difference in flexural strength is noted between the two test speeds, except at the highest densities. Deflection at fail in the dynamic range is only half that in the static range for all

densities.

The reversal noted in flexural modulus is attributed to an error incurred in the flexural test applied to foam materials. Since the samples were loaded as a simple beam and loaded in the center, all specimens had a noticeable indentation of the foam at the supports and loading nose. Thus, the observed strain is greater than the strain which would have been observed in the absence of indentation, and the observed modulus is lower than the actual modulus. This indentation and thus the error incurred is probably different for each density, and this difference is reflected to a greater extent in static tests than in dynamic tests. This error also accounts for the lack of agreement noted in modulus values in the static range. Flexural modulus was in a lower order of magnitude than the tensile and compressive modulus.

The small change of dynamic, tensile and compressive moduli with density as density increases from 14 to 30 lb/ft^3 in contrast to the large change in the static values may be attributed to one or both of the following factors:

1. The mechanism of loading on the sample.
2. Temperature effects.

Mechanism of Loading - In static tests in tension, for example, both polymeric chains and cell structure orient along the direction of pull, thus increasing the stiffness and tensile strength in the process. In dynamic tests, since the pulling action is complete in a few milliseconds, there is no time for such orientation to take place. This

is indicated to some extent by the nature of the break. Samples broken in static tests possess a rough contour at the cross section. The cross section of the same material broken in dynamic tests is considerably smoother, almost conchoidal in appearance.

Temperature Effects - The time for fracture of the tensile specimen varied from 3 milliseconds for the 8 lb/ft^3 foam to 4 milliseconds for the 30 lb/ft^3 foam. During this rapid load application enough heat may have been generated to contribute to the low modulus of elasticity observed for the higher density foams. It is logical that this heat could be more readily dissipated into the air spaces of the low density foams so that this effect is not as noticeable below 14 lb/ft^3 density.

Figure 9 summarizes the test results obtained on structural laminates. Flexural and compressive tests were run on Paraplex 43, Hetron 92 and Epon 828 each made up into 1/8-in. laminates with each of two glass cloths; 181 and 184 (Volan Finish). As you can see, flexural modulus was 10-20 percent lower in the dynamic range than in the static range. Compressive modulus and compressive strength were also generally lower in the dynamic range than in the static range, but by an amount that was somewhat greater and less consistent from material to material. Flexural strength, however, was greater in the dynamic range than in the static range for all materials except Hetron 92 with 184 glass cloth. These values appear to correlate with the appearance of the broken specimen. Samples broken on the Plastechon showed more

evidence of delamination than those broken on the Instron. Hetron 92 with 184 glass cloth, on the other hand, showed a completely different type of fracture on the Plastechon. One ply separated from the body of the specimen during the test, and this may have resulted in the lower strength value.

The large variation noted in comparative compressive properties is attributed to the small number of tests averaged. While five specimens were tested for each material, in some instances averages were based on less than five tests due to difficulties associated with testing technique. Refinements in technique are desirable to prevent misalignment of the compression cage and to prevent slippage of the extensometer.

CONCLUSIONS

In conclusion, tensile, flexural and compressive properties were measured on polyester polyurethane foams of 6 to 32 lb/ft^3 density, and flexural and compressive properties were measured on a limited number of structural laminates. Data was obtained at static loading rates of 0.05-0.1 in/min with failure occurring in a matter of minutes and at shock loading rates in the order of magnitude of 2000 in/min with failure occurring in a matter of milliseconds. The latter velocity corresponds to that of some wind gusts in stormy weather. Modulus and strength values of some of these materials were significantly different when measured at shock loading rates than when measured under static loading rates.

Strength values of materials in the shock loading range should therefore be considered in the design of rigid radomes, which are occasionally subjected to high wind velocities.

ACKNOWLEDGEMENT

Sincere thanks are due Mr. M. M. Hannoosh and Mr. S. C. ...o of the ... Laboratory for defining the scope of the program and to Professor Albert G. H. Dietz of M.I.T. for his valuable assistance in interpreting the significance of the data.

BIBLIOGRAPHY

1. Dietz, A. G. H. and McGarry, F. J., "The Effects of Speed in the Mechanical Testing of Plastics", Symposium on Speed of Testing, ASTM, 1956.

2. Forsey, J., McGarry, F. J., and Dietz, A. G. H., "High Speed Tension Testing Machine for Plastics", ASTM Bulletin, January 1956.

3. Ely, R. E., "High Speed Tensile Tests of Thermoplastics," Plastics Technology, November 1957.

4. Strella, S., Sigler, H., Chmura, M., and Holman, E., "A High Speed Tension Testing Machine", ASTM Bulletin, February 1958.

5. Rugger, G. R., McAbee, and Chmura, M., "Effects of Rate on Tensile Properties of Plastics", Papers and Program for the 1958 Design Engineering Conference, ASME.

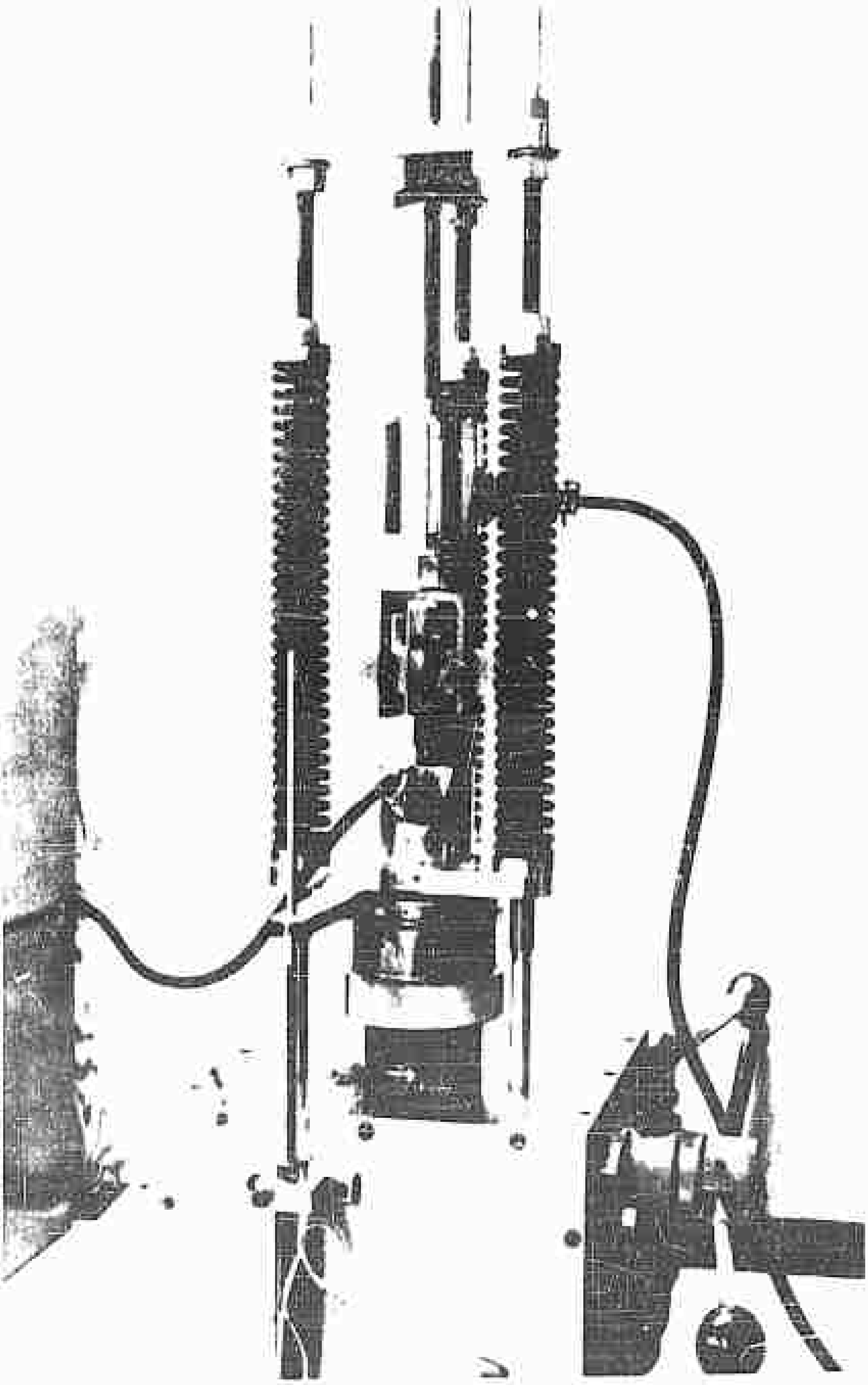

FIGURE 1 [illegible] with [illegible] Sample Mounted ([illegible])

FIGURE 2 **PROPERTIES OF POLYURETHANE FOAM OBTAINED UNDER STATIC AND DYNAMIC RATES OF LOADING**

Density, lb/ft^3	Static 6	Static 14	Static 30	Dynamic 6	Dynamic 14	Dynamic 30
Tensile						
Strength at Break, psi	102(5)	257(4)	1040(3)	122(5)	222(4)	760(3)
Elongation at Break, %	5.1	2.8	1.8	3.5	1.8	3.3
Modulus, psi	2460	8260	289,000	2620	10,100	10,400
Flexural						
Strength at Break, psi	180(5)	655(3)	2070(4)	206(5)	630(3)	1995(4)
Deflection at Break, in.	0.[illegible]6	0.13	0.11	0.17	0.05	0.08
Modulus, psi	1010	4750	17,[illegible]	2890	19,400	79,100
Compressive						
Stress at 2% Strain, psi ∥	82.5(5)	429(4)	1[illegible]0(4)	102*(5)	347(5)	514(5)
⊥	126 (5)	465(4)	1[illegible]70(4)	131**(5)	345(4)	502(4)
Stress at Yield, psi, ∥	39.3	450	2020	102	671	1045
⊥	140	51[illegible]	2300	148	697	1833
Modulus, psi ∥	18,500	27,000	129,000	23,000	54,400	44,600
⊥	34,600	29,500	102,000	24,100	56,500	43,000

* 3 out of 5 specimens yielded below 2% deformation.

** 4 out of 5 specimens yielded below 2% deformation.

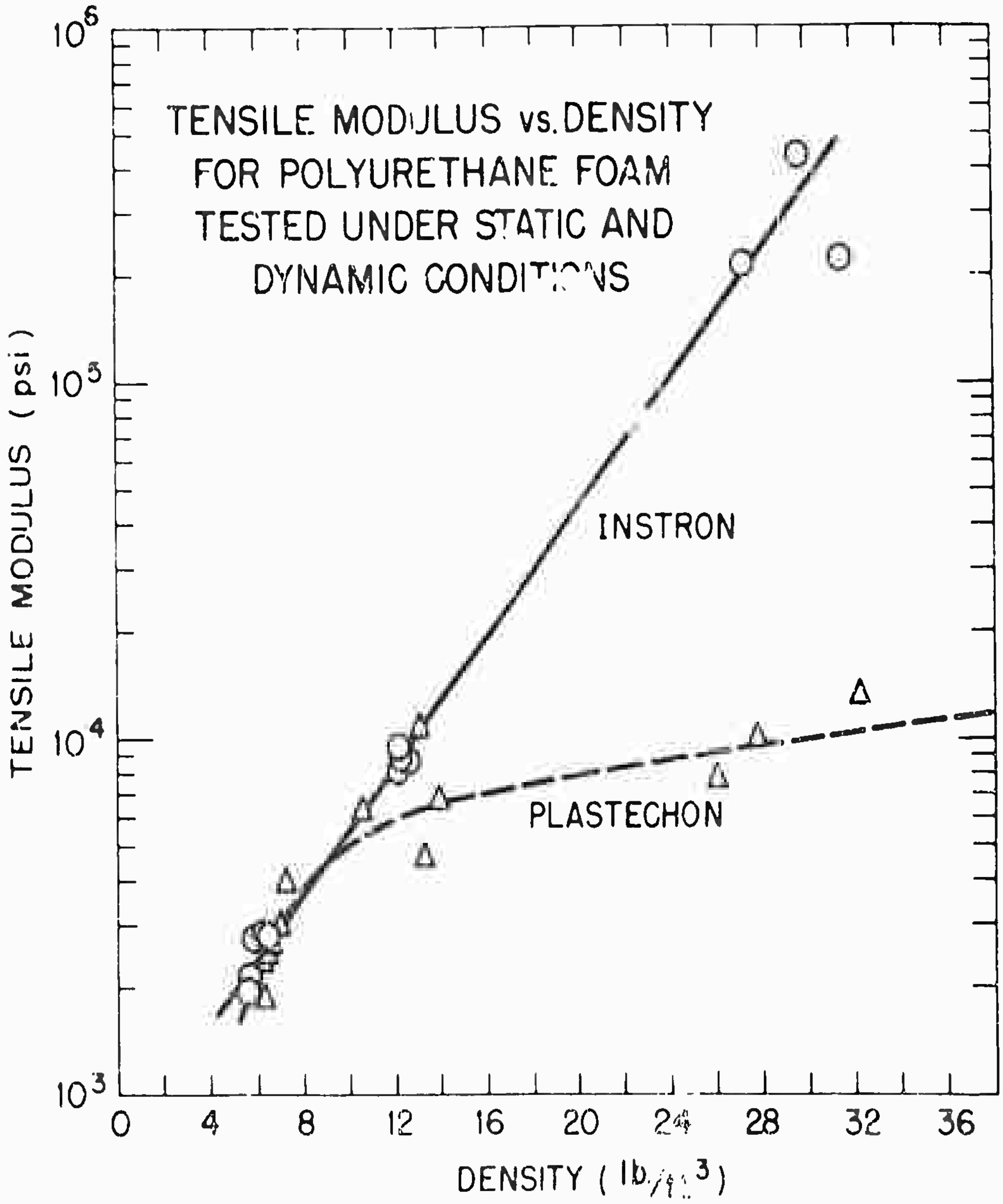

FIGURE 3 Tensile vs Density

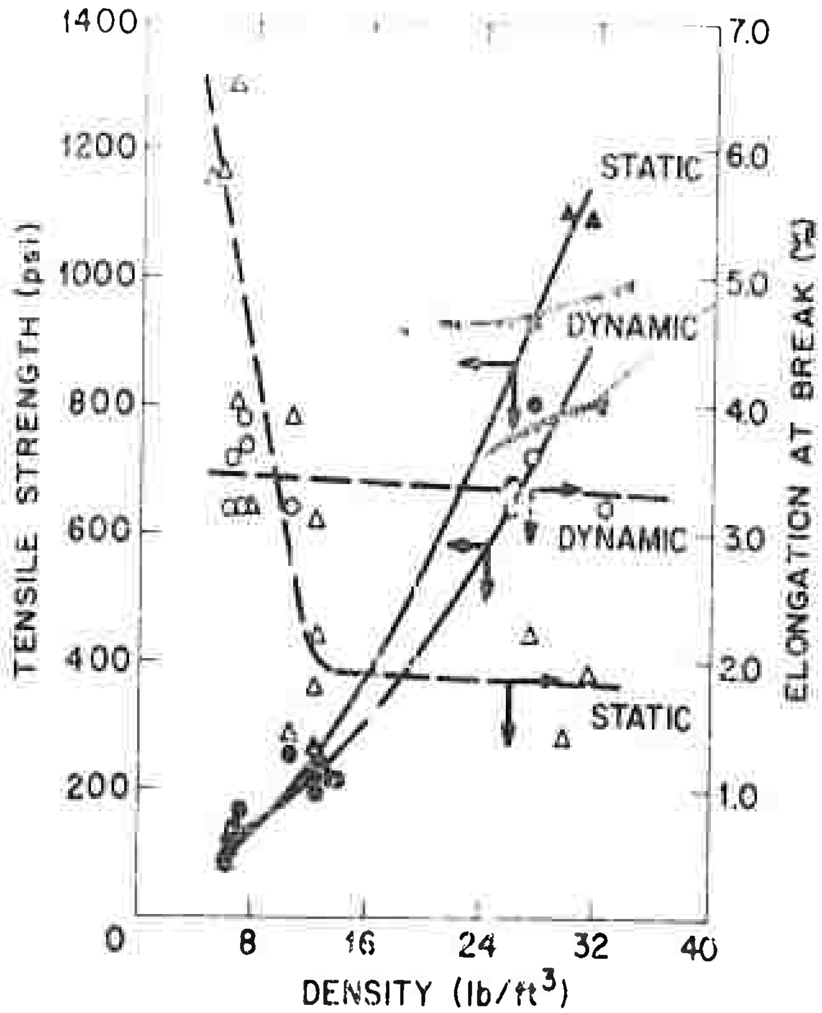

TENSILE PROPERTIES vs. DENSITY FOR POLYURETHANE FOAM OBTAINED UNDER STATIC AND DYNAMIC LOADING RATES.

FIGURE 4 Tensile Properties vs Density

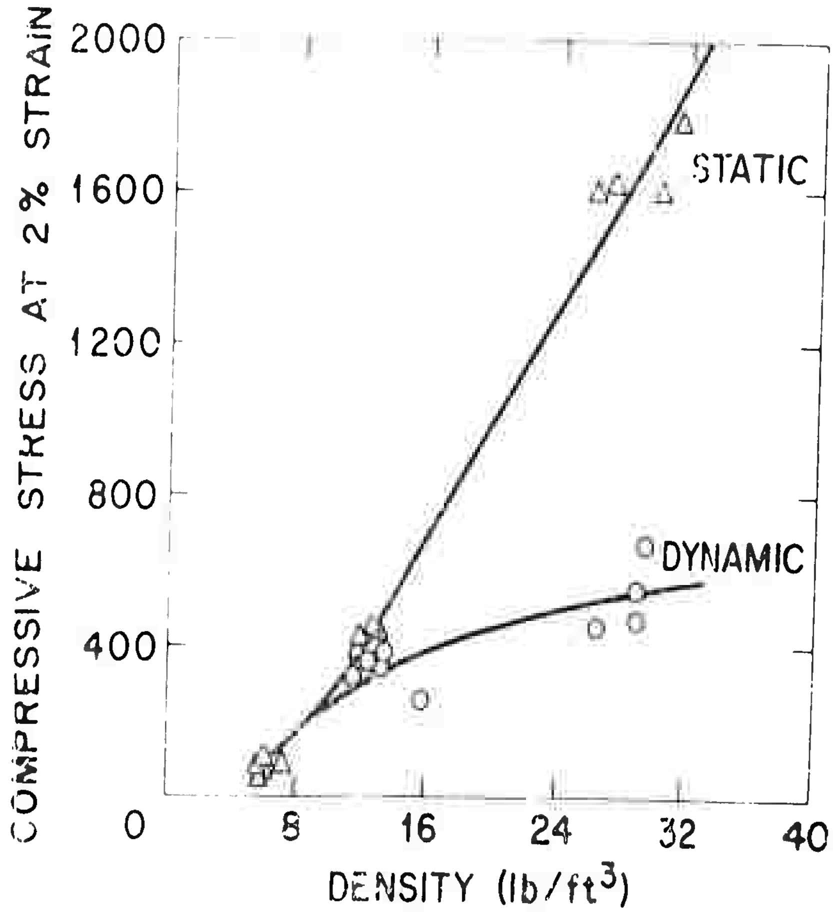

COMPRESSIVE STRESS AT 2% STRAIN vs. DENSITY FOR POLYURETHANE FOAM OBTAINED UNDER STATIC AND DYNAMIC LOADING RATES (lead applied parallel to direction of foaming).

FIGURE 6 Compressive Stress at 2 Percent Strain

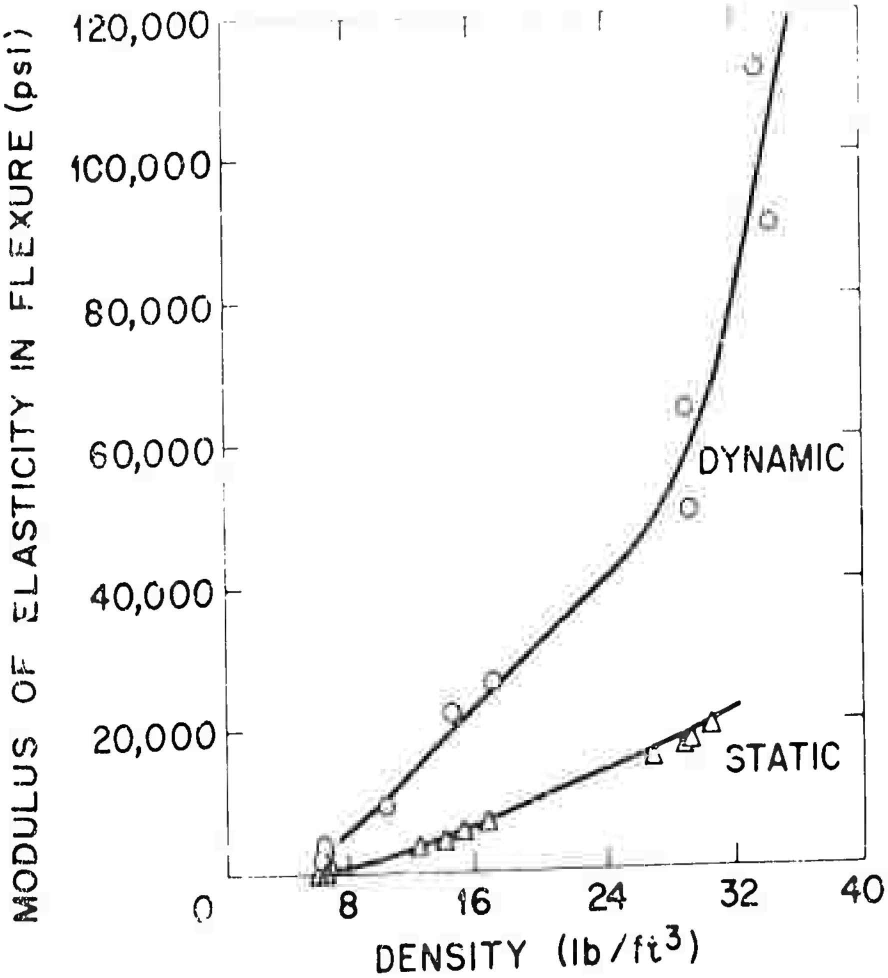

FLEXURAL MODULUS vs. DENSITY FOR POLYURETHANE FOAM OBTAINED UNDER STATIC AND DYNAMIC LOADING RATES.

FIGURE 7 Flexural vs Density

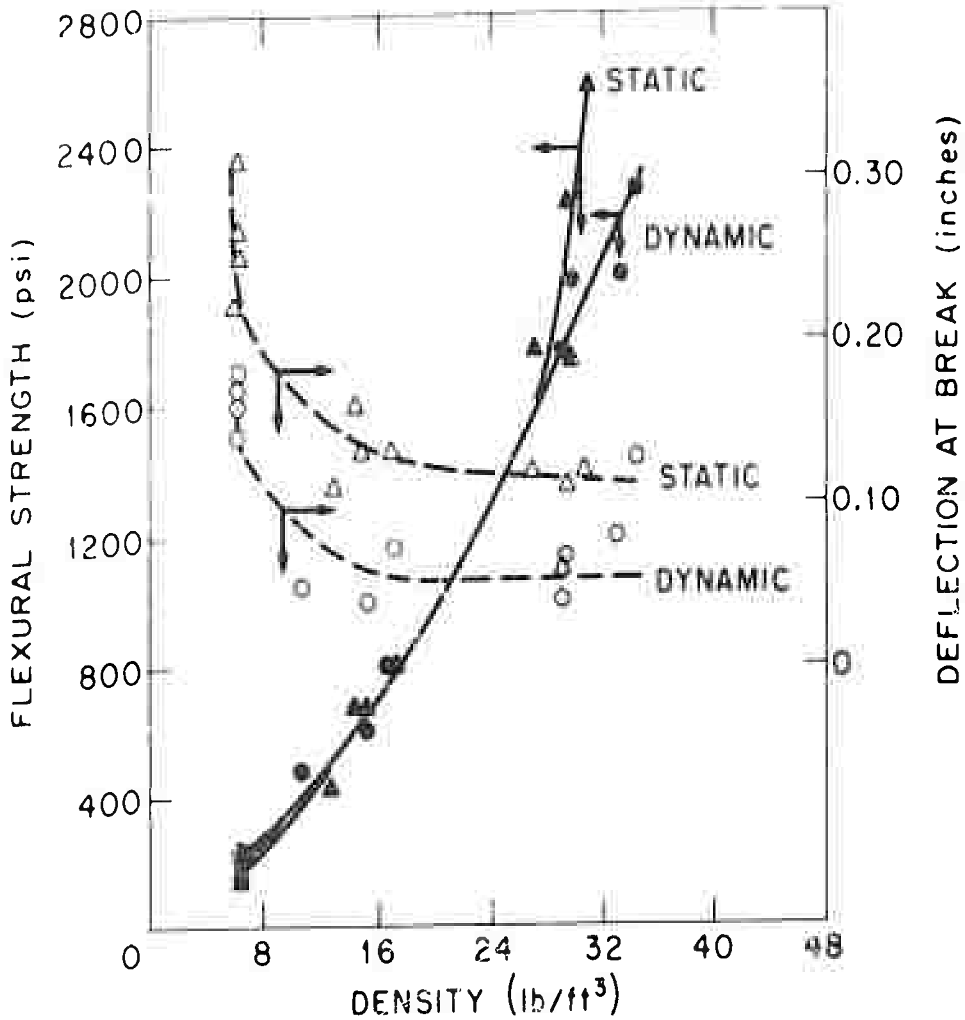

FLEXURAL PROPERTIES VS. DENSITY FOR POLYURETHANE FOAM OBTAINED UNDER STATIC AND DYNAMIC LOADING RATES

FIGURE 8 Flexural Properties vs Density

Resin						
[illegible]						
TENSION:						
Strength at [illegible]	[illegible]	[illegible]	[illegible]	[illegible]	[illegible]	[illegible]
[illegible]	[illegible]	[illegible]	[illegible]	[illegible]	[illegible]	[illegible]
Modulus, psi x 10 [illegible]	[illegible]	[illegible]	[illegible]	[illegible]	[illegible]	[illegible]
COMPRESSION:						
Strength at [illegible]	[illegible]	[illegible]	[illegible]	[illegible]	[illegible]	[illegible]
Modulus, psi x [illegible]	[illegible]	[illegible]	[illegible]	[illegible]	[illegible]	[illegible]

* All values [illegible] indicated [illegible]

[illegible] Laminates Obtained Under Static and Dynamic Loading